



**UCL**

**Micromechanical investigation of  
hydrate-bearing sediments with  
Discrete Element Method**

Yanxin Yu

Department of Civil, Environmental and Geomatic Engineering

University College London (UCL)

A thesis submitted for the degree of

*Doctor of Philosophy*

December 2014



## **Declaration**

I, Yanxin Yu, hereby declare that, except where specific references are made to the work of others, the contents of this dissertation are original and have not been submitted in whole or in part for consideration for any other degree of qualification at any other University. This dissertation is the result of my own work and includes nothing which is the outcome of work done in collaboration. This dissertation contains less than 60,000 words.

---

Yanxin Yu

December 2014

## **Abstract**

Natural methane hydrate soil sediments attract worldwide interest, as there is huge commercial potential in the immense global deposits of methane hydrate that lies under deep seabeds and permafrost regions. Methane hydrate develops and exists in the pores of soil sediments under the conditions of high pressure and low temperature. The methane hydrate-bearing sediment can be exploited to extract methane gas, as methane gas is the predominant element of natural gas. However, the sediment's geomechanical behaviour is poorly understood, but it has impacts on geotechnical issues, such as the instability of the seabed sediment layers and wellbore collapse, and it may also cause various negative environmental effects, particularly in regards to the exploration and exploitation process. Hence, further scientific research is needed.

Due to the limitations of in-situ and laboratory studies, in this PhD research, a numerical method Discrete Element Method (DEM) was employed to provide a unique particle-scale insight into the granular geomechanical behaviours of hydrate-bearing sediment. A comprehensive DEM research was performed in order to simulate two commonly used geomechanical investigation methods employed in hydrate-related studies: the triaxial compression test and seismic wave propagation.

Accordingly, the six major contributions of this DEM research are: (1) two typical types of microscopic hydrate distribution patterns within soil pores were investigated via a consistent basic soil model: the pore-filling hydrate pattern and the cementation hydrate pattern; (2) The large-strain deformation and the critical state behaviours were explored; (3) a wave propagation study was performed using the DEM hydrate-bearing sediment samples; (4) the bonding strength effect in the cementation model was systematically discussed; (5) the effect of elongated soil particles on the geomechanical behaviours of sediments was studied; and most importantly (6) a comprehensive particle-scale microscopic analysis was conducted to assist the interpretation of the macro responses in the in-situ, laboratory and numerical studies.

## **Acknowledgements**

The completion of this PhD research project was only made possible thanks to the support of numerous people. Without their kind help, I would not have been able to complete, or have enjoyed my studies, at University College London (UCL).

Firstly, I would like to express my extreme gratitude to Dr Yi Pik Helen Cheng, my principal supervisor. Since accepting my PhD application in 2009, she has been supportive, attentive, caring, inspiring, encouraging and patient with me throughout my studies. I feel lucky to have had such an intelligent, enthusiastic and hardworking supervisor. Besides all the regular meetings with her at UCL and University of Cambridge, she spent lots of her own time, including weekends, holidays and even late nights advising me in online meetings and over emails. I can remember all her encouragement and support during my scholarship application; the online meetings on a Saturday during her sabbatical in Singapore; her patience when repeatedly revising my first research poster and conference paper ; as well as her support and positivity when I began to attend international conferences. Many thanks, Helen.

I am also sincerely grateful to my external supervisor Professor Kenichi Soga. It has been a great pleasure, and extremely fruitful to have had a monthly meeting with him at University of Cambridge. His insight, vision and experience has helped inspire me and helped foster a great many fresh ideas and thoughts. For every step of my study, he has always helped me progress, pointing out problems in the most constructive and polite fashion, and kindly advising me in further investigations and towards a more in-depth understanding of my research. I would also like to thank him for recommending me to Schlumberger for my internship. Always happy and supportive, it has been an honour to work with him.

I would like to thank my subsidiary supervisor Dr Paul Greening. He has been very supportive and caring, especially in my first year at UCL when Helen was on her sabbatical. I benefitted from his guidance in our weekly meetings. He encouraged me

to read more published papers and report to him each week. I also obtained lots of important advice from him about my initial DEM sample preparation.

I would like to give special thanks to my best friend and colleague Dr Xiaomin Xu. His wide and in-depth knowledge of soil mechanics and DEM constantly enlightened me; his extreme diligence and working attitude also inspired me, and he was always there with a helping hand. Without him, it would have been impossible to have completed my PhD project successfully. I will not forget all of our hard working days and nights.

I would like to thank the Ministry of Education of China, the UK government's BIS Department and UCL, for the UK-China Scholarships for Excellence and their full financial support, providing me tuition fees, living expenses, and research funding. I would also like to thank UCL for financially supporting me to attend many international conferences abroad. In addition, I really cherished my half a year part-time study at London Business School (LBS) under the UCL Advances Enterprise Scholarship.

I am very grateful for the help given by my two best friends: Stefano Belloro and Ewan Wilson. Stefano Belloro taught me how to produce high quality research posters, as well as helping me with graphic design throughout my whole PhD research period. Ewan Wilson helped me with the proof reading of my written work since my first published research paper at UCL. He was always there when I needed his help. I really bothered both of them far too much, especially towards the end of my PhD thesis. Thank you very much, my friends!

Much of my PhD world builds on the earlier research of Mr. Juan Brugada, and so I sincerely thank him for his previous research. I would also like to thank Dr Jongwon Jung for his kind help with the discussions of the DEM sample preparation. I must thank Dr Beatrice Anne Baudet who kindly passed my PhD application to Helen. I am also thankful to Dr Pedro Ferreira who gave me a lot of precious advice in my MPhil/PhD upgrade examination. I would also like to thank Dr John O'Donovan for his help and our discussions of the DEM simulations.

I'm very grateful for all the help given to me by those at UCL: Dr Hop Minh Nguyen, Prof Zhengxiao Guo, Ms Jing Chang, Mr George Printezis, Ms Shanaz Begum, Dr Taku Fujiyama, Dr Raul Fuentes, Prof Itai Einav, Mr Lee Phillips, Prof Nick Tyler, Ms Sarah Davies, Ms Cerine Yudin, Simon, Mr Mike Dunderdale, Ms Janette Yacoub, Mr Richard Sharp, Ms Liselot Hertel, Mr Les Irwin, Mr Nuo Duan, Mr Hossein Bahrami, Dr Benjy Marks, Dr Thomas Miller, Dr Philippe Duffour, Dr Andy Chow, Dr Yun Bai, to name but a few.

I also cherish all my friends who have seen me through both the good and bad times in the UK and helped shoulder the stressful load built up through my studies. I must thank Yin Wang, Di Tony Wu, Geng Ashley Zhao, Quanquan Peng, Caiyun Alice Zhang, Xiaobao Mike Chen, Zeping Zhu, Haoyu Yang, Jingtong Zhou, Frank Hu, Xilun Zhang, Jie Wu, Lei Wang, Pin Lu, Caifa Guo, Xiaoyu Han, Ermao Xu, Mingliang Carter Zhou, Ziyi Jiang, Jiaqiu Wang, Yiqi Deng, Betty Wang, Penglei Li, Bo Fang, Zurui Zheng, Ran Gu, Zhenzhen Wang, Ye Pan, Xia Bian, Qi He, Yi Zhang, Fei Jin, Shuai Yuan, Han Xia, Shuyan Chen, Ben Xu, Lei Zhang, Lanna, Billy Ryan, Charlie George, Patrick Rouxel, Yassin Benserghin, Vic Varani, Daniele Varani, and many other friends I will remember for my whole life.

Thanks to all the experiences in my international conference travelling in the United Kingdom, France, the United States, Japan, Australia, etc.. I learned a lot from all of the attendees and was honoured to meet them: Prof Carlos Santamarina, Prof Masayuki Hyodo, Dr Xia Li, Dr Liang Cui, Dr Catherine O'Sullivan, Dr Colin Thornton, Prof Malcolm Bolton, Prof Fulong Ning, Dr Dai Sheng, Prof Yongchen Song, Prof Yong Wang, Dr Jiafei Zhao, Prof Weiguo Liu, Prof Guodong Zheng, Dr Yunfeng Liang, Dr Miko Fohrmann, Prof Hideki Minagawa, Prof Masanori Kurihara, Prof Carolyn Ann Koh, Dr Simon Falser, Dr Wei Ke, Dr Junhui Xing, Prof Jingming Xu, Prof Jingsheng Ma, Dr Evgeny Chuvilin, to name but a few.

I would also like to thank Mr Kaibin Qiu for recommending me to Beijing Geoscience Centre (BGC) of Schlumberger for the four months internship. I am very grateful to Mr Gongrui Yan at BGC because he gave me 100% freedom and support to conduct a new research project on the instability analysis of borehole using DEM. The results turned out to be very satisfactory.

Lastly and most importantly, I would like to thank my loving and faithful family: my grandparents, my parents and my sister. Any step and progress which I make in my life are all due to their selfless love and care. I love you!

I am grateful to everyone who helped and cared for me. I wish you all very happy, healthy and successful lives.

# Contents

<b>Contents.....</b>	<b>9</b>
<b>List of Figures .....</b>	<b>17</b>
<b>List of Tables.....</b>	<b>28</b>
<b>Nomenclature.....</b>	<b>29</b>
<b>Chapter 1.....</b>	<b>35</b>
<b>Introduction</b>	
1.1 Background and motivation.....	35
1.1.1 Introduction of methane hydrate.....	35
1.1.2 Methane hydrate sediments .....	36
1.1.3 Difficulties in the exploitation of hydrate-bearing sediments.....	39
1.2 Objectives, research methods and main contributions.....	40
1.2.1 Current research gap of geomechanical investigations into hydrate-bearing sediment.....	40
1.2.2 Objectives, research methods and main contributions.....	41

1.3 Outline of the thesis .....	44
<b>Chapter 2.....</b>	<b>48</b>
<b>Literature review</b>	
2.1 Geomechanical investigations of hydrate-bearing sediments.....	48
2.1.1 Granular material behaviour of hydrate-bearing sediment .....	48
2.1.2 Hydrate distribution patterns in hydrate-bearing sediments .....	50
2.1.3 Geomechanical investigation methods .....	51
2.2 Geomechanical characteristics of hydrate-bearing sediments .....	58
2.2.1 Small-strain stiffness .....	58
2.2.2 Stiffness, strength and dilatancy .....	63
2.2.3 Mechanism analysis of hydrate saturation and bonding strength .....	69
2.3 Numerical modelling: Discrete Element Method .....	71
2.3.1 Pore-filling model.....	71
2.3.2 Cementation model.....	74
2.4 Summary.....	77
<b>Chapter 3.....</b>	<b>80</b>
<b>Sample preparation with Discrete Element Method</b>	
3.1 Introduction .....	80
3.2 Numerical tool: Discrete Element Modelling.....	82

3.2.1 Discrete Element Method .....	82
3.2.2 Particle Flow Code 3 Dimensions .....	85
3.3 Choice of the sample preparation procedures .....	93
3.4 Sample preparation of pore-filling and cementation models .....	95
3.4.1 Input parameters of soil and hydrate particles .....	95
3.4.2 Walls .....	98
3.4.3 Hydrate saturation.....	99
3.4.4 Pore-filling model.....	101
3.4.5 Cementation model.....	102
3.4.6 Models with elongated soil particles .....	105
3.5 Summary .....	107
 <b>Chapter 4.....</b>	 <b>108</b>
 <b>Large deformation behaviour of pore-filling and cementation hydrate-bearing sediments</b>	
4.1 Introduction .....	108
4.2 Triaxial tests setting using DEM .....	109
4.3 DEM simulation results .....	110
4.3.1 Stress-strain responses and comparisons to experimental data.....	110
4.3.2 Stiffness .....	113

4.3.3 Strength.....	118
4.3.4 Volumetric responses.....	121
4.3.5 Critical state.....	123
4.4 Particle-scale analysis.....	127
4.4.1 Particle-scale mechanism analysis.....	127
4.4.2 Bond breakage between particles in cementation model.....	129
4.4.3 Particle-particle contact number in total contacts.....	131
4.4.4 Particle-particle contact force contribution to total deviatoric stress.....	133
4.5 Summary.....	138
<b>Chapter 5.....</b>	<b>141</b>
<b>Small-strain stiffness</b>	
5.1 Introduction .....	141
5.2 Seismic wave propagation procedures in the DEM sample.....	142
5.3 Simulation results and discussions .....	143
5.3.1 Small-strain stiffness at 1MPa confining pressure .....	143
5.3.2 Wave propagation at the confining pressure of 3MPa.....	146
5.3.3 Relations between small-strain stiffness and mid-strain and large-strain behaviours .....	151
5.4 Summary.....	153
<b>Chapter 6.....</b>	<b>156</b>

**Effects of hydrate growth patterns and bonding strength in the cementation model**

6.1 Introduction .....156

6.2 DEM simulation results .....158

    6.2.1 Stress-strain responses .....159

    6.2.2 Strength.....163

    6.2.3 Stiffness .....165

    6.2.4 Volumetric responses.....167

6.3 Bond breakage between particles during the tests .....169

    6.3.1 Bond breakage .....169

    6.3.2 Particle-scale mechanism analysis.....172

6.4 Particle-particle contact force contribution and effect of hydrate/soil contact stiffness ratio .....174

    6.4.1 Particle-particle contact force contribution to the total deviatoric stress.....174

    6.4.2 Effect of hydrate/soil contact stiffness ratio .....176

6.5 Local and global measurement .....179

6.5 Summary.....182

**Chapter 7..... 185**

**Effects of elongated soil particle shape**

7.1 Introduction .....185

7.2 Simulation results and analysis.....	186
7.2.1 Stress-strain responses .....	186
7.2.2 Stiffness .....	189
7.2.3 Strength.....	192
7.2.4 Friction and cohesion.....	197
7.2.5 Volumetric responses.....	200
7.3 Rose diagram .....	204
7.4 Summary.....	210
<b>Chapter 8.....</b>	<b>212</b>

## **Conclusions and recommendations for future work**

8.1 Conclusions .....	212
8.1.1 Sample preparation of DEM hydrate-bearing sediment .....	212
8.1.2 Large deformation behaviour of pore-filling and cementation models .....	212
8.1.3 Small-strain stiffness .....	215
8.1.4 Bonding strength effect and hydrate growth patterns in the cementation model.	216
8.1.5 Effects of elongated soil particle shape .....	217
8.2 Recommendations for future DEM work .....	218
8.2.1 Further parametric studies .....	219
8.2.2 Hydrate distribution patterns .....	220

8.2.3 Particle shape .....	220
8.2.4 Sizes of soils .....	220
8.2.5 Fluid and gas.....	221
8.2.6 Temperature.....	221
8.2.7 Dissociation of hydrate .....	221
8.2.8 Contact models .....	222
8.2.9 Up-scale research.....	222
<b>Appendix A .....</b>	<b>223</b>
<b>Calculation of hydrate saturation in DEM study</b>	
1. Accurate calculation .....	223
2. Close packing .....	224
3. Wasted void space volume at particle contacts .....	226
4. Discussions .....	229
<b>Appendix B.....</b>	<b>230</b>
<b>Yield surface</b>	
<b>Appendix C .....</b>	<b>236</b>
<b>Microstructure evolution</b>	
<b>Appendix D .....</b>	<b>243</b>

## **Commercial potential and exploitation of methane hydrate**

1. The increasing global needs of natural gas.....	244
2. Commercial potential of methane hydrate.....	245
3. Conditions of methane hydrate formation.....	246
4. Exploitation methods of methane hydrate.....	247
5. Difficulties of large-scale commercial exploitation of methane hydrate.....	248
6. Industry of methane hydrate.....	250
7. Summary.....	251
<b>Reference.....</b>	<b>253</b>

## List of Figures

**Figure 1.1:** The burning methane hydrate; the inset: molecule structure of methane hydrate (United States Geological Survey, 2013).

**Figure 1.2:** Known and inferred locations of methane hydrate occurrences worldwide (Collett et al., 2009)

**Figure 1.3:** Sketch diagram of methane hydrate sediment layer zone under deep seabeds and permafrost regions

**Figure 1.4:** 2 Dimensions sketch diagram of natural methane hydrate soil (Soga et al., 2006)

**Figure 1.5:** Methane hydrate phase equilibrium relationship (modified from Soga et al., 2006)

**Figure 2.1:** The methane hydrate resource pyramid (Courtesy of Science Magazine: U. S. Department of Energy, 2011)

**Figure 2.2:** 2-Dimension sketch of the hydrate distribution patterns inside the hydrate-bearing sediments: (a) pore-filling, (b) cementation (yellow: soils; blue: hydrates)

**Figure 2.3:** Mallik 2L-38 wellbore data, Mackenzie Delta, Canada (Collett et al., 1999; Walia et al., 1999; Chand et al., 2004): (a) hydrate saturation estimated from resistivity data, (b) porosity, (c) compression wave velocity  $V_p$  and shear wave velocity  $V_s$  data from acoustic log measurements and VSP (vertical seismic profile) data

**Figure 2.4:** ODP Site 997 wellbore data, Blake Ridge, Leg 164 (Collett and Ladd, 2000; Lee, 2000; Guerin et al., 1999; Wood and Ruppel, 2000; Chand et al., 2004): (a) hydrate saturation estimated from resistivity data, (b) porosity, (c) compression wave velocity  $V_p$  and shear wave velocity  $V_s$  data from acoustic log measurements and VSP (vertical seismic profile) data

**Figure 2.5:** Methane hydrate soil experiment apparatus (Hyodo et al., 2011)

**Figure 2.6:** Cell appurtenances and piping system (Hyodo et al., 2011)

**Figure 2.7:** Observation of Methane hydrate generation (Hyodo et al., 2011)

**Figure 2.8:** Cross section through seismic test apparatus (the pressure cell is omitted in the figure). (Modified from Strokoe et al., 1999 and Priest et al., 2005)

**Figure 2.9:** Wave velocities (compression  $P$  wave and shear  $S$  wave) in the methane hydrate sediments where open symbols represent the field, solid symbols represent the laboratory results, and solid and dashed curves represent the modelling results: (A) compression wave; (B) shear wave (Waite et al., 2009)

**Figure 2.10:** Conclusions of the trends of compression P-wave velocity with hydrate saturation for various growth patterns (Dai et al., 2012)

**Figure 2.11:** The effect of hydrate distribution patterns on small strain stiffness by Clayton et al. (2010)

**Figure 2.12:** The stress-strain behaviour and volumetric response of natural hydrate-bearing sandy specimens obtained from Nankai Trough (Masui et al., 2006)

**Figure 2.13:** Deviatoric stress against axial strain at various hydrate saturation: (a) strong bond samples (b) weak bond samples (Masui et al., 2005)

**Figure 2.14:** (a) Peak strength; (b) mid-strain stiffness  $E_{50}$  at various hydrate saturation (Ebinuma et al., 2005; Masui et al., 2005; Waite et al., 2009)

**Figure 2.15:** Cohesions, friction angles and dilation angles at the various hydrate saturations of the natural hydrate-bearing specimens (Masui et al., 2006; Soga et al., 2006) and the laboratory synthetic cementation specimens (Masui et al., 2005).

**Figure 2.16:** Toyoura cementation hydrate-bearing sediments with 34% (solid line: Masui et al, 2005) and 38.5% (dashed line: Ebinuma et al., 2003) synthetic methane hydrate under different confining pressures

**Figure 2.17:** Degradation of the secant stiffness of cementation synthetic hydrate-bearing sediment during drained triaxial compression test by Masui et al. (2005)

**Figure 2.18:** Mechanisms of the particle movement controlling the shear strength of methane hydrate sediments (Yun et al., 2007; Waite et al., 2009)

**Figure 2.19:** Triaxial compressional test results (Brugada et al., 2010): (a) stress-strain responses; (b) volumetric responses

**Figure 2.20:** Derived data from simulation results by Brugada et al. (2010): (a) secant stiffness  $E_{sec}$ ; (b) friction angle and cohesion

**Figure 2.21:** Triaxial compressional test results under various confining pressure (Brugada et al., 2010): (a) stress-strain responses; (b) volumetric responses

**Figure 2.22:** Triaxial compressional test results under various hydrate-soil contact stiffness ratios (Brugada et al., 2010): (a) stress-strain responses; (b) volumetric responses

**Figure 2.23:** Triaxial compressional test results under two different initial porosities (Jung et al., 2012): (top) stress-strain relationship; (bottom) void ratio against axial strain

**Figure 2.24:** Critical state line for the cementation model (Jung et al., 2012): (a) critical state line projection on  $p'-q$  plane; (b) critical state line projection on void ratio  $p'-e$  plane

**Figure 2.25:** Biaxial test results under various bonding strength (Jiang et al., 2013): (a) stress-strain responses; (b) volumetric responses.  $R_{tb}$  refers to the bonding strength applied to the hydrate particles.

**Figure 3.1:** Hydrate distribution patterns of methane hydrate soil sample in DEM model: (a) pore-filling, (b) cementation

**Figure 3.2:** Schematic diagram of calculations in a DEM simulation (modified from O'Sullivan, 2011)

**Figure 3.3:** PFC<sup>3D</sup> graphical user interface with plot window (Itasca Consulting Group, Inc., 2008). (a) a plot window; (b) contact forces due to footing load (black and red lines represent the compression and tension forces separately, and the thickness of the lines illustrates the value of forces)

**Figure 3.4:** Notations used to describe a ball-ball contact (Itasca, 2008)

**Figure 3.5:** Force-displacement behaviour of contact occurring at a point (Itasca, 2008)

**Figure 3.6:** 2D Sketch of clump and sphere in PFC

**Figure 3.7:** 2-Dimension sketch diagram of the DEM sample preparation procedure of the hydrate-bearing soil

**Figure 3.8:** Gaussian distribution of soil particles' sizes

**Figure 3.9:** 2-Dimension simplified schematic diagram of the walls at the initial state and the large strain state

**Figure 3.10:** The remaining void space inside the DEM hydrate-bearing soil sediment (2D sketch)

**Figure 3.11:** DEM hydrate-bearing soil samples

**Figure 3.12:** Contact bonds with directions when particles are set transparent in cementation model of  $S_h=10\%$

**Figure 3.13:** Hydrate growth patterns of the cementation model: (a) soil surface coating (b) soil-soil contact gathering

**Figure 3.14:** Replacement of spherical soil particles by elongated clumps.

**Figure 4.1:** Sketch diagram of triaxial compression test

**Figure 4.2:** Deviatoric stress as a function of axial strain: (a) pore-filling; (b) cementation (DEM study)

**Figure 4.3:** Comparisons of deviatoric stress as a function of axial strain between pore-filling and cementation cases at  $S_h=40\%$  (DEM study)

**Figure 4.4:** Deviatoric stress as a function of axial strain of the synthetic weak bond hydrate-bearing sample which was considered as pore-filling case in the laboratory (Experiment study on synthetic hydrate-bearing sediments, Masui et al., 2005)

**Figure 4.5:** Deviatoric stress as a function of axial strain of the synthetic strong bond hydrate-bearing sample which was considered as cementation case in the laboratory (Experiment study on synthetic hydrate-bearing sediments, Masui et al., 2005)

**Figure 4.6:** Stiffness  $E_{sec}$  degradation curve against axial strain: (a) pore-filling model (DEM); (b) cementation model (DEM); (c) experiment cementation case (Masui et al., 2005)

**Figure 4.7:** Mid-strain stiffness  $E_{50}$ : Pore-filling and Cementation models: (a) DEM study; (b) experiment (Masui et al., 2005)

**Figure 4.8:** Mohr circle and failure envelope

**Figure 4.9:** Maximum deviatoric stress  $q'_{(max)}$  at different hydrate saturations: (a) DEM study; (b) experimental study (Masui et al., 2005)

**Figure 4.10:** Peak Failure Envelopes on  $p'-q'$  plane

**Figure 4.11:** Relationship of volumetric strain - axial strain

**Figure 4.12:** Angles of dilation at various hydrate saturations

**Figure 4.13:** Critical State Line (CSL) projection on the  $p'-q'$  plane

**Figure 4.14:** Angles of friction at different hydrate saturations

**Figure 4.15:** Cohesion at different hydrate saturations

**Figure 4.16:** Critical State Line projection on Granular Void Ratio  $e-\ln p'$  plane: (a) pore-filling model; (b) cementation model; (c)  $e-p'$  plane of the DEM study on cementation model (Jung et al., 2012)

**Figure 4.17:** Sketch diagram of the particle-scale mechanisms of particle movements in the deformation process

**Figure 4.18:** Bond breakage in the triaxial test of cementation model

**Figure 4.19:** Particles bond breakage in the triaxial test of cementation model

**Figure 4.20:** Percentage of particles' contact number in total contacts

**Figure 4.21:** Particles' contacts contribution to the deviatoric stress in the triaxial compression test

**Figure 4.22:** Percentage of particles' contacts stress contribution to total deviatoric stress

**Figure 4.23:** Percentage of particles' contacts force contribution at the peak strength state and critical state in the triaxial compression test

**Figure 5.1:** The model for wave propagation

**Figure 5.2:** Comparison of shear  $S$  wave velocities between pore-filling and cementation models at different hydrate saturations (at 1MPa confining pressure)

**Figure 5.3:** Comparison of small-strain shear modulus  $G_{max}$  at different hydrate saturations between pore-filling and cementation models (at 1MPa confining pressure)

**Figure 5.4:** Growth and formation pattern of hydrate particles in (a) pore-filling and (b) cementation models (red lines represent contact bonds)

**Figure 5.5:** Comparison of shear  $S$  wave velocities between pore-filling and cementation models at different hydrate saturations (at 3MPa confining pressure): (a) DEM study; (b) modelling, field and experimental data (reviewed by Waite et al., 2009)

**Figure 5.6:** Comparison of compression  $P$  wave velocities between pore-filling and cementation models at different hydrate saturations (at 3MPa confining pressure): (a) DEM study; (b) modelling, field and experimental data (reviewed by Waite et al., 2009)

**Figure 5.7:** Comparison of small-strain shear modulus  $G_{max}$  at different hydrate saturations between pore-filling and cementation models (at 3MPa confining pressure)

**Figure 5.8:** Comparison of Young's modulus  $E$  at different hydrate saturations between pore-filling and cementation models (at 3MPa confining pressure)

**Figure 5.9:** Relation between small-strain shear modulus  $G_{max}$  and mid-strain stiffness  $E_{50}$  at various hydrate saturation for pore-filling and cementation patterns (at 3MPa confining pressure)

**Figure 5.10:** Relation between small-strain shear modulus  $G_{max}$  and maximum deviatoric stress  $q_{max}$  of the pore-filling and cementation models at various hydrate saturation (at 3MPa confining pressure)

**Figure 5.11:** Relation between small-strain shear modulus  $G_{max}$  and critical stength of the pore-filling and cementation models at various hydrate saturation (at 3MPa confining pressure)

**Figure 6.1:** Hydrate growth patterns of the cementation model: (a) soil surface coating (b) soil-soil contact gathering

**Figure 6.2:** Measurement spheres inside the sample

**Figure 6.3:** Deviatoric stress as a function of axial strain of the Coating and Contact-gathering models

**Figure 6.4:** Deviatoric stress against axial strain at various hydrate saturation: (a) experiment strong bond samples (Masui et al., 2005); (b) experiment weak bond samples (Masui et al., 2005); (c) 2-Dimension DEM data (Jiang et al., 2013), where  $R_{tb}$  refers to the bonding strength applied to the hydrate particles

**Figure 6.5:** Peak deviatoric strength of the Coating and Contact-gathering models at various bonding strength at  $S_h=10\% \sim 40\%$

**Figure 6.6:** Stiffness  $E_{sec}$  degradation curves against axial strain (Coating and Contact-gathering models at  $S_h=30\%$ )

**Figure 6.7:** Volumetric strain as a function of axial strain of the Coating and Contact-gathering models ( $S_h=10\% \sim 40\%$ )

**Figure 6.8:** Volumetric responses from the biaxial test under various bonding strength (Jiang et al., 2013), where  $R_{tb}$  refers to the bonding strength applied to the hydrate particles.

**Figure 6.9:** Bond breakage between particles during the triaxial tests of  $S_h=30\%$  Coating and Contact-gathering models at various bonding strength

**Figure 6.10:** Axial strain at the beginning of obvious bond breakage (0.5% of total bonding contacts) at various bonding strength

**Figure 6.11:** Sketch diagram of the particle-scale mechanisms of particle movements in the deformation process of the coating, contact-gathering and pore-filling models

**Figure 6.12:** Particles' contacts contribution to the deviatoric stress in the triaxial tests with various bonding strength (Coating and Contact-gathering model at  $S_h=30\%$ )

**Figure 6.13:** Particles' contacts contribution to the deviatoric stress in the triaxial tests with the hydrate/soil stiffness ratio of 0.23 at the bonding strength of 0.500 MPa (Coating and Contact-gathering model at  $S_h=30\%$ )

**Figure 6.14:** Triaxial compressional test result of the stress-strain responses under various hydrate-soil contact stiffness ratios (Brugada et al., 2010)

**Figure 6.15:** Stress-strain responses measured by measurement spheres (localization), average particles' contact forces (homogenization) and the wall-based logic (boundary measurement) at  $S_h=30\%$  with 0.005 MPa bonding strength

**Figure 6.16:** Stress-strain responses measured by measurement spheres (localization), average particles' contact forces (homogenization) and the wall-based logic (boundary measurement) at  $S_h=30\%$  with 0.500 MPa bonding strength

**Figure 6.17:** Coating and contact-gathering samples at the axial strains of 0%, 5% and 30% at  $S_h=30\%$  with 0.005 MPa and 0.500 MPa bonding strength

**Figure 7.1:** Replacement of spherical soil particles by elongated clumps.

**Figure 7.2:** Comparisons of deviatoric stress as a function of axial strain of three soil models ( $S_h=0\%$ ).

**Figure 7.3:** Comparisons of deviatoric stress as a function of axial strain: (a)-(d) of three different soil particle shapes models at  $S_h = 20\%$  and  $40\%$  with DEM; (e) experiment weak bond samples (Masui et al., 2005); (f) experiment strong bond samples (Masui et al., 2005)

**Figure 7.4:** Degradation of secant Young's modulus as a function of axial strain of three soil models ( $S_h = 0\%$ ).

**Figure 7.5:** (a)-(d) degradation of secant Young's modulus as a function of axial strain of the three soil models ( $S_h = 20\%$  and  $40\%$ ); (e) change in the secant stiffness of cementing type synthetic hydrate-bearing soils during drained triaxial compression test by Masui et al. (2005)

**Figure 7.6:** Mid-strain stiffness  $E_{50}$  at various hydrate saturations of three soil particle model

**Figure 7.7:** Peak strength (1) of three soil models in DEM study and (2) in experimental study (Masui et al., 2005)

**Figure 7.8:** Critical state strength of three soil models

**Figure 7.9:** Peak Failure Envelopes on  $p' - q'$  plane

**Figure 7.10:** Critical State Line projection on  $p' - q'$  plane

**Figure 7.11:** Angles of friction of three soil models: (a) – (c) DEM study with different aspect ratios of soil particles; (d) Experiment study on the friction angle and cohesion (Masui et al., 2005)

**Figure 7.12:** Cohesions of three soil models

**Figure 7.13:** Comparisons of volumetric strain as a function of axial strain of three kinds of soil models ( $S_h = 0\%$ )

**Figure 7.14:** Comparisons of volumetric strain as a function of axial strain of three kinds of soil models at  $S_h = 20\%$  and  $40\%$

**Figure 7.15:** Dilation angle as a function of hydrate saturation at different aspect ratios

**Figure 7.16:** Critical State Line projection on Granular Void Ratio  $e - \ln p'$  plane

**Figure 7.17:** Rose diagram of contact normal distribution at initial state ( $S_h=0\%$ )

**Figure 7.18:** Rose diagram of contact normal distribution at peak state ( $S_h=0\%$ )

**Figure 7.19:** Rose diagram of contact normal distribution at critical state ( $S_h=0\%$ )

**Figure 7.20:** Rose diagram of contact normal distribution at initial state ( $S_h=40\%$ )

**Figure 7.21:** Rose diagram of contact normal distribution at peak state ( $S_h=40\%$ )

**Figure 7.22:** Rose diagram of contact normal distribution at critical state ( $S_h=40\%$ )

**Figure A-1:** Hexagonal close packing of spherical particles

**Figure A-2:** 2-Dimension sketch of wasted space at particle contacts

**Figure A-3:** Five contact types within the DEM hydrate-bearing sediment and the wasted void space

**Figure B-1:** Dilation enhanced by hydrates (Uchida et al., 2012)

**Figure B-2:** Cohesion enhanced by hydrates (Uchida et al., 2012)

**Figure B-3:** Yield surface of MHCS model (Uchida et al., 2012)

**Figure B-4:** Stress paths of DEM simulations and yield surfaces obtained from the yield points at various hydrate saturations: pore-filling model

**Figure B-5:** Stress paths of DEM simulations and yield surfaces obtained from the yield points at various hydrate saturations: cementation model

**Figure B-6:** Comparisons of yield surfaces of the pure soil samples ( $S_h=0\%$ ), pore-filling samples ( $S_h=40\%$ ) and cementation samples ( $S_h=40\%$ )

**Figure C-1:** Anisotropy evolution during the triaxial tests (spherical soil particles)

**Figure C-2:** Anisotropy evolution during the triaxial tests ( $S_h=0\%$  with various soil shapes)

**Figure C-3:** Anisotropy evolution during the triaxial tests ( $S_i=20\%$  pore-filling samples with various soil shapes)

**Figure C-4:** Anisotropy evolution during the triaxial tests ( $S_i=20\%$  cementation models with various soil shapes)

**Figure D-1:** Global total energy consumption by fuel (BP plc., 2014)

## List of Tables

**Table 1.1:** Methods of geomechanical investigation into methane hydrate sediments

**Table 2.1:** Stiffness and wave velocities for various typical sediments (modified from Mavkov et al., 1998; Soga et al., 2006)

**Table 3.1:** Input parameters for soil and hydrate particles used in the DEM model

**Table 3.2:** Number of soil and hydrate particles at various hydrate saturation in DEM simulations

**Table 4.1:** Comparisons between the obtained peak state friction angle in this DEM research and the calculated peak state friction angle by the sand model

**Table A-1:** Assumption value of hydrate saturation in DEM study according to close packing theory

## Nomenclature

$a$	Material constant that dominates the dilation
$a_d^n$	Normal contact force
$a_{ij}^n$	Symmetric second-order deviatoric tensor (normal contact force)
$a_d^r$	Contact normal
$a_{ij}^r$	Symmetric second-order deviatoric tensor (contact normal)
$a_d^t$	Tangential contact force
$a_{ij}^t$	Symmetric second-order deviatoric tensor (tangential contact force)
$b$	Material constant that dominates the dilation
$B_n$	Normal bonding strength of a hydrate particle
$B_s$	Shear bonding strength of a hydrate particle
$c$	Material constant that dominates the cohesion
$d$	Material constant that dominates the cohesion
$D$	Diameter of a particle
$D_{50}$	Mean value of the particle diameters

$dH$	Axial displacement
$dV$	Volume change of the sample during the triaxial compression test
$e$	Granular void ratio
$c'$	Cohesion
$E_{50}$	Mid-strain Young's modulus
$E_c$	Elastic Young's modulus
$E_c^{hyd} / E_c^{soil}$	Hydrate/soil elastic modulus ratio
$E_{sec}$	Secant Young's modulus
$E(\Omega)$	Symmetric fabric tensor distribution function
$f$	Yield function
$F$	Vector of contact force
$F_n$	Normal force vector at the contact
$F_s$	Shear force vector at the contact
$F_c^n$	Normal contact bond strength
$F_c^s$	Shear contact bond strength
$F_{max}^s$	Maximum allowable shear contact force
$G$	Shear modulus
$G_0$	Initial shear modulus

$G_{max}$	Small-strain shear modulus
$H$	Property of the peak strength state frictional behaviour of the sediment
$H_0$	Initial sample height before shearing
$K$	Bulk modulus
$k_n$	Normal contact stiffness
$K_n$	Normal stiffness at the contact
$k_n^{hyd} / k_n^{soil}$	Hydrate/soil contact stiffness ratio
$k_n^{wall}$	Normal stiffness of a wall
$k_s$	Shear contact stiffness
$K_s$	Shear stiffness at the contact
$k_s^{wall}$	Shear stiffness of a wall
$M$	Property of the critical state frictional behaviour of the sediment
$n$	Porosity of the sediment
$n^c$	Contact normal orientation
$p'$	Effective mean stress
$p'_{cc}$	Hardening parameter for cohesion
$p'_{cd}$	Hardening parameter for dilation

$p'_{cs}$	Yield locus of soil
$q$	Deviatoric stress
$q'$	Effective deviatoric stress
$q'_{(cs)}$	Critical state deviatoric stress
$q'_{(max)}$	Maximum deviatoric stress
$r$	Radius of a ball
$R$	Radius of a ball
$R'$	Hashiguchi's sub-loading surface ratio
$R_{tb}$	Bonding strength
$S_h$	Saturation of hydrate
$S_{MH}$	Saturation of methane hydrate
$u$	Material constant that dominates the plastic deformation
$U$	Overlap of particles' contact
$U_n$	Normal displacement
$U_s$	Shear displacement
$V$	Volume
$V_0$	Initial sample volume
$V_n$	Normal velocity vector at the contact

$V_p$	Compression wave velocity
$V_s$	Shear wave velocity
$x$	Position vector of the centre of a ball
$\varepsilon_a$	Axial strain
$\varepsilon_{a(0)}$	Axial strain at the origin
$\varepsilon_{a(50)}$	Axial strain at the half of the peak effective deviatoric stress
$\varepsilon_v$	Volumetric strain
$\Delta t$	Time step
$\sigma_3$	Confining stress
$\sigma'_a$	Effective axial stress
$\sigma'_c$	Effective isotropic consolidating stress
$\sigma'_d$	Effective deviatoric stress
$\sigma'_{d(0)}$	Effective deviatoric stress at the origin
$\sigma'_{d(50)}$	Half of the peak effective deviatoric stress
$\sigma'_{d(\max)}$	Maximum effective deviatoric stress
$\sigma_{ij}$	Stress tensor

$\sigma_{ij}^{h-h}$	Hydrate-hydrate contact stress tensor
$\sigma_{ij}^{h-s}$	Hydrate-soil contact stress tensor
$\sigma_{ij}^{s-s}$	Soil-soil contact stress tensor
$\sigma'_r$	Effective radial stress
$\phi'$	Angle of friction
$\phi'_c$	Critical state friction angle
$\phi'_p$	Peak strength state friction angle
$\psi$	Angle of dilation
$\tau'$	Shear stress
$\mu$	Coefficient of friction
$\mu^{wall}$	Coefficient of friction of a wall
$\rho$	Density of the sediment
$\rho_t$	Total soil mass density

# Chapter 1

## Introduction

### 1.1 Background and motivation

#### 1.1.1 Introduction of methane hydrate

Methane hydrate ( $\text{CH}_4 \cdot 5.75\text{H}_2\text{O}$ ) is a solid matter formed from water ( $\text{H}_2\text{O}$ ) and methane ( $\text{CH}_4$ ) gas compounding under the high-pressure and low-temperature condition, and is an ice-like clathrate crystalline compound. It looks very much like ice and snow or solid alcohol in appearance, and is combustible upon ignition. Hence, as shown in Figure 1.1, it is also called “Burning Ice” or “Fiery Ice”.

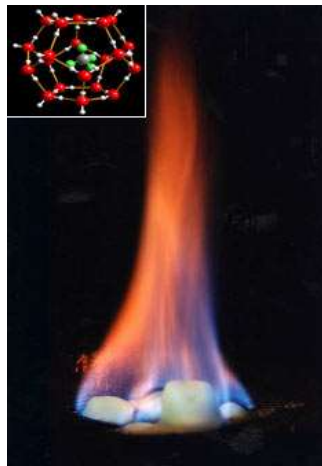


**Figure 1.1:** The burning methane hydrate; the inset: molecule structure of methane hydrate (United States Geological Survey, 2013).

It is positively believed that the history of human’s fuel use will be prolonged for a few centuries in the case of the successful large-scale commercial exploitation of methane hydrate. Methane hydrate contains a huge quantity of heat, in that  $164 \text{ m}^3$  methane gas can be released from  $1 \text{ m}^3$  methane hydrate. It is also known that methane gas is the main constituent of natural gas. The worldwide estimated deposit of methane

hydrate is an astonishingly large figure, which is between tens of thousand trillion and hundreds of thousand trillion cubic meters. Due to the insufficient work actually done on geological exploration, the exact volume of the reserves of methane hydrate has not yet been determined. It is reckoned that the total organic carbon of methane hydrate amounts to more than twice that of the whole world's known reserves of oil, coal and conventional natural gas (Kvenvolden, 1998). The other advantage of methane hydrate is that methane hydrate only produces a small quantity of carbon dioxide and water upon combustion, compared to oil, coal and other fossil fuels that produce additionally miscellaneous oxide pollution. Together this makes methane hydrate a cleaner energy resource with huge deposit.

Since the 1960s, the research and exploration of methane hydrate has drawn more and more attention globally. On 12<sup>th</sup> March 2013, Japan Oil, Gas and Metals National Corporation (JOGMEC) launched a large-scale industrial exploration and successfully extracted methane from a deep-sea methane hydrate sediment layer near the Aichi Prefecture of Japan by means of a depressurization technology, thus making Japan the first country to master the technology of seabed natural gas hydrate excavation. In the depressurization process, the well pressure is decreased in order to allow flow into the well and cause the methane hydrate dissociation by the pressure reduction in the surrounding soil sediment. By pumping the water out of the methane hydrate so as to depressurize it, the methane is separated from the water and finally extracted. Japan is expecting to realize commercial exploitation on an industry scale by 2018. This was the first time that methane gas was successfully extracted from a deep seabed. It is good news for Japan, a country where natural resources are scarce, and also a big breakthrough in the new energy development for the world.

### 1.1.2 Methane hydrate sediments

Methane hydrate can be found in the deep seabed sediment or terrestrial permafrost regions, because only under high pressure and low temperature conditions can it maintain stability. So that methane gas and water forms such an ice-like crystalline material (Brugada et al., 2010). Figure 1.2 shows the known and inferred locations of methane hydrate-bearing sediments in the ocean and the permafrost regions worldwide

(Collett et al., 2009). Moreover, the amount of methane hydrate in the sea is considerably greater than that found in the permafrost areas. One of the reasons for this may be that the deep seabed provides sufficient methane gas for the hydrate formation, due to the production of bacteria methane and the upwelling of methane gas caused by the oceanic plate movement.

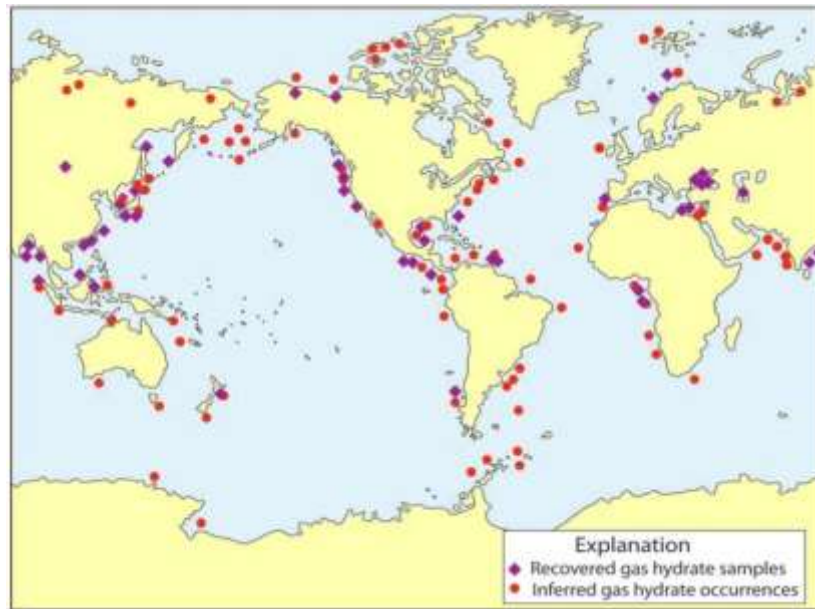


**Figure 1.2:** Known and inferred locations of methane hydrate occurrences worldwide (Collett et al., 2009)

Methane hydrate-bearing sediment is the soil sediment layer in which methane hydrate exists within the pore space of the sediment under the low-temperature and high-pressure deep seabeds or the terrestrial permafrost regions, as illustrated in Figure 1.3. Generally, methane hydrate develops and exists in the pores of highly compacted soil sediments in various distribution patterns, as shown schematically in Figure 1.4 (Soga et al., 2006). The gradual formation of methane hydrate within the pore space of the soil sediment was allowed by the conditions of high pressure and low temperature (for example 100 kPa at  $-80\text{ }^{\circ}\text{C}$  and 2.5 MPa at  $0\text{ }^{\circ}\text{C}$ ), until water or methane gas is 100% used in the formation. As shown in Figure 1.5, the pressure and temperature conditions control the stability of hydrates. The hydrate-gas phase equilibrium line separates hydrates (above the line) from the free gas phase (below the line). This is the reason that methane hydrate sediments are usually found under the deep seabed and the permafrost regions.

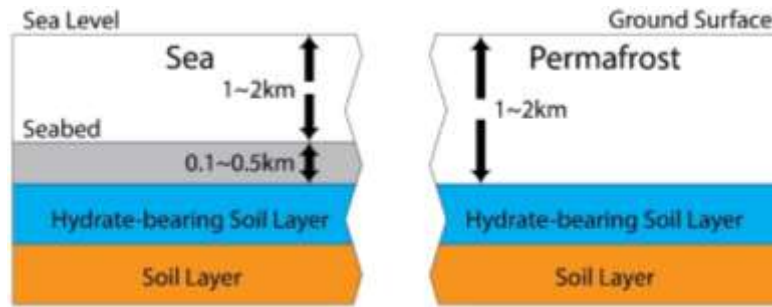


**Figure 1.3:** Sketch diagram of methane hydrate sediment layer zone under deep seabeds and permafrost regions

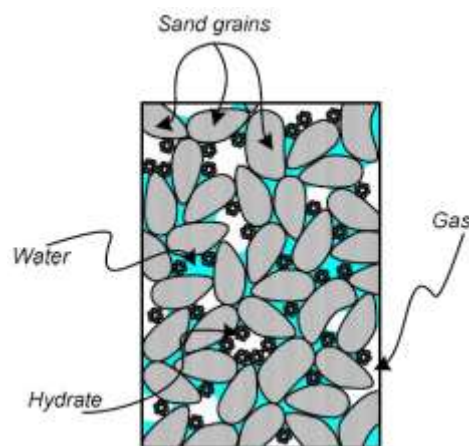


**Figure 1.4:** 2 Dimensions sketch diagram of natural methane hydrate soil (Soga et al., 2006)

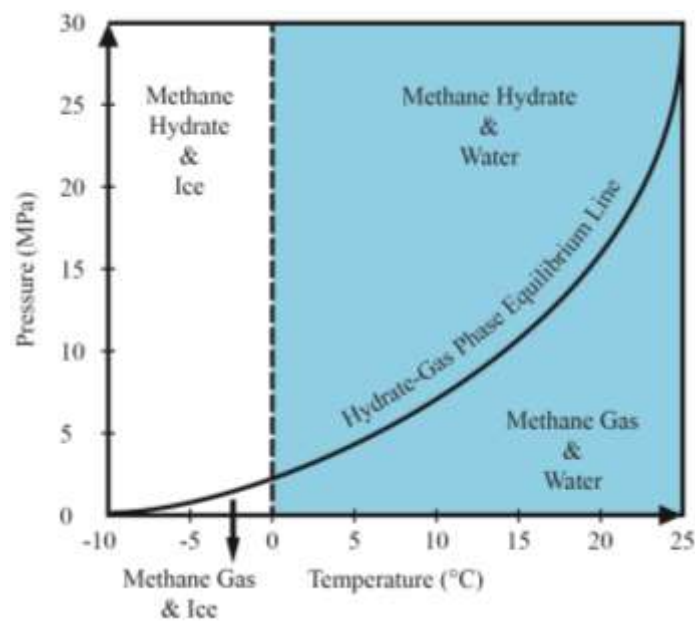


**Figure 1.5:** Methane hydrate phase equilibrium relationship (modified from Soga et al., 2006)

### **1.1.3 Difficulties in the exploitation of hydrate-bearing sediments**

Currently, the large-scale commercial exploitation of methane hydrate from the hydrate-bearing sediments generally confronts three main problems: (1) the technical difficulties; (2) the very high cost; and (3) the environmental disruption. As the exploitation of methane hydrate requires complex and integrated systematic engineering, there is no mature and economical technical solutions for exploitation as of yet, although Japan has experimentally extract methane gas from the methane hydrate sediment in industrial scale. The most acceptable exploitation methods include heat injection, depressurization and chemical injection, which are all costly at present and cannot ensure a stable and safe production process.

From the perspective of the particular geological structure of hydrate-bearing sediments, since methane hydrate typically exists as a filling material with various distribution patterns in the sediments, its formation and dissociation effects on the sediment's strength may induce serious geological disasters and cause geomechanical issues, which do harm to existing underground or under-seabed constructions such as submarine transmission or communication cables. There is also a wellbore stability issue and problems with offshore oil and gas drilling platforms. One example is the BP Gulf explosion in which 3 million gallons of crude oil was poured into the Gulf of Mexico in 2010. The oil drilling process caused the instability of the hydrate-bearing sediment layer near the wellbore, hence inducing the explosion of the platform due to a series of unpredictable issues.

Due to the complexity of its soil sediment's geomechanical properties and the induced instability of its chemical property due to geomechanical issues, the exploitation of gas hydrate may cause various negative environmental effects such as greenhouse effect and damage to ocean ecology balance. It is deemed that methane contributes to global warming 10~20 times more than carbon dioxide does. Even minimal damage to methane hydrate deposits is enough to cause a large quantity of methane gas to release. In addition, if there is a blowout accident in the exploitation process, it may cause serious disasters such as tsunamis, submarine landslides or sea-water poisoning.

Therefore, methane hydrate, as an energy of the future, possesses an impressive prospect, but its development and utilization is a “double-edged sword”, and requires careful approach. In these cases, an in-depth understanding of the geomechanical behaviours of the hydrate-bearing sediments is necessary to be able to improve the characterization and to address both the scientific and industrial needs from one of the essential aspects of methane hydrate research – the mechanism of sediment instability in the drilling process and near the wellbore.

## **1.2 Objectives, research methods and main contributions**

### **1.2.1 Current research gap of geomechanical investigations into hydrate-bearing sediment**

Currently, a combination of various research methods are being conducted to investigate the geomechanical behaviours of hydrate-bearing sediments, including field work, experimental tests and numerical modelling, as briefly summarized in Table 1.1. The seismic technology is mainly used as a geophysics tool for mapping the occurrences of hydrate-bearing sediments, as well as for estimating the saturation of hydrate in the sediment. Besides this, the study of the hydrate-bearing sediments’ strength and how the sediments deform under a loading situation is essential to the industrial analysis of the sediment’s failure near the borehole; and this is also significant to the evaluation of the seafloor stability (Waite et al., 2009)

The in-situ field and laboratory studies provide real data for further studies even though there are still plenty of limitations. One of these limitations is the challenge to proper interpret data without exact knowledge of the hydrate formation, distribution and saturation. On the other hand, most of the existing in-situ, laboratory studies and the numerical modelling methods study only the macro-scale geomechanical behaviours of the methane hydrate soil sediment, missing the links into micro-scale methane hydrate formation and distribution in the pore space of the sediment. It is also important to relate the micro-mechanical behaviours to the geomechanical behaviours observed in the on-site and laboratory studies.

**Table 1.1:** Methods of geomechanical investigation into methane hydrate sediments

<b>Geomechanical Investigation Approach</b>	<b>Field Work</b>	<b>Laboratory Test</b>	<b>Numerical Modelling</b>
<b>Main Method</b>	<ul style="list-style-type: none"> <li>➤ Mapping technologies: seismic / other remote sensing tests</li> <li>➤ On-site sample drilling</li> </ul>	<ul style="list-style-type: none"> <li>➤ Synthetic sample formation</li> <li>➤ Triaxial compression test</li> <li>➤ Seismic wave test</li> </ul>	<ul style="list-style-type: none"> <li>➤ Finite Element Modelling</li> <li>➤ Constitutive Modelling</li> <li>➤ Discrete Element Modelling</li> </ul>

As a complex granular material, the hydrate-bearing sediment, in nature, is not a continuum mass but reflects discrete nature. Within the soil voids, there is hydrate, making the hydrate-bearing sediment a complex aggregate of discrete particles of various sizes and shapes interacting with one another at their contact points. Therefore, the essential and crucial particle-scale investigation is still a research gap which should be systematically conducted.

### 1.2.2 Objectives, research methods and main contributions

In this PhD research, the numerical method Discrete Element Method (DEM) was employed for more insights into the granular geomechanical behaviours of the methane hydrate soil sediment. DEM is a useful numerical simulation tool that models granular materials by specifically considering their actual particulate nature. It also becomes much easier and more convenient to properly control the methane hydrate formation, distribution and saturation. And it is a cheap and safe way to simulate the experiments. Furthermore, the DEM research results can be compared with lab studies in order to improve and develop our understanding of its physical properties. For the simplification, in this research, the temperature is always assumed to be below 0 °C and the pressure at the low temperature should be set above the hydrate-gas phase

equilibrium line as shown in Figure 1.5, in order to avoid the equilibrium phase transition and keep the sample at the hydrate phase all the time.

In this research, a comprehensive DEM simulation study was performed to investigate the material micro-mechanical behaviour in two typical geomechanical methods: the triaxial compression test and seismic wave propagation. Accordingly, this DEM research mainly contributes six major advances to the study of the geomechanics of methane hydrate-bearing soil sediments from the particle scale.

(1) Two typical types of microscopic hydrate distribution patterns within soil pores were studied via a consistent basic soil model: the pore-filling distribution pattern and the cementation distribution pattern.

In most of the previous DEM studies (Brugada et al. 2010, Jung et al. 2012, Jiang et al. 2013), DEM was employed to simulate only one hydrate distribution pattern – pore-filling or cementation. There was no consistent DEM model for the comprehensive comparisons among different hydrate distribution patterns. Hence, it is important to build such a consistent hydrate-bearing sediment model for various hydrate distribution patterns, in order to conduct the comparison studies.

(2) The large-strain deformation and the critical state behaviours were explored.

In the experimental research, there are the limitations for conducting the large-strain deformation study and obtain the critical state behaviours of hydrate-bearing sediments. And in the previous DEM studies, the critical state behaviours were not discussed systematically. A good understanding of critical state behaviour is crucial for developing a comprehensive modelling of the methane hydrate behaviour. Thus, our interest in the sediments' behaviours extended to the large strain deformation and critical state behaviours in the triaxial tests.

(3) Wave propagation was simulated within the DEM hydrate-bearing sediment samples.

Various seismic technologies and remote sensing data are used for identifying the occurrence and concentration of hydrate in the sediment, because the existence of

hydrate causes a sensitive increase in the propagated wave velocity due to the increase in the stiffness (Soga et al., 2006; Dai et al., 2008; Hutchinson et al., 2008; Jones et al., 2008; Waite et al., 2009). Hence, the study of small-strain stiffness is crucial to the geomechanical investigation of hydrate-bearing sediments as some investigations compared the actual hydrate formation with the wave responses. But, to this day, none of the methane hydrate research on the wave propagation used the method of DEM which reflects the particle-scale behaviours of the sediment. This is a big research gap for the microscopic study of the geomechanical behaviours of hydrate-bearing sediments.

(4) The bonding strength effect in the cementation model was systematically discussed.

In the research on the cementation pattern, the effect of hydrate bonding strength in the DEM simulations has never been discussed systematically in terms of various aspects. However, it is essential to better understand how the given bonding strength influences mechanical behaviours.

(5) The effect of elongated soil particles on the geomechanical behaviours of the sediments was studied.

Within the hydrate-bearing sediment, there are a complex aggregate of discrete particles of various sizes and shapes interacting with one another at contact points. But all the previous DEM studies were performed assuming that all the soil and hydrate particles were spheres, but in fact actual shape of natural soil particles could dominate the sediment's mechanical behaviour.

(6) And most importantly, a comprehensive particle-scale microscopic discussions and analysis were conducted accordingly.

DEM is regarded as a competent tool in the particle-scale microscopic study, but the published DEM studies focused mainly on the macroscopic behaviours of the sediments compared to the experimental data, while they did not provide the particle-scale analysis for the obtained mechanical behaviours.

### **1.3 Outline of the thesis**

This PhD thesis is organized into eight main chapters, as well as three appendices for some further discussions and information. The content of each chapter and appendix is described as follows:

#### **Chapter 1:**

Chapter 1 introduces the background of methane hydrate and the hydrate-bearing sediment. It also describes the motivation of an in-depth understanding of the geomechanical behaviours of hydrate-bearing sediments. Moreover, the objective and research method are proposed, and the main contributions of this PhD research are presented.

#### **Chapter 2:**

The hydrate distribution patterns in the hydrate-bearing sediments are presented in this chapter, as well as the granular material behaviour of the sediment. Past research regarding the geomechanical behaviour of the sediment by field work and laboratory studies are reviewed. And the previous DEM studies of hydrate-bearing sediments are also presented.

#### **Chapter 3:**

A review of the numerical tool in this research, Discrete Element Modelling by Particle Flow Code 3 Dimensions (PFC<sup>3D</sup>) is presented. Afterwards, this chapter describes the sample preparation of the DEM hydrate-bearing soil samples with pore-filling and cementation hydrate distribution patterns. The sample preparation procedures are introduced in the aspects of their important principles. The preparation of the pore-filling and cementation models are stated in detail, and the prepared models will be used in the simulations described in Chapter 4 and 5. Furthermore, the two hydrate growth patterns in the cementation model with various bonding strength are exhibited and prepared separately so as to make the comparisons in Chapter 6. In order

to investigate the shape effect of the elongated soil particles (Chapter 7), the sample preparation of hydrate-bearing sediments with elongated soil particles is also presented.

#### **Chapter 4:**

A series of drained triaxial compression tests are systematically performed to study the geomechanical effects of hydrate saturation ( $S_h$ ) and hydrate growth patterns on hydrate-bearing samples. Comparisons of various aspects between the pore-filling and cementation models are made. We explore the effects of hydrate saturation and growth patterns on the sediments' stiffness, strength and volume change. Besides this, our interest in the sediments' behaviours extends to the large strain deformation and the critical state behaviours in the triaxial tests, as these cannot be obtained easily in the laboratory studies due to the limitations. A particle-scale micro-investigation into the DEM hydrate-bearing sediments is also performed, including the bond breakage between particles throughout the tests, the particles' contact information, as well as the particle-particle contact force contribution to the total deviatoric stress. All the particle-level analysis assists interpretation of the macro responses discussed in this chapter.

#### **Chapter 5:**

The relationship between wave velocity (shear wave and compression wave) and hydrate saturation is established by the DEM simulations. This chapter also shows the DEM simulations for wave propagation within the hydrate-bearing sediment helps relate the obtained wave velocity to the hydrate saturation, and also relate the small-strain stiffness with the saturation, as well as characterize hydrate-bearing sediments with seismic data. In addition, it may be concluded that the initial state behaviours may have an influence on the large strain behaviour of hydrate-bearing sediments.

#### **Chapter 6:**

In this chapter, drained triaxial compressional tests are systematically conducted to study the effects of hydrate growth patterns and hydrate bonding strength in the cementation model. The comparisons between the coating and contact-gathering

models are made through the stress-strain and volumetric responses. We also explore the effects of bonding strength on the sediments' stiffness, strength and large strain deformation behaviour in the triaxial tests. Furthermore, we monitor the bond breakage between particles throughout the tests, as well as the particles' contact information -- the particles' contact force contribution to the total measured deviatoric stress. A discussion is also raised regarding the effect of the hydrate/soil contact stiffness ratio on the strength of the samples. In addition, the comparisons of measuring the stresses and strains are made using three measurement techniques: measurement spheres (local measurement), average particles' contact forces (global measurement) and wall-based logic (boundary measurement).

### **Chapter 7:**

The soil particles are modelled separately using spherical particles and elongated clumps with two different aspect ratios, in order to discuss the influence of the soil particle shape effect on the geomechanical behaviour of hydrate-bearing sediments. The drained triaxial compression tests are conducted to make a comparison between how pore-filling and cementation models interacted with both spherical and elongated soil particles. There is also a discussion on how the elongated shape of soil particles influences the anisotropy in the contact orientation.

### **Chapter 8:**

Chapter 8 reaches a series of conclusions on the work presented in this thesis. The contributions made by this thesis towards the macro- and micro- investigations of the hydrate-bearing sediments are highlighted. Furthermore, recommendations for future research work are given here.

### **Appendix A:**

In order to calculate the hydrate saturation more accurately in various situations in the future DEM studies, in this appendix, three methods are proposed for the calculation of hydrate saturation when all the particles are spherical: accurate calculation, close packing and wasted space volume at particle contacts.

**Appendix B:**

Based on the simulations in Chapter 4, various stress paths are obtained for the pore-filling and cementation models, by which the yield surfaces are plotted in order to investigate the effect of the presence of hydrates.

**Appendix C:**

In this appendix, the pure soil samples (with spherical soil particles or elongated soil particles) and the according hydrate-bearing sediment samples as described in Chapter 4 and Chapter 7 are programmed for a microstructure evolution study.

**Appendix D:**

A brief report of the methane hydrate industry is made in this appendix, including the current needs and outlook of natural gas industry, the exploitation methods, the technology difficulties and the contributions conducted by countries, as well as the commercial potential of methane hydrate exploitation.

## Chapter 2

### Literature review

#### 2.1 Geomechanical investigations of hydrate-bearing sediments

##### 2.1.1 Granular material behaviour of hydrate-bearing sediment

As an inherently discontinuous medium, soils are considered as granular material. Its granular characteristics such as structure and fabric governs the distinct and complex response of soil to imposed loads and deformations. Due to the small size and the opaqueness of soil grains, however, it is not easy to monitor the relationship between the soil mechanical behaviours and its granular characteristics. Recent development of the experimental microscopic technologies and the numerical methods have improved the study of the mechanical behaviour of soils systematically.

The hydrate-bearing soil is a more complex granular material than the pure granular soil, because it contains methane hydrate within its pores hence showing different mechanical behaviours from normal soils. Therefore, there is a need to investigate the mechanical behaviours and its relationship to the micro-mechanisms of hydrate-bearing granulate soil.

Figure 2.1 shows the methane hydrate resource pyramid (U. S. Department of Energy, 2011) which illustrates hydrate resources on the basis of reservoir type, gas recoverability, and estimated total potential natural gas quantity. Hydrate resources that are the most easily recoverable are seated at the top of the pyramid, while those that are the most technically challenging to extract lie at the bottom of the pyramid. Estimates of the total volume of natural gas resource contained in each reservoir type are also indicated (less at the top and more at the bottom). Tackling the challenges of safe and economic development of this energy resource requires continuing research

to decide which exploring and producing technologies will be suitable for the specific hydrate-bearing sediment deposit.

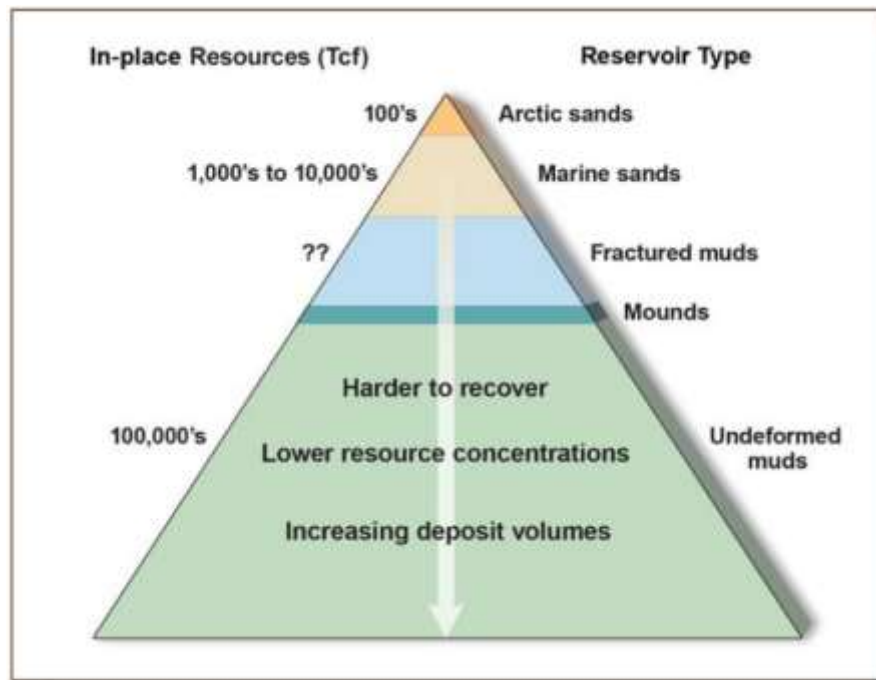


**Figure 2.1:** The methane hydrate resource pyramid (Courtesy of Science Magazine: U. S. Department of Energy, 2011)

For the purpose of making comprehensive comparisons between the numerical study of the hydrate-bearing sediments in this PhD research and the current experimental work conducted by other research teams, the sand was considered as the focus of the soil in the sediment, as the past and current exploration of methane hydrate focuses on the sand rather than the other fine-grained soil. This can minimize the difficulties and challenges of the technical production (Boswell and Collect, 2006; JIP Leg II Science Team, 2009), which can also benefit the commercial purpose of conducting the methane hydrate sediment research. The study of the methane hydrate fine-grained soil deposits has not been conducted systematically, because there is less interest in them from the perspective of resource potential, and there are difficulties in hydrate formation in mechanical testing (Waite et al., 2009). Furthermore, the numerical simulation method Discrete Element Modelling (DEM) used in this PhD research is a good tool for the research of sands, but not for clay. Hence, this literature review is concerned with the hydrate-bearing sandy sediments.

### 2.1.2 Hydrate distribution patterns in hydrate-bearing sediments

Methane hydrate-bearing sediment is the soil sediment layer in which methane hydrate exists within the pore space of the sediment. These sediments are found under deep seabeds and the permafrost regions. Generally, under the conditions of low temperature and high pressure, methane hydrate develops and exists in the pores of highly compacted soil sediments with various distribution patterns.

The hydrate growth and distribution patterns are different within the pores of the sediments, which include pore-filling, cementation, load-bearing, supporting-matrix, patchy pattern, etc.. The comprehensive geophysical research reviews (Soga et al., 2006; Waite et al., 2009) have shown that the pore-scale growth patterns of hydrates strongly control the macro-scale geophysical behaviours of methane hydrate soil sediments.

Among all the known hydrate distribution patterns, the most typical patterns are the pore-filling pattern and the cementation pattern, which are discussed in Section 2.2, as shown in Figure 2.2. In the pore-filling pattern, hydrates freely grow in the pores without connecting two or more soil particles together (Helgerud et al., 1999; Soga, et al., 2006). However, in the cementation pattern, hydrates grow at the inter-granular contacts and along the soil surface, and the compacted soil skeleton is bonded by the hydrates, while the soil-soil contacts are not bonded (Dvorkin et al., 1999; Soga et al., 2006). In both patterns, the soil skeleton, which has been formed by consolidation under high pressure, is not broken by the growth of hydrates inside the pores.

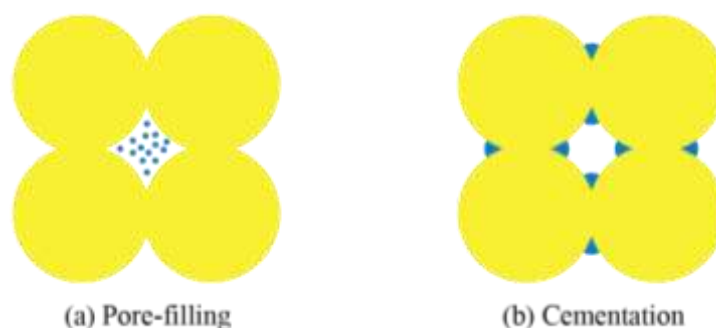


**Figure 2.2:** 2-Dimension sketch of the hydrate distribution patterns inside the hydrate-bearing sediments: (a) pore-filling, (b) cementation (yellow: soils; blue: hydrates).

However, in some other patterns, the soil skeleton may be broken by the hydrate growth. In addition to the pore-filling and cementation patterns, other commonly observed methane hydrate distribution patterns are as follows:

- Load-bearing: hydrates contribute to the mechanical stability of the sediment skeleton by bridging the neighbouring grains and evolving in the load-bearing matrix. And in the pore-filling hydrate pattern, as the hydrate saturation is above  $S_h=25\%-30\%$ , the hydrates function as the load-bearing hydrates (Berge et al., 1999; Yun et al., 2005; Waite et al., 2009).
- Supporting-matrix: hydrates are part of the skeleton matrix of the sediment (Soga et al., 2006).
- Patchy: hydrates coat the soil particles, and then the clusters of the mineral grains form the sediment's skeleton matrix (Soga et al., 2006; Jung et al., 2012).
- Fracture-filling: hydrates grow in the pores of the sediment and break the original sediment skeleton structure by filling the gaps among soil particles (Al-Bulushi, 2012).

### 2.1.3 Geomechanical investigation methods

The geomechanical properties of hydrate-bearing sediments play an essential role in the sites' resource potential evaluation, the production efficiency and safety, and the reservoir management (Waite et al., 2009). Therefore, the geomechanical research of hydrate-bearing sediments is an important task for both the industry and scientific research.

At present, the combination of various researching methods are being conducted to investigate the geomechanical behaviours of hydrate-bearing sediments, mainly field work and experimental tests which provide real data for further studies.

#### 2.1.3.1 Field work

Currently, various seismic technologies and other remote sensing data are being used to identify the geophysical properties (e.g.: small-strain stiffness, porosity, hydrate saturation, etc.) of the hydrate-bearing sediment (Hutchinson et al., 2008; Jones et al.,

2008). The seismic in-situ survey is commonly employed in geomechanical observations, and the hydrate causes a sensitive increase in wave velocity within bearing sediment (Dai et al., 2008).

The typical log measurement data of seismic survey obtained from two different sites with different sediment properties are shown in Figure 2.3 and Figure 2.4 (modified from Chand et al., 2004). In the case of the hydrate occupancy in the hydrate-bearing sediments, the term ‘hydrate saturation’ ( $S_h$ ) is introduced by referring to the percentage of hydrate volume occupancy in the void space of the pure soil sample, which is detailed in Chapter 3 and Appendix A. ‘Porosity’ refers to the percentage of the void space volume in the total sediment volume.

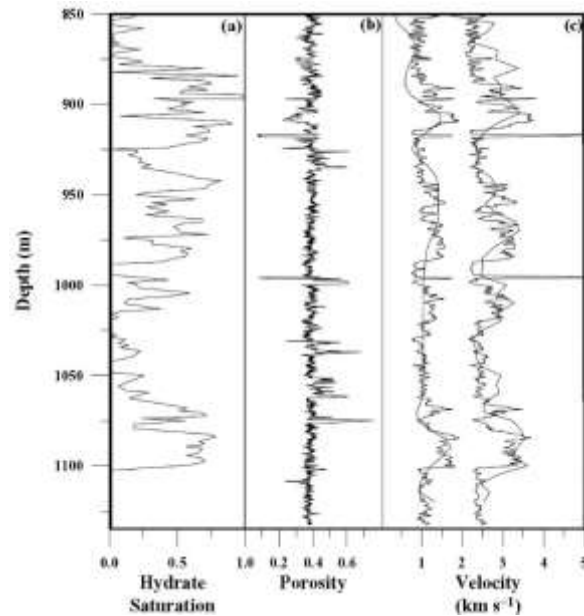


**Figure 2.3:** Mallik 2L-38 wellbore data, Mackenzie Delta, Canada (Collett et al., 1999; Walia et al., 1999; Chand et al., 2004): (a) hydrate saturation estimated from resistivity data, (b) porosity, (c) compression wave velocity  $V_p$  and shear wave velocity  $V_s$  data from acoustic log measurements and VSP (vertical seismic profile) data.

As shown in both Figure 2.3 and Figure 2.4, the wave propagated under the deep seabed. As the depth increased, the measured geophysical data exhibited various values in terms of hydrate saturation, porosity and the wave velocity (compressional wave and shear wave). By comparisons among the measured saturation, porosity and wave velocity at the same depth, generally, it indicates that the increase in the elastic

wave velocity increased with a higher hydrate saturation and decrease in porosity. But the information obtained from the field work is limited.

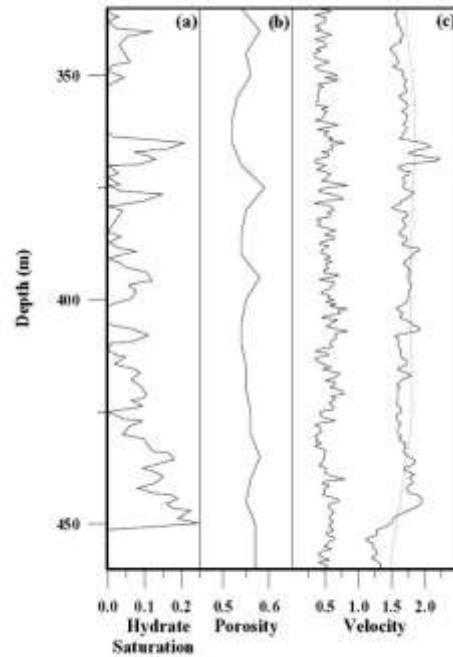


**Figure 2.4:** ODP Site 997 wellbore data, Blake Ridge, Leg 164 (Collett and Ladd, 2000; Lee, 2000; Guerin et al., 1999; Wood and Ruppel, 2000; Chand et al., 2004): (a) hydrate saturation estimated from resistivity data, (b) porosity, (c) compression wave velocity  $V_p$  and shear wave velocity  $V_s$  data from acoustic log measurements and VSP (vertical seismic profile) data.

On the other hand, hydrate-bearing sediment properties may determine the related drilling processes (Waite et al., 2009). The wellbore is drilled through the hydrate-bearing soil layer, which alters the stresses, and also cause shear and volumetric deformation (Rutqvist et al., 2008; Kwon et al., 2008) that may potentially result in the collapse of the production borehole and instability within the hydrate-bearing layers surrounding the drilling wellbore (Briaud and Chaouch, 1997; Hadley et al., 2008).

One example is the BP Gulf explosion in which 3 million gallons of crude oil was poured into the Gulf of Mexico in 2010. The drilling process caused the instability of the hydrate-bearing sediment layer near the wellbore, hence inducing the explosion of the platform due to a series of unpredictable issues. Unfortunately, there is not enough existing data that investigated the influence of the hydrate-bearing sediments' geomechanical behaviours on the production process, because the industrial

exploitation has not started, and the first experimental exploitation was just done in 2013 in Japan. More research is needed.

### **2.1.3.2 Laboratory tests**

As a major approach for carrying out the geomechanical investigations of hydrate-bearing sediments, laboratory studies provide scientific support for the field work, and make connections between the mechanical behaviours to indicate the responses of the methane hydrate sediment to the alterations in the wellbore surroundings (Waite et al., 2009).

Since the methane hydrate sediment is a mixture of soils and hydrates, experimental methods of soil mechanics could be employed in the geomechanical investigations of hydrate-bearing sediments. Yet, due to the hydrate formation and existing conditions of high pressure and low temperature, triaxial tests with specific designs has been widely chosen for the seismic wave studies and other geomechanical researches (Soga et al., 2006; Waite et al., 2009; Hyodo et al., 2011).

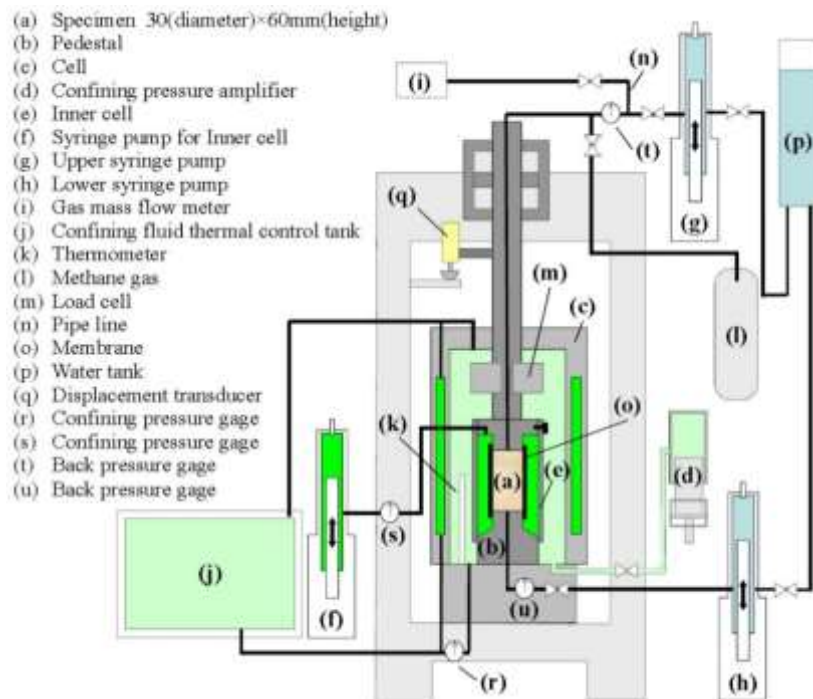
A conventional triaxial test sample is a cylinder with a height usually about twice the diameter of the sample. The rigid platens at the top and bottom are designed to be smooth and to keep horizontal during a test, in order that the top and bottom sides of the sample are principal planes. Normally, drained and undrained tests are conducted for different objectives and situations. In a triaxial test, the applied vertical stress can be different from the controlled horizontal stress. The triaxial compression test is designed to measure the limit of how much shear stress the sampled granular material can withstand. The steadily increased stress on the platens causes the material in the cylinder to fail and form the sliding regions (shear bands). The geometry of the shearing in a triaxial test typically make the sample become shorter vertically while expand horizontally. In the process of the test, a granular material will contract or expand in volume. Generally, triaxial compression tests are applied together with other tests to make engineering predictions.

Figure 2.5 shows a typical apparatus for methane hydrate soil experiment. The temperature-controlled high pressure triaxial testing apparatus was designed such that the back pressure and confining pressure could operate under varying temperatures

and high pressure conditions for the purpose of the examination of the mechanical behaviour of hydrate-bearing sand specimens under deep seabed stress and low temperature conditions (Hyodo et al., 2011). Figure 2.6 shows the schematic diagram of the triaxial apparatus in Figure 2.5 in detail. These triaxial compressional tests are commonly employed to acquire the geomechanical behaviours of the methane hydrate soil samples.



**Figure 2.5:** Methane hydrate soil experiment apparatus (Hyodo et al., 2011)



**Figure 2.6:** Cell appurtenances and piping system (Hyodo et al., 2011)

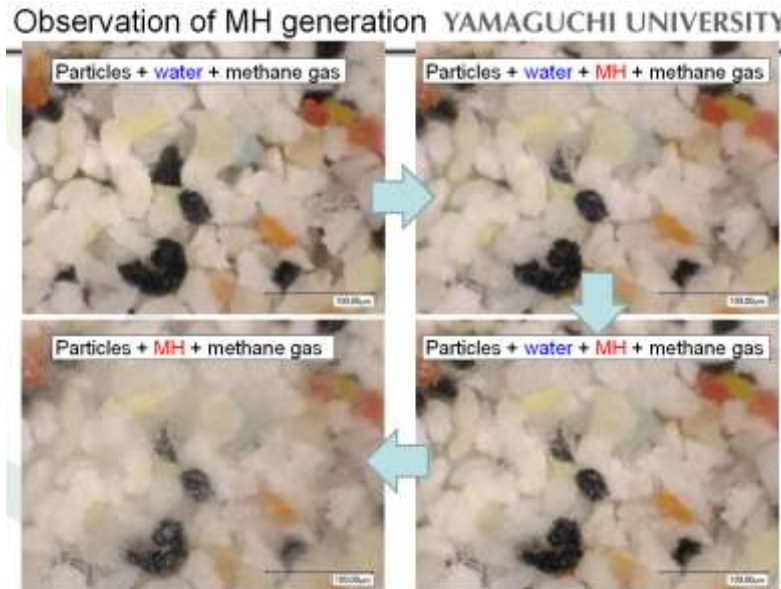
In the experimental studies, it is extremely expensive and difficult to acquire the natural methane hydrate sediments. It is also very hard to obtain the natural samples with the same soil size distribution and sediment skeleton but different hydrate saturations. At present, obtaining a comprehensive geomechanical investigation of natural hydrate-bearing sediments is still a challenging task compared to the synthetic hydrate-bearing samples. Moreover, the laboratory test results have already proved that the synthetic samples can adequately interpret the geomechanical behaviours of hydrate-bearing soil samples (Masui et al., 2005; Priest et al., 2005; Soga et al., 2006; Waite et al., 2009; Hyodo et al., 2011), which is shown in Section 2.2.

Figure 2.7 shows the observation test of the formation process of hydrate in a sand sample prepared in Yamaguchi University (Hyodo et al., 2011). A sample of the mixture of sand particles, water and methane gas was first prepared in the sealed container. And then methane gas was injected into the sample till the formation process finished. The methane gas dissolved in the water and became hydrate under the controlled high pressure and low temperature. By controlling the specific low temperature and high pressure, the mixture of methane gas and water gradually formed methane hydrate until finally 100% of the water was used during the formation process.

In fact, in the laboratory synthetic sample preparation process, the crystalline solid methane gas hydrate alters the hydrate-bearing soil sample's mechanical behaviour (Waite, et al., 2011). Waite et al. (2011) succeeded preparing the load-bearing hydrate in their synthetic samples, and the formed hydrate was part of the load-bearing systems of the sediment sample, which changed the initial stiffness of the sediment. In addition, due to the low solubility of methane in water and the flow process for methane to dissolve in water, researchers have been trying to accelerate this process. Priest et al. (2009) managed to form the methane hydrate by the supply of methane bubbles. However, this method could only form the hydrate at no more than the saturation of 40%.

Masui et al. (2005) prepared two different synthetic hydrate-bearing and samples: the strong bond sample (cementation pattern) and the weak bond sample (normally considered as the pore-filling pattern). The sediment sand is Toyoura sand. However, the initial consolidated soil skeleton was broken by the growth of hydrate which will

be further discussed in Section 2.2.2. The bonding strength was controlled by the flow of water through the porous sand during the formation process, although the strength could not be controlled properly in values.



**Figure 2.7:** Observation of Methane hydrate generation (Hyodo et al., 2011)

As previously discussed, seismic tests are applicable to evaluate the distribution and saturation of hydrate-bearing sediment on site by measuring the wave velocity (compression and shear wave). Besides, the interpretation of seismic data needs to be connected to the measured geomechanical behaviours of methane hydrate soil sediments from the laboratory tests. Hence, the hydrate resonant column apparatus illustrated in Figure 2.8 was designed (modified from Priest et al., 2005). The wave is excited and received within the cylindrical hydrate-bearing sample, and the vibration frequency at resonance of the column determine the wave velocity (Richart et al., 1970; Drnevich et al., 1978) under the conditions of the hydrate formation inside soil specimens. The synthetic samples were tested in the laboratory, as well the obtained natural sediment samples. Many researches have been conducted on the wave propagation of in-situ and laboratory samples, such as Berge et al. (1999), Priest et al. (2005), Yun et al. (2005), Clayton et al. (2010), to name but a few. The obtained results from the laboratory tests and the comparisons with the field work are presented in Section 2.2.1.

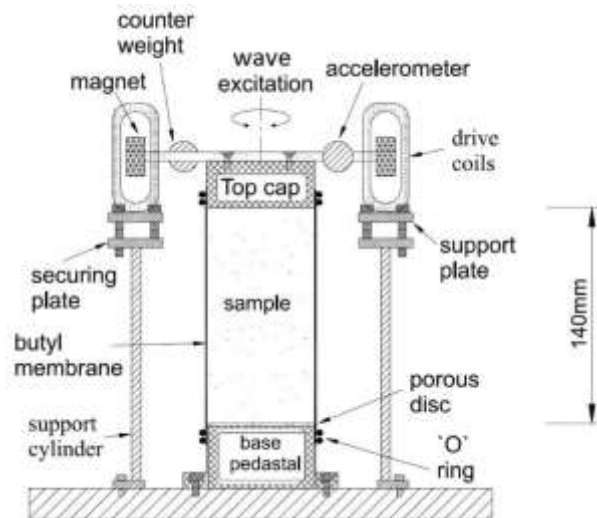


**Figure 2.8:** Cross section through seismic test apparatus (the pressure cell is omitted in the figure). (Modified from Strokoe et al., 1999 and Priest et al., 2005)

## 2.2 Geomechanical characteristics of hydrate-bearing sediments

### 2.2.1 Small-strain stiffness

The small-strain shear modulus  $G_{max}$  is usually measured through seismic wave propagation as fundamental stiffness of soils and hydrate-bearing sediments. The value of  $G_{max}$  can be measured through laboratory and/or on-site field tests. Some of the crucial factors affecting the small-strain stiffness of  $G_{max}$  include mean effective stress, void ratio, stress history, rate of loading, soil plasticity for silts and clays, and stress anisotropy for sands creep (Hardin et al, 1972; Lo Presti et al., 1996).

The most decisive and reliable method to determine  $G_{max}$  is by employing seismic studies at the shear wave velocity  $V_s$  that has a direct relation to the maximum shear modulus  $G_{max}$  (Elhakim, 2005):

$$G_{max} = \rho_t V_s^2 \quad (2.1)$$

where  $\rho_t$  is the total soil mass density.

Generally, the stiffness of methane hydrate is a little harder than that of ice. Table 2.1 shows the stiffness and wave velocities for various typical sediments (modified from Mavkov et al., 1998; Soga et al., 2006):

**Table 2.1:** Stiffness and wave velocities for various typical sediments (modified from Mavkov et al., 1998; Soga et al., 2006)

Region	Density (g/cm <sup>3</sup> )	K (GPa)	G (GPa)	V <sub>p</sub> (km/s)	V <sub>s</sub> (km/s)
Quartz	2.65	36.6	45.00	6.0	4.1
Clay	2.58	20.9	6.85	3.4	1.6
Pure methane hydrate	0.90	7.9	3.30	3.7	1.9
Water	1.03	2.4-2.6	0	1.6	0.0
Ice	0.92	6.7	2.60	3.3	1.7

The small-strain shear modulus  $G_{max}$  may provide indicator for hydrate saturation and distribution pattern at a specific confining stress. The wave velocities and the stiffness of methane hydrate sediments are determined by both the hydrate saturation and the hydrate distribution pattern in the pore spaces (Soga et al., 2006). In addition, as mentioned in Section 2.1, the seismic wave propagation of compression  $P$  wave and shear  $S$  wave is widely used for locating hydrate-bearing sediment occurrences and estimating the concentration of hydrate in the field, as the hydrate stiffens the sediment and increases the wave velocities (Waite et al., 2009).

The propagation of the compression  $P$  wave induces longitudinal strains within the particles' motion along the wave propagation direction. The shear  $S$  wave causes shear strains with the particles' motion perpendicular to the wave propagation direction (Waite et al., 2009). Supposing that the hydrate-bearing sediment is an isotropic elastic material, the propagation speeds of compression and shear wave are shown in Equation 2.2 and Equation 2.3 respectively:

$$\text{Compression wave velocity: } V_p = \sqrt{\frac{K + 4G/3}{\rho}} \quad (2.2)$$

Shear wave velocity: 
$$V_s = \sqrt{\frac{G}{\rho}} \quad (2.3)$$

where  $\rho$  is density of the sediment,  $G$  is the shear modulus, and  $K$  is bulk modulus.

Figure 2.9 shows that the wave velocities increased with hydrate saturation for most of the hydrate growth patterns. The modelling results are represented by solid and dashed curves. The modelling results are from Kleinberg and Dai (2005), in which Equation 2.2 and Equation 2.3 were used where the modulus were calculated according to the hydrate morphology – cementation, coating, load-bearing and pore-filling. The dashed curves show wave velocities for the cementation pattern and coating pattern. The cementation pattern increased most significantly with the wave velocity, particularly for low hydrate saturations (dotted-dashed curve). And the coating pattern (dashed curve) exhibited lower wave velocity than the cementation case but there was a similar trend of increase with the saturation. The solid curves represent the matrix-supporting hydrate which increased the wave velocity in the sediment especially the saturation was higher. And the pore-filling distribution did not show any evident effect on the wave velocity at the low saturation (Waite et al., 2009).

The on-site (open symbols) and laboratory (solid symbols) results are also shown in Figure 2.9. The results were obtained under different conditions (e.g.: confining pressure, gas, water, porosity, etc.), but the trends are similar to the modelling ones, especially the cementation case (Priest et al., 2005) and the pore-filling case (Yun et al., 2005), even though the values differ from the modelling results. And the on-site results from the Mallik 5L-38 (Lee and Collett, 2005) compared well with the matrix-supporting model (solid curve). However, other obtained results (Berge et al., 1999; Chand et al., 2004; Westbrook et al., 2005) only showed the limited data at the low saturation or few data at various saturations, which cannot be compared systematically with the predicted model. It appears easier to predict hydrate saturations through wave velocities. However, the in-situ measurements of wave velocities still may be unreliable because the geological conditions are too complex (Dai et al., 2008; Lee and Waite, 2008). Hence, a series of new technologies should be carried out to control the wave propagation adequately.

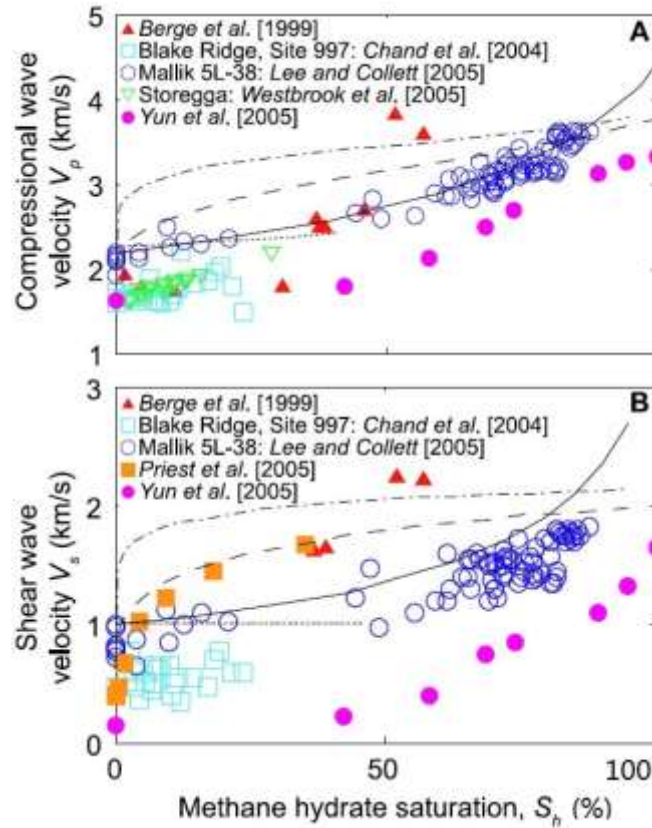


**Figure 2.9:** Wave velocities (compression  $P$  wave and shear  $S$  wave) in the methane hydrate sediments where open symbols represent the field, solid symbols represent the laboratory results, and solid and dashed curves represent the modelling results: (A) compression wave; (B) shear wave (Waite et al., 2009)

As shown in Figure 2.10, Dai et al. (2012) also summarised the trends of the compression  $P$ -wave with hydrate saturation for different growth patterns based on their literature research. The plots concluded the  $P$ -wave data of cementation, coating, patchy, load-bearing and pore-filling patterns. The cementation and coating pattern showed similar trends as described in Figure 2.9. And the patchy and load-bearing patterns in Figure 2.10 behaved similarly to the matrix-supporting model (solid curve) in Figure 2.9. Nevertheless, by the  $S$ -wave velocity plots for cementation pattern (Priest et al., 2005) in Figure 2.9 and the  $P$ -wave velocity plots for cementation and pore-filling patterns in Figure 2.10, it is shown that the wave velocities for pore-filling and cementation cases at high hydrate saturation were not verified with enough data. Dai et al. (2012) also claimed that the existing data was not sufficient to plot the wave velocity trends of the cementation case to high saturation. It could only be assumed on the basis of the hydrate morphology.

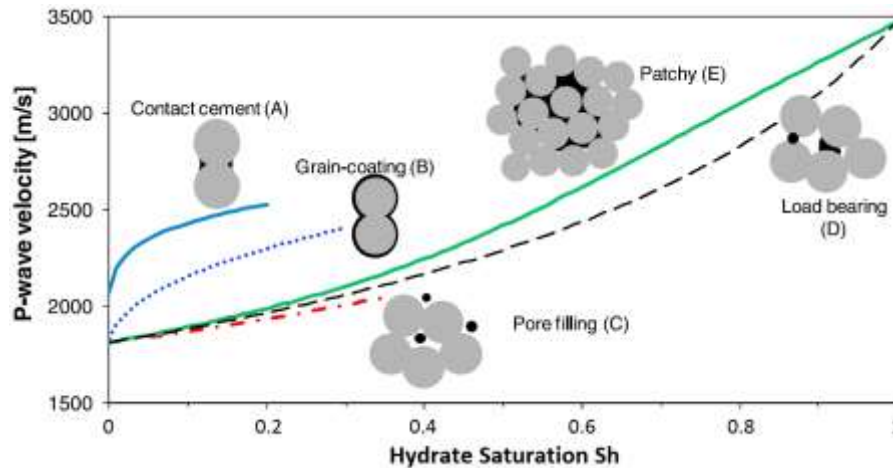


**Figure 2.10:** Conclusions of the trends of compression P-wave velocity with hydrate saturation for various growth patterns (Dai et al., 2012)

Moreover, the pore-filling pattern and the cementation pattern have shown the two most typical geophysical behaviours of hydrate-bearing sediments – lowest and highest wave propagation velocities respectively in the sediment. And the wave velocity data of all the other reported hydrate distribution patterns were all between the velocity values of the pore-filling and cementation cases. And the mainly discussed patterns are also pore-filling and cementation patterns in most of the published research which were comprehensively reviewed by Soga et al. (2006) and Waite et al. (2009).

With regards to the hydrate saturation effect on the small-strain shear stiffness of hydrate-bearing sediments, several studies have been carried out by means of measuring the *S*-wave velocity. The studies demonstrated that the shear stiffness increase is dependent on hydrate morphology (e.g. Clayton et al., 2005, 2010; Priest, 2005; Priest et al., 2009; Santamarina & Ruppel, 2008; Yun et al., 2011). Figure 2.11 shows the hydrate saturation effect on small-strain shear stiffness for various hydrate morphologies by expected data of Clayton et al. (2010). The increase rate of the shear stiffness for the cementation samples with the low saturation of hydrate was greater than that of the pore-filling samples. And as the saturation increased, the increase rate in the shear stiffness of the cementation case began to decrease; while the shear stiffness of the pore-filling pattern began to increase when the saturation was above 20%.

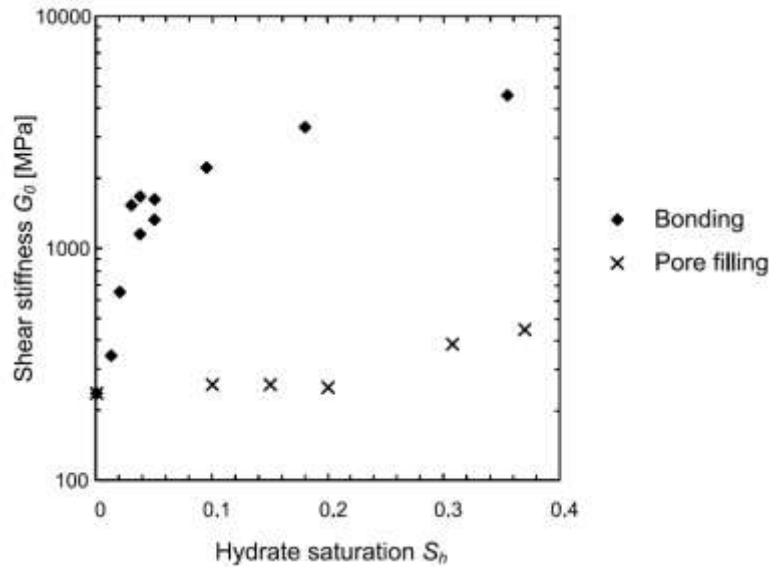


**Figure 2.11:** The effect of hydrate distribution patterns on small strain stiffness by Clayton et al. (2010)

## 2.2.2 Stiffness, strength and dilatancy

### 2.2.2.1 Drained tests

Masui et al. (2006) conducted a typical example of the drained triaxial compressional tests on the obtained natural hydrate-bearing sandy specimens collected from Nankai Trough, which were isotropically consolidated. Figure 2.12 shows the stress-strain and volumetric behaviours of the samples with various methane hydrate saturations measured from the tests. The hydrate saturations ranged between 7.7% and 37.6%. The initial consolidation pressure was 1 MPa. And Figure 2.12 demonstrates that the dilatancy rate can be acquired by the changes of volumetric strain and axial strain, or dilation angle  $\psi$ . It can be seen that the higher hydrate saturation increased the strength and dilation of the hydrate-bearing samples. Moreover, most experimental studies reported by Soga et al. (2006) and Waite et al. (2009) have concluded that at a given confining stress, the strength of methane hydrate soil sediment increased with the hydrate saturation and the hydrates increased the stiffness, the dilation, and the strength of the sediment.

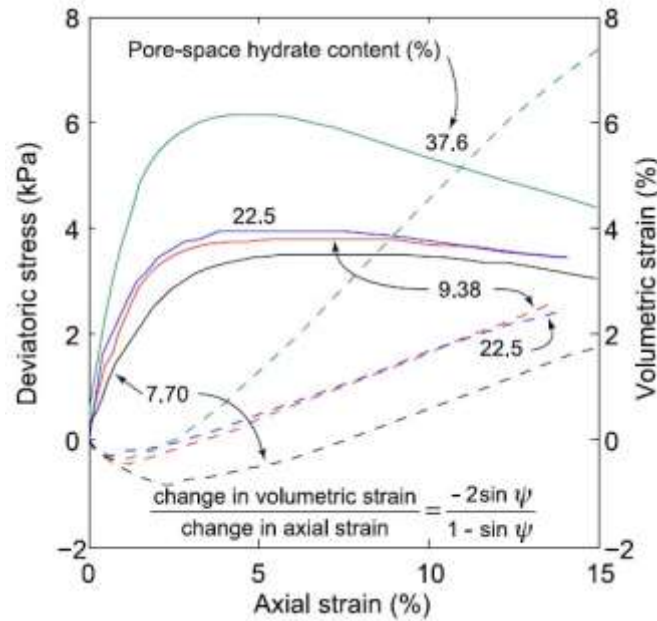


**Figure 2.12:** The stress-strain behaviour and volumetric response of natural hydrate-bearing sandy specimens obtained from Nankai Trough (Masui et al., 2006)

The strong bond sample (cementation pattern) and the weak bond sample (normally considered as the pore-filling pattern) were prepared by Masui et al. (2005) in their synthetic methane hydrate specimens. The sediment sand is Toyoura sand. The triaxial compression test results under the initial isotropic effective confining stress of 1 MPa for the strong bond samples (cementation) and the weak bond samples (pore-filling) are shown in Figure 2.13. The constant shearing rate was 0.1%/min under drained conditions.

Generally, the strength increased with the hydrate saturation. In Figure 2.13 (a) for the strong bond model, the strength increase began even at a low hydrate saturation; while in Figure 2.13 (b) for the weak bond model (considered as pore-filling model), the obvious increase in strength started from  $S_h=26.4\%$ . And at the same saturation, the stiffness and strength of the strong bond case showed a higher value than those of the weak bond case. In addition, at the large strain, the higher saturation samples of the weak bond case exhibited a lower strength than the relatively lower saturation sample; while the strong bond model did not show this phenomenon obviously. Hence, it is suggested that the stiffness and strength are influenced by both the hydrate saturation and the growth pattern in the pore space of the sediment.

As a set of widely cited data, however, it is obviously found in Figure 2.13 that the strength of the strong bond sample at  $S_h=0\%$  (hydrate-free) was larger than that of the weak bond sample at  $S_h=26.4\%$ . Due to the fact that the increase in hydrate saturation strengthens the consolidated sediment, there must be some limitations in the synthetic hydrate-bearing sample preparation process of the weak bond samples. One obvious reason may be that the formed methane hydrate in the pores had already broken the existing sand skeleton before the triaxial test, and the relatively softer hydrate in stiffness had played a role in the skeleton at the initial state of the test. In the laboratory tests, such a limitation is not be easily avoided.

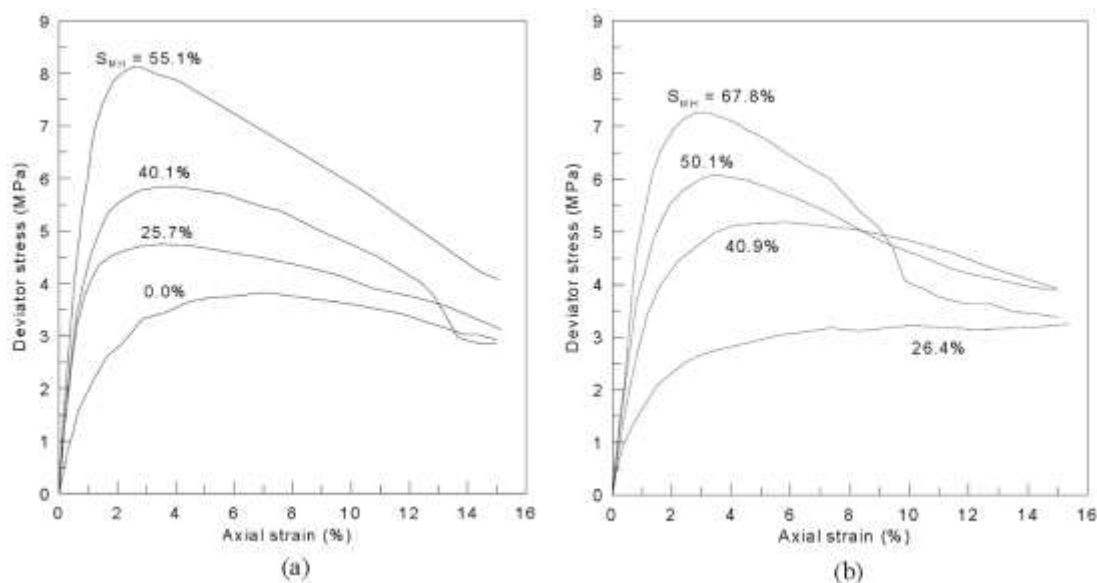


**Figure 2.13:** Deviatoric stress against axial strain at various hydrate saturation: (a) strong bond samples (b) weak bond samples (Masui et al., 2005)

Both Ebinuma et al. (2005) and Masui et al. (2005) conducted triaxial tests on the artificial hydrate samples suggesting that, as plotted in Figure 2.14(a), the increase in the peak strength (maximum deviatoric stress) increased with a higher hydrate saturation, but the hydrate growth pattern determined the increasing rate. From the results by Ebinuma et al. (2005), it is concluded that the peak strength of the pore-filling case increased only when the hydrate saturation was above approximately 25%, and then increased obviously; while the cementation case's peak strength began to increase even from the low saturation. And from the data by Masui et al. (2005), it is also suggested that the strength of the pore-filling case increased just when the

saturation was above around 25%, while the cementation sample began to show an increase in the peak strength from a low saturation. Moreover, in the both studies, at the same saturation, the cementation case showed a higher peak strength than the pore-filling case. The deviation between the two studies is because of the difference of the confining pressure: Ebinuma et al. (2005) applied the confining pressure of 3 MPa, while Masui et al. (2005) used 1 MPa.

In addition, as shown in Figure 2.14(b), the higher hydrate saturation increased the mid-strain stiffness  $E_{50}$  (Masui et al., 2005). Cementation hydrate samples indicate great effect of hydrate at low hydrate saturation. While the pore-filling hydrate has no significant effect on peak strength or mid-strain Young's modulus  $E_{50}$  until  $S_h$  was above 25%.

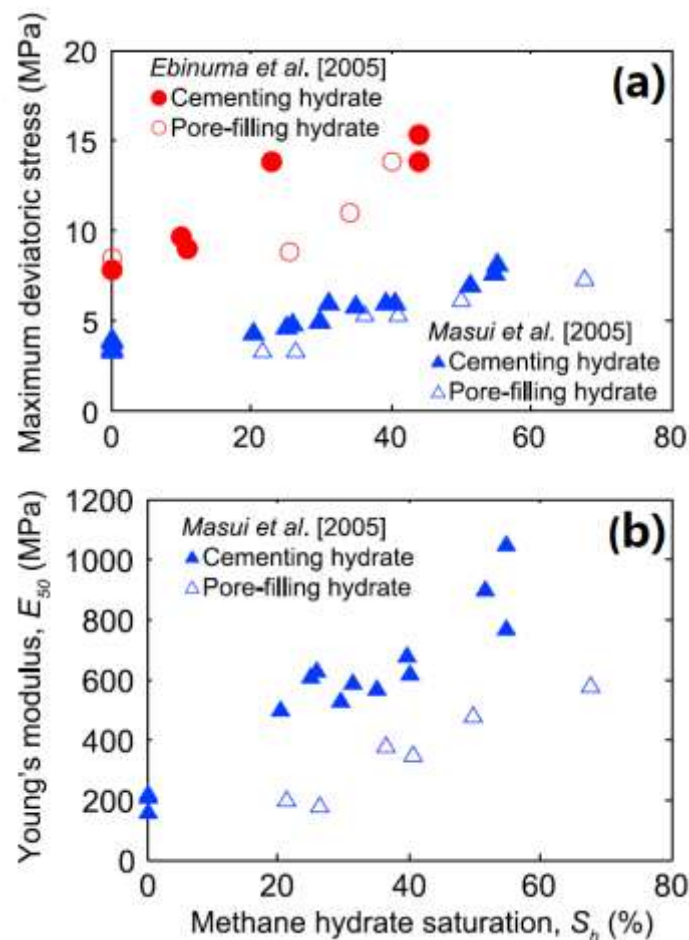


**Figure 2.14:** (a) Peak strength; (b) mid-strain stiffness  $E_{50}$  at various hydrate saturation (Ebinuma et al., 2005; Masui et al., 2005; Waite et al., 2009)

Figure 2.15 (Waite et al., 2009) shows the increasing hydrate saturation and its influence on the magnitude changes of friction angle, cohesion and dilation. As shown in Figure 2.15, an obvious increase occurred in the friction angle and dilation angle even at a low hydrate saturation in the cementation pattern, while it occurred after the hydrate saturation was above approximately 30% in the pore-filling pattern. The data were collected from tests at the confining pressure of 1 MPa; at higher confining pressures, the dilation should be expected to be lower. And the higher hydrate saturation increased the cohesion obviously, as shown in Figure 2.15 (a). It is clearly suggested that although the higher hydrate saturation increased cohesion and the dilation angle, the higher hydrate saturation did not surely determine the changes of the friction angle.

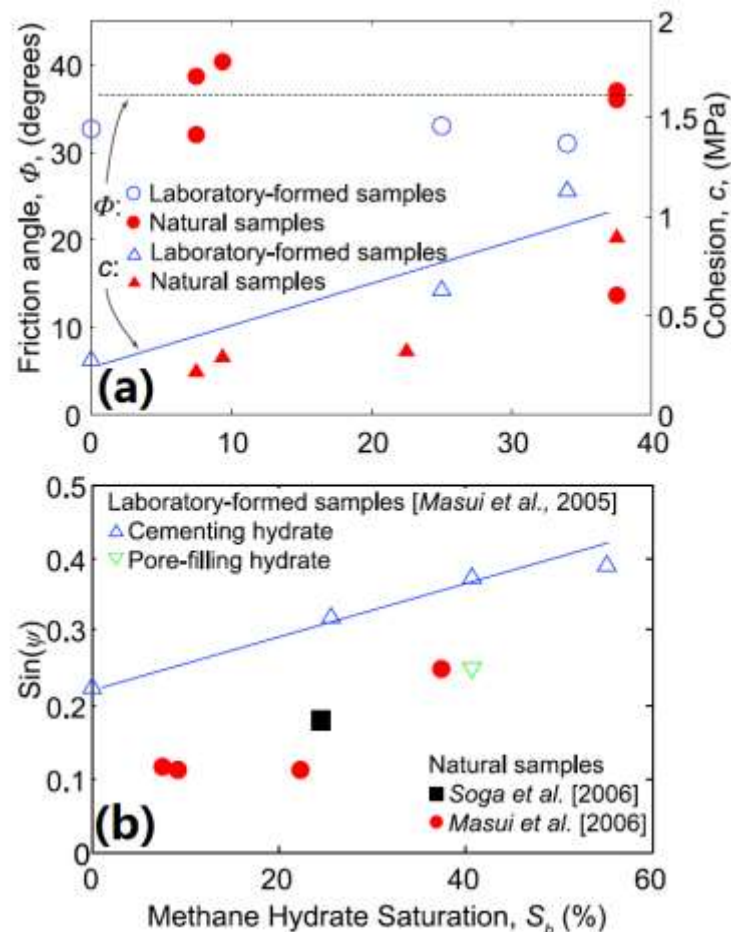


**Figure 2.15:** Cohesions, friction angles and dilation angles at the various hydrate saturations of the natural hydrate-bearing specimens (Masui et al., 2006; Soga et al., 2006) and the laboratory synthetic cementation specimens (Masui et al., 2005).

### 2.2.2.2 Confining pressure

Confining pressure has effects on the geomechanical behaviour of hydrate-bearing sediment. As shown in Figure 2.16, the stress-strain responses were plotted for the synthetic hydrate-bearing specimens at the hydrate saturation of 34.0% and 38.5% (Ebinuma et al., 2003; Masui et al., 2005) when isotropically consolidated at three different confining stresses. When the confining stress was reduced, the sediment typically showed a greater strain softening behaviour than the medium dense sands.

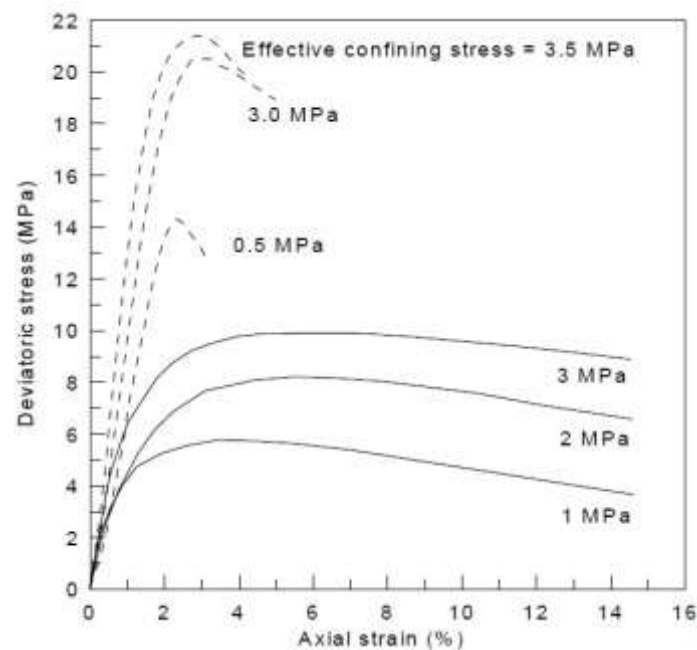


**Figure 2.16:** Toyoura cementation hydrate-bearing sediments with 34% (solid line: Masui et al, 2005) and 38.5% (dashed line: Ebinuma et al., 2003) synthetic methane hydrate under different confining pressures

### 2.2.2.3 Stiffness degradation

To this day, some studies have been performed on the structure degradation of hydrate-bearing soils during soil shearing. It would be ideal to monitor the degradation of wave velocity during the process of shearing hydrate-bearing soils. Nevertheless, the secant Young's stiffness can be obtained from the results of drained triaxial compression tests on hydrate-bearing sand specimens. Figure 2.17 shows the change in the secant stiffness of hydrate-bearing sediment (cementation) acquired by Masui et al. (2005).

It is quite clear that the stiffness degrades as the soil is sheared, and the higher the hydrate saturation is, the greater degradation is.

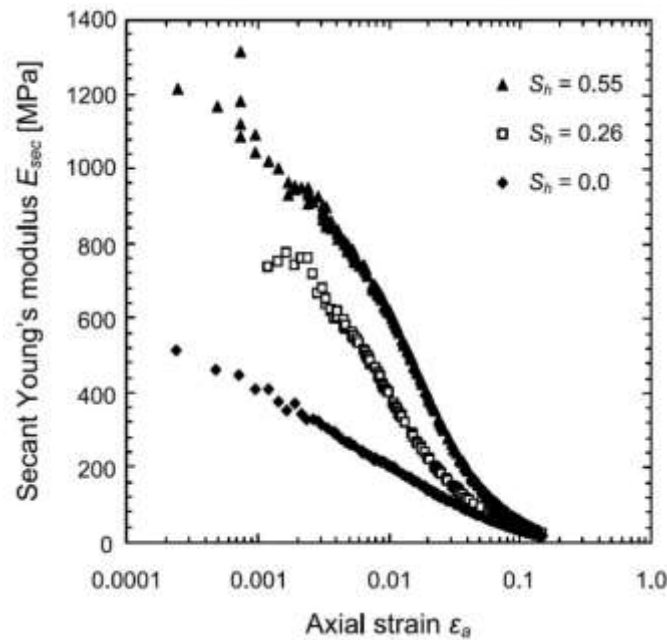


**Figure 2.17:** Degradation of the secant stiffness of cementation synthetic hydrate-bearing sediment during drained triaxial compression test by Masui et al. (2005)

#### 2.2.2.4 Undrained tests

In fact, there is currently a lack of data on the undrained tests in the experimental studies. Winters et al. (2002) and Yun et al. (2007) proved that undrained stiffness and strength in sediments with high hydrate saturation depend on the hydrate phase rather than the confining pressure (Waite et al., 2009). Undrained tests are usually used for the clay sediments, while the drained tests are employed for the sandy sediments. Hence, for the purpose of making comprehensive comparisons with current experimental results and making further analysis with enough supporting data from the experiments, this PhD study focussed only on the drained triaxial compression tests.

#### 2.2.3 Mechanism analysis of hydrate saturation and bonding strength

As discussed above, the existence of methane hydrate increases the stiffness, strength and dilation of the hydrate-bearing sediment. A few studies have hypothesized the micro-mechanisms for shear strength at various hydrate concentration (Yun et al.,

2005; Soga et al., 2006; Yun et al., 2007; Waite et al., 2009). Figure 2.18 shows the mechanisms of the shear resistance and dilation at various hydrate saturation inside the pores (modified from Yun et al., 2007; Waite et al., 2009).

In Figure 2.18, white circles represent sediment grains, black represents hydrate, and blue represents water. When there is no hydrate,  $S_h = 0\%$ , shear induces rotation and the rearrangement of particles; dilation or slippage overcomes rotational frustration. Regarding the shear strength, hydrate saturation  $S_h < 30\%$  is considered a low saturation, and  $S_h > 40\%$  considered a high one. Above  $S_h = 80\%$ , conditions are considered rare, and there is occluded water in the void space within the sediments.

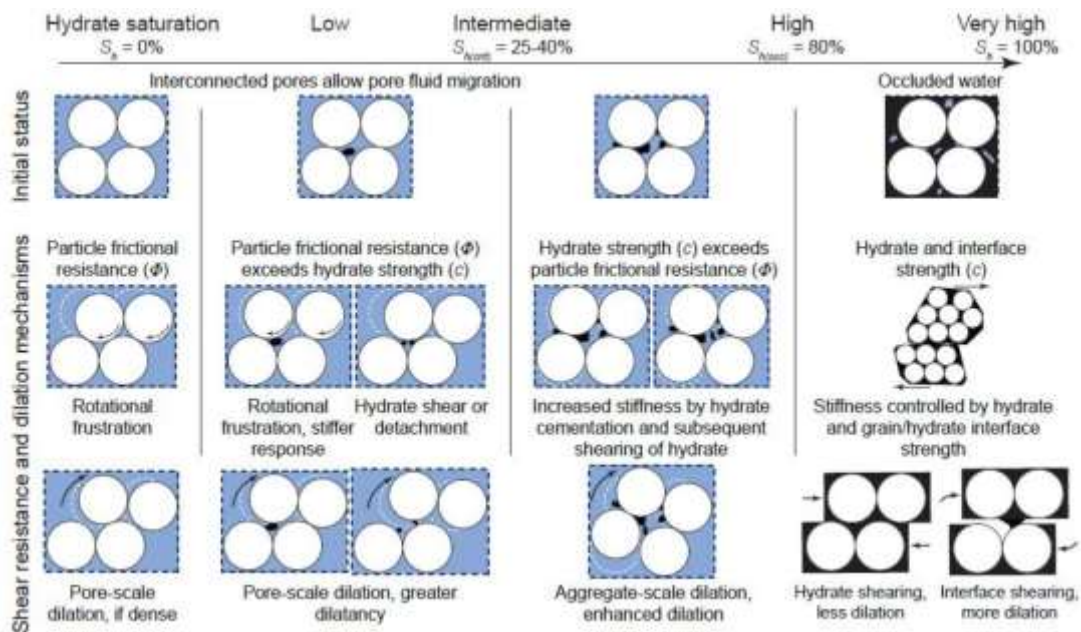


**Figure 2.18:** Mechanisms of the particle movement controlling the shear strength of methane hydrate sediments (Yun et al., 2007; Waite et al., 2009)

It is clearly shown in Figure 2.18 that at low hydrate saturation, hydrate crystals may shear, detach or interfere with rotation, and induce a slight increase in sediment strength; the extent of this effect is determined by the hydrate-particle bonding strength, hydrate strength and hydrate concentration. At high hydrate saturation, the cementing strength offered by hydrate mass and the particle-hydrate bonding govern deformation and strength response.

The micro-mechanism analysis in past studies illustrated only the possible particle-level mechanisms that may describe the role of hydrates on sediment strength. However, in the experimental studies and most of the numerical research, there is difficulty in carrying out an adequate particle-scale mechanism analysis of the presence of hydrates, not to mention the effect of various bonding strengths on the shear resistance and dilation mechanisms.

## **2.3 Numerical modelling: Discrete Element Method**

In fact, it is very expensive to obtain the natural sediments, and it is challenging to control the temperature and pressure of the natural samples during the drilling and shipping process. In addition, it is also difficult to obtain the natural samples with the same soil properties and the various desired hydrate saturations for a comprehensive research. Because of this, synthetic samples are employed in the laboratory tests, as discussed above in Section 2.2. However, it is also challenging to obtain well-controlled and consistent synthetic hydrate-bearing samples, as it is difficult to control hydrate formation, the distribution pattern and saturation during the synthetic sample preparation process.

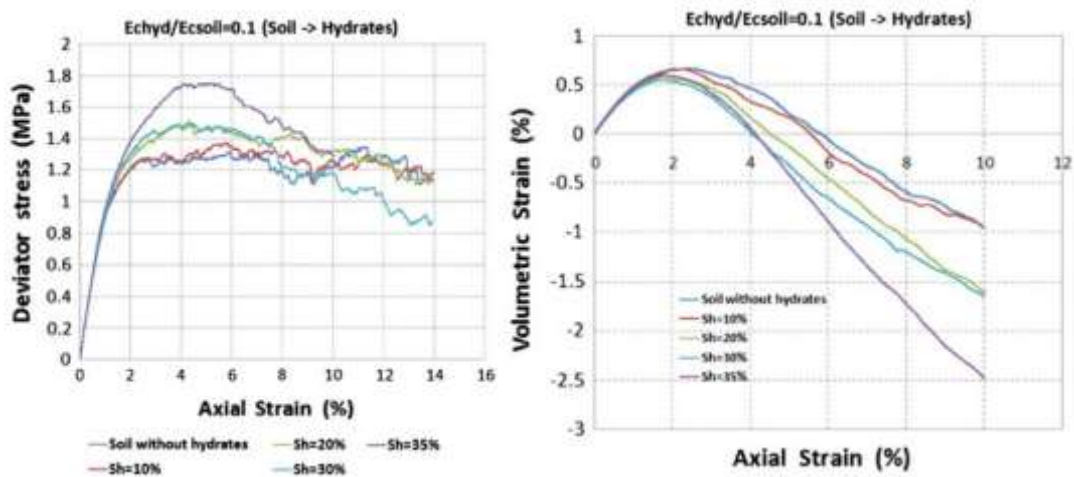
Hence, the numerical method of Discrete Element Modelling is employed as a useful tool to replicate the particle behaviour usually experienced during laboratory sample preparation and testing, and to perform the particle-scale micro-mechanism interpretation of the macroscopic geomechanical behaviours discussed in Section 2.1 and 2.2. The most recent studies on the geomechanical characteristics of methane hydrate sediments with DEM were those done by Brugada et al. (2010), Jung et al. (2012), Jiang et al. (2013), etc.. More details about Discrete Element Method (DEM) are introduced in Chapter 3.

### **2.3.1 Pore-filling model**

Brugada et al. (2010) carried out the 3-Dimension DEM simulations on the pore-filling hydrate pattern. The simulated triaxial tests aimed to discuss how hydrate saturation

influenced the stress-strain and volumetric responses, as well as to acquire some other macroscopic geomechanical behaviours.

Figure 2.19 shows the stress-strain responses and volumetric behaviours during the DEM triaxial tests under the 1 MPa confining pressure. The hydrate-soil contact Young's modulus ratio  $E_{\text{chyd}}/E_{\text{csoil}}$  was set as 0.1. And the sample preparation method 'Soil -> Hydrates' referred that the hydrate particles were generated in the pores of the consolidated soil sample. The simulated results show the similar behaviours as discussed in Section 2.2. The hydrate increase caused an increase in the strength and dilation.

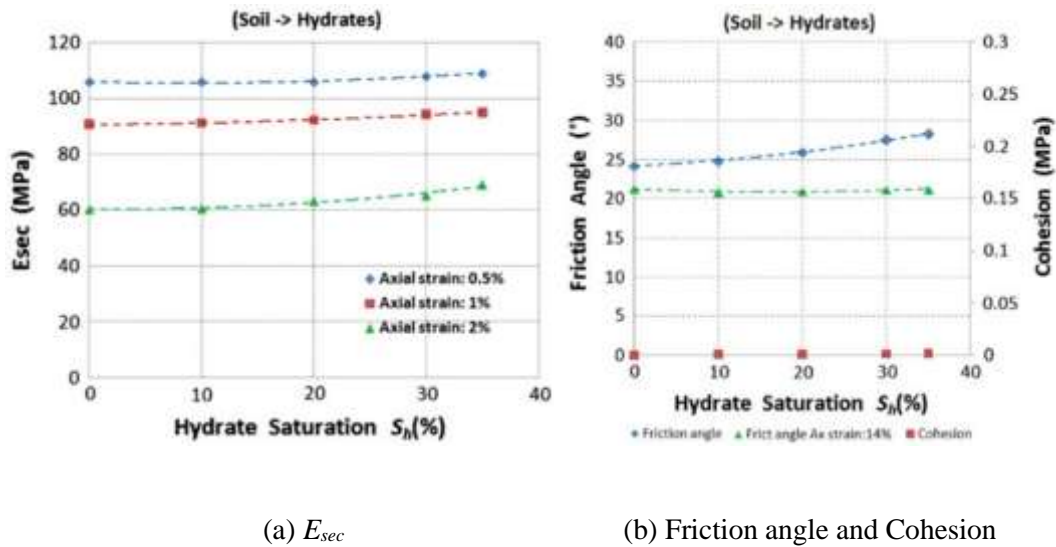


(a) stress-strain responses

(b) volumetric responses

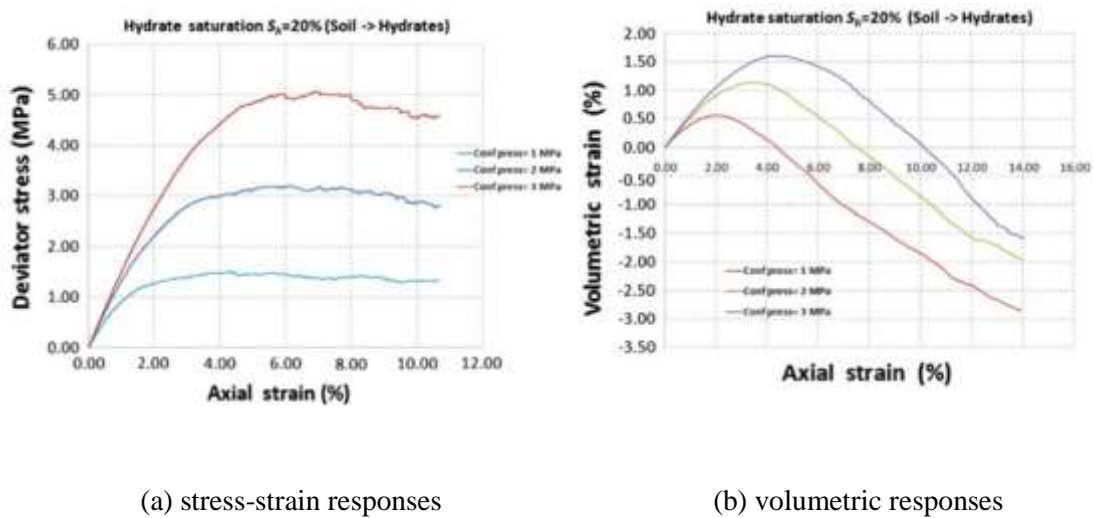
**Figure 2.19:** Triaxial compressional test results (Brugada et al., 2010): (a) stress-strain responses; (b) volumetric responses

Figure 2.20 (a) shows the secant stiffness at different axial strain. Firstly, it is suggested that as the axial strain increased, the stiffness decreased, which corresponds to the results in Figure 2.17. Secondly, as the hydrate saturation increased in the pore-filling model, the obvious increase in stiffness only happened when the saturation was above 20%, which is similar to the results shown in Figure 2.14. In addition, in Figure 2.20 (b), the peak friction angle increased with hydrate saturation, while the large-strain (14%) friction angle remained at a constant value when the saturation increased. Moreover, in the pore-filling model, the cohesion was zero.



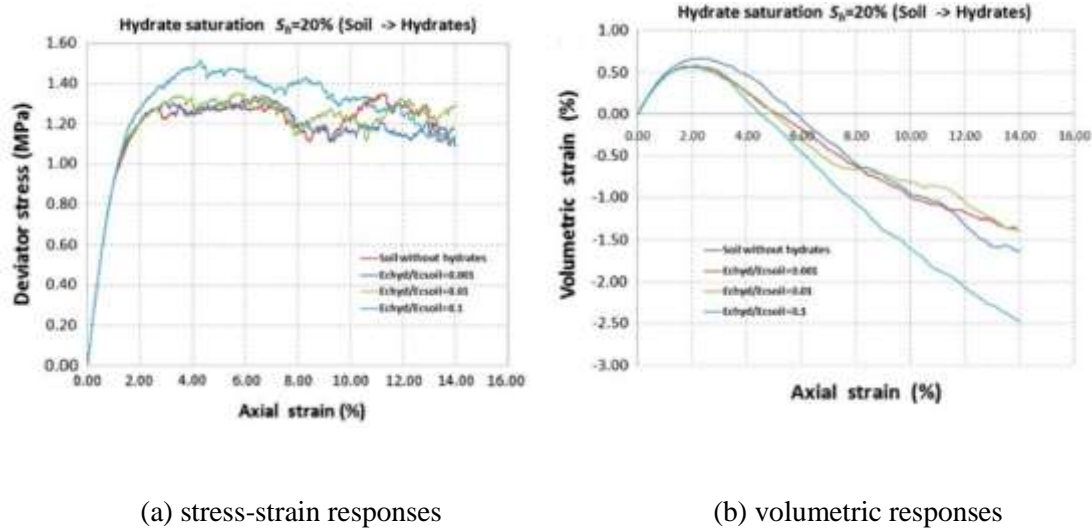
**Figure 2.20:** Derived data from simulation results by Brugada et al. (2010): (a) secant stiffness  $E_{sec}$ ; (b) friction angle and cohesion

As shown in Figure 2.21, Brugada et al. (2010) also explored the effect of confining pressure in this research. It can be seen in Figure 2.21 (a) that as the confining pressure increased, the stiffness and strength of the pore-filling sample at  $S_h=20\%$  increased evidently. And the magnitude of the increase in the strength was about 2 MPa, although the strength of the sample at 1 MPa confining pressure was only slightly above 1 MPa. However, as shown in Figure 2.21 (b), the contraction was enhanced by the increased confining pressure, while the dilation as weakened.



**Figure 2.21:** Triaxial compressional test results under various confining pressure (Brugada et al., 2010): (a) stress-strain responses; (b) volumetric responses

Brugada et al. (2010) also explored the hydrate-soil contact stiffness ratio which ranged from 0.001 to 0.1 at  $S_h=20\%$  of the pore-filling model. It can be seen in Figure 2.22 that hydrates only contributed to the strength and dilation when the ratio was at the value of 0.1. Regarding other ratios, the behaviours were quite similar to the pure soil sample's responses.



(a) stress-strain responses

(b) volumetric responses

**Figure 2.22:** Triaxial compressional test results under various hydrate-soil contact stiffness ratios (Brugada et al., 2010): (a) stress-strain responses; (b) volumetric responses

### 2.3.2 Cementation model

Similar 3-Dimension simulations were also performed by Jung et al. (2012) on the macroscopic behaviour of the cementation model. Concerning the cementation pattern, Jiang et al. (2013) expounded the application of their defined contact bond model to the study of stress-strain and volumetric responses in their 2-Dimension DEM cementation case.

Figure 2.23 (Jung et al., 2012) showed the stress-strain and void ratio responses of the prepared cementation model at two different initial porosities of the pure soil sample during the triaxial tests under the confining pressure of 1 MPa. Firstly, it needs to be noted that this cementation model cannot be directly compared with the pore-filling model prepared by Brugada et al. (2010), because they were not based on the same soil model, and the input parameters were different as well.

When the soil sample initial porosity was 0.361 in Figure 2.23, the stiffness at the elastic phase did not increase obviously with the hydrate saturation. But the strength increased steadily. However, when the initial porosity was 0.393, the stiffness increased evidently with the hydrate saturation. The strength at low saturation (5% and 20%) of the  $n=0.393$  sample was lower than that of the  $n=0.361$  sample. When  $S_h=50\%$ , the strength of the  $n=0.393$  sample was higher than that of the  $n=0.361$  sample, which might be because that more hydrate particles were generated inside the loose sample and contributed more to the strength of the sample at high hydrate saturation.

At the bottom of Figure 2.23, the void ratio responses during the triaxial tests were plotted. When the soil initial porosity was 0.361, the dilation was enhanced by higher hydrate saturation steadily. But the dilation in the  $n=0.393$  sample only happened obviously when  $S_h=50\%$ . It needs to be mentioned that the void ratio in the study of Jung et al. (2012) refers to the granular void ratio which considers the hydrate volume as part of the pore volume. This will be introduced further in Chapter 4.

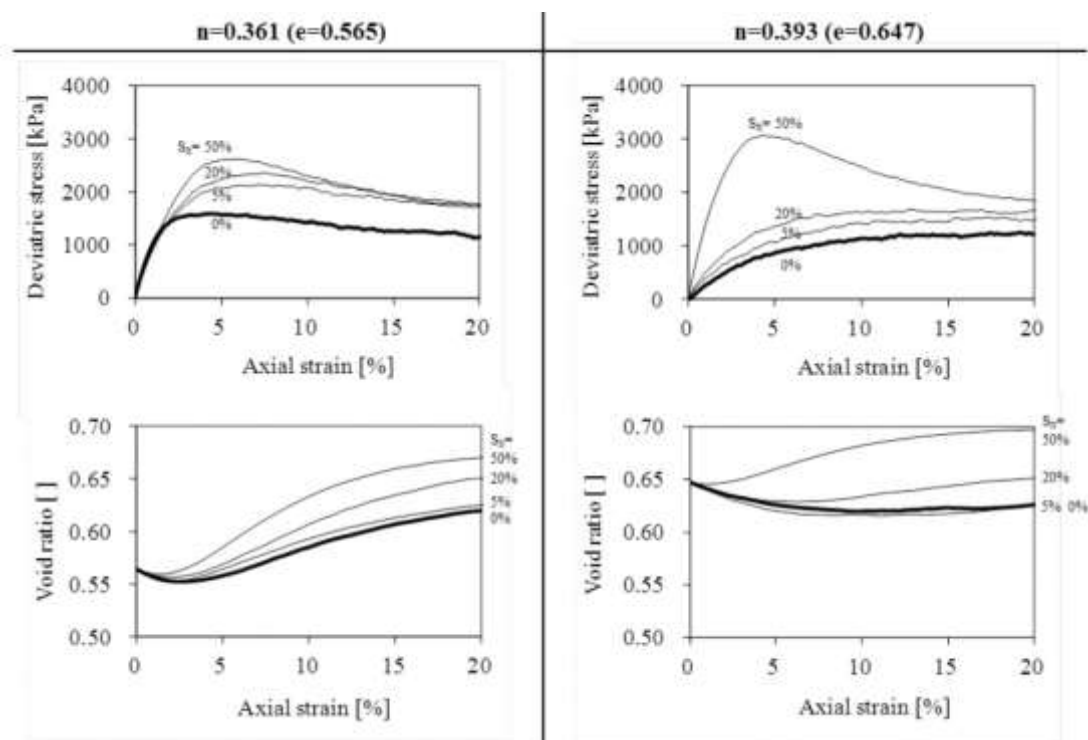


**Figure 2.23:** Triaxial compressional test results under two different initial porosities (Jung et al., 2012): (top) stress-strain relationship; (bottom) void ratio against axial strain

Figure 2.24 shows the critical state line projection on the  $p'$ - $q$  plane and  $p'$ - $e$  (void ratio) plane for the cementation model (Jung et al., 2012). It is shown that as the hydrate saturation increased, at various confining pressure, the critical state strength decreased. But the critical state granular void ratio increased with the hydrate saturation, although the dilation was weakened by the increased confining pressure.

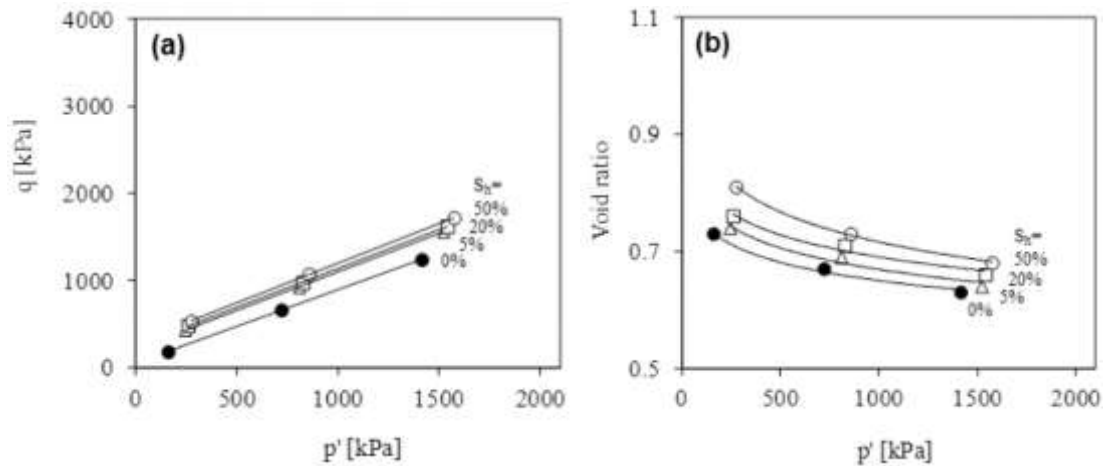
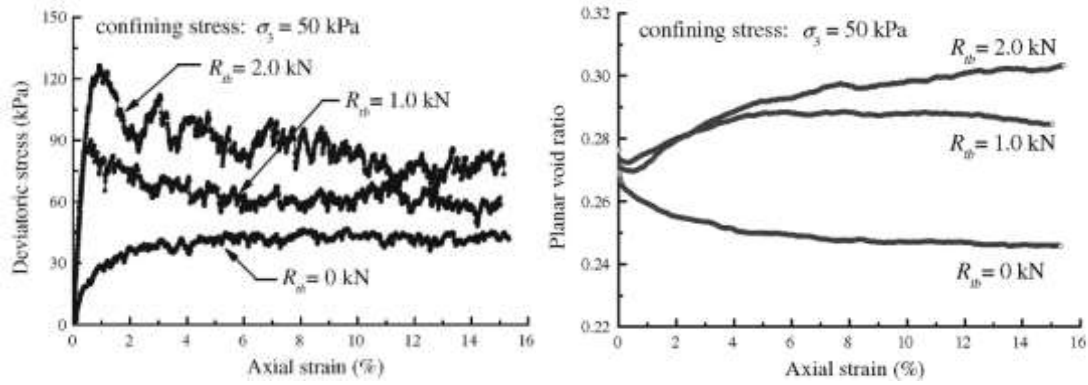


**Figure 2.24:** Critical state line for the cementation model (Jung et al., 2012): (a) critical state line projection on  $p'$ - $q$  plane; (b) critical state line projection on void ratio  $p'$ - $e$  plane

Furthermore, Jiang et al. (2013) applied their defined contact bond model to the study of stress-strain and volumetric responses in their 2-Dimension DEM cementation case. As shown in Figure 2.25, Jiang et al. (2013) conducted a series of biaxial tests on the 2D hydrate-bearing soil sample with a set saturation under the confining pressure of 50 kPa with three different bonding strength  $Rtb$ : 0 kN (considered as 0 kN although hydrate particles were set at a contact with soil particles), 1.0 kN and 2.0 kN.

It is suggested in Figure 2.25 (a) that a bonding strength can increase the stiffness. However, the increase in the bonding strength did not further increase the stiffness, while it increased the peak strength and critical state strength. Moreover, from the planar void ratio responses, it can be seen that, in this case, the dilation only happened when there was a bonding strength of the hydrate particles. And the dilation was enhanced by the increased in the bonding strength.



(a) stress-strain responses

(b) volumetric responses

**Figure 2.25:** Biaxial test results under various bonding strength (Jiang et al., 2013): (a) stress-strain responses; (b) volumetric responses.  $R_b$  refers to the bonding strength applied to the hydrate particles.

However, in both DEM cementation models discussed above, the bonding strength was set at different values. It can also be seen that the choice of the bonding strength may be still under discussion according to the specified DEM parameter inputs in each study.

## 2.4 Summary

In this Chapter, the granular material characteristics of the hydrate-bearing sand sediment is explored comprehensively through the reviews of the published studies by field work, experiments and DEM numerical modelling.

Field work is the most direct method for the exploration of the hydrate-bearing sediment, but there are currently many limitations for the in-situ studies due to the location of the sediment and the accuracy of the obtained data. In addition to the field work, laboratory studies are required to study the hydrate-bearing sediments and connect hydrate saturation with measured geomechanical properties in order to interpret the field data. And other scientific research methods are also required to carry out comprehensive studies on the geomechanical properties of hydrate-bearing sediments, and to provide support for exploration, production and reservoir process and management. Yet, there is still a lack of data on the analysis from the particle scale,

but the hydrate-bearing sediment possess the particulate characteristics. Hence, in addition to the field work and experimental research, Discrete Element Modelling are also employed for the investigation of the macro- and micro- mechanical behaviours of the hydrate-bearing sediments. The summary of the reviews are listed as follows:

(1) From the field work by remote seismic technology, generally, it indicates that the elastic wave velocity increases with a higher hydrate saturation and decreases in porosity. And through the experimental studies, it is found that wave velocities and the small-strain stiffness of methane hydrate sediments depend on both the hydrate saturation and the hydrate growth pattern within the pore space.

Moreover, the pore-filling pattern and the cementation pattern have shown the two most typical geophysical behaviours of hydrate-bearing sediments – lowest and highest wave propagation velocities respectively in the sediment. And the wave velocity data of all the other reported hydrate distribution patterns were all between the velocity values of the pore-filling and cementation cases. And the mainly discussed patterns are also pore-filling and cementation patterns in most of the published research which were also comprehensively reviewed by Soga et al. (2006) and Waite et al. (2009). Hence, in this PhD research, the pore-filling pattern and the cementation pattern were chosen as the main hydrate distribution patterns for study.

(2) From the drained triaxial compressional tests by experiments and DEM simulations, it has been confirmed that hydrates increase stiffness, strength and dilation of the sediment. However, the hydrate saturation and hydrate distribution patterns determine the sediment's mechanical behaviours. Generally, as the hydrate saturation increased, the stiffness and strength increases, and the dilation is also enhanced. It is also found that, regarding the hydrate contribution to the strength of the sediments, the pore-filling hydrate is of a frictional nature, whilst the cementation hydrate is of a frictional and cohesive nature. The effect of the cohesion in the cementation pattern enhances the hydrate contribution to the mechanical behaviours of the sediment, compared to the pore-filling pattern.

(3) Nevertheless, in most of the previous DEM studies (Brugada et al. 2010, Jung et al. 2012, Jiang et al. 2013), DEM was employed to simulate one hydrate distribution

pattern – pore-filling or cementation. There was no consistent DEM model for the comprehensive comparisons among different hydrate distribution patterns. Secondly, the critical state behaviours of the sediment were not studied systematically. In the third place, the study on small-strain stiffness is crucial to the geomechanical investigation of hydrate-bearing sediments, whereas none of the past DEM research has simulated the wave propagation. In the fourth place, all the DEM studies were performed assuming that all the soil and hydrate particles were spheres, but the actual shape of natural soil particles could dominate the sediment's mechanical behaviour. Moreover, in the cementation pattern research, the effect of the hydrate bonding strength in the DEM simulations has never been discussed systematically. Most importantly, DEM is regarded as a competent tool in the particle-scale microscopic study, but the published DEM studies focused mainly on the macroscopic behaviours of the sediments compared to the experimental data.

Accordingly, in this PhD research, a comprehensive DEM research was performed, and all the above-mentioned research gaps are covered:

- Two typical types of microscopic hydrate distribution patterns within soil pores were investigated via a consistent basic model: the pore-filling model and the cementation model.
- The large-strain deformation and the critical state behaviours were explored.
- Wave propagation was simulated within the DEM hydrate-bearing sediment samples.
- The effect of elongated soil particles on the geomechanical behaviours of sediments was studied.
- The bonding strength effect in the cementation model was systematically discussed. And
- The comprehensive particle-scale microscopic discussions and analysis were conducted.

## Chapter 3

# Sample preparation with Discrete Element Method

### 3.1 Introduction

As previously noted, in general, natural methane hydrate develops in the pores of highly compacted soil sediments under deep seabeds or permafrost regions under the high-pressure and low-temperature conditions. Methane hydrate grows in different patterns and distributions in the void space of the sediments because of the various formation conditions. In the laboratory tests, the synthetic hydrate-bearing soil samples are prepared according to the hydrate growth process in the natural hydrate-bearing sediment. Both natural hydrate-bearing sediment samples and synthetic hydrate-bearing soil samples are used within the laboratory studies (Soga et al., 2006).

In fact, it is very expensive to obtain the natural sediments, and it is challenging to control the temperature and pressure of the natural samples during the drilling and shipping process. In addition, it is also difficult to obtain the natural samples with the same soil properties and the various desired hydrate saturations for a comprehensive research. Because of this, synthetic samples are employed in the laboratory tests. However, it is also challenging to obtain well-controlled and consistent synthetic hydrate-bearing samples, as it is difficult to control hydrate formation, the distribution pattern and saturation during the synthetic sample preparation process.

Hence, the numerical method of Discrete Element Modelling (DEM) were employed as a useful tool in this research to replicate the particle behaviour usually experienced during laboratory sample preparation and testing, and to perform the particle-scale micro-mechanism interpretation in this study. The obtained DEM results in the next chapters will be compared with those from the laboratory and DEM studies discussed in Chapter 2.

In most of the previous DEM studies (Brugada, et al., 2010; Jung, et al., 2012; Yu, et al., 2012; Jiang, et al., 2013), DEM was applied to simulate only one hydrate distribution pattern. There was not a consistent DEM model for comprehensive comparisons amongst the various hydrate distribution patterns. Therefore, in this study, two typical types of microscopic hydrate distribution patterns inside soil pores were studied: the pore-filling model and the cementation model. As shown in Figure 3.1, in the pore-filling pattern, hydrate particles freely grow in the pores without connecting two or more soil particles together (Helgerud et al., 1999; Soga, et al., 2006). However, in the cementation pattern, hydrate particles grow at the soil-soil contacts and along the soil surface, and the compacted soil skeleton is bonded by the hydrates, while the soil-soil contacts are not bonded (Dvorkin et al., 1999; Soga et al., 2006; Jung et al., 2012). In both patterns, the soil skeleton, which has been formed by consolidation under high pressure, is not broken by the growth of hydrates inside the pores.

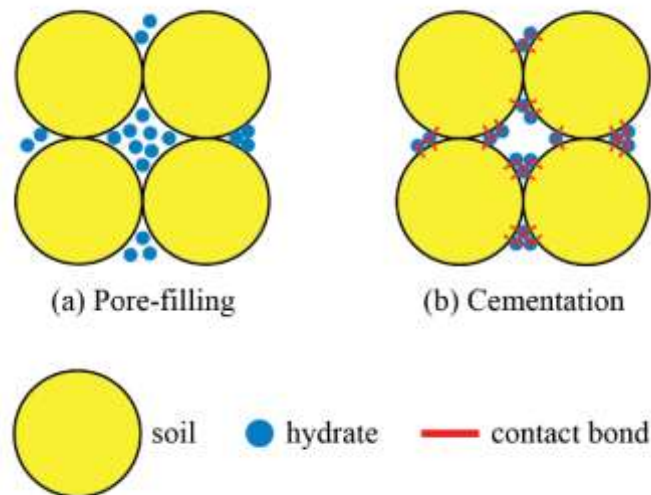


**Figure 3.1:** Hydrate distribution patterns of methane hydrate soil sample in DEM model: (a) pore-filling, (b) cementation

In this chapter, the numerical tool Discrete Element Method (DEM) and the DEM code Particle Flow Code 3 Dimensions (PFC<sup>3D</sup>) used in this study are introduced. And the DEM sample preparation procedures of the methane hydrate soil samples are discussed in the aspects of their important principles. The preparation of the pore-filling and cementation models have been stated in detail. Furthermore, the two hydrate

growth patterns in the cementation model are exhibited in this chapter. And the hydrate-bearing sediments with elongated soil particles were prepared in this research.

## **3.2 Numerical tool: Discrete Element Modelling**

### **3.2.1 Discrete Element Method**

#### **3.2.1.1 Overview of Particulate DEM**

As previously mentioned, for decades there has been many researches on the geomechanical behaviour of methane hydrate sediments. Nevertheless, the essential and crucial particle-scale investigation still appears as a research gap, which needs to be systematically conducted. It is also important to achieve the micro-mechanical insight into the geomechanical behaviours observed in the on-site and laboratory studies. Thus, because of the limitations of field work and experiments, numerical simulation modelling is a useful tool for particle-scale research.

Geomechanical behaviours of granular materials are generally studied at two scales: macro-scale and micro-scale. The macro-scale study focuses on the boundary value problems, which are to be solved using global constitutive equations, based upon continuum mechanics. On the other hand, the micro-scale study deals with the microstructure which determines material behaviour (Cheng, 2004; Kwok, 2008).

Geomechanical analysis is typically conducted by means of the continuum-based Finite Element Method (FEM). In a continuum model, granular material is assumed to act as a continuous material, and the relative movements and rotations of the particles within the material are not considered. Nevertheless, hydrate-bearing sediment, in nature, is not a continuum and its behaviour is accordingly non-linear. As noted in Section 2.1.1, within the soil voids, there is hydrate together with soils. There are also a complex aggregate of discrete particles of various sizes and shapes interacting with one another at contact points. During the deformation process, the soil particles may slide, rotate, deform or crush, which causes change in the soil skeleton (Kwok, 2008).

With hydrate inside the soil pores, the skeleton of hydrate-bearing soil changes in ways that are even more complicated.

As a numerical method, Discrete Element Method (DEM) models granular materials by specifically considering their actual particulate nature. For geotechnical engineers, this method is applicable to the study of micro-mechanisms underlying the complex response of soil. DEM is regarded, by Cundall and Strack (1979), as a particular discrete element method which employs deformable particle contacts and a specific time-domain solution of the original equations of motion (Cheng, 2004). Many researchers have used this method to study the interactions of individual particles within an assembly. It is this method's unique feature that allows it to consider the actions of individual particles with a granular material.

In DEM, the displacements and stresses of granular material can both be calculated and measured. Numerical modelling is more flexibly performable than analytical modelling, and has the advantage over physical modelling. The important data (average stresses and deformations, contact forces, particle positions, velocities, etc.) can be obtained at any stage of the test. The flexibility of numerical modelling also lies in the parameters and physical properties of the particles, as well as the loading configurations (Kwok, 2008). As developed by Cundall & Strack (1979), DEM considers the finite displacement of elements and their rotation and separation, and recognizes new particle contacts in the simulation. A DEM simulation accounts for equilibrium by considering the dynamic equilibrium of each particle at each time increment during the analysis. An overview of the sequence of calculations involved in a DEM simulation is given in Figure 3.2 (modified from O'Sullivan, 2011).

#### **3.2.1.2 Advantages and limitations of using DEM**

DEM can be employed as a fundamental research tool, with a view to the micromechanics of granular material, providing insight gained to advance constitutive models for continuum modelling. It also has the advantage of providing information on mechanisms at the particle scale which cannot be easily observed in the laboratory (O'Sullivan, 2011).

DEM is useful for meso- and micro- scale problems, since current computing power is still incapable of modelling millions of particles in a boundary value problem. In contrast, the Finite Element Method (FEM) applies more suitably to macro boundary problems. The future of soil mechanics lies no doubt in producing precise constitutive models with solid micro-mechanical bases (Kwok, 2008).

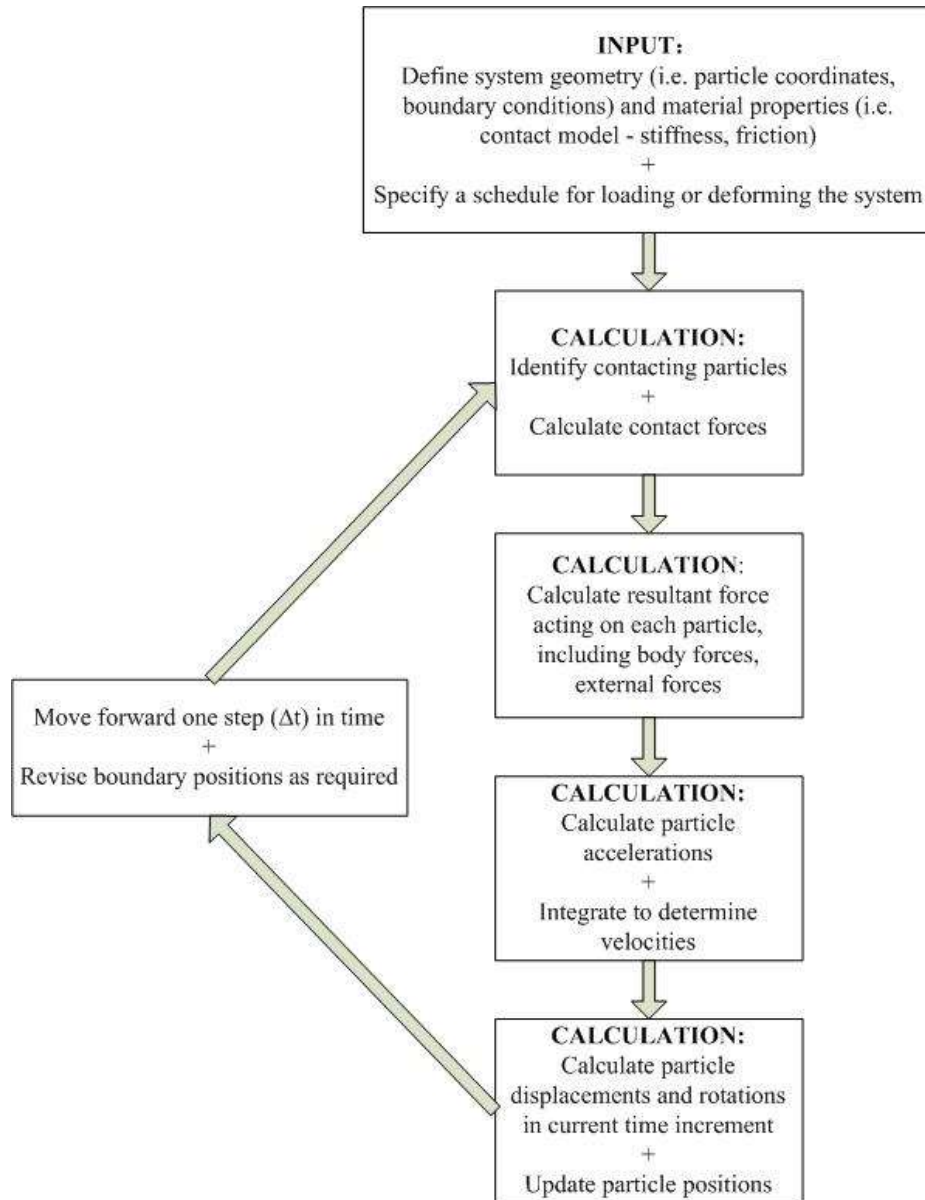


**Figure 3.2:** Schematic diagram of calculations in a DEM simulation (modified from O’Sullivan, 2011)

The computational time cost of DEM calculation is the major problem, restricting DEM research with the field- or industrial-scale numbers of particles and boundary

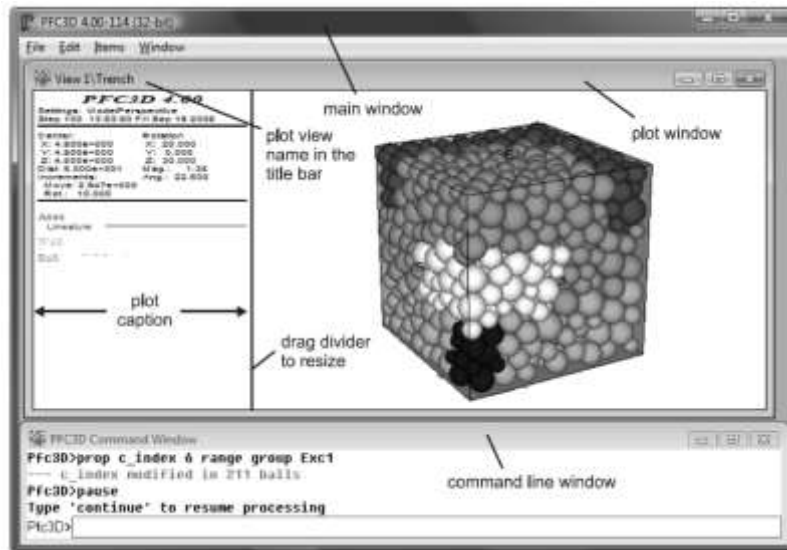
value problems, as well as the realistic particle geometries. Solving this problem is a crucial and ongoing challenge for DEM analysts (O'Sullivan, 2011). Looking forward, DEM will certainly not supplant continuum modelling to predict granular material deformations, nor will it supplant physical laboratory tests to improve the fundamental interpretation of granular material response. It has however definitely established itself as one of the important tools that can be used for the research of granular materials.

#### 3.2.2 Particle Flow Code 3 Dimensions

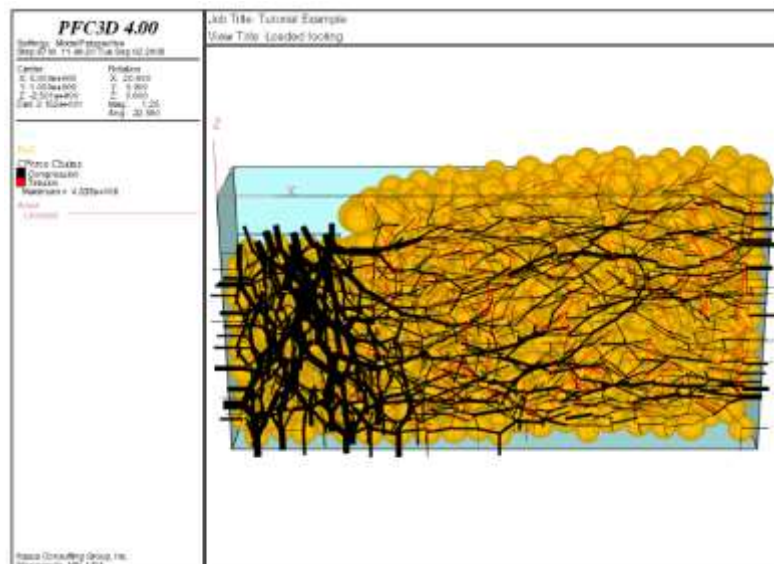
Particle Flow Code in 3 Dimensions (PFC<sup>3D</sup>) is employed to model the interaction of simulated particles as well as their movement with DEM following the descriptions of Cundall and Strack (1979). Devised by Itasca Consulting Group Inc., PFC<sup>3D</sup> is an effective tool to model the complex problems of solid mechanics and granular flow. In this study, PFC<sup>3D</sup> version 4.0 (Itasca, 2008) was used for the study of the geomechanical behaviour of modelled methane hydrate soil samples, as well as the involved micro-mechanisms.

In this programme, the particle interactions are monitored contact by contact, and the particle motions are modelled particle by particle. Contact forces and displacements are accounted for by equilibrium conditions, assuming that increments of contact forces are dependent on incremental displacements of particle centres. The observed macroscopic behaviour completely results from the interactions between individual particles.

Forces are imposed on each ball via their contacts with other balls or walls. At equilibrium, the algebraic sum and vectorial sum of these forces is approximately zero (i.e. the forces acting on each ball are almost in balance). The continuous movement of particles is indicated to be proceeding within the model when the unbalanced forces draw near a non-zero value. Both the maximum unbalanced force and the mean unbalanced force are automatically calculated for the entire assembly of balls during time-stepping in a PFC<sup>3D</sup> run, so as to diagnose the state of the model. Figure 3.3 shows the PFC<sup>3D</sup> graphical user interface with the plot window.



(a) A plot window



(b) Contact forces due to footing load

**Figure 3.3:** PFC<sup>3D</sup> graphical user interface with plot window (Itasca Consulting Group, Inc., 2008). (a) a plot window; (b) contact forces due to footing load (black and red lines represent the compression and tension forces separately, and the thickness of the lines illustrates the value of forces)

PFC<sup>3D</sup> provides the assumptions of a particle flow model (Itasca, 2008):

- (1) All the particles are regarded as rigid solids.

- (2) The contacts are taken into account even on a vanishingly small area (i.e. a point).
- (3) The behaviour at the contact points applies a scheme of soft contacts, where at points the overlapping between particles is allowed.
- (4) The overlapping magnitude is correlated with the contact force by the force displacement law. There is little relation between the overlaps and the sizes of the particles.
- (5) Bonds can exist at the granular contacts.
- (6) Particles are spheres. Yet, the generation of arbitrary shape is supported by the clump logic. Each clump is constitutive of a group of particles overlapping one another, acting as a rigid solid which cannot be broken while possesses the deformable boundary.

### 3.2.2.1 Notation

An overview of the common parameters in PFC<sup>3D</sup> is listed below, and shown in Figure 3.4 (Itasca Consulting Group, Inc., 2008):

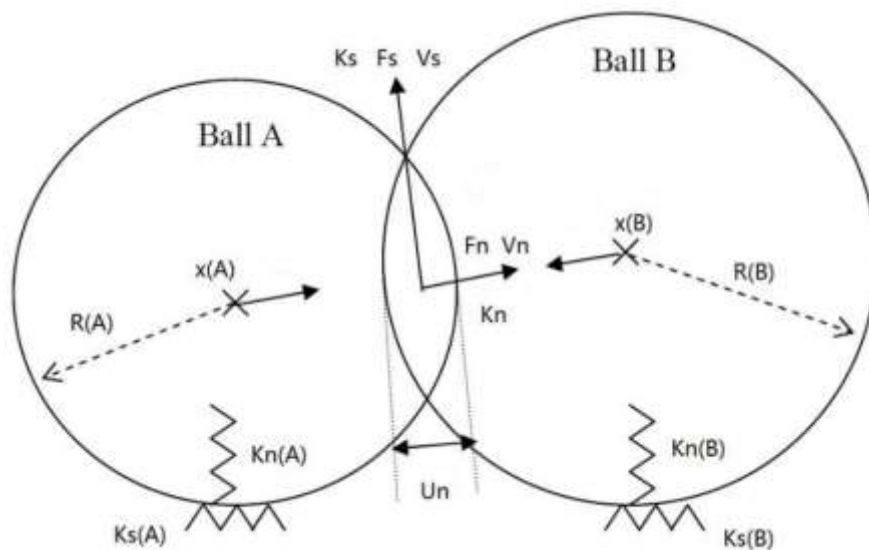


**Figure 3.4:** Notations used to describe a ball-ball contact (Itasca, 2008)

At a contact between two balls:

$U_n$  denotes overlap

$K_n$  and  $K_s$  are the normal and shear stiffness at the contact

$F_n$  and  $F_s$  are the normal and shear force vectors at the contact

$V_n$  and  $V_s$  are the normal and shear velocity vectors at the contact

For an individual ball:

$R(A)$  and  $R(B)$  are the radii of ball A and ball B

$x(A)$  and  $x(B)$  are the position vectors of the centres of ball A and ball B

$K_n(A)$  and  $K_n(B)$  are the normal stiffness of ball A and ball B

$K_s(A)$  and  $K_s(B)$  are the shear stiffness of ball A and ball B

Sign Conventions:

- (1) The vector of contact force ( $F$ ) stands as both the action and direction of ball A on ball B for contact between balls and represents the action of the ball on the wall for contact between balls.
- (2) Positive normal contact forces indicate compression, while negative normal contact forces indicate tension.

#### 3.2.2.2 Contact Model

In this study, in the light of the manual of PFC<sup>3D</sup> Version 4.0 (Itasca, 2008), the constitutive relationship at contact points includes (1) the stiffness model; (2) the slip model; and (3) the contact bond model

- (1) Stiffness model

The stiffness of contact connects the contact forces with the corresponding displacements in the directions of the normal and shear forces. The normal stiffness  $K_n$  relates the total normal force  $F_n$  to the total normal displacement  $U_n$ . Thus it is secant stiffness, as given by Equation 3.1:

$$F_n = K_n U_n \quad (3.1)$$

The shear stiffness  $K_s$  relates the increment of shear force  $F_s$  to the increment of shear displacement  $U_s$ . Hence it is tangent stiffness, as given by Equation 3.2:

$$F_s = -K_s U_s \quad (3.2)$$

In this study, the linear contact model is used, supposing that the the two contacting entities stiffness take effect in succession. The contact normal secant stiffness is given by Equation 3.3 and the contact shear tangent stiffness is calculated by Equation 3.4:

$$K_n = \frac{K_n(A) \times K_n(B)}{K_n(A) + K_n(B)} \quad (3.3)$$

$$K_s = \frac{K_s(A) \times K_s(B)}{K_s(A) + K_s(B)} \quad (3.4)$$

Actually, there are two main reasons for using the linear contact model in this PhD research. The first reason is for the simplification. A simple contact model at the initial stage of the DEM research on methane hydrate sediment is necessary. The second reason is that the popular Hertz contact model cannot apply to the cementation model when doing the seismic wave propagation simulation. Hence, the linear contact model was chosen at this stage. In the future work, a more complicated model should be applied to the DEM research.

#### (2) Slip model

Slip behaviour is provided through enforcing a connection between the shear and normal force, so that the two interacting contact entities are capable of slipping relative

to one another. The relation does not provide normal strength in tension, but allows slippage to happen by means of limiting the shear force. The slip behaviour is always active, unless a contact bond is present - in which case the contact bond behaviour supplants the slip behaviour. The linear model describes the force-displacement behaviour, as shown in Figure 3.5. The slip behaviour is defined by:

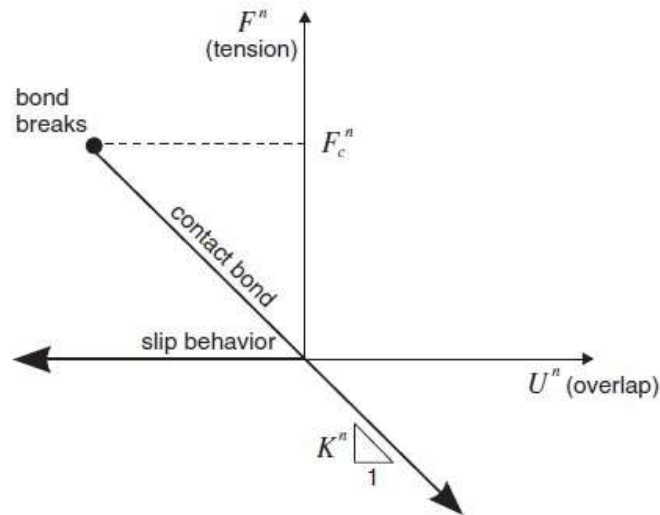
$$F_{max}^s = \mu | F_n | \quad (3.5)$$

where  $F_{max}^s$  is the maximum allowable shear contact force,  $\mu$  is the coefficient of friction, and  $F_n$  is the normal contact force at the contact. When the limiting Coulomb's shear force has been reached, slippage is allowed to happen.

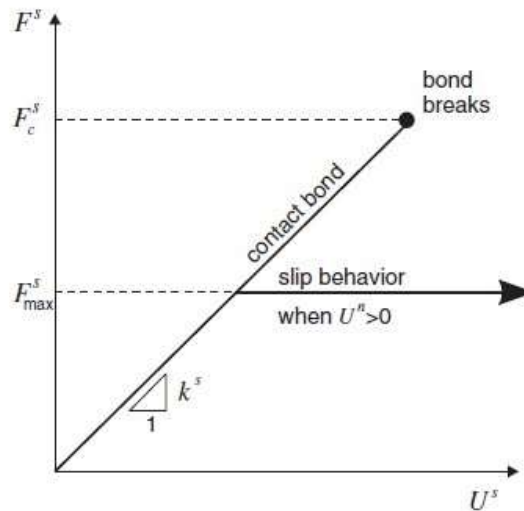
#### (3) Bonding model

In PFC<sup>3D</sup>, particles are allowed to be bonded together at contact points. Bonded granular material is employed in order to represent breakable grains in the simulations. A contact bond can be considered as a point of glue or a pair of elastic springs with the constant normal and shear stiffness occurring at the contact point, and in which the two springs specify the tensile normal strength and the shear strength. The contact bond glues the spheres at a vanishingly small size, acting only at the contact. The contact bond transmits a force, but not a moment. The presence of a contact bond deactivates the slip model. When a bond is formed at a particle-particle contact point, the contact will continue to exist until bond breakage happens.

Both the normal contact bond strength  $F_c^n$  and the shear contact bond strength  $F_c^s$  define a contact bond. When the tensile normal contact force is above or equal to the normal contact bond strength, the bond will break as a result, and contact forces will become zero. When the shear contact force is above or equal to the shear contact bond strength, the bond will break too as a result, but the contact forces will not be changed if the shear force is not above the friction limit and the normal force is still compressive. Figure 3.5 shows the force-displacement behaviour of contact occurring at a point. Both the contact bond model and the slip model are active at any given time.



(a) normal component of contact force



(b) shear component of contact force

**Figure 3.5:** Force-displacement behaviour of contact occurring at a point (Itasca, 2008)

In PFC, there is another bond model – parallel bond. It is described in the PFC<sup>3D</sup> manual (Itasca, 2008) that a parallel bond approximates the physical behaviour of a cement-like substance lying between, and joining, the two bonded particles. Parallel bonds establish an elastic interaction between particles that acts in parallel with any other contact model at the contact. Parallel bonds can transmit both force and moment between particles, while contact bonds can only transmit force acting at the contact point. Hence, the definition of the parallel bond requires more parameters than the contact bond.

According to the discussion of the laboratory formation of hydrate-bearing samples in Chapter 2, the parallel bond seems to be a better solution for building the cementation model of the DEM hydrate-bearing samples. However, for simplification in this research, instead the contact bond model was used in the cementation model. There were several reasons for this choice. One reason is that the stiffness of hydrate was much smaller than that of soils, which means the soil particles were the dominating particles in the mixture while the soil particles were not bonded to each other. Another reason is that the cementation sample with the contact bond model could be more easily and directly compared with the pore-filling model, rather than with the parallel model which is more complex. But in the next step of this research, a parallel bond should also be considered.

#### 3.2.2.3 Clump

In PFC<sup>3D</sup>, there is a clump logic (Itasca Consulting Group, Inc., 2008) serving to study the granular materials with different shapes of particles. The clump function provides a technique to generate groups of clump particles, as indicated in Figure 3.6. A clump models one rigid body, and the particles that constitute the clump remain at a fixed distance from one another and do not rotate from one another. Contacts inside the clump are ignored during the calculation, which also helps to save computational time. Particles of a clump can overlap to any extent, whilst there are no contact forces between these particles. Hence, clumps behave as rigid bodies which will never break apart, despite of the forces acting on them. By this logic, a clump is different from a cluster, which refers to a group of particles that are bonded to one another.

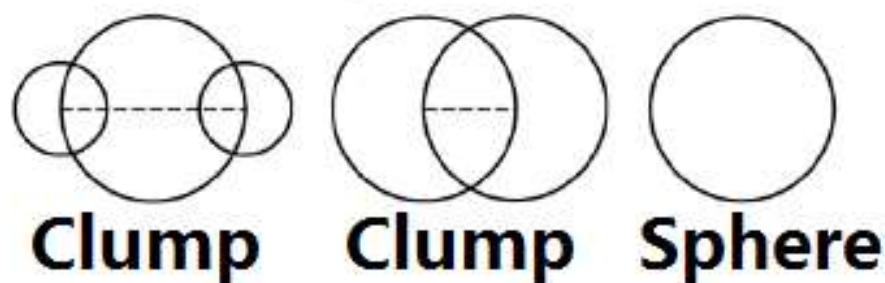


**Figure 3.6:** 2D Sketch of clump and sphere in PFC

### **3.3 Choice of the sample preparation procedures**

There are various methods for the DEM sample preparation published in literature. One typical way is known as the ‘multi-layer with under compaction method’ (Jiang et al., 2003), in which particles are placed in different compacted layers, and generating a homogenous specimen. Another typical method is to simulate the sedimentation process by applying the gravity to particles (Marketos, 2007). However, both methods are not quite similar enough to the formation process of hydrate-bearing sediments. As mentioned previously, natural methane hydrate develops in the pores of highly compacted soil sediments, which means the highly compacted soils exist first before the formation of hydrates. In addition, the formation process of hydrate is that a large amount of methane, which is trapped within a crystal structure of water, forms solid methane hydrate which can be enlarged by the on-going hydrate growth.

Hence, in this research, the ‘radius expansion method’ provided in PFC<sup>3D</sup> (Itasca, 2008) was employed so as to model the growth process of hydrate in the pores of consolidated soil particles. Using this method, particles are first generated at half the value of the target sizes, and then enlarged to their final sizes. This method can also help reduce overlapping between particles in the particle generation process and reach equilibrium in a shorter computational time.

Two synthetic sample preparation methods are usually used in the laboratory tests and the numerical simulations: ‘Hydrate + Soil’ and ‘Hydrate → Soil’ (Brugada et al., 2010). The ‘Hydrate + Soil’ method is used by mixing soil particles with hydrates. The hydrates are randomly placed into a sample together with the soil particles at low confinement and low temperature, and then the sample is isotropically consolidated to a desired effective stress. Alternatively, the ‘Hydrate → Soil’ method challenges the laboratory studies, because the loose soil sample should be initially isotropically consolidated to form the soil skeleton under the desired effective stress, where following on from this, hydrates are generated in the void space of the sample to reach different hydrate saturations by injecting methane gas into the void space which is full of water. And then methane hydrate formed with the decreasing low temperature in the pores of the consolidated soil samples.

Between the above two sample preparation methods, the ‘Hydrate → Soil’ sample preparation method is closer to the natural hydrate formation process in sediments under deep seabeds and permafrost regions, where there is high pressure and low temperature, and the soil skeleton is formed first before the growth of methane hydrate. Hence, in this DEM study, the ‘Hydrate → Soil’ sample preparation procedure was adopted. Figure 3.7 shows a 2-Dimension sketch diagram of the sample preparation procedure.

The basic DEM sample preparation procedure of the hydrate-bearing sediments generally included: (1) to design the input property parameters of the soil and hydrate particles; (2) to set the boundary (walls) conditions for the particle generation and the upcoming tests; (3) to generate the consolidated soil sample at a desired confining pressure; (4) to generate the pore-filling or cementation hydrate particles inside the pores of the prepared soil sample to reach a desired hydrate saturation under the given confining pressure.

However, regarding the accuracy which the DEM simulation can achieve, it is actually challenging to properly compare the prepared DEM methane hydrate sediment sample with the actual microstructure of the real methane hydrate sediment. Firstly, for the simplification there is no water included in this DEM model, so that the comparison cannot be made easily. Secondly, the DEM hydrates are sphere particles rather than the hydrate mass.

In this DEM model, although the DEM microstructures are not equivalent to the actual microstructure of the natural hydrate-bearing sediment, the spherical hydrate particles were generated exactly according to the definition of the hydrate growth patterns: in the pore-filling pattern, hydrate particles freely grow in the pores without connecting two or more soil particles together (Helgerud et al., 1999; Soga, et al., 2006); in the cementation pattern, hydrate particles grow at the soil-soil contacts and along the soil surface, and the compacted soil skeleton is bonded by the hydrates, while the soil-soil contacts are not bonded (Dvorkin et al., 1999; Soga et al., 2006; Jung et al., 2012). Because the methane hydrate research is a relatively new area, and methane hydrate are buried under the deep seabed, it is not really possible to find the observations of the microstructure on site. Hence, according to the limited data of

hydrate microstructure, this DEM research is among the first attempts in this research direction, although the DEM model cannot be assumed to be the actual sediment.

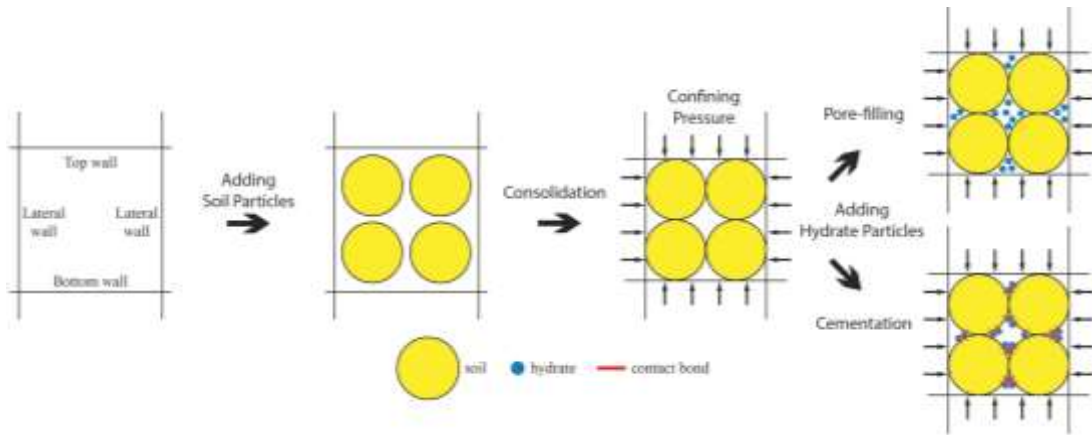


**Figure 3.7:** 2-Dimension sketch diagram of the DEM sample preparation procedure of the hydrate-bearing soil

### 3.4 Sample preparation of pore-filling and cementation models

#### 3.4.1 Input parameters of soil and hydrate particles

Generally, the input property parameters of the DEM samples originated from the data measured through the experiments and assumptions. However, samples also required some appropriate numerical changes. The main property parameters which are necessary to be considered includes friction (inter-particle & wall-particle), number of particles, density, initial void ratio, grain shape, grain size and size distribution pattern, aspect ratio (sample & particles), stiffness (particles & walls), etc.. The input parameters for the DEM sample preparation are shown on Table 3.1.

The spherical particle diameters (0.1 mm – 0.25 mm) of the soils followed Gaussian distribution, as shown in Figure 3.8. Actually, in this research, there are six groups of soil particles with different sizes within the range of 0.1 mm – 0.25 mm. The diameters of the six groups of soil particles are 0.1125 mm, 0.1375 mm, 0.1625 mm, 0.1875 mm, 0.2125 mm and 0.2375 mm respectively. By doing this, it is more convenient for the study on the effect of elongated soil particles when replacing the spherical particles with elongated clumps in PFC<sup>3D</sup>.

**Table 3.1:** Input parameters for soil and hydrate particles used in the DEM model

Property	Soil	Methane hydrate
Particle size $D$ (mm) (Gaussian distribution)	0.1 ~ 0.25	0.04
Density $\rho$ (kg/m <sup>3</sup> )	2600	900
Elastic Modulus $E_c$ (MPa)	286	28.6
Normal contact stiffness $k_n$ (N/m)	$2DE_c$ $= 0.572 \times 10^5 \sim 1.430 \times 10^5$	$2DE_c$ $= 2.288 \times 10^3$
Shear contact stiffness $k_s$ (N/m)	$0.7k_n$ $= 0.4004 \times 10^5 \sim 1.001 \times 10^5$	$0.7k_n$ $= 1.6016 \times 10^3$
Inter-particle friction $\mu$	0.75	0.75

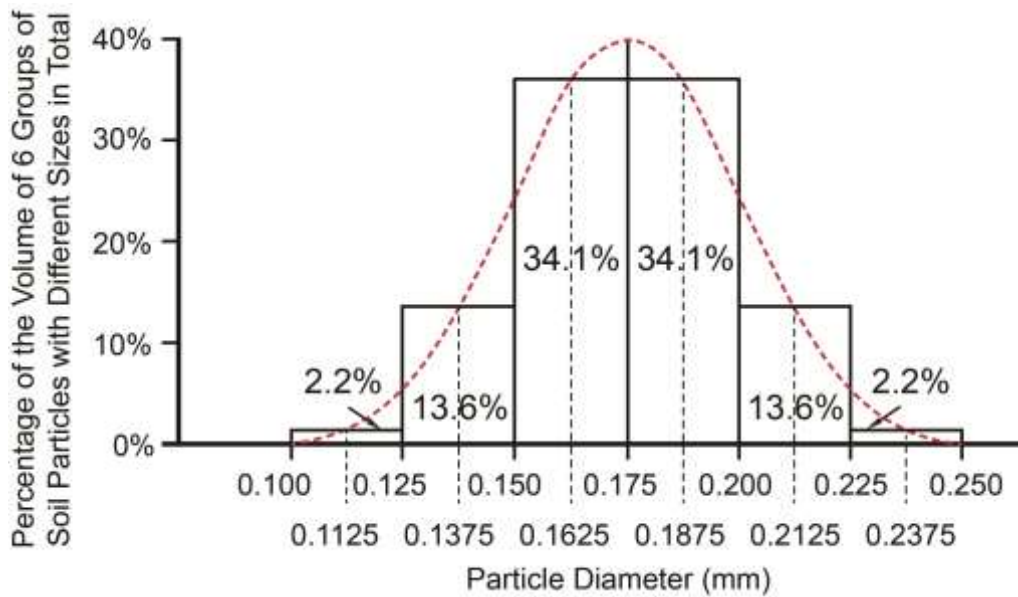


**Figure 3.8:** Gaussian distribution of soil particles' sizes

The spherical hydrate particle size needed to be set smaller than the soil particles in order to properly simulate the hydrates' formation at the soil-soil contacts, as well as along the soil surface and in the pore spaces. This way, the hydrate influence on the sediment's skeleton would be obvious during the simulation process. However, the

computational time during the DEM simulation depends on the particle number. Thus, the hydrate particles could not be made as small as possible. A hydrate particle diameter of 0.04 mm was chosen. The results in Chapter 4 show that the chosen particle size of hydrates had already properly simulate the geomechanical behaviour of hydrate-bearing samples according to the published laboratory studies, in both the pore-filling and cementation models. Hence, a smaller size did not have to be chosen due to the limited computational time. In addition, gravity was not applied to the particles.

According to the published research (Kezdi, 1974; Prat et al, 1995), the elastic Young's modulus of the dense well-graded sand is between 160 MPa and 320 MPa. And actually, the real dense sand's elastic modulus can be as high as 1000 MPa. Since this research originally followed the research of Brugada et al. (2010), the elastic modulus of 286 MPa was chosen for the soil particles, in order to be properly compared with the published studies. However, there is a lack of data in the literature and the experimental results about the contact elastic modulus  $E_c$  of hydrates. The stiffness of methane hydrate is described as being only a bit higher than that of ice (Soga et al., 2006). Therefore, in this research, the hydrate/soil elastic modulus ratio  $E_c^{hyd} / E_c^{soil}$  was assumed to be 0.1 according to the published DEM research of Brugada et al. (2010). For the DEM simulations, the normal contact stiffness  $k_n$  is proportional to the particle elastic modulus  $E_c$  and the particle diameter  $D$ , by Equation 3.6. The hydrate/soil contact stiffness ratio  $k_n^{hyd} / k_n^{soil}(D_{50})$  was 0.023, where  $D_{50}$  was the mean value of the particle diameters 0.175 mm. A higher hydrate/soil contact stiffness ratio hydrate/soil elastic modulus ratio  $E_c^{hyd} / E_c^{soil}$  of 1.0 was also used in the discussion in Chapter 6.

$$\text{Normal contact stiffness: } k_n = 2DE_c \quad (3.6)$$

It is now generally recognized by the research community that the main objective of DEM-based investigation is not to provide quantitatively reproduction of material behaviour, but to understand qualitatively the particle-scale mechanism affecting the continuum-scale responses. Hence, the input parameters for the particles were

principally designed for the numerical simulation purpose. And the obtained results in the next chapters have proved that the input parameters were reasonable for the qualitative interpretation in the DEM modelling.

#### 3.4.2 Walls

The prepared DEM sample was a cylinder of 3.5 mm (height)  $\times$  1.75 mm (diameter) and a height/diameter ratio of 2:1, which was confined by the lateral cylindrical wall and the planar walls at the top and bottom. The three smooth walls were used to confine and load the sample, and were made longer to meet the needs for large straining during the tests (Itasca, 2008), as illustrated in Figure 3.9.

It is important to note that in PFC<sup>3D</sup> the walls intersect with one another but do not interact, the walls only interact with particles. In DEM research, a rigid boundary is the most widely used (O’Sullivan, 2011). Cheng et al. (2003) exhibited that the servo-controlled rigid boundaries in DEM analysis was effective. Hence, in this research the normal stiffness of the walls was set to be approximately 100 times that of the biggest soil particles’ normal stiffness ( $k_n^{wall} = 1.5 \times 10^7$  N/m,  $k_s^{wall} = 1.5 \times 10^7$  N/m,  $\mu^{wall} = 0$ ), which would be an effective confinement when the particles were moved and rotated by large contact forces inside the walls.

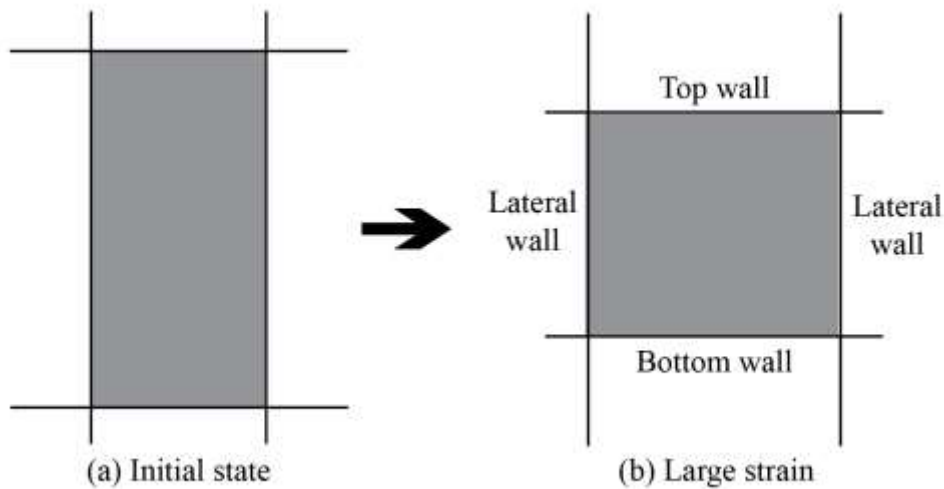


**Figure 3.9:** 2-Dimension simplified schematic diagram of the walls at the initial state and the large strain state

### 3.4.3 Hydrate saturation

Regarding the hydrate occupancy in the hydrate-bearing sediments, the term ‘hydrate saturation’ ( $S_h$ ) was introduced by referring to the percentage of hydrate volume occupancy in the void space in the pure soil sample (Equation 3.7). The total number of soil particles was 2000. As for the hydrate particle number, as an example, the total number of hydrate particles varied from 10114 to 40459 at the hydrate saturation of 10% and 40%, respectively. The numbers of the soil and hydrate particles at various saturation are shown in Table 3.2.

$$\text{Hydrate saturation: } S_h = \frac{\text{Volume}_{(\text{hydrates})}}{\text{Volume}_{(\text{pores})}} \quad (3.7)$$

**Table 3.2:** Number of soil and hydrate particles at various hydrate saturation in DEM simulations

Hydrate Saturation	Particle Number	
	Soil	Hydrate
0%	2000	0
10%	2000	10114
20%	2000	20229
30%	2000	30344
40%	2000	40459

It should be noted that the hydrate saturation computed here may not be the same as the hydrate saturation measured in the laboratory. The simulated hydrate saturation ( $S_h$ ) should correspond to a higher hydrate saturation than the natural hydrate-bearing soil sediments for several reasons, such as the size and shape of the assumed soil and

hydrate particles, the void space limitations, and the existence of other materials in the pores of the natural sediment. Because of the spherical shape of the soil and hydrate particles in the DEM model, after adding  $S_h = 40\%$  of hydrate particles, there would be no single void space for placing a single hydrate particle inside, although the total remaining (wasted) void space volume would still be large, as illustrated in Figure 3.10. However, the overlapping of hydrate particles would cause higher mean contact force than the confining pressure, which would cause the sample to expand. The volume and void ratio would also be changed. In other words, in this research, after the 40% saturation of hydrate particles were generated in the consolidated soil sample, no more hydrate particles could be added when the particles' overlapping and the sample volume were properly controlled. It is likely that hydrate saturation was underestimated. However, the actual 40% saturation could not simply be assumed as 100% saturation, as there were still void spaces in the sample. Hence, the behaviour observed in this study should be examined qualitatively rather than quantitatively.

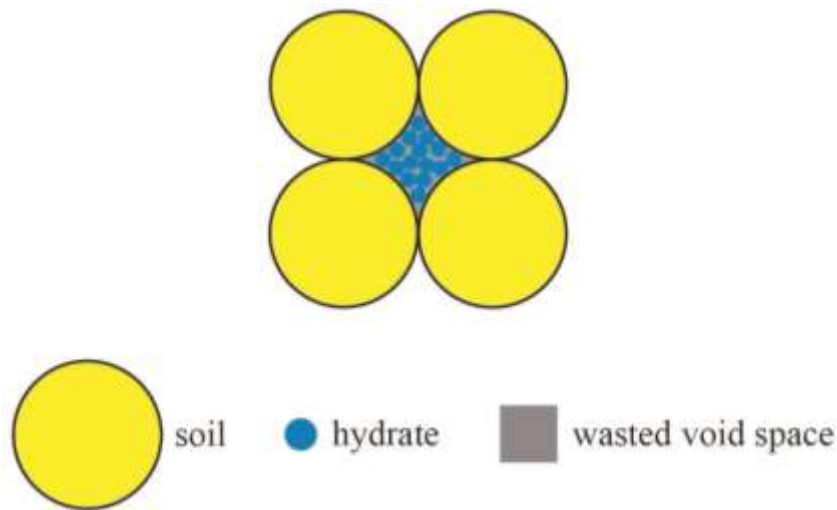


**Figure 3.10:** The remaining void space inside the DEM hydrate-bearing soil sediment (2D sketch)

In the natural sediments, hydrates grow in the pores of the existing soil sediments. But cases are different. In some sediments, methane hydrate forms in the unsaturated condition; while in other sediments, hydrate forms in the saturated condition. In fact, the laboratory hydrate sample preparation mostly follows the second case that methane gas was injected into the saturated soil sample to obtain the different hydrate saturations. However, due to the low temperature in the sample, it is challenging to

control the extra ice which forms without dissolving the methane gas. In order to solve this problem, in the laboratory sample preparation, there is another method to prepare the hydrate-bearing sediment – mixing the soils and the prepared hydrates. However, this method not only breaks the original soil skeleton, but also cannot control the hydrate growth patterns.

In this DEM research, as discussed earlier, it is obvious to see that the hydrate particle size is still a big issue for the accuracy of the hydrate saturation in the sample preparation process. The particle size affects how the particles are packed in the void space, and also affects the wasted volume size. A smaller size of the hydrate particles can definitely increase the volume occupancy of the hydrate in the void space. But the much larger number of hydrate particles challenges the computational time during the simulation process. Hence, the sample preparation is still a difficult and challenging job at this stage. A further study on the assumption of the hydrate saturation in this DEM study is discussed in details in Appendix A of this thesis. The principles of comparing the DEM saturation with the laboratory saturation could depend on the assumptions to some extent.

#### 3.4.4 Pore-filling model

In the pore-filling model prepared in this study, as shown in Figure 3.11, hydrate particles were generated in the void space of the consolidated soil sample to reach different hydrate saturations ( $S_h$ ). The soil particles were first generated at half the value of the target sizes, and they were then enlarged to the final sizes in order to reduce the overlapping between particles in the particle generation process and to reach equilibrium in a shorter computational time. After that, the soil sample (with initial porosity  $n=0.43$ ) was consolidated to the isotropic effective stress of 1 MPa, 2 MPa or 3 MPa, as natural methane hydrate develops and exists under the high pressure in sediments under deep seabeds and permafrost regions. Following on from this, hydrates are generated randomly in the void space of the sample at half the value of the target sizes, and then enlarged to the final sizes so as to reach a chosen hydrate saturation.

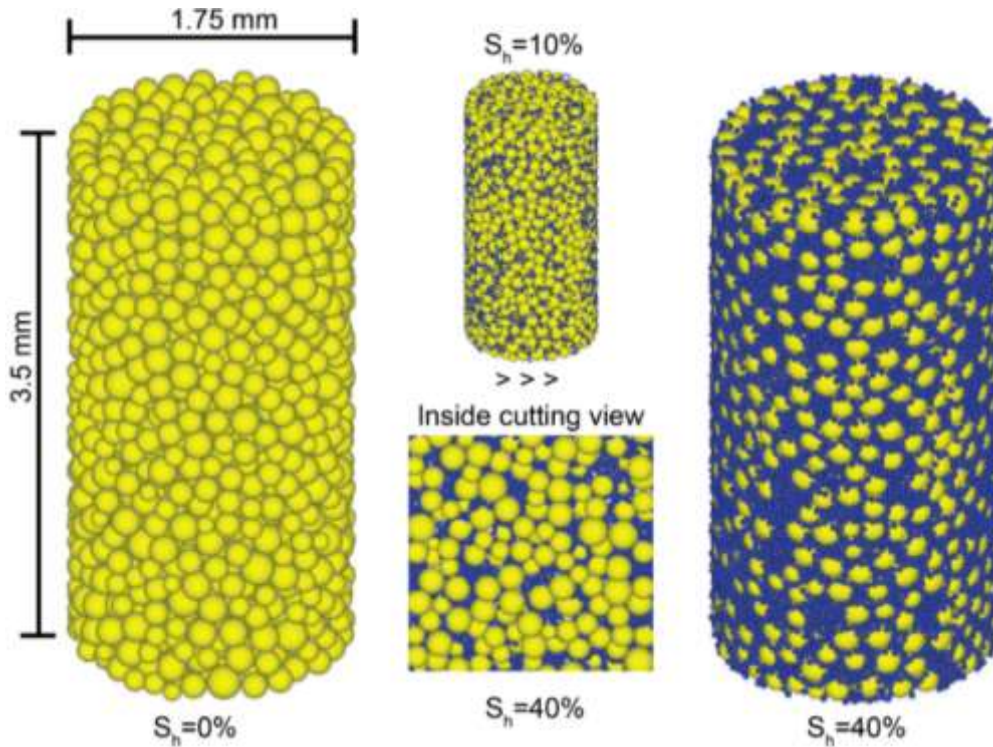


**Figure 3.11:** DEM hydrate-bearing soil samples

In the pore-filling model, there was no bonding strength between particles. At the low hydrate saturation, the hydrate particles were inside the pores without contacting with the soil particles, as gravity was not applied. Yet, as the hydrate saturation increased, the number of contacts between hydrate particles and other particles (soil or hydrate) would increase. The simulation data and analysis on the pore-filling model are discussed in Chapter 4, Chapter 5 and Chapter 7.

### 3.4.5 Cementation model

The cementation model was generated using a consistent soil model which was used in the pore-filling model. However, compared to the pore-filling model, the difference in the cementation model was that the generated hydrate particles were bonded to soil, or other hydrate particles with the normal bonding strength  $B_n$  of  $5 \times 10^3 \text{ N/m}^2$  (0.005 MPa) and shear bonding strength  $B_s$  of  $5 \times 10^3 \text{ N/m}^2$  (0.005 MPa) imposed by the contact bond model in PFC<sup>3D</sup>, while soil particles were not bonded together. The cementation is evenly distributed in the sample, as shown in Figure 3.12.

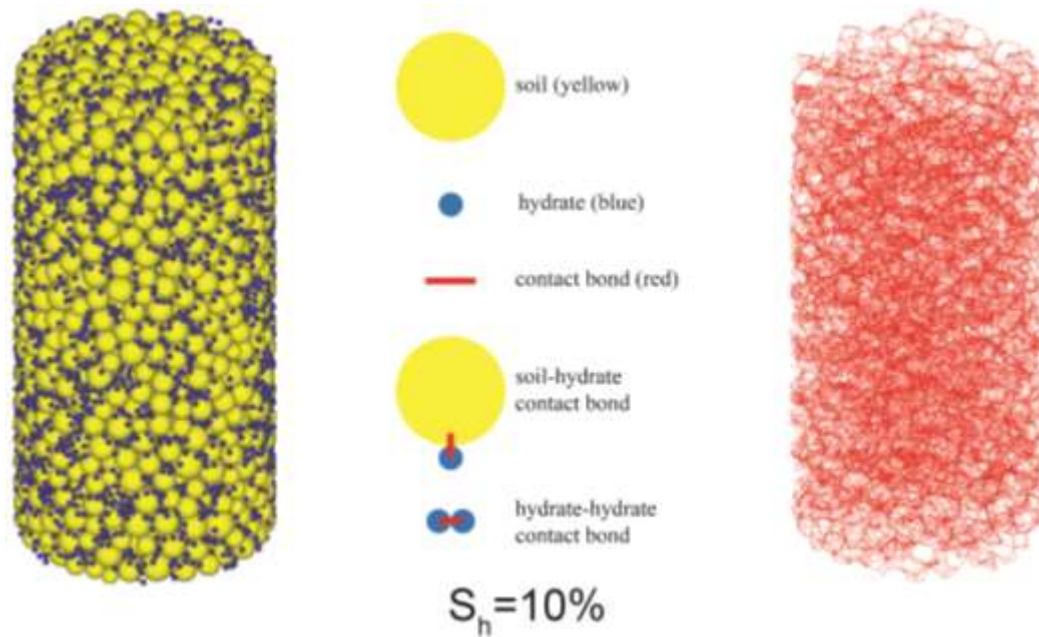


**Figure 3.12:** Contact bonds with directions when particles are set transparent in cementation model of  $S_h=10\%$

In this DEM modelling, the cementation hydrate was made in the compacted soil sample in the following steps: (1) to apply very high bonding strength to the existing soil-soil contacts of the skeleton, in order to make sure the soil-soil contacts will not be broken by the movement of hydrate particles; (2) to divide the target number of added hydrate particles into six groups; (3) to generate one group of hydrate particles in the void space, and then apply gravity of the negative direction of Z axis to the hydrate particles; (4) hydrate particles drop along the gravity direction until they stopped at the contacts with soil particles, and then the hydrate with the gravity accumulate at the soil-soil contacts; (5) as more hydrate particles at the soil-soil contacts accumulate, some hydrate particles just begin to stop and accumulate along the soil surface; (6) to apply bonding strength to the hydrate particles' contacts with other particles (soil and hydrate) in order to fix these contacts; (7) to generate the second group of hydrate particles in the void space, and apply gravity of the positive direction of Z axis to the hydrate particles, and follow the steps of (4) ~ (6); (8) to repeat the steps of (3) ~ (6) by applying the gravity of the positive or negative direction of X axis or Y axis, hence the six groups of hydrate particles are all bonded to the induced contacts in order to form the cementation hydrate model; (9) to set the bonding strength at soil-soil contacts to zero, and set the target bonding strength of hydrate particles. It should be noted that, during the whole process, a special PFC<sup>3D</sup> function

was applied to set all the induced contact overlap to zero for each time step in order to avoid the induced contact force which may influence the existing soil skeleton.

This hydrate formation and growth process followed the laboratory observation (Priest et al., 2005) that hydrates formed first at the grain contacts (soil-soil contacts), and then they grew into the pores and along the soil surface from the grain contacts. In the whole sample preparation process, the soil skeleton and soil-soil contacts were not broken or changed. The comparisons of the simulated data and analysis between pore-filling and cementation models are discussed in Chapter 4, Chapter 5 and Chapter 7.

In the cementation model, the hydrate growth patterns could govern the sediment's mechanical behaviour. The cementation hydrate particles either gathered at the soil-soil contacts or bonded to the soil surface. The location of these two different types of cementation hydrate particles may influence the mechanical behaviour differently. A comparison should be conducted in order to study the effect of hydrate growth patterns in the cementation hydrate-bearing soil model.

Hence, these two typical hydrate growth patterns of the cementation model were considered: soil surface coating (hydrates accumulating at grain surface) and soil-soil contact gathering (hydrates aggregating near the grain contacts). As shown in Figure 3.13, the DEM simulations in Chapter 6 were performed using samples of the two different growth patterns: (i) hydrates placed around grain surfaces ("Coating" in Figure 3.13(a)) and (ii) hydrates placed near grain contacts ("Contact gathering" in Figure 3.13(b)). The sample preparation of these two patterns was according to the hydrate particle's contact types: among all the contacts of one hydrate particle, if there is only one contact with soil particles, it is the coating hydrate; if there are no less than two contacts with soil particles, it is considered as the contact-gathering hydrate. By controlling the hydrate particle's contacts, these two different models were made accordingly.

The bonding strength of hydrate-hydrate and hydrate-soil was varied, as shown in Figure 3.13 (a)-(a') and (b)-(b'). The DEM simulations in Chapter 6 were conducted on the two cementation hydrate growth patterns at various bonding strengths from 0

MPa (no bond) to 0.500 MPa, In order to study the bonding strength effect of the hydrate particles.

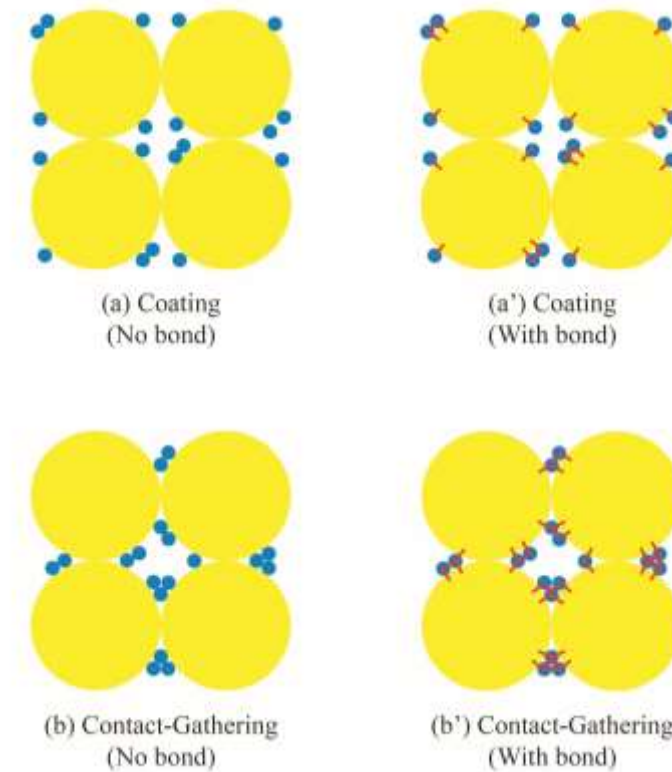


**Figure 3.13:** Hydrate growth patterns of the cementation model: (a) soil surface coating (b) soil-soil contact gathering

### 3.4.6 Models with elongated soil particles

DEM samples with elongated soil particles were prepared, in order to study the effect on shape of soil particles in the DEM simulations of hydrate-bearing sediments (Chapter 7). To make the DEM samples using the elongated soil particles, soil samples with spherical particles were first generated and consolidated under the given confining pressure. Elongated soil particles were prepared by replacing spherical soil particles by elongated clump particles of the same volume as the replaced spherical particles, in the consolidated DEM spherical soil samples under the controlled confining pressure. This will ensure the total solid volume was not changed. The particle replacement process could not be finished simultaneously, because that will totally change the original fabric. Hence, it was performed by replacing one after

another with a time interval for each replace in order that the induced particles' overlap was reduced. This is a trial and error process.

As shown in Figure 3.14, two aspect ratios were chosen for the elongated particles: 1.5 (2-ball clump) and 2.0 (3-ball clump). The spherical particle's aspect ratio was 1.0. And the diameter of the spherical particles in the clump was accordingly smaller than that of the replaced original spherical particle, in order to ensure that the clump volume was the same as the replaced original sphere by careful calculation.

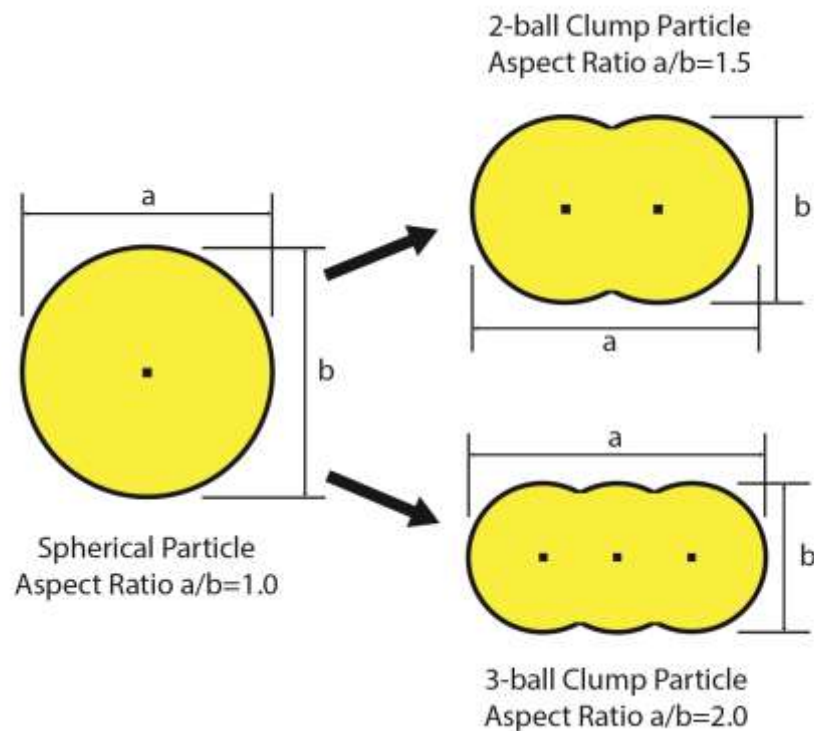


**Figure 3.14:** Replacement of spherical soil particles by elongated clumps.

Initially, all the elongated particles were generated horizontally, as the soils distribute horizontally in the natural hydrate-bearing sediments. In addition, the volume of the elongated particle was the same as that of the replaced spherical particle, so that the initial void ratios of the three soil samples were the same before the triaxial test. They had the same inter-particle friction. The pore-filling model and the cementation model were then prepared in the 2-ball clump and 3-ball clump soil samples using the same hydrate-bearing soil sample preparation process as mentioned above.

## 3.5 Summary

It should be noted that the initial state before the testing plays an essential role, and the initial state totally depends on the sample preparation. And the DEM sample preparation procedures of the methane hydrate soil samples are discussed in the aspects of their important principles. The preparation of the pore-filling and cementation models have been stated in detail. Furthermore, the two hydrate growth patterns in the cementation model are exhibited in this chapter, and were prepared separately in order to make the comparisons in Chapter 6. The hydrate-bearing sediments with elongated soil particles were prepared in this research, so as to study the shape effect of the soil particles (Chapter 7).

In order to make a comprehensive study of hydrate-bearing sediment and a proper comparison between various hydrate distribution patterns, a consistent DEM soil model should be considered carefully. The input parameters for the particles and boundary conditions are also essential to the accuracy of the DEM modelling.

## Chapter 4

# Large deformation behaviour of pore-filling and cementation hydrate-bearing sediments

### 4.1 Introduction

In this chapter, numerical simulation using Discrete Element Method (DEM) was employed to provide unique insights into the macro and micro mechanical behaviour of hydrate-bearing sediments with two typical hydrate distribution patterns: pore-filling and cementation.

The simulated drained triaxial compressional tests were systematically conducted to investigate the effects of hydrate saturation ( $S_h$ ) and hydrate growth patterns on hydrate-bearing samples. Comparisons of various aspects between the pore-filling and cementation models were made.

Firstly, comprehensive analyses were discussed in regards to the aspects of stress-strain responses and volumetric responses. We explored the effects of hydrate saturation and growth patterns on the sediments' stiffness, strength and volume change. Besides this, our interest in the sediments' behaviours extended to the large strain deformation and critical state behaviours in the triaxial tests, as these could not be obtained easily in the laboratory studies. In addition, the confining pressure effect was also explored.

A particle-scale micro-investigation into the DEM hydrate-bearing sediments was performed. We monitored the bond breakage between particles throughout the tests, as well as the particles' contact information. We also explored the particle-particle contact force contribution to the total contact force. All the particle-level analysis assisted interpretation of the macro responses discussed in this chapter.

## 4.2 Triaxial tests setting using DEM

After the sample preparation, the simulated drained triaxial compressional tests were systematically performed at different hydrate saturations using both models. The principle of triaxial compression test has been introduced in Chapter 2. Before the drained triaxial compression tests, the sample was subject to the effective stress: an isotropic consolidating stress  $\sigma'_c = 1$  MPa, 2 MPa or 3 MPa. The test was then started by increasing the axial load  $\sigma'_a$  (by moving the top wall and the bottom wall at a constant speed of  $1 \times 10^{-10}$  m/s) while the servo-controlled lateral pressure was held at the constant confining stress  $\sigma'_c$ , as illustrated in Figure 4.1.

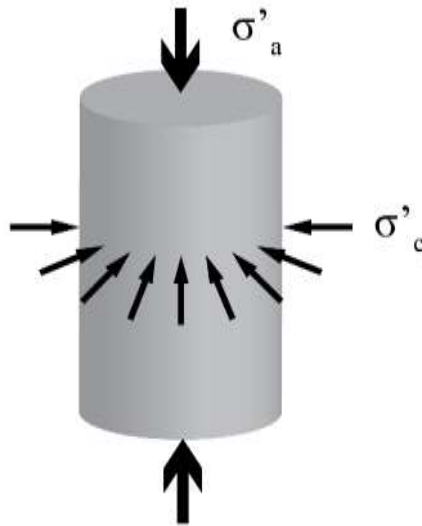


**Figure 4.1:** Sketch diagram of triaxial compression test

The axial (vertical) compressive stress was increased by  $\sigma'_d$ , which was termed to deviatoric stress. Thus, the final stress was:

$$\text{Final axial stress, } \sigma'_a = \sigma'_c + \sigma'_d \quad (4.1)$$

$$\text{Final radial stress, } \sigma'_r = \sigma'_c \quad (4.2)$$

The history of loading a sample was recorded by the plots of the deviatoric stress as a function of axial strain, defined as:

$$\text{Deviatoric stress, } \sigma'_d = \sigma'_a - \sigma'_r \quad (4.3)$$

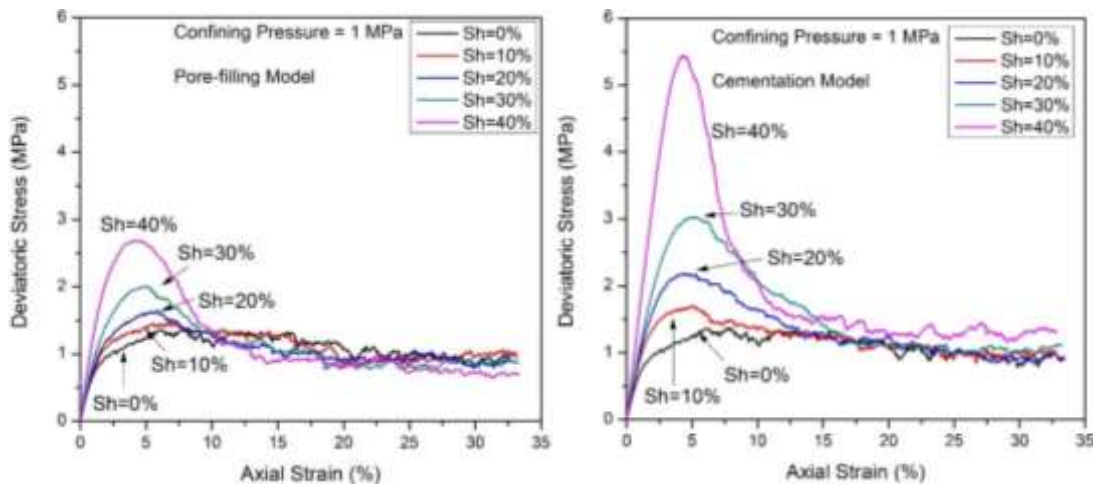
$$\text{Axial strain, } \varepsilon_a = \frac{dH}{H_0} \quad (4.4)$$

where  $H_0$  is the initial sample height before shearing, and  $dH$  is the axial displacement of the sample during the triaxial compression test.

### 4.3 DEM simulation results

#### 4.3.1 Stress-strain responses and comparisons to experimental data

Under the conditions of the confining pressure  $\sigma'_c$  of 1 MPa and a hydrate/soil contact stiffness ratio  $k_{n\text{-hyd}}/k_{n\text{-soil}}(D_{50})$  of 0.023, the stress-strain relationships of hydrate-bearing samples are plotted in Figure 4.2 for the pore-filling model and the cementation model with the hydrate saturations ( $S_h$ ) of 0%, 10%, 20%, 30%, 40%. Generally, in the triaxial test of the dense hydrate-bearing sample, the stress-strain curve arrived at a peak point, and after that, fell to some constant critical state values.



(a) Pore-filling model (DEM)

(b) Cementation model (DEM)

**Figure 4.2:** Deviatoric stress as a function of axial strain: (a) pore-filling; (b) cementation (DEM study)

Firstly, in both pore-filling and cementation models, the increase in the stiffness and the peak strength (maximum deviatoric stress) increased with a higher hydrate saturation. In the pore-filling samples, the maximum deviatoric stress increased from 1.37 MPa ( $S_h=0\%$ ) to 2.75 MPa ( $S_h=40\%$ ). In the cementation samples, the maximum deviatoric stress increased from 1.37 MPa ( $S_h=0\%$ ) to 5.50 MPa ( $S_h=40\%$ ). Hence, the hardening effect of hydrates was shown in both cases.

Secondly, however, the rate of peak stress increase with hydrate saturation was influenced by the distribution pattern of hydrate within the pores of the soil sample. It can be seen in Figure 4.2 that in the pore-filling model, the strength increased more obviously when the hydrate saturation was more than 20%. However, in the cementation model, the strength increased just after there were some hydrates growing in the sediments. At the same hydrate saturation, the elastic stiffness and the peak strength of the pore-filling sample were smaller than those of the cementation sample, and such an example is shown in Figure 4.3. At low hydrate saturations, hydrates in the pore-filling case did not contribute to the strength of the sediments at the beginning of the triaxial test, as hydrates were formed inside the pore space rather than at the soil particles' contacts. The hydrates in the cementation case grew at the soil particle contacts and along the surfaces of the soil particles, hence hydrate particles contributed to the strength of the soil skeleton during deformation. At a high hydrate saturation, the contribution of hydrate particles in the pore-filling case became more evident.

Furthermore, compared to previous experimental and numerical studies (Masui et al., 2005; Soga, et al., 2006; Brugada, et al., 2010; Jung, et al., 2012; Jiang, et al., 2013), our interest in this research extended to large strain deformation and critical state behaviour. At large axial strain levels, softening behaviour was observed, and the deviatoric stress at the critical state reduced to some constant values. At higher hydrate saturation of the pore-filling case, compared to the  $S_h=0\%$  sample's critical state shear strength, there was a reduction in the critical state strength as shown in Figure 4.2(a) and Figure 4.3. And Figure 4.3 shows that the reduction was very evident at the highest hydrate saturation of 40%. In the cementation case, on the contrary, the critical state shear strength at  $S_h=40\%$  was greater than that at  $S_h=0\%$ , as shown in Figure 4.2(b) and Figure 4.3.

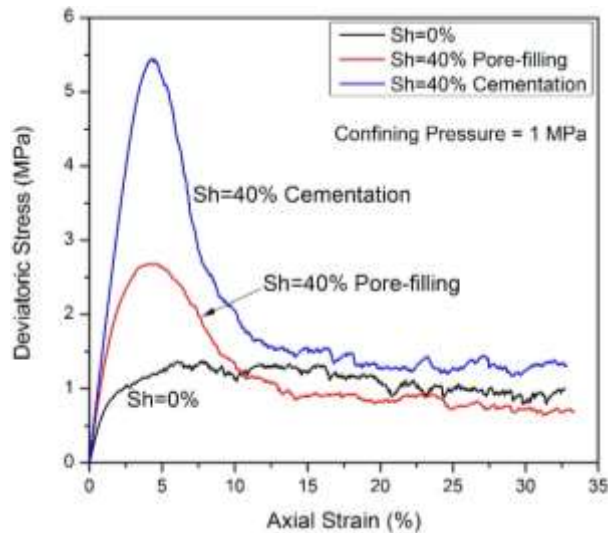


**Figure 4.3:** Comparisons of deviatoric stress as a function of axial strain between pore-filling and cementation cases at  $S_h=40\%$  (DEM study)

The DEM study on the stress-strain responses in Figure 4.2 showed a similar trend to the experimental study of the drained triaxial compressional tests conducted by Masui et al. (2005), as shown in Figure 4.4 and Figure 4.5. The synthetic weak bond hydrate-bearing sediments in Figure 4.4 shows that the increase in stiffness and strength only occurred when the hydrate saturation exceeded 26.4%, where the weak bond specimens were usually considered as the pore-filling pattern in the laboratory.

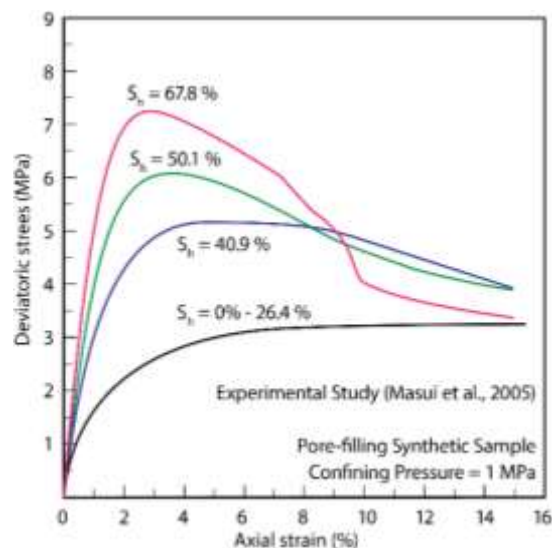


**Figure 4.4:** Deviatoric stress as a function of axial strain of the synthetic weak bond hydrate-bearing sample which was considered as pore-filling case in the laboratory (Experiment study on synthetic hydrate-bearing sediments, Masui et al., 2005)

However, Figure 4.5 reveals that the synthetic strong bond case (considered as the cementation pattern) presented a strengthened mechanical behaviour even at a low hydrate saturation. Similar to the DEM simulation data, the cementation samples also showed a greater strength than the pore-filling case at the same hydrate saturation. Yet, because of the particle shape effect, the DEM study with spherical particles showed a lower strength value than the experimental research, which is discussed in detail in Chapter 7.

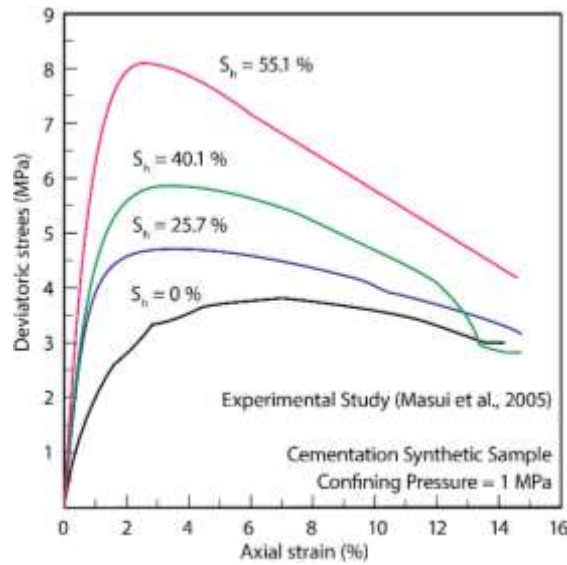


**Figure 4.5:** Deviatoric stress as a function of axial strain of the synthetic strong bond hydrate-bearing sample which was considered as cementation case in the laboratory (Experiment study on synthetic hydrate-bearing sediments, Masui et al., 2005)

### 4.3.2 Stiffness

The secant Young's modulus  $E_{sec}$  refers to the stress/strain ratio at a point of the stress-strain curve. In Equation 4.5, both the deviatoric stress  $\sigma'_{d(0)}$  and axial strain  $\varepsilon_{a(0)}$  are zero at the origin. The mid-strain stiffness  $E_{50}$  is the secant Young's modulus at half the peak deviatoric stress  $\sigma'_{d(50)}$  with the corresponding axial strain  $\varepsilon_{a(50)}$ , as defined by Equation 4.6.

$$\text{Secant Young's modulus, } E_{\text{sec}} = \frac{\sigma'_d - \sigma'_{d(0)}}{\varepsilon_a - \varepsilon_{a(0)}} = \frac{\sigma'_d}{\varepsilon_a} \quad (4.5)$$

$$\text{Mid-strain stiffness, } E_{50} = \frac{\sigma'_{d(\max)} \times 0.5}{\varepsilon_{a(50)}} = \frac{\sigma'_{d(50)}}{\varepsilon_{a(50)}} \quad (4.6)$$

The initial stiffness increased with hydrate saturation. It is clearly shown in Figure 4.6: (1) higher saturations had more influence on stiffness; and (2) bonded hydrates exhibited a greater effect on stiffness. The stiffness degradation curves were obtained from the triaxial tests under the 3 MPa confining pressure. The detail observations from the secant stiffness degradation curves are as following:

(1) In the pore-filling case in Figure 4.6(a), at the low hydrate saturations ( $\leq 20\%$ ) the sediments exhibited the initial stiffness at similar values because the initial stiffness depended on the soil skeleton's stiffness. However, when the hydrate saturation increased to 30% and 40%, the initial stiffness was increased by the larger amount of hydrates in contact with soil particles, where hydrates played the load-bearing role.

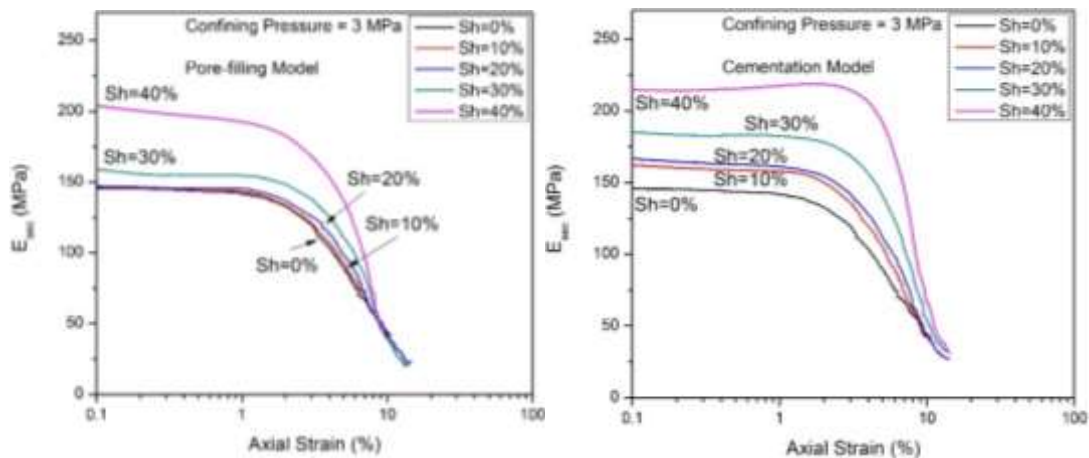
(2) However, in the cementation model, the initial stiffness exhibited an evident increase even when the saturation was low, as shown in Figure 4.6(b).

(3) At the same hydrate saturation, the initial stiffness of the cementation sediment was higher than that of the pore-filling case.

(4) The sudden drop in stiffness was observed at an axial strain between 2% and 3%. The stiffness degradation curves converged at a similar value when at large strains.

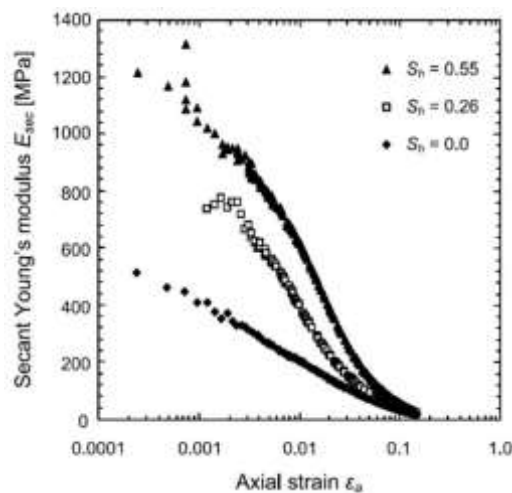
Figure 4.6 (c) shows the experimental results on the secant Young's modulus  $E_{\text{sec}}$  degradation of the cementation case by Masui et al. (2005). It is quite clear that the stiffness degrades as the soil is sheared, and the higher the hydrate saturation is, the greater degradation is. The DEM simulation results are compared well to the published experimental data. But the values in the experimental data were higher than the simulated data in this study. Due to the limitations of the DEM modelling of spherical particles, this study is qualitative rather than quantitative. The study on the effect of

elongated soil particle shape in Chapter 7 discusses more about this issue. In addition, the stiffness of the soil and hydrate particles was another reason. In this DEM research, the elastic modulus of the particles were chosen at relatively small values, which caused the DEM results smaller than the laboratory ones. As discussed in Chapter 3, it is now generally recognized by the research community that the main objective of DEM-based investigation is not to provide quantitatively reproduction of material behaviour, but to understand qualitatively the particle-scale mechanism affecting the continuum-scale responses.



(a) Pore-filling model (DEM)

(b) Cementation model (DEM)



(c) Cementation case (Experiment, Masui et al., 2005)

**Figure 4.6:** Stiffness  $E_{sec}$  degradation curve against axial strain: (a) pore-filling model (DEM); (b) cementation model (DEM); (c) experiment cementation case (Masui et al., 2005)

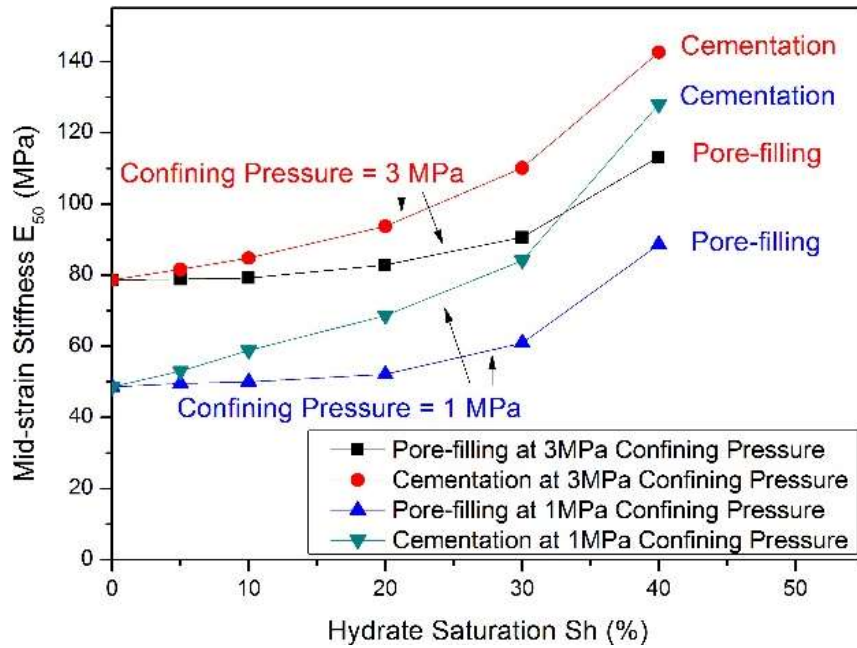
It also should be noted that, in Figure 4.6, the choice of 0.1% as the starting point of recording the axial strain was mainly due to the size of the DEM sample. Because of the limitations of computational time and the number of hydrate particles, the sample height was set to 3.5 mm. The axial strain of 0.1% then corresponded to  $3.5 \times 10^{-3}$  mm, which was a reasonable value to begin recording the initial stiffness, due to the minimum diameter of soil particle being 0.1 mm.

Regarding the mid-strain stiffness  $E_{50}$ , there are also some detail observations can be seen in Figure 4.7 (a). (1) As hydrate saturation increased,  $E_{50}$  generally increased. The increase in the mid-strain stiffness of the pore-filling cases became a bit more obvious when hydrate saturation was higher than 20%, while the increase in the stiffness of the cementation cases started to apparently increase with hydrate saturation. (2) It is also clear in Figure 4.7 (a) that at the same hydrate saturation,  $E_{50}$  of the cementation model was higher than that of the pore-filling model. In addition, the rate of stiffness increase was higher when the saturation was higher.

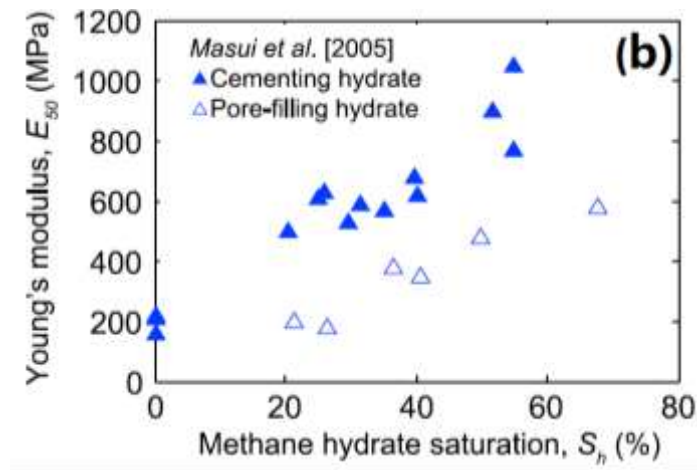
The above two observations are compared well to the experimental data in the qualitative aspect (Masui et al., 2005) shown in Figure 4.7 (b). The experiment was conducted under 1 MPa confining pressure. The increased saturation increased the stiffness obviously from low saturation in the cementation case but from 25% saturation for the pore-filling case. It can also be seen in Figure 4.7 (b) that the cementation hydrate samples indicate great effect of hydrate at low hydrate saturation, while the pore-filling hydrate has no significant effect on peak strength or mid-strain Young's modulus  $E_{50}$  until  $S_h$  was above 25%.

Furthermore, at the same hydrate saturation, the confining stress influenced the sample's geomechanical behaviour, since the increasing confining pressure increased coordination number and density, hence the shear strength and skeleton stiffness. The variations of mid-strain stiffness  $E_{50}$  at the 1 MPa and 3 MPa confining pressures are exhibited in Figure 4.7 (a). Regarding the soil sample ( $S_h=0\%$ ),  $E_{50}$  increased with the effective confining pressure. However,  $E_{50}$  was relatively independent of confining pressure when the saturation was as high as 40% in the cementation model. This was because the soil stiffness was mainly controlled by the large number of bonding

contacts of the hydrate particles, but not by the soil-soil interaction (Soga et al., 2006; Yun et al., 2007).



(a) DEM study



(b) Experiment (Masui et al., 2005)

**Figure 4.7:** Mid-strain stiffness  $E_{50}$ : Pore-filling and Cementation models: (a) DEM study; (b) experiment (Masui et al., 2005)

### 4.3.3 Strength

We recorded the history of the loading of a sample by plotting its stress path with axes  $q'$  and  $p'$ , where  $q'$  is the deviatoric stress and  $p'$  is the mean effective stress:

$$\text{Mean effective stress, } p' = \frac{\sigma'_a + \sigma'_r + \sigma'_r}{3} = \frac{\sigma'_a + 2\sigma'_r}{3} \quad (4.7)$$

$$\text{Deviatoric stress, } q' = \sigma'_d = \sigma'_a - \sigma'_r \quad (4.8)$$

In the case of a shear slip failure or continuous yielding, the Mohr circle containing the normal stress  $\sigma'$  and shear stress  $\tau'$  on the slip plane is clearly a limiting circle. Limiting circles at different values of normal stress will all touch a common tangent, known as a failure envelope (Figure 4.8).

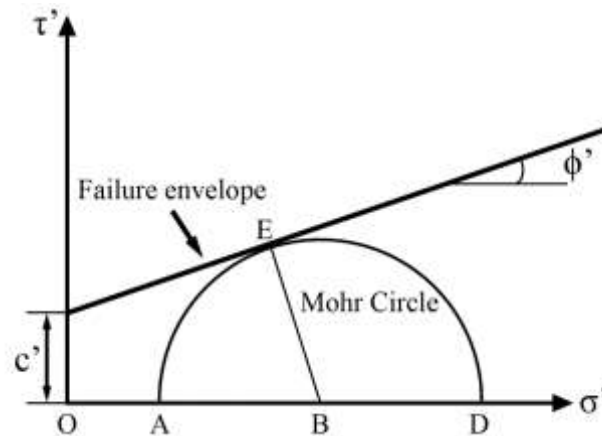


**Figure 4.8:** Mohr circle and failure envelope

The equation of this failure envelope is usually referred to as Coulomb's equation:

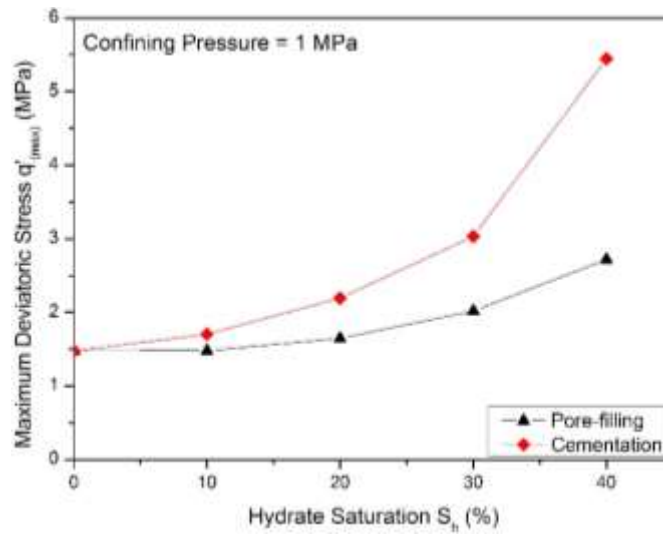
$$\text{Coulomb's equation (failure envelope), } \tau' = c' + \sigma' \tan \phi' \quad (4.9)$$

where  $\phi'$  is the friction angle, and  $c'$  is the apparent cohesion.

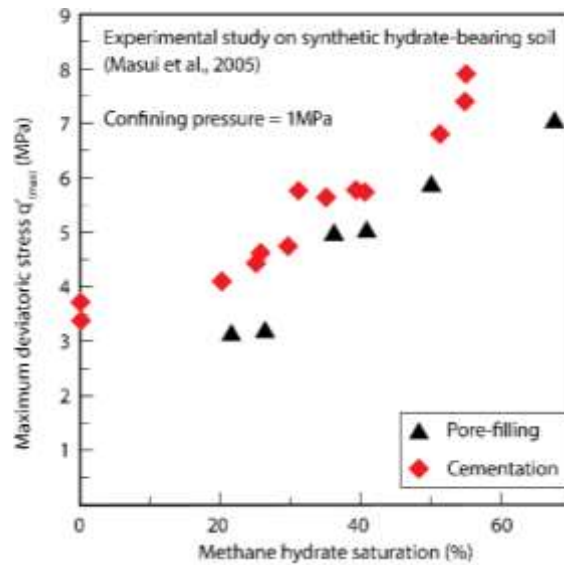
Figure 4.9 shows that the peak strength  $q'_{(\max)}$  (maximum deviatoric stress) steadily increased with the higher hydrate saturation. Figure 4.9(a) is the result of the

#### 4. Large deformation behaviour of pore-filling and cementation hydrate-bearing sediments

DEM study in this research, and Figure 4.9(b) is the experimental result (Masui et al., 2005).



(a) DEM study



(b) Experimental study (Masui et al., 2005)

**Figure 4.9:** Maximum deviatoric stress  $q'_{(max)}$  at different hydrate saturations: (a) DEM study; (b) experimental study (Masui et al., 2005)

The difference of the increase rate depended on the hydrate growth pattern. In the cementation model, hydrates formed at the soil-soil particles' contacts with bonding

#### 4. Large deformation behaviour of pore-filling and cementation hydrate-bearing sediments

strength, and contributed to the increase in strength even when the hydrate saturation was low. However, the hydrate particles in the pore space of pore-filling sediments did not make much of a contribution, as hydrate distributed within the pore spaces rather than at the soil-soil particles' contact locations. The pore-filling hydrates were floating in the pores but did not increase the sediment's strength at a low saturation, and the shear resistance was mainly due to the soil-soil interactions. However, when the hydrate saturation was higher ( $\geq 20\%$ ), the increase in strength was obviously shown, as more hydrate particles were in contact with soil particles and they began to contribute to the stiffness and strength increase, which is usually known as the load-bearing hydrate growth pattern. The peak strength of the cementation cases, however, measured much higher than that of the pore-filling cases due to the bonding strength of the cementation hydrate particles at the soil-soil contacts.

Figure 4.10 with the failure envelopes on  $p'-q'$  plane indicates the stress states at failure for the pore-filling cases and the cementation cases. The shear strength increased with the mean effective stress, which are compared well to the confining pressure studies (Figure 2.16) by Masui et al. (2005) and Ebinuma et al. (2003) that the increased confining pressure caused a greater strain hardening behaviour. The slope  $H$  in Figure 4.10 relates to the peak strength state friction angle  $\phi'_p$ , which is discussed in detail in Section 4.3.5.

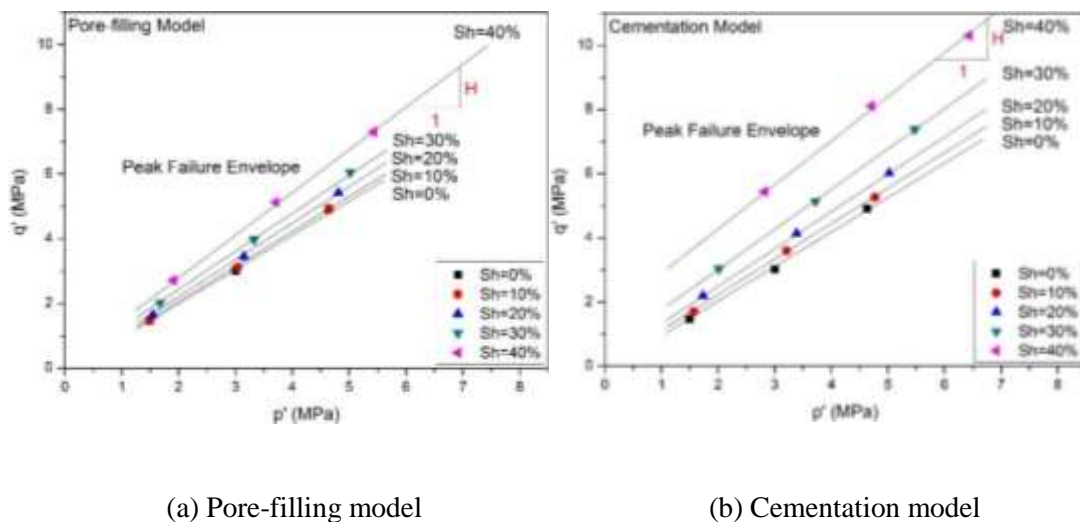


**Figure 4.10:** Peak Failure Envelopes on  $p'-q'$  plane

In the pore-filling model, the increase in the peak strength became obvious when the saturation was above 20%. While in the cementation model, the rate of increase in the shear strength exhibited higher results even at a low hydrate saturation.

#### 4.3.4 Volumetric responses

The volumetric strain  $\varepsilon_v$  refers to the unit change in volume due to a deformation, as defined in Equation 4.10:

$$\text{Volumetric strain, } \varepsilon_v = \frac{dV}{V_0} \quad (4.10)$$

where  $V_0$  is the initial sample volume, and  $dV$  is the volume change of the sample during the triaxial compression test.

Figure 4.11 shows the volumetric strain as a function of axial strain during the triaxial tests of the hydrate-bearing samples with various hydrate saturations. The sediments initially showed contractive behaviour, which was followed by a dilative tendency. In addition, the dilatancy was enhanced by an increased hydrate saturation. The peak contractive values in the pore-filling model were similar at different hydrate saturations, whereas those in the cementation model increased with hydrate saturation. Peak contractive values in the cementation model, particularly at  $S_h=40\%$ , saw a large number of bonding contacts and a higher occasion of interlocking particles. At the beginning, this made the soil particles immobile relative to one another, and due to the elastic deformation of the particles, caused the sample to compress more. When particles started to move relative to one another, dilation happened, where the rate of dilation of the cementation model (see Figure 4.11(b)) was greater than that of the pore filling model (see Figure 4.11(a)), meaning cementation affected enhanced dilation.

Regarding the dilation during the deformation process, there is a point on the  $\varepsilon_v - \varepsilon_a$  curve where there is a maximum value in the dilation angle, defined as:

$$\text{Angle of dilation, } \psi = \arcsin\left(\frac{d\varepsilon_v / d\varepsilon_a}{2 + d\varepsilon_v / d\varepsilon_a}\right) \quad (4.11)$$

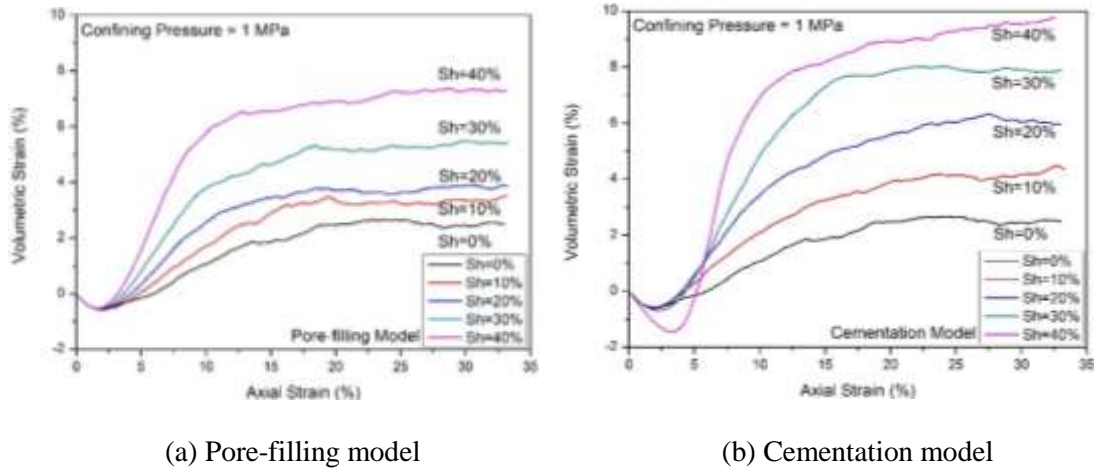


Figure 4.11: Relationship of volumetric strain - axial strain

The increased hydrate saturation enhanced the characteristics of dilation of the hydrate-bearing sediments. It is shown in Figure 4.12 that the maximum dilation angle increased with a higher hydrate saturation, and this increase was more obvious the higher saturation was. The cementation effect increased the dilation angle at the same saturation, which was observed in the comparisons between the pore-filling and cementation models. At the critical state, the volume of the hydrate-bearing sample became constant, as expected, while shearing continued: the soil was then in the critical state and the volume was critical, as shown in Figure 4.11.

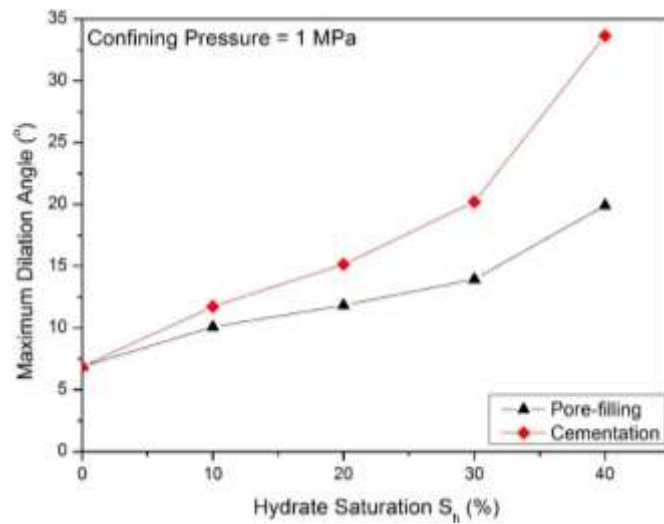
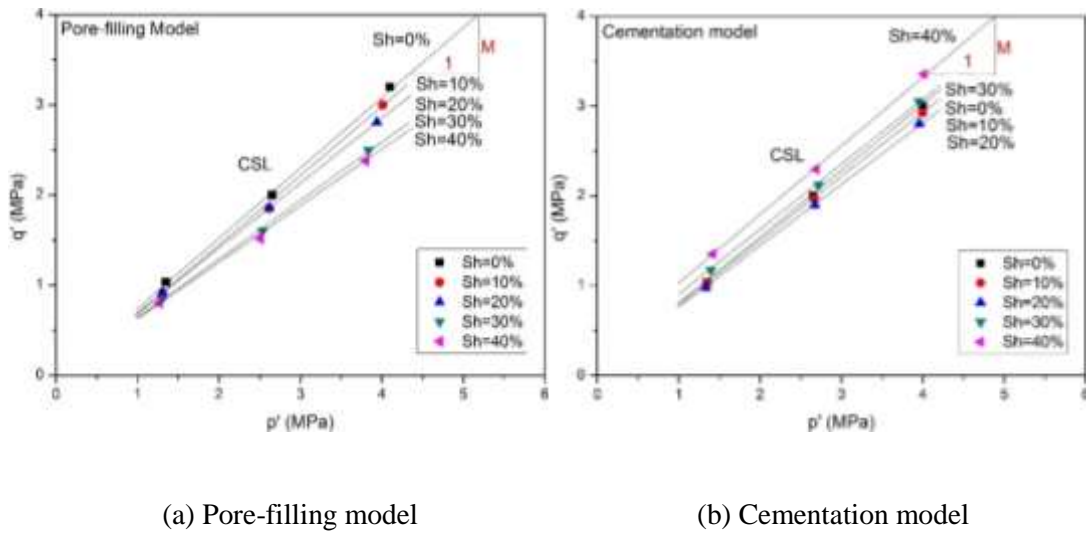


Figure 4.12: Maximum dilation angles at various hydrate saturations

### 4.3.5 Critical state

The contribution of hydrates to the sediments' skeletal strength could be shown clearly at large strains. As shown in Figure 4.13, the critical state lines (CSL) plotted on the  $p'-q'$  plane show that the shear strength increased with the mean effective stress.



**Figure 4.13:** Critical State Line (CSL) projection on the  $p'-q'$  plane

The CSL plots of the pore-filling model revealed skeleton softening behaviour when the hydrate saturation increased. As the saturation increased, the critical state strength of the pore-filling model decreased, which was enhanced by the increased mean effective stress. This may be due to the inclusion of hydrate particles in the soil matrix at the critical state. However, the cementation model CSL plots showed a different result. And this result was not similar to the DEM results shown in Figure 2.27 (a) by Jung et al. (2012). In Figure 4.13 (b), when the hydrate saturation was low, the critical state strength of cementation hydrate-bearing sediments exhibited lower strength than that of hydrate-free soil sediments, because some inter-particles bonds were broken and the soft hydrate particles moved into the sediment's skeleton. However, the higher saturation and much larger number of bonding contacts strengthened the critical state of the cementation hydrate-bearing sediments. Therefore, the critical state strength for 30% and 40% hydrate saturations was higher than the pure soil sample.

#### 4. Large deformation behaviour of pore-filling and cementation hydrate-bearing sediments

From the peak failure envelopes and critical state lines mentioned above, the slope  $H$  and  $M$  in Figure 4.10 and Figure 4.13 relates to the peak strength state friction angle  $\phi'_p$  and the critical state friction angle  $\phi'_c$ . The following equivalence expressions can be used to obtain the friction angles:

$$H = \frac{6 \sin \phi'_p}{3 - \sin \phi'_p} \quad (4.12)$$

$$M = \frac{6 \sin \phi'_c}{3 - \sin \phi'_c} \quad (4.13)$$

$$\text{Friction angle of peak strength state, } \phi'_p = \arcsin\left(\frac{3H}{6+H}\right) \quad (4.14)$$

$$\text{Friction angle of critical state, } \phi'_c = \phi'_p + 0.8\psi \quad (4.15)$$

The values of the derived friction angles are shown at various hydrate saturations as plotted in Figure 4.14.

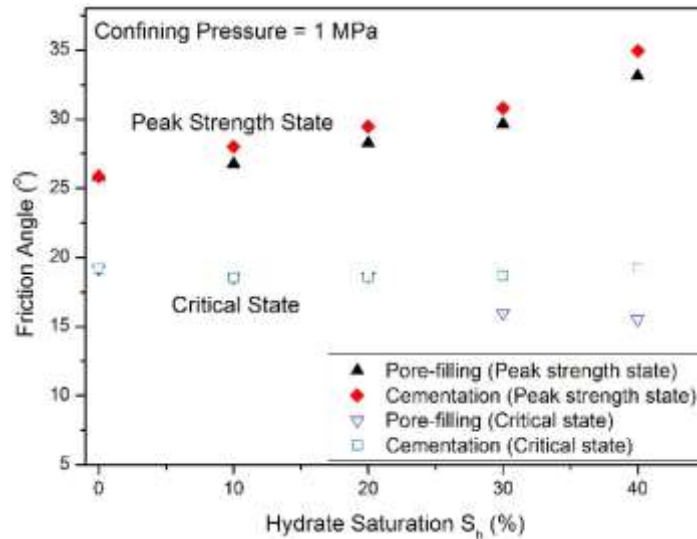


**Figure 4.14:** Angles of friction at different hydrate saturations

Regarding the peak strength state, the friction angles increased as the hydrate saturation got higher. The peak strength state friction angle of the cementation model

#### 4. Large deformation behaviour of pore-filling and cementation hydrate-bearing sediments

was larger than that of the pore-filling model. However, the friction angles in critical state showed a decrease for the pore-filling model as the hydrate saturation got higher. However, the friction angle of the cementation model in the critical state decreased slightly at 10% hydrate saturation, and then levelled off at saturations of 20% and 30%. When the hydrate saturation was 40%, the friction angle increased slightly to the value of the soil sample's friction angle.

Bolton (1986) proposed a developed expression for sand:  $\phi'_p = \phi'_c + 0.8\psi$ . In this model of sand, the peak state friction angle of sand can be calculated by the critical state friction angle and the dilation angle. However, after adding the softer and smaller hydrate particles into the pores of the existing consolidated sand sample, the expression for sand proposed by Bolton (1986) did not work, especially at a high saturation, as shown in Table 4.1. In the pore-filling model, when the hydrate saturation was low, the value of the obtained peak state friction angle were very close to the calculated value. But as the saturation increased, the deviation was enlarged to some extent, and the calculated value was smaller than the obtained one. In the cementation model, however, the cementation effect caused a different situation. The deviation was much larger than that in the pore-filling model, and the calculated value was much larger than the obtained value at a high saturation.

**Table 4.1:** Comparisons between the obtained peak state friction angle in this DEM research and the calculated peak state friction angle by the sand model

$S_h$	Pore-filling Model		Cementation Model	
	$\phi'_p$	$\phi'_c + 0.8\psi$	$\phi'_p$	$\phi'_c + 0.8\psi$
0%	25.9	25.7	25.9	25.7
10%	26.8	26.6	28	27.9
20%	28.3	28.1	29.5	30.7
30%	29.6	27.1	30.8	34.9
40%	33.2	31.4	34.9	46.2

The values of cohesion are shown at various hydrate saturations as plotted in Figure 4.15. The comparisons between the pore-filling model and the cementation model indicates that the only contribution to the increase in the cohesion was the bonds between hydrates and other particles (hydrates or soils), while there was no cohesion existing in the pore-filling hydrate samples. Due to the bond breakage in the deformation process, the cohesion at the peak strength state was higher than that at the critical state in the cementation model, especially at high saturation. Further discussion about the bond breakage will be analysed below.

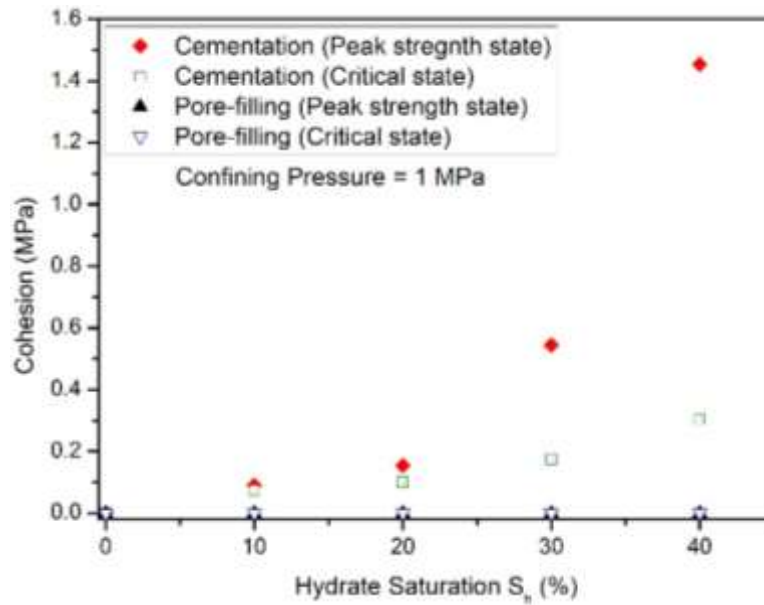
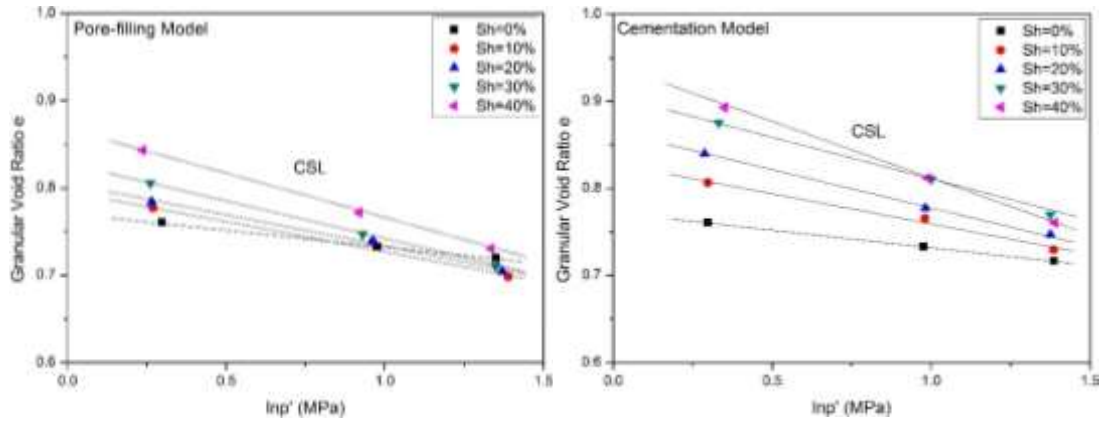


**Figure 4.15:** Cohesion at different hydrate saturations

Furthermore, the critical state granular void ratio  $e - \ln p'$  projections were plotted in Figure 4.16. The simulations showed that the resulting critical state granular void ratios  $e$  may not be unique, indicating the possible effect of fine hydrate particles on the critical state behaviour. Note that granular void ratio  $e$  was obtained by the following equation:

$$\text{Granular void ratio, } e = \frac{V_v + V_h}{V_s} \quad (4.16)$$

where  $V_v$  is the void volume,  $V_h$  is the hydrate volume and  $V_s$  is the soil volume.



(a) Pore-filling model

(b) Cementation model

**Figure 4.16:** Critical State Line projection on Granular Void Ratio  $e$ - $\ln p'$  plane: (a) pore-filling model; (b) cementation model

The hydrate effects on strength and dilation produced higher critical state void ratios as the saturation increased. It should be noted that the rate of dilatancy changed with confining pressure. In addition, the hydrate-induced dilatancy was less evident at a high confining pressure. As the confining pressure increased, the dilation characteristic tended to diminish in the pore-filling model, as shown in Figure 4.16 (a). The dilation behaviour was also weakened by the confining pressure in the cementation model (Figure 4.16 (b)), although due to the remaining bonds it could not be similar to the pore-filling case.

## 4.4 Particle-scale analysis

### 4.4.1 Particle-scale mechanism analysis

The particle-scale mechanisms of the DEM pore-filling and cementation models are illustrated in Figure 4.17. At  $S_h=0\%$ , the hydrate-free soil sample showed the movements of soil particles in the deformation process – rotation, slippage and rearrangement.

However, when the pore-filling particles formed in the pores at the beginning of the deformation process, the contact forces made a few hydrate particles move to the

soil-soil contact, which to some extent started to support the soil skeleton. However, in the large strain, due to the movements of soil and hydrate particles, some of these small-size hydrate particles became involved in the soil matrix and also transmitted the main contact forces in the skeleton. Consequently, the much softer and smaller-sized hydrate particles in the skeleton weakened the overall strength of the samples. This may explain why the critical state strength of the pore-filling sediments was smaller than that of the pure soil sample.

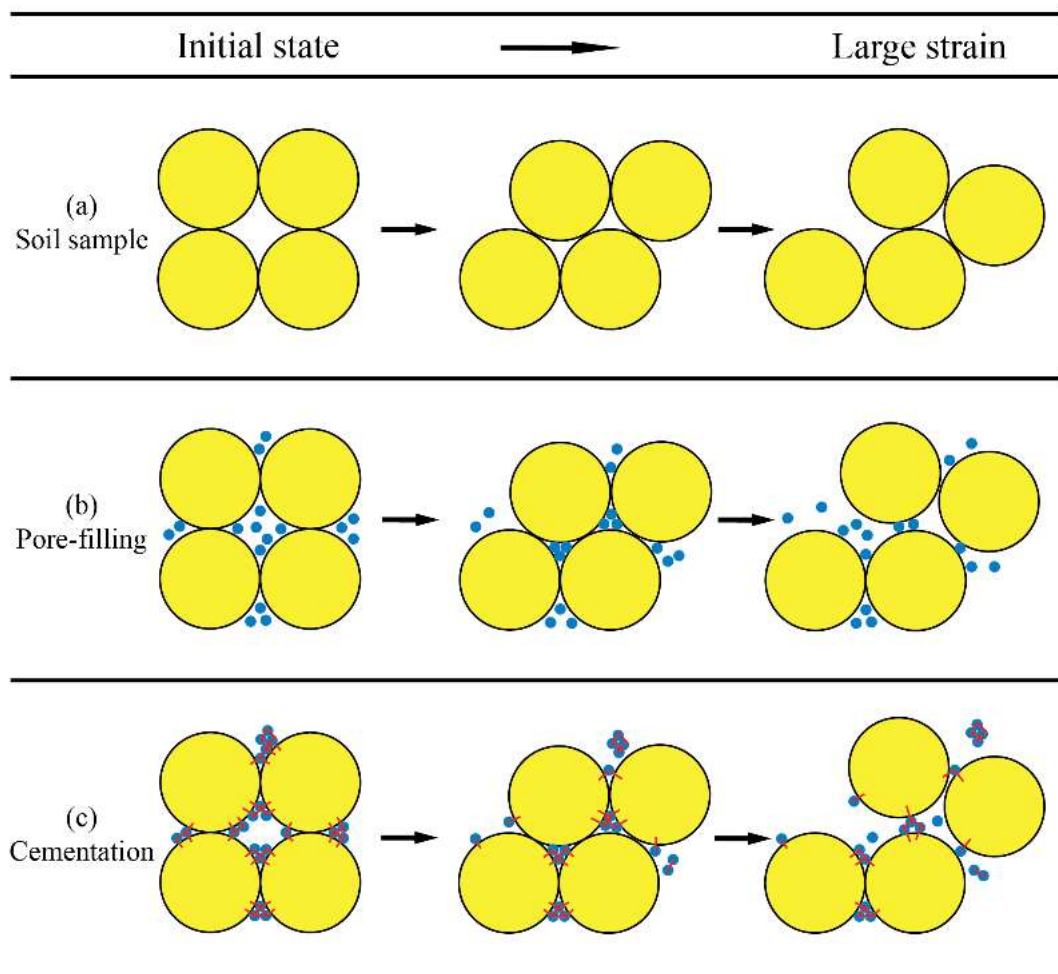


**Figure 4.17:** Sketch diagram of the particle-scale mechanisms of particle movements in the deformation process

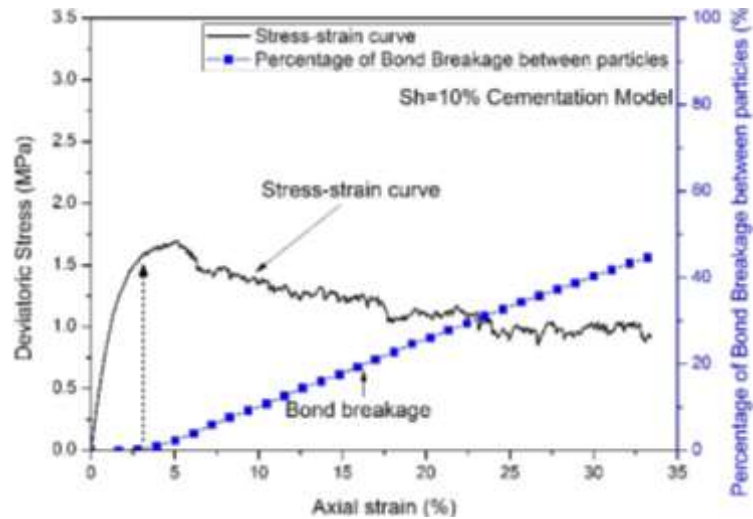
In contrast, the cementation hydrates supported the soil skeleton at the initial state with the given bonding strength. Because they located at the soil-soil contacts or along the soil surface, it strengthened soil skeleton. During the triaxial shearing process, some of the bonds between particles were broken by the deformation; these hydrate

particles without bonds then moved to the pore space. At a large axial strain, out of the movement of particles, the cementation hydrate particles and the hydrate particles without bonds became involved in the matrix and still weakened the sample skeleton. However, there were also a large number of remaining bonded particles formed a bigger irregularly shaped clusters that induced a larger critical state strength in the cementation samples when compared to the pure sand.

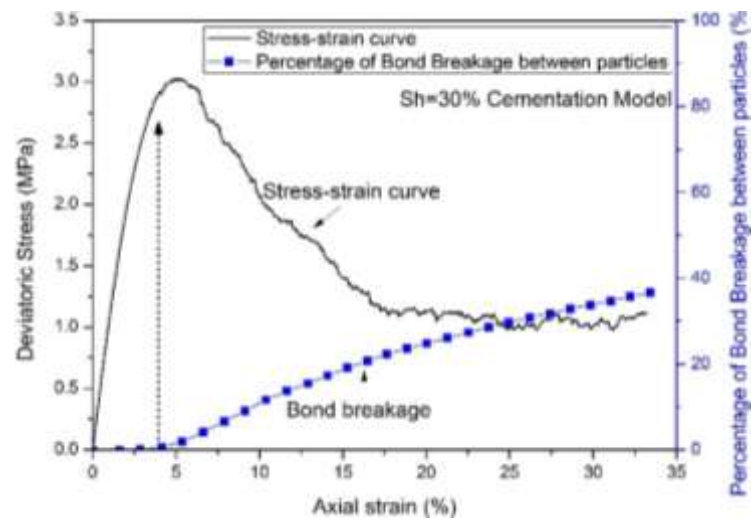
#### **4.4.2 Bond breakage between particles in cementation model**

Figure 4.18 exhibits the bond breakage between particles throughout the triaxial test at  $S_h=10\%$  and  $S_h=30\%$  in the cementation model. Although the number of the contact bond breakage was very small in the initial state, it is shown that the evident bond breakage began to happen just after the elastic phase, and the percentage of bond breakage in total bonds increased steadily. This means there began to be a number of pore-filling pattern hydrate particles in the pores, at the soil-soil contacts or in the soil skeleton after the bond breakage, so that at  $S_h=10\%$  and  $S_h=20\%$  the critical state strength of the cementation models was smaller than that of the pure soil sample. But it is also found that in this figure, at a large strain of 33%, the percentage of bond breakage in total bonds only reached 44% at  $S_h=10\%$  and 38% at  $S_h=30\%$ . Hence, there are still a large number of bonding contacts in the sample at the critical state – 56% ( $S_h=10\%$ ) and 62% ( $S_h=30\%$ ) of initial total bonds.

Yet, at a high saturation, there were many more remaining bonded contacts. Firstly, it is because that the total number of bonded contacts at the initial state of the high saturation sample was much larger than that of the low saturation sample. Secondly, it can be seen in Figure 4.18 that at the large axial strain, the percentage of bond breakage of the total bonded contacts within the high saturation sample was lower than that within the low saturation sample. This may also explain why, at high saturations of 30% and 40%, in the cementation model, the critical strength was higher than that of the pure soil sample, as shown in Figure 4.2(b), Figure 4.3 and Figure 4.13(b). The large number of bonding contacts plays an essential role in the strength of hydrate-bearing sediments.



(a) Cementation  $S_h=10\%$



(b) Cementation  $S_h=30\%$

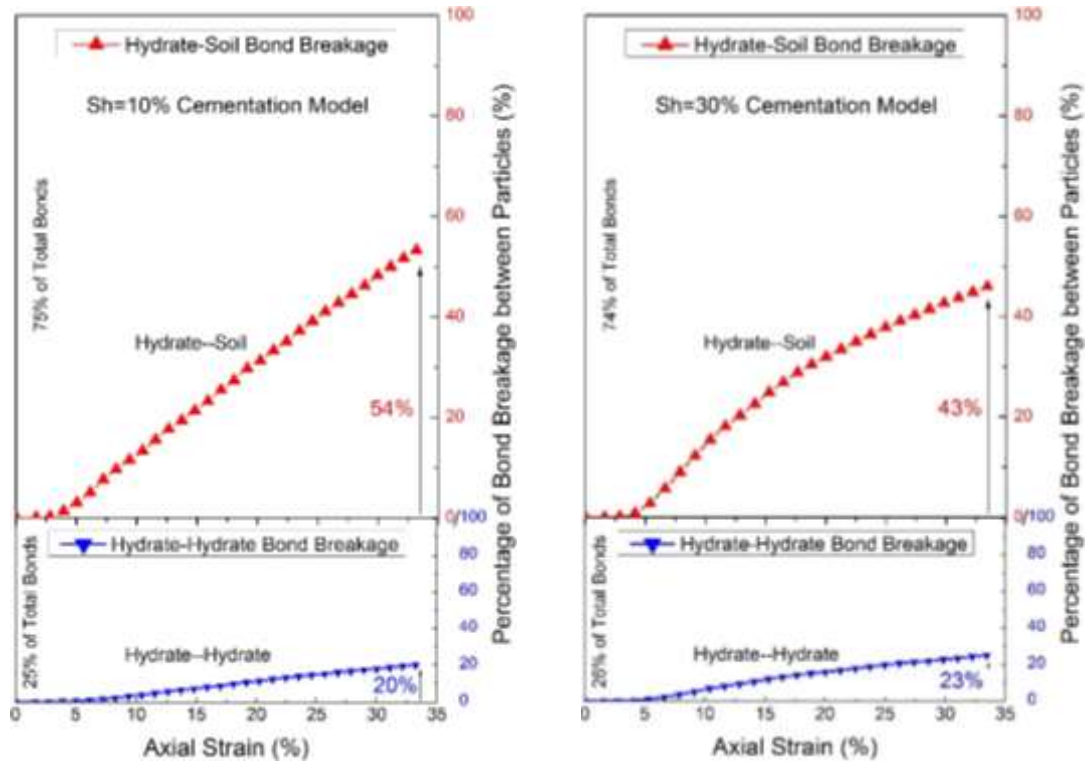
**Figure 4.18:** Bond breakage in the triaxial test of cementation model

The bonding contacts between particles included two types: hydrate-soil (h-s) contact and hydrate-hydrate (h-h) contact. As shown in Figure 4.19, the hydrate-soil bonding contacts accounted for 75% ( $S_h=10\%$ ) and 74% ( $S_h=30\%$ ) of the total bonds, while the hydrate-hydrate bonding contacts took up 25% ( $S_h=10\%$ ) and 26% ( $S_h=30\%$ ).

This is because in the cementation model, hydrates first formed at the soil-soil contacts before bonding, and then formed along the soil surface layer by layer. So when the main skeleton was deformed in the triaxial test, the main bond breakage must have been the hydrate-soil contact bond breakage. The rate of bond breakage of the

#### 4. Large deformation behaviour of pore-filling and cementation hydrate-bearing sediments

hydrate-soil contacts was greater than that of the hydrate-hydrate contacts. At the axial strain of 33%, the percentage of bond breakage between hydrates and soils in the  $S_h=10\%$  model reached 54%, while bond breakage between hydrates and hydrates was 20%. However, at  $S_h=30\%$ , the hydrate-soil bond breakage only reached 43%, while the hydrate-hydrate bond breakage was 23% at the large strain of 33%. After the bond breakage with the soils, there might be some clusters of bonded hydrates floating in the pores at the large strain, and there might also be some clusters of soil particles which are bonded by hydrates. Compared to the pore-filling case, the clusters of bonded particles (soil-hydrate and hydrate-hydrate) at the large strain might cause a larger dilation.



(a) Cementation  $S_h=10\%$

(b) Cementation  $S_h=30\%$

**Figure 4.19:** Particles bond breakage in the triaxial test of cementation model

#### 4.4.3 Particle-particle contact number in total contacts

Figure 4.20 shows the percentage of the particle-particle contact number in the total contacts, including soil-soil, soil-hydrate and hydrate-hydrate contact types, at the

peak strength state and the critical state respectively.

In the pore-filling model, at the peak strength state shown in Figure 4.20(a), as the hydrate saturation increased (more hydrate particles were generated), the number of hydrate-hydrate (h-h) contacts and hydrate-soil (h-s) contacts increased dramatically. At  $S_h=10\%$ , the main contacts were soil-soil (s-s) contacts. However, at  $S_h=40\%$ , the percentage of the h-h contacts increased to almost the same percentage of h-s contacts. But the percentage of the h-s contacts dropped slightly when the saturation increased from 30% to 40%. However, the percentage of the s-s contacts in total contacts dropped dramatically.

At the critical state of the pore-filling model in Figure 4.20(b), the h-s contacts were the main contact type after  $S_h \geq 20\%$ . In the same case, in Figure 4.16(a), the increase of granular void ratio became obvious when the hydrate saturation was above 20%. The critical state h-h contact number percentage at each saturation was lower than the peak state h-h contact number percentage. But compared to the peak strength state, more hydrate particles have contacts with soil particles in the critical state. This can explain why there was the reduced critical state strength in the pore-filling model.

In Figure 4.20(c) and Figure 4.20(d), it is obvious that because hydrate particles in the cementation model were bonded to soils or other hydrate particles, the main contact types were h-s and h-h contacts. In Figure 4.8, the peak strength of the cementation model began to increase from low saturation, and the increase became more evident after  $S_h \geq 30\%$ . At  $S_h=30\%$ , the contact number for h-h and h-s were similar because the h-h contacts were increasing as the saturation was getting higher. At  $S_h=40\%$ , the h-h contacts became the main contact both at peak strength state and critical state. The granular void ratio of the cementation in Figure 4.16(b) increased with hydrate saturation, even when the saturation was low. In the cementation model, the difference in the contact number percentage between at the peak and critical state was not obvious. On the other hand, the difference between the two states was obvious in the pore-filling model.

#### 4. Large deformation behaviour of pore-filling and cementation hydrate-bearing sediments

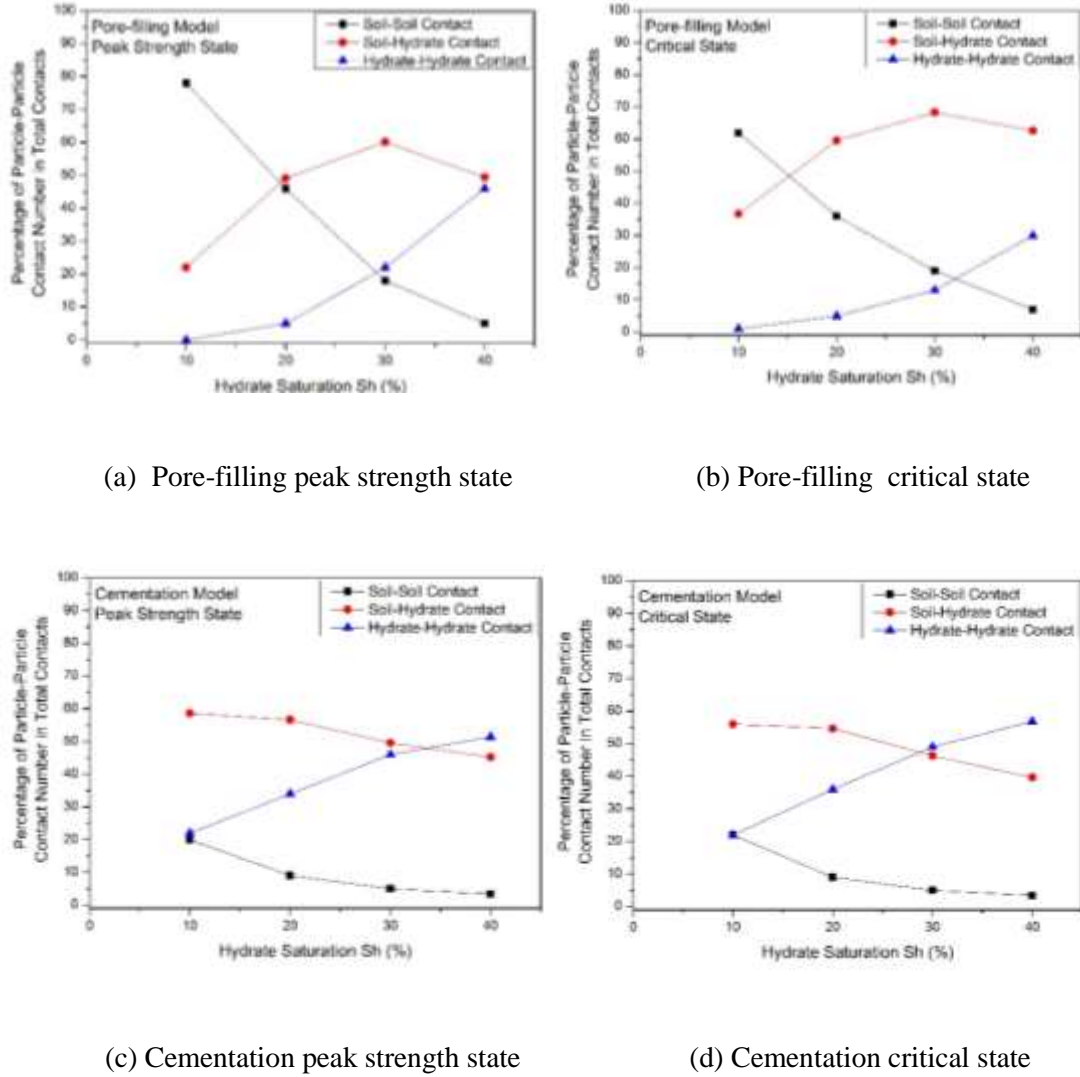


Figure 4.20: Percentage of particles' contact number in total contacts

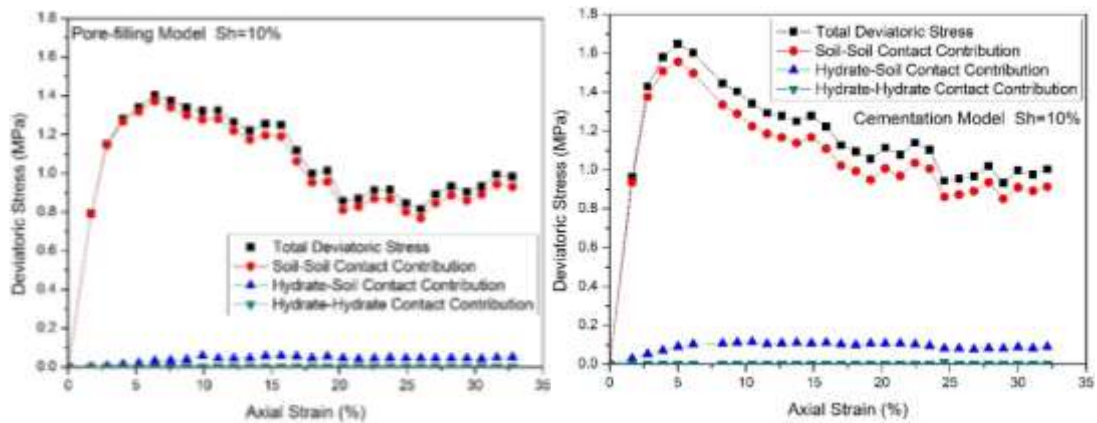
#### 4.4.4 Particle-particle contact force contribution to total deviatoric stress

According to the published research of Minh et al. (2014), the average stress tensor  $\sigma_{ij}$  can be expressed at the summation of the stress tensors of the three contact types: soil-soil contact stress tensor  $\sigma_{ij}^{s-s}$ , hydrate-soil contact stress tensor  $\sigma_{ij}^{h-s}$  and hydrate-hydrate contact stress tensor  $\sigma_{ij}^{h-h}$ , as shown in Equation (4.17).

$$\sigma_{ij} = \sigma_{ij}^{s-s} + \sigma_{ij}^{h-s} + \sigma_{ij}^{h-h} \quad (4.17)$$

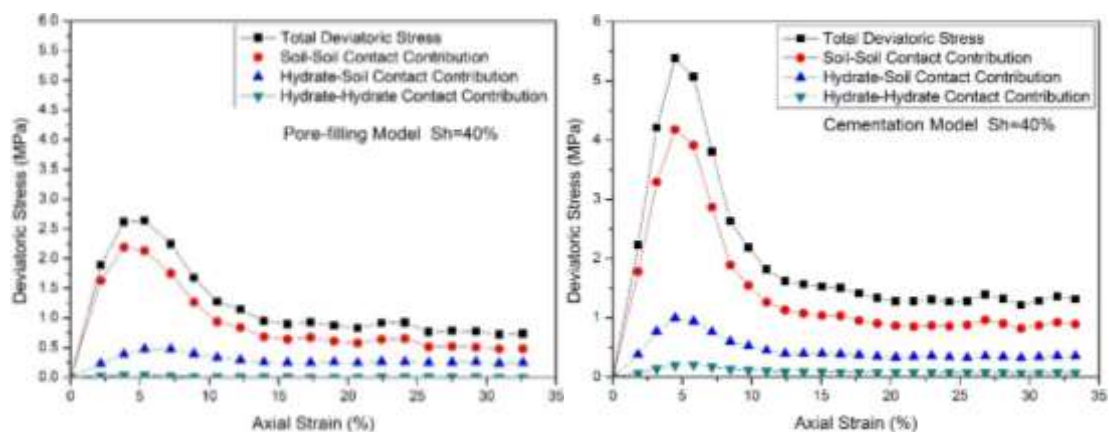
#### 4. Large deformation behaviour of pore-filling and cementation hydrate-bearing sediments

Both Figure 4.21 and Figure 4.22 show the process of the particles' contact force contribution changes during the triaxial tests. As shown in Figure 4.21, the deviatoric stress – axial strain curves are plotted by s-s contact contribution, h-s contact contribution and h-h contact contribution, separately. It is illustrated that the cementation hydrate particles showed greater contribution than the pore-filling hydrates. This is not only because of the effect of h-s and h-s contacts, but also due to the hydrate bonding effect at the soil-soil contacts, which strengthened the soil skeleton. It is still obvious that at the higher hydrate saturation of 40%, the hydrate particles' contribution played a more important role throughout the tests, especially at the peak strength state.



(a) Pore-filling  $S_h = 10\%$

(b) Cementation  $S_h = 10\%$



(c) Pore-filling  $S_h = 40\%$

(d) Cementation  $S_h = 40\%$

**Figure 4.21:** Particles' contacts contribution to the deviatoric stress in the triaxial compression test

In Figure 4.21, from the comparison between  $S_h=10\%$  and  $S_h=40\%$ , it can be clearly seen that the hydrate-hydrate contact force contribution increased obviously at  $S_h=40\%$  due to the accumulated contact stiffness although the hydrate stiffness was low. And from the comparison between the pore-filling and cementation model, the cementation effect can be seen to contribute to the hydrate-hydrate contact force accumulation.

According to the research of Minh & Cheng (2013), the crossover points in Figure 4.20 shows the dominant role of the soil particles was taken over by the hydrate particles. However, as shown in Figure 4.21, all the samples showed only the dominant behavior of soil particles, although there was still a great influence of hydrate particles throughout the tests, especially after the crossover points in Figure 4.20. Hence, it is also important to note that the stiffness of soil particles was much larger than that of hydrate particles. The stiffness effect is also essential according to the published research of Brugada, et al. (2010) as discussed in Section 2.3.1 of Chapter 2. This is the reason that hydrate particles could not play the dominant role in the particle matrix.

In Figure 4.22, at the hydrate saturation of 10%, the h-s and h-h contacts in the pore-filling case (Figure 4.22(a)) initially did not contribute to the initial skeleton contact force, but the cementation model in Figure 4.22(b) showed a small percentage of h-s contact contribution because hydrates formed at the s-s contacts and increased the initial stiffness of the skeleton. However, because of the very large number of hydrate particles in contact with soil particles at  $S_h=40\%$  in Figure 4.22(c) and Figure 4.22(d), the initial skeleton strength was affected by all the particles' contacts, although the s-s contacts were still the most dominant contacts. The s-s contact contribution dropped obviously due to the apparent increase in the h-s contact contribution. In the cementation model, the h-h contact contribution was obviously exhibited in Figure 4.22(d).

It can be seen in Figure 4.22 that in the triaxial test, the s-s contact contribution dropped until the sample reached the critical state, while the h-s contact contribution increased at the beginning and then levelled off at the critical state. But in the pore-filling model at  $S_h=40\%$ , at the large axial strain of 17% and 24%, the h-s contact contribution showed a slight increase, although s-s contact seemed to contribute less

#### 4. Large deformation behaviour of pore-filling and cementation hydrate-bearing sediments

contact forces. This may be because during the deformation process more hydrate particles moved into the skeletal matrix. It is still necessary to mention that due to the hydrate/soil contact stiffness ratio, the relatively softer hydrate particles could not change the sample's strength dominant role or show obvious contribution.

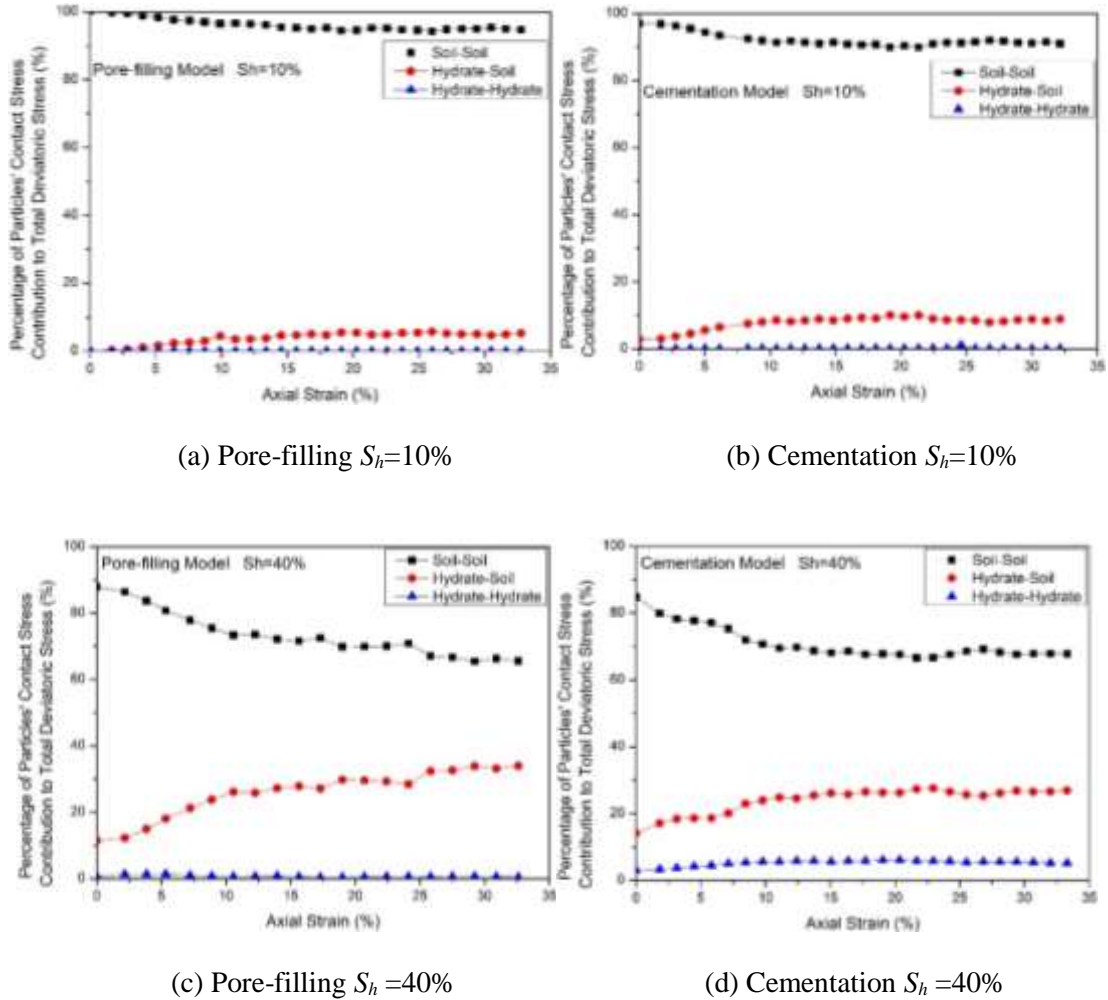


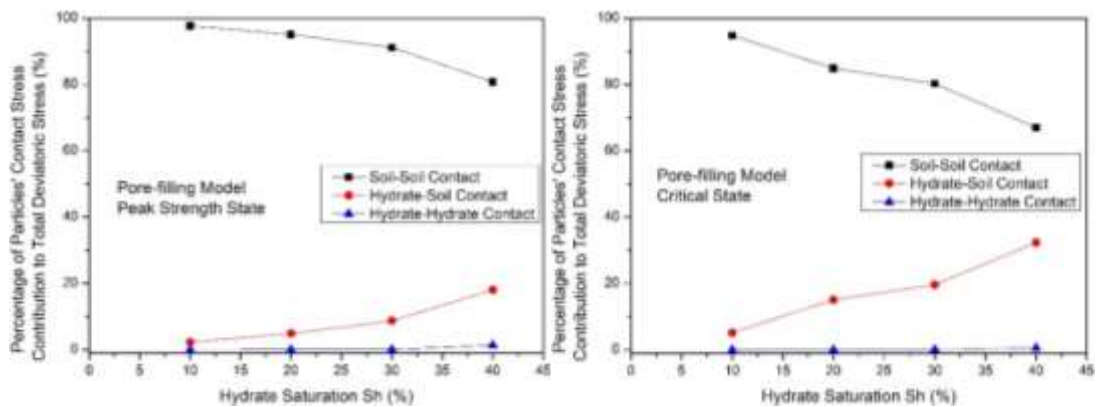
**Figure 4.22:** Percentage of particles' contacts stress contribution to total deviatoric stress

The percentage of particles' contact force contribution to the deviatoric stress at the peak strength state and the critical state was plotted in Figure 4.23.

Generally, in both hydrate growth patterns, the soil-soil contact force contribution decreased as the hydrate saturation increased, but still played the dominant role. It is however obvious that the soil-soil contribution in the critical state exhibited lower values than that seen at the peak strength state. However, as the hydrate saturation increased, the contribution of hydrate particles was shown obviously in the plots,

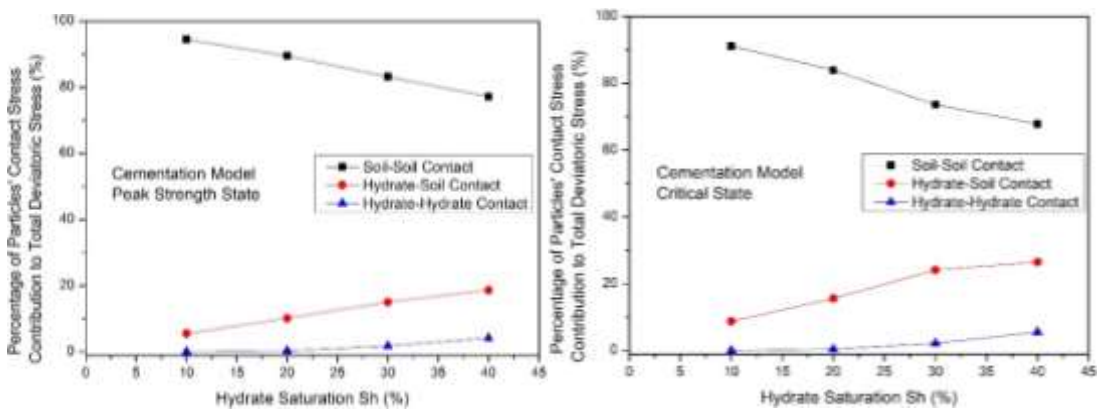
#### 4. Large deformation behaviour of pore-filling and cementation hydrate-bearing sediments

especially the hydrate-soil contact force contribution. In addition, in the critical state, the h-s contact force contribution was greater than that seen at the peak strength state. Furthermore, at higher hydrate saturations, the hydrate-hydrate contact force contribution in the cementation model was higher than in the pore-filling model, which may be interpreted by the jamming role of cementation hydrates in the critical state. There may also be a large number of hydrate clusters lost during the bond with the soil or other hydrate particles, which existed in the pores without easily bridging the main matrix due to the cluster sizes. This may explain why in the critical state, at  $S_h=40\%$  the hydrate contact force contribution in the pore-filling model was greater than in the cementation model.



(a) Pore-filling peak strength state

(b) Pore-filling critical state



(c) Cementation peak strength state

(d) Cementation critical state

**Figure 4.23:** Percentage of particles' contacts force contribution at the peak strength state and critical state in the triaxial compression test

## 4.5 Summary

In this chapter, a series of DEM triaxial compression tests were conducted to make comparisons between pore-filling and cementation models. Comprehensive analyses of stress-strain responses and volumetric responses were discussed. We explored the effects of hydrate saturation and growth patterns on the sediments' stiffness, strength and pore habit. Besides, our interest in the sediments' behaviours extended to the large strain and critical state behaviours in the triaxial tests. In addition, a particle-scale micro-investigation into the DEM hydrate-bearing sediments was also performed. The particle-scale micro-investigation into the DEM hydrate-bearing sediments was also implemented. The contribution of hydrates to the mechanical behaviour of the sediments was of a frictional nature for the pore-filling hydrate distribution pattern, whilst of a frictional and cohesive nature for the cementation case.

Through this research, the following conclusions were made:

(1) Comprehensive analyses were discussed in the aspects of stress-strain responses and volumetric responses. It is revealed that the mechanical behaviours of methane hydrate soil sediments were controlled by both the hydrate saturation and hydrate distribution patterns. The hardening effect of the increase in hydrate saturation was shown obviously in both hydrate growth pattern cases. The presence of hydrates caused the increase in stiffness, strength and dilative tendency, especially when  $S_h \geq 20\%$  for the pore-filling hydrate distribution pattern, and  $S_h > 0\%$  for the cementation model, which was also enhanced by the bonding strength effect and hydrate growth locations at the soil-soil contacts or along the soil surface. In addition, at the same hydrate saturation, the cementation model showed higher values than the pore-filling model in terms of initial stiffness, mid-strain stiffness, peak shear strength, friction angle, cohesion, dilation and granular void ratio.

(2) The interest in this research extended to the samples' large strain and critical state behaviours. For the pore-filling model, hydrate effects on strength produced lower critical state strength as the saturation increased, while in the cementation model the critical state behaviours were shown to be different. In both of the hydrate growth patterns, due to the movements of soil and hydrate particles, the softer hydrates became

part of the soil matrix and transmitted the main contact forces in the skeleton. The hydrates in the skeleton weakened the strength of the critical state. However, the remaining bonding contacts in the cementation samples appeared to produce a resistance to the critical state, weakening behaviour of the soil-hydrate matrix.

(3) Meanwhile, the confining pressure effect was also explored. The stiffness and strength of the samples was enhanced with the greater effective confining pressure, while the dilation appeared to diminish. Yet, the bonding effect at very high saturation in the cementation model caused the sediments' stiffness to become relatively independent of the confining pressure, and produced the dilation, though less evident than that seen at the lower confining pressure.

(4) From the particle-scale investigations of the bond breakage between particles throughout the tests in the cementation model, we found that the hydrate-soil bonding contacts were the main bonding contacts, and also played the main role in the bond breakage process, although hydrate-hydrate bond breakage also happened during the deformation process. The obvious bond breakage started just after the elastic phase, and the number increased steadily. This means there began to be a number of pore-filling pattern hydrate particles in the pores, at the soil-soil contacts or in the soil skeleton after the bond breakage, because at  $S_h=10\%$  and  $S_h=20\%$  the critical state strength of the cementation models was smaller than that of the pure soil sample. There was however still more than half of the bonding contacts remaining in the sample at the large strain. This may explain why, at high saturations of 30% and 40% in the cementation model, the critical strength was greater than that of the pure soil sample.

(5) We also monitored the particles' contact information. The contact number domination of soil-soil contacts changed into hydrate-contact domination with the changing saturation. However, from the research of particle-particle contact force contribution, although the soil-soil contact contribution decreased and the hydrate-contact contribution increased as the hydrate saturation increased, all the samples still showed the soil-particle-dominated behaviour. Hence, it is also important to note that the stiffness of soil particles was much larger than that of hydrate particles. This is the reason that hydrate particles could not play the dominant role in the particle matrix. Further investigations should be conducted on the hydrate/soil contact stiffness ratio.

#### **4. Large deformation behaviour of pore-filling and cementation hydrate-bearing sediments**

However, the bonding effect of hydrates at the soil-soil contacts and along the soil surface still played an important role in strengthening the skeleton in the cementation model.

(6) The large deformation was studied till as high as 33% axial strain. From some macroscopic data, such as deviatoric stress, the curves of the DEM results stabilized for the axial strain range from 15% to 33%. But the larger deformation from 15% to 33% allowed the volumetric changes stabilized at different axial strains because of the various hydrate saturations; it also allowed the stiffness degradation to continue. Moreover, as the deformation got larger, the number of bond breakage still steadily increased, and the microstructure evolution still continued. DEM proved to be a useful tool to conduct a macro- and micro- study on a larger deformation behaviour of the hydrate-bearing sediments. This is why our interest in the sediments' behaviours extended to the large strain behaviours in the triaxial tests.

## Chapter 5

### Small-strain stiffness

#### 5.1 Introduction

As discussed in Section 2.2.1 of Chapter 2, the small-strain shear modulus  $G_{max}$  is usually measured through seismic wave propagation as a fundamental stiffness. The value of  $G_{max}$  can be measured through laboratory and/or on-site field tests. In wave propagation, the propagation of the compression  $P$  wave induces longitudinal strains within the particles' motion along the wave propagation direction. The shear  $S$  wave causes shear strains with the particles' motion perpendicular to the wave propagation direction (Waite et al., 2009). From the wave velocities data summarized in Section 2.2.1 (2006), it was found that shear and compression wave velocity is a good indicator of the hydrate existence and its growth patterns.

As discussed in Chapter 2, various seismic testing techniques have been extensively applied to detect the presence of hydrates and estimate the hydrate saturation on site, as the hydrates increase the stiffness of hydrate-bearing sediments and increase the wave velocity through the sediments (Waite et al., 2009). With the recognition of limitations in laboratory and field tests, wave propagation modelling using Discrete Element Method (DEM) was conducted in this chapter in order to provide the insights on the hydrate-bearing sandy sediments models with pore-filling and cementation hydrate distributions. The relationship between wave velocity and hydrate saturation was established by the DEM simulations. In this research the DEM simulations helped relate wave velocity to the properties of stiffness at various hydrate saturations, and characterize hydrate-bearing sediments with the seismic data.

Furthermore, studies were conducted to relate the small-strain stiffness with the mid-strain and large-strain geomechanical behaviours, in order to help predict the mid-strain and large-strain responses in the wellbore through the wave propagation.

## 5.2 Seismic wave propagation procedures in the DEM sample

There are three steps for modelling compression  $P$  wave and shear  $S$  wave propagation in the hydrate-bearing DEM soil samples, which followed the published research by Xu et al. (2012):

- (1) Noise elimination: to make particles reach equilibrium by cycling a number of time steps after the consolidated sample was prepared;
- (2) Transmitter and receiver installation: as shown in Figure 5.1, 2 groups of particles in a short cylindrical shape region were chosen at the top and bottom inside the sample - one was the transmitter and the other was the receiver;
- (3) Transmitting and monitoring: then the excitation was started by exciting a single sine velocity pulse to the transmitter in a certain direction ( $P$  wave or  $S$  wave). The averaged velocity of the receiver in the same direction is then monitored for detecting the arrival of the disturbance.

All the input parameters are shown in Table 3.1 in Section 3.4. In this study, the frequency and amplitude of the applied velocity pulse was chosen to be 10 kHz and  $1 \times 10^{-5}$  m/s respectively. Thus, the maximum displacement for the transmitter would only be  $1.59 \times 10^{-10}$  m (i.e.  $9.09 \times 10^{-8}$  for strain), which is still within the elastic range.

The prepared DEM sample was a cylinder of 3.5 mm (height)  $\times$  1.75 mm (diameter) and a height/diameter ratio of 2:1, which was confined by the lateral cylindrical wall and the planar walls at the top and bottom. The three smooth walls were used to confine the sample. The numbers of the soil and hydrate particles at various saturation are shown in Table 3.2.

As illustrated in Figure 5.1 (b), regarding the transmitter and the receiver, 2 groups of particles in a short cylindrical shape region were chosen at the top and bottom inside the sample. In order to avoid the influence of the boundaries, in this research, truncated signal method was employed: when the complete receipt of the wave signal had been taken by the receiver, the signal would be truncated. Meanwhile,

it was important to set the receiver relatively far from the boundary for minimizing the influence caused by the bottom reflection. To specify, the diameter of both the transmitter and the receiver was 0.875 mm, and their height was 0.25 mm. Hence, about 1/55 of the number of particles was chosen to be set as the transmitter or the receiver.

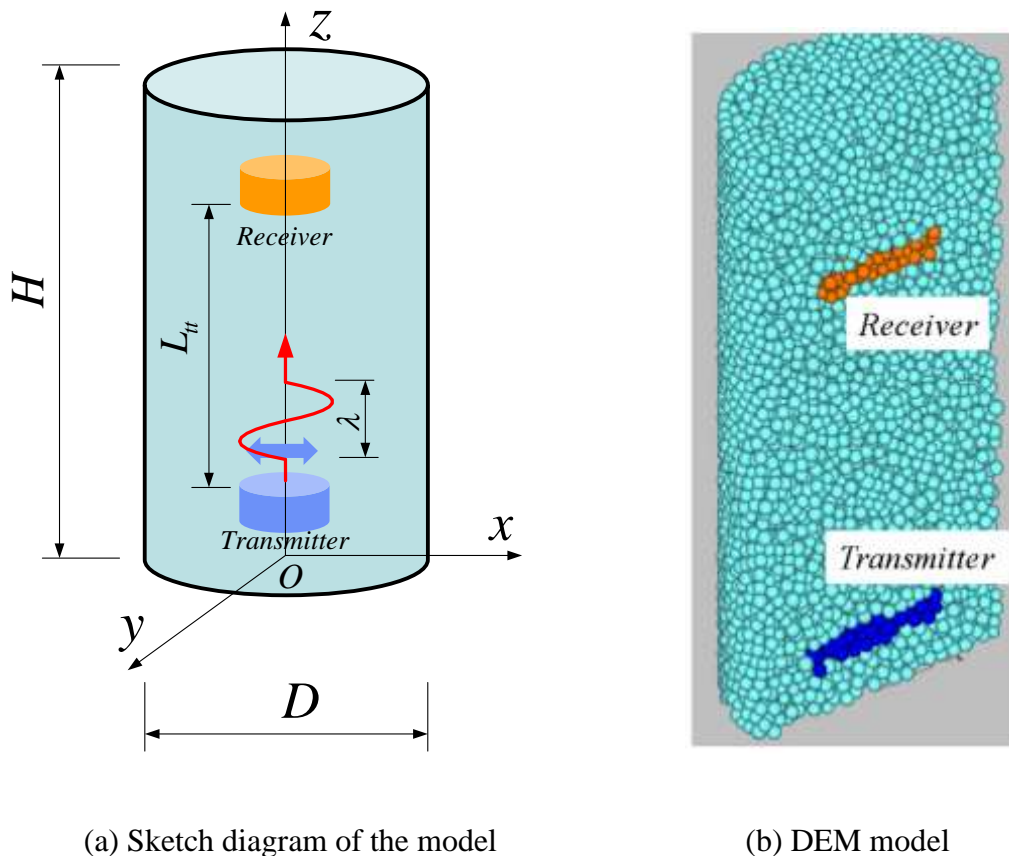


**Figure 5.1:** The model for wave propagation

### 5.3 Simulation results and discussions

#### 5.3.1 Small-strain stiffness at 1MPa confining pressure

Under the confining pressure of 1MPa, comparisons of shear  $S$  wave velocities through the DEM hydrate-bearing sediment samples are shown in Figure 5.2 at different hydrate saturations. Generally, the wave velocities increased when the hydrate saturation was growing. It is shown that, in the pore-filling model,  $S$  wave velocities

$V_s$  kept at a relatively constant value at low hydrate saturation, and then began to increase when the saturation became higher. However, in the cementation model,  $V_s$  increased obviously from lower hydrate saturations, and then increased steadily when the volume of hydrates was growing. At the same hydrate saturation,  $V_s$  in the cementation model was larger than that in the pore-filling model. It is suggested in Figure 5.2 that the shear wave velocity is controlled by both hydrate saturation and hydrate growth pattern.

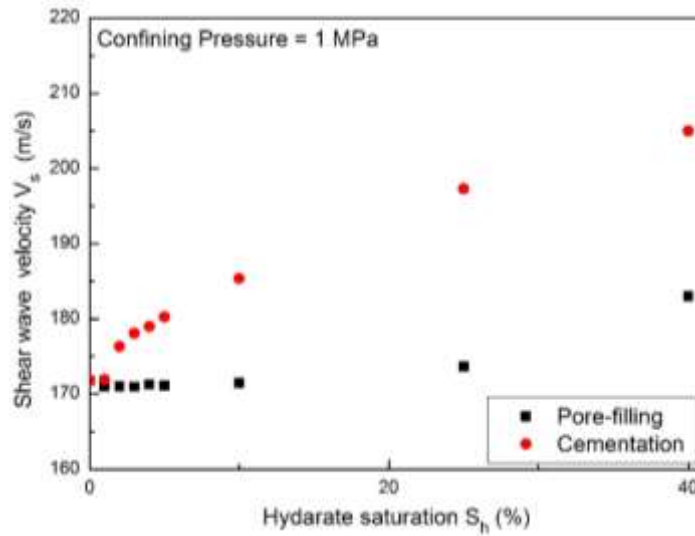


**Figure 5.2:** Comparison of shear  $S$  wave velocities between pore-filling and cementation models at different hydrate saturations (at 1MPa confining pressure)

As previously mentioned in Chapter 2, the shear wave velocity  $V_s$  has a direct relation to the small strain shear modulus  $G_{max}$ :

$$G_{max} = \rho V_s^2 \quad (5.1)$$

where  $\rho$  is the total density of the sediment.

According to the wave velocities through the DEM hydrate-bearing sediment samples of pore-filling and cementation models, small-strain shear modulus  $G_{max}$  can be obtained by Equation 5.1, as shown in Figure 5.3. It is shown that the increasing hydrate saturation resulted in the increase of small strain shear stiffness in the cementation model, while the shear modulus remained constant in pore-filling hydrate

samples at low hydrate saturations whilst increasing with higher saturations. It is found that the cementation hydrates increased the small strain stiffness of the sediment much more obviously than pore-filling hydrates when at the same hydrate saturation. By Equation 5.1, it can also be found that the increased density by adding more hydrate particles contributed to the increase of  $G_{max}$  as the saturation increased.

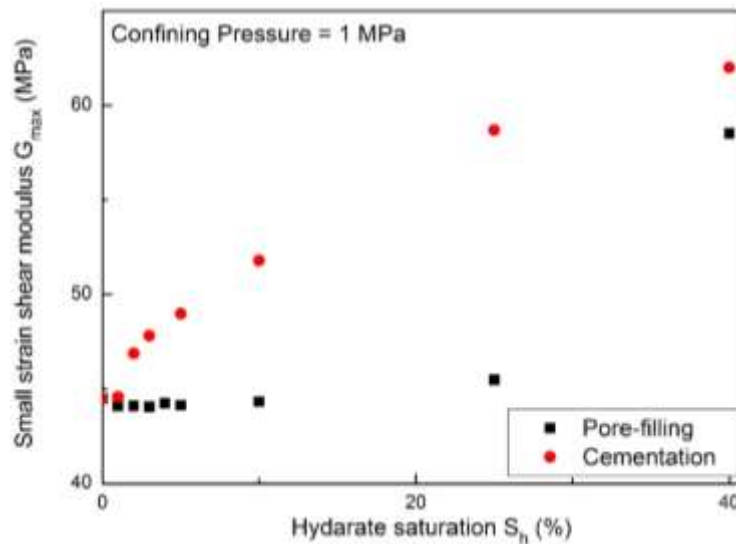


**Figure 5.3:** Comparison of small-strain shear modulus  $G_{max}$  at different hydrate saturations between pore-filling and cementation models (at 1MPa confining pressure)

Methane hydrate has a slightly larger stiffness than ice (Soga et al., 2006), but it has a much smaller stiffness compared to soil. From the results of wave propagations through the pore-filling model and cementation model, it is found that the wave velocities and the shear stiffness of methane hydrate sediments are governed by two main aspects: (1) pore space hydrate saturation, and (2) the growth and formation pattern of hydrate in the sediments' pore space.

In Figure 5.4(a), hydrate particles in the pore-filling model do not affect the shear stiffness as the hydrate particles are suspended in the pore space, and especially when the hydrate saturation is low. However, in Figure 5.4(b) of the cementation pattern, hydrates form first at the grain contacts, and then they grow in the pores from the grain contacts.

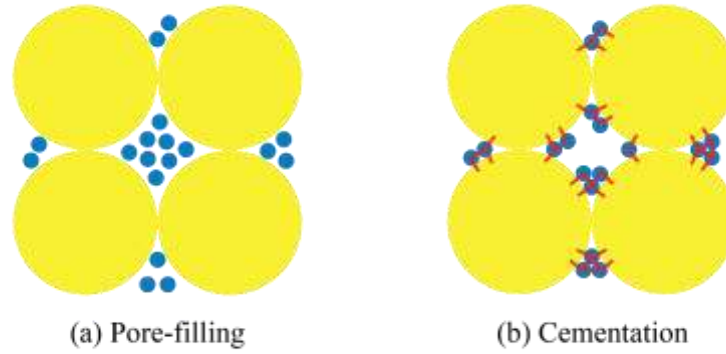


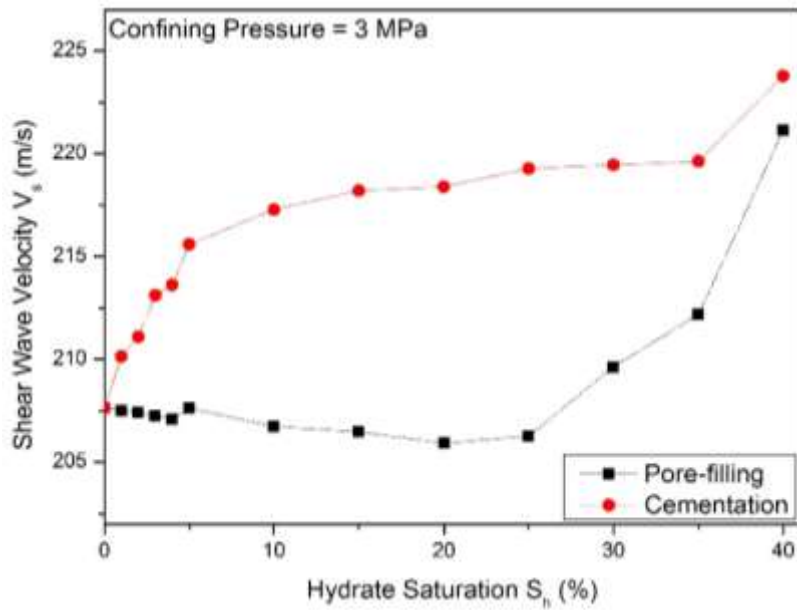
**Figure 5.4:** Growth and formation pattern of hydrate particles in (a) pore-filling and (b) cementation models (red lines represent contact bonds)

The wave propagation in the samples was simulated by exciting the particle movements. In three dimensions (3D) DEM simulations, there are six degrees of freedom for each particle: three translational degrees and three rotational degrees. In the pore-filling model, when the wave went through the grain skeleton, the particles of the grain skeleton would move with the wave. The six degrees of freedom of the particles in the pore-filling model caused large energy loss and caused the wave propagation time to become longer. However, in the cementation model, as hydrates were in contact with grain sediment and the existing soil skeleton structure was cemented, the rotational movements of particles were restricted by the bonding strength between particles. Hence, the energy loss in the cementation model was less than that in the pore-filling model. Additionally, compared to the pore-filling model, the wave propagation time costs were shortened, so that the shear wave velocities  $V_s$  increased from lower hydrate saturations in the cementation model. In a similar way,  $V_s$  in the pore-filling model increased at higher hydrate saturation because pore-filling hydrate particles began to bridge the grain skeleton and showed load-bearing behaviour after 25% hydrate saturation.

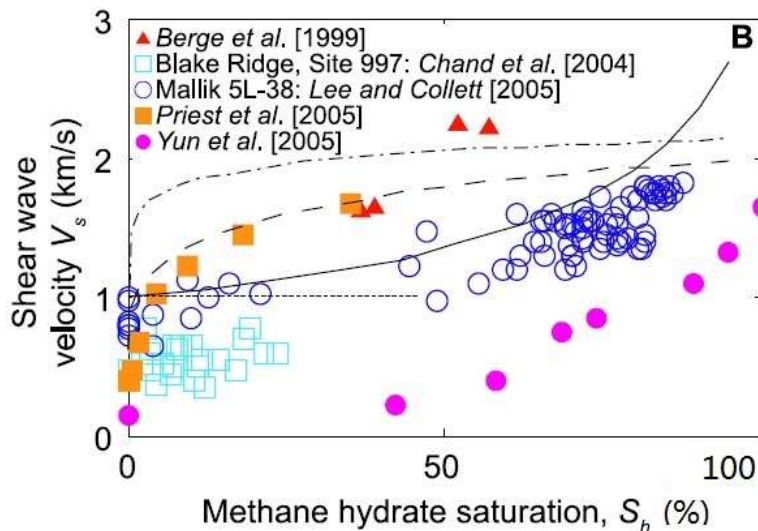
### 5.3.2 Wave propagation at the confining pressure of 3MPa

It was previously discussed in Chapter 2 that the wave velocity and small-strain stiffness generally increase with confining pressure. Hence, a series of wave

propagation simulations were conducted within the hydrate-bearing samples consolidated under the isotropic confining pressure of 3MPa. Figure 5.5 (a) shows the comparisons of shear  $S$  wave velocities between pore-filling and cementation models at various hydrate saturations. While Figure 5.6 (a) shows the comparisons of compression  $P$  wave velocities.

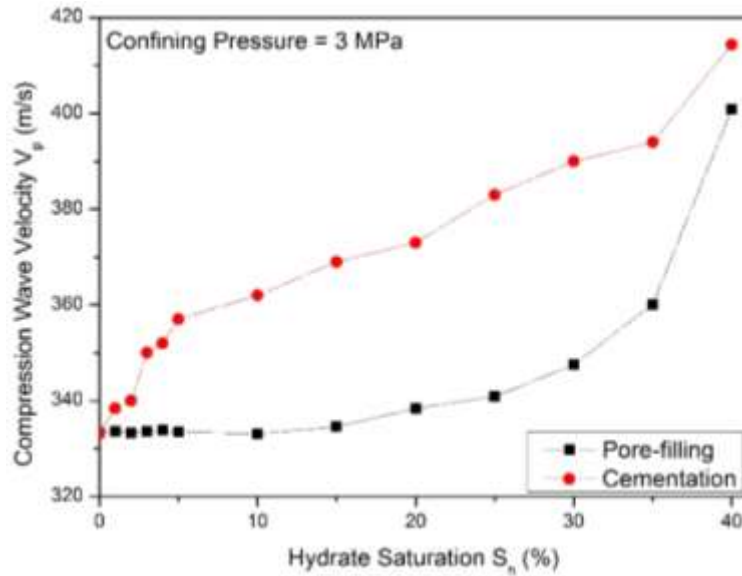


(a) DEM study

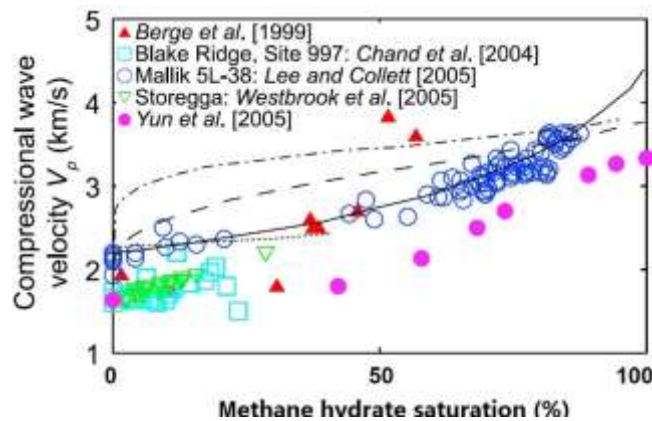


(b) Modelling, field and experimental data (concluded by Waite et al., 2009)

**Figure 5.5:** Comparison of shear  $S$  wave velocities between pore-filling and cementation models at different hydrate saturations (at 3MPa confining pressure): (a) DEM study; (b) modelling, field and experimental data (reviewed by Waite et al., 2009)



(a) DEM study



(b) Modelling, field and experimental data (concluded by Waite et al., 2009)

**Figure 5.6:** Comparison of compression  $P$  wave velocities between pore-filling and cementation models at different hydrate saturations (at 3MPa confining pressure): (a) DEM study; (b) modelling, field and experimental data (reviewed by Waite et al., 2009)

In these simulations under the confining pressure of 3MPa, a larger variation of hydrate saturations were chosen to form clearer curves of wave velocities. Similarly, as discussed above, in the pore-filling model,  $S$  and  $P$  wave velocities  $V_s$  and  $V_p$  were kept at the relatively constant values at low hydrate saturation, and then began to increase with the higher saturation. Whereas, in the cementation model,  $V_s$  and  $V_p$  increased obviously from lower hydrate saturations, and then increased steadily when

the saturation of hydrate was growing. At the same hydrate saturation,  $V_s$  and  $V_p$  in the cementation model were larger than those in the pore-filling model.

As discussed in Section 2.2.1 of Chapter 2, Figure 5.5 (b) and Figure 5.6 (b) show the  $S$  and  $P$  wave velocities  $V_s$  and  $V_p$  respectively from the field exploration (hollow symbol), laboratory tests (solid symbol), and modelling data (solid and dashed curve). The details of the data have been discussed in Chapter 2. It is clearly seen that the trends of the wave velocities against various hydrate saturation in this DEM study in Figure 5.5 (a) and Figure 5.6 (a) are compared well to the trends in Figure 5.5 (b) and Figure 5.6 (b). But the fact is that the wave velocity values in the DEM study may be lower than some of the field and laboratory studies, or higher sometimes. This is because of the DEM input parameters, confining pressure, porosity, etc.. But the obtained wave velocities for both pore-filling and cementation models seemed to be reasonable.

The derived small-strain shear modulus  $G_{max}$  from the wave velocities is shown in Figure 5.7 at various hydrate saturations under the confining pressure of 3MPa. It is illustrated that the increasing hydrate saturation led to the increase of small strain shear stiffness in the cementation model, while the shear modulus remained constant in the pore-filling hydrate samples at low hydrate saturations, increasing with higher saturations. As for the cementation model, the increasing rate of the shear stiffness with small hydrate saturation is greater than that of the pore-filling case. It is also found that the cementation hydrates increased the small strain stiffness of the sediment much more obviously than the pore-filling hydrates at the same hydrate saturation.

A similar conclusion can also be found regarding the Young's modulus  $E$ , as shown in Figure 5.8. The stiffness of methane hydrate soil sediments increased with the higher hydrate saturation, and the increase rate depended on the formation pattern of hydrate in the sediments' pore space, which has been discussed in Chapter 4 as well.

It is also necessary to note that, as discussed in Chapter 3, the hydrate saturation computed here may not be the same as the hydrate saturation measured in the laboratory. The simulated hydrate saturation ( $S_h$ ) should correspond to a higher hydrate saturation than the natural hydrate-bearing soil sediments for several reasons, such as

the size and shape of the assumed soil and hydrate particles, the void space limitations, and the existence of other materials in the pores of the natural sediment.

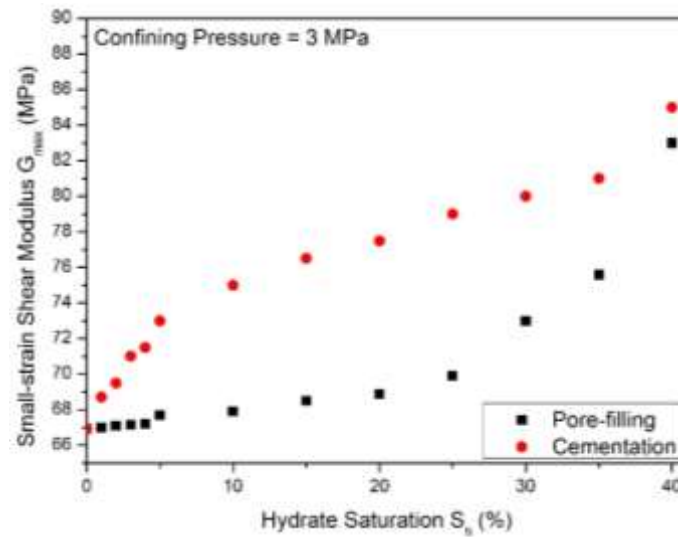


**Figure 5.7:** Comparison of small-strain shear modulus  $G_{max}$  at different hydrate saturations between pore-filling and cementation models (at 3MPa confining pressure)

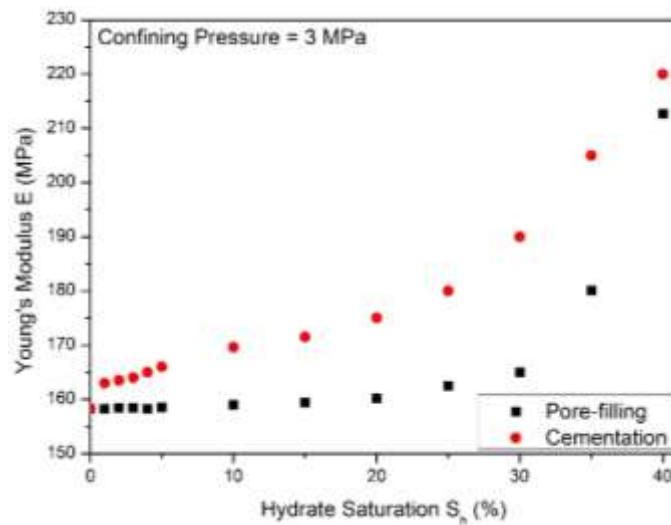


**Figure 5.8:** Comparison of Young's modulus  $E$  at different hydrate saturations between pore-filling and cementation models (at 3MPa confining pressure)

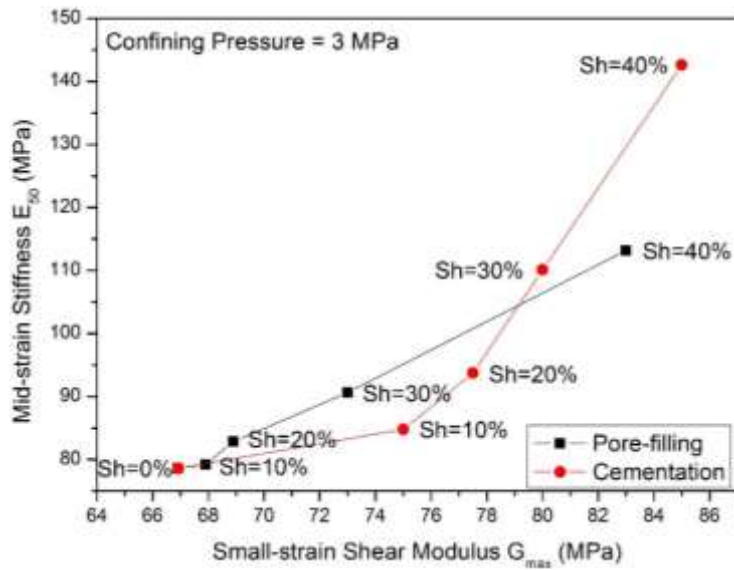
And from comparisons between the DEM study and the field & experimental work on the obtain wave velocity and small-strain shear modulus trends against the hydrate saturation, it can be confirmed that the hydrate saturation ( $S_h$ ) in this DEM study should correspond to a higher hydrate saturation. Further discussions are presented in Appendix A.

### 5.3.3 Relations between small-strain stiffness and mid-strain and large-strain behaviours

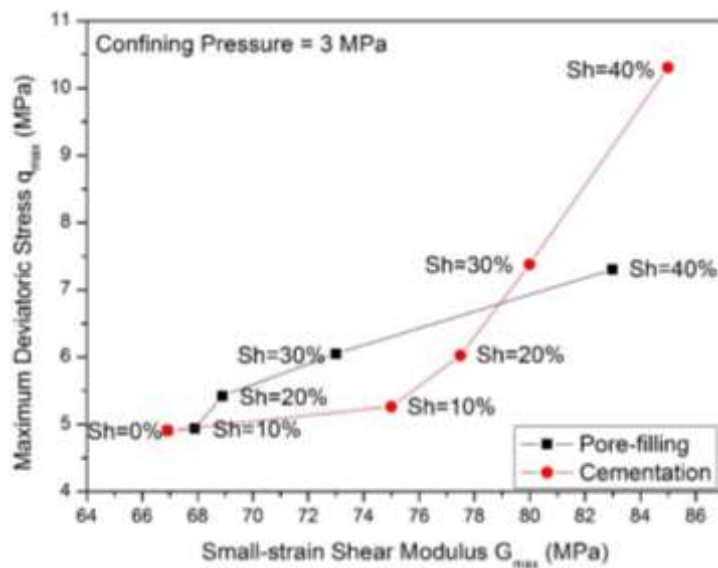
In addition to the basic studies on the small-strain stiffness and wave velocities within the hydrate-bearing samples, our interest in the sediments' behaviours extended to the large strain deformation and critical state behaviours in the triaxial tests, but these could not be obtained easily in the laboratory studies due to the limitations. Hence, the relationship between small-strain stiffness and the large strain geomechanical behaviours are also explored in this chapter. It is believed that the initial state behaviours may have an influence on the large strain behaviour of granular materials. Hence, studies were conducted to relate the small-strain stiffness with the mid-strain and large-strain geomechanical behaviours discussed in Chapter 4, in order to help predict the mid-strain and large-strain responses in the wellbore through the wave propagation.

Figure 5.9 shows the relations between small-strain shear modulus  $G_{max}$  and mid-strain stiffness  $E_{50}$ . Under the confining pressure of 3MPa, the mid-strain stiffness  $E_{50}$  values were plotted against the corresponding small-strain shear modulus  $G_{max}$  at various hydrate saturations. It is clearly illustrated that as the small-strain shear modulus  $G_{max}$  increased, the corresponding mid-strain stiffness  $E_{50}$  evidently increased. At the same hydrate saturation, the mid-strain stiffness  $E_{50}$  of the cementation model was larger than that of the pore-filling model. The variation of the mid-strain stiffness  $E_{50}$  values at the same hydrate saturation between the pore-filling and cementation cases increased with the saturation.

During the deformation process in the triaxial test at a 3MPa confining pressure, the maximum deviatoric stress  $q_{max}$  was plotted in Figure 5.10 against the small-strain shear modulus  $G_{max}$  of the pore-filling and cementation models at various hydrate saturations. Firstly, it can be seen that the maximum deviatoric stress  $q_{max}$  increased with the small-strain shear modulus  $G_{max}$  for both hydrate-bearing models. Secondly, at the same hydrate saturation,  $q_{max}$  in the cementation model was larger than that of the pore-filling model. The variation of  $q_{max}$  values at the same hydrate saturation between the pore-filling and cementation cases increased with the saturation.



**Figure 5.9:** Relation between small-strain shear modulus  $G_{max}$  and mid-strain stiffness  $E_{50}$  at various hydrate saturation for pore-filling and cementation patterns (at 3MPa confining pressure)



**Figure 5.10:** Relation between small-strain shear modulus  $G_{max}$  and maximum deviatoric stress  $q_{max}$  of the pore-filling and cementation models at various hydrate saturation (at 3MPa confining pressure)

As shown in Figure 5.11, however, the critical state strength showed a decrease for the pore-filling model as the hydrate saturation got higher. It can be suggested that the critical state strength could be predicted through the wave propagation in the pore-filling hydrate sediment, because the critical state strength  $q_{cs}$  of the pore-filling

decreased with the increase in the small-strain shear modulus  $G_{max}$ . However, the critical state strength  $q_{cs}$  of the cementation model decreased from 0% to 20% hydrate saturation, and then increased from 20% to 40% saturation. Hence, it could not be predictable for the critical state strength of the cementation model through the wave propagation as there is no regular pattern between the increase in the small-strain shear modulus  $G_{max}$  and the changes of the critical state strength of the cementation model. According to this DEM data, it is suggested that the small-strain stiffness or initial state wave velocity should be not related to the critical state of the hydrate-bearing sediment.

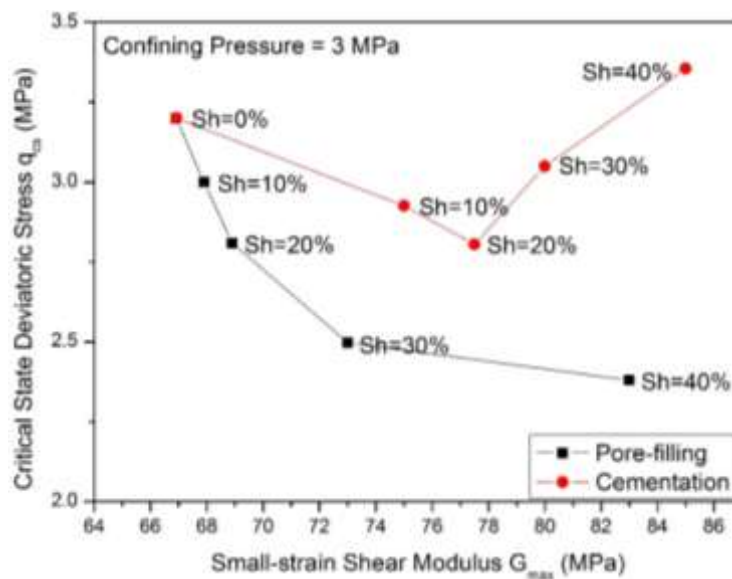


**Figure 5.11:** Relation between small-strain shear modulus  $G_{max}$  and critical strength of the pore-filling and cementation models at various hydrate saturation (at 3MPa confining pressure)

## 5.4 Summary

In summary, the wave velocity measurement and the particle-scale analysis show that the small-strain mechanical properties of hydrate-bearing sandy sediments are governed by not only the pore space hydrate saturation, but also the hydrate formation and distribution patterns. The influence of the cementation hydrate pattern on the small-strain behaviour becomes obvious from low hydrate saturation, because hydrates grow first at the grain contacts and the existing soil skeleton structure was cemented. This restriction cuts down the energy loss and shortens the wave

propagation time. However, pore-filling hydrate does not have an impact on the small-strain behaviour of the sediment's grain skeleton at low hydrate saturation. But, as the volume of hydrate increased to a higher saturation, the small strain stiffness increased both in cementation and pore-filling cases. It was also found that the wave velocity and small-strain stiffness generally increased with confining pressure.

And from comparisons between the DEM study and the field & experimental work on the obtain wave velocity and small-strain shear modulus trends against the hydrate saturation, it can be confirmed that the hydrate saturation ( $S_h$ ) in this DEM study should correspond to a higher hydrate saturation.

It may be concluded that the initial state behaviours may have an influence on the large strain behaviour of hydrate-bearing sediments. As the hydrate saturation increased, the small-strain stiffness increased. Accordingly, the corresponding mid-strain stiffness and the peak strength increased with the saturation and the small-strain stiffness. This could be a regular pattern for predicting the large-strain behaviours through the wave propagation. However, the critical state strength did not follow the trend of the observations mentioned above. According to this DEM data, it is suggested that the small-strain stiffness or initial state wave velocity should be not related to the critical state of the hydrate-bearing sediment.

Seismic exploration of the underground resources is still a very challenging job at this stage. Even when the resource is detected at one site, it cannot be guaranteed that in this site the exploitation can be successful or the deposit is worth an exploitation. As a qualitative study and an early stage numerical work, this DEM research cannot be applied to the field work due to the field challenges. And in this DEM research, the saturation could only reach 40% which cannot represent the real saturation, as discussed in Chapter 3 and this chapter. Secondly, two different hydrate growth patterns show the different trends of small-strain stiffness against the hydrate saturation. Hence, the relation between hydrate saturation and small-strain stiffness may be a proper implication for the engineering applications, although this is not enough and it is the first step towards that direction. A series of further steps should be taken to bring the DEM model closer to the real field characteristics, such as the contact model modification, parametric studies, inclusion of fluid and gas, etc.. Most

importantly, in the future study a proper relationship should be proposed between the hydrate saturation and the sediment's shear modulus value, in order to be useful for the engineering application. One difficulty which should be solved in the future is that this relationship should include the hydrate growth pattern issue.

## Chapter 6

# Effects of hydrate growth patterns and bonding strength in the cementation model

### 6.1 Introduction

Laboratory observations by Priest et al. (2005) indicated that, in the cementation specimen, hydrates formed first at the grain contacts, and then grew in the pores and along the soil surface from the grain contacts. From the discussions in Chapter 4 and Chapter 5, it was found that the hydrate growth patterns and distribution could govern the sediment's mechanical behaviour.

The cementation hydrate particles either gathered at the soil-soil contacts or bonded to the soil surface. The location of these two different types of cementation hydrate particles may influence the mechanical behaviour differently. Soga et al. (2006) concluded that in the nature there is a 'coating' hydrate growth pattern in which the hydrates are bonded to the soil surface rather than at the soil-soil contact points. Hence, for both hydrate-bearing sediment study and the DEM extension research, a comparison should be conducted in order to study the effect of hydrate growth patterns in the cementation hydrate-bearing soil model. Hence, in this study, the hydrate growth process of cementation hydrate sediments was separated into two hydrate growth patterns so as to study the effect that the hydrate growth patterns had on the geomechanical behaviour of the methane hydrate soil sediments.

Therefore, the two hydrate growth patterns of the cementation model were considered: soil surface coating (hydrates accumulating at grain surface) and soil-soil contact gathering (hydrates aggregating near the grain contacts). As shown in Figure 6.1, the DEM simulations in Chapter 6 were performed with samples from the two different growth patterns: (i) hydrates placed around grain surfaces ("Coating" in

Figure 6.1(a) and (ii) hydrates placed near grain contacts (“Contact gathering” in Figure 6.1(b)).

The effects of the bonding strength between particles of the cementation model were also considered as a further discussion for the numerical simulations of hydrate-bearing sediments and other particle-level research, which currently cannot be obtained easily in the laboratory studies. The bonding strength of hydrate-hydrate and hydrate-soil was varied, as shown in Figure 6.1 (a)-(a’) and (b)-(b’).

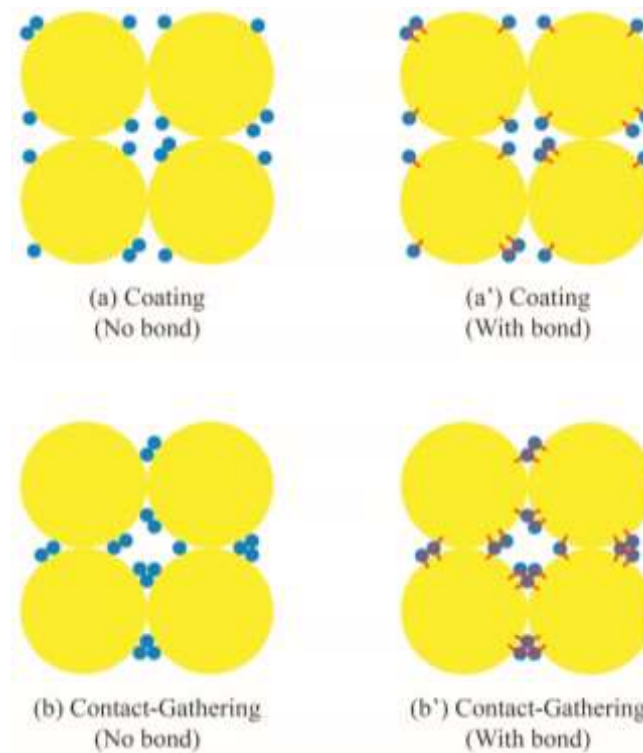


**Figure 6.1:** Hydrate growth patterns of the cementation model: (a) soil surface coating (b) soil-soil contact gathering

In order to study the bonding strength effect of the hydrate particles, the DEM simulations in Chapter 6 were conducted on the two cementation hydrate growth patterns at various bonding strengths – 0 MPa (no bond), 0.005 MPa, 0.010 MPa, 0.025 MPa, 0.050 MPa and 0.500 MPa using the contact bond model in PFC<sup>3D</sup>. The soil particles were not bonded together. The bonding strength of 0.005 MPa has been proved to be a good value for the cementation model in Chapter 4 and 5 for the qualitative study. In fact, it is also interesting to know if the hydrate particles are in contact with the soil particles without a bonding strength, which means the bonding

strength is 0 MPa, what kind of behaviour the samples have. Regarding the pure DEM studies, it is also interesting to know the difference of the sample's behaviour if the smaller and softer particles (hydrates) have a higher bonding strength. Hence, a series of trial simulations were made with different higher bonding strength values - 0.010 MPa (twice of the 0.005 MPa), 0.025 MPa (five times), 0.050 MPa (ten times) and 0.500 MPa (one hundred times).

In this chapter, the drained triaxial compressional tests were systematically conducted to study the effects of hydrate growth patterns and hydrate bonding strength in the cementation model. The comparisons between the coating and contact-gathering models were made using a few aspects. The stress-strain responses and volumetric responses were compared and discussed. We also explored the effects of hydrate growth patterns and bonding strength on the sediments' stiffness, strength and large strain deformation behaviour in the triaxial tests. Furthermore, particle-scale micro-investigation into DEM hydrate-bearing sediments was also performed. We monitored the bond breakage between particles throughout the tests, as well as the particles' contact information -- the particles' contact force contribution to the total measured deviatoric stress. A discussion was also raised regarding the effect of the hydrate/soil stiffness ratio of the particle-particle contact force contribution to the strength of the samples. In addition, the comparisons of measuring the stresses and strains were made among three measurement techniques: measurement spheres (local measurement), average particles' contact forces (global measurement) and wall-based logic (boundary measurement).

### **6.2 DEM simulation results**

In the Stress and Strain Measurement Schemes of PFC<sup>3D</sup>, stresses and strains can be measured using three methods as mentioned above in Section 6.1: (1) average forces on walls by the ball-wall contact and ball-ball contact transmission (boundary measurement); (2) average values from three measurement spheres inside the sample (local measurement); (3) the average contact force of particle-particle and particle-wall (global measurement). The wall-based measurements are used by comparison with the physical laboratory measurements, used in most of the research in this PhD thesis, such

as in Chapter 4 and 7. However, in this chapter, the measurement spheres logic was chosen, because if the bonding strength between particles was too large, the large strain deformation might cause a loss of ball-wall contacts due to the brittle failure along the shear band.

Three measurement spheres were set in the middle of the sample, as shown in Figure 6.2, and will be inside the sample throughout the triaxial test. The average stresses and strains were measured using the three measurement spheres, and the volumetric responses were obtained from the changes of porosity inside the measurement spheres.

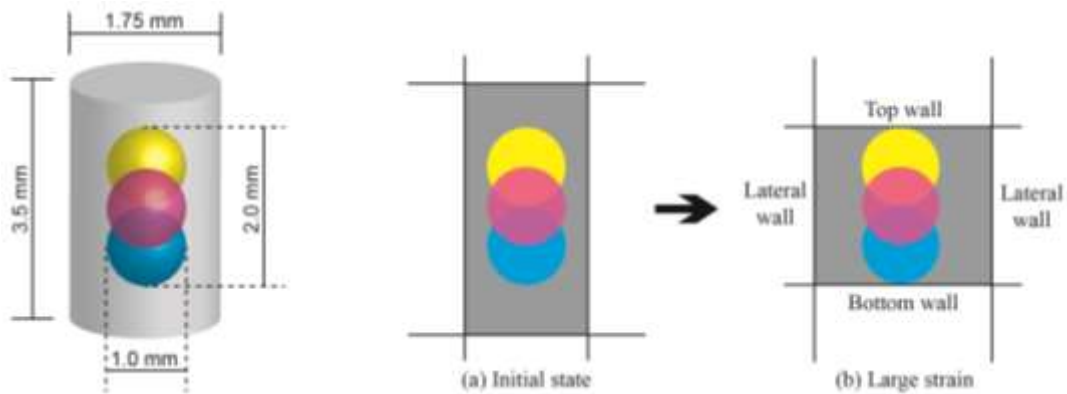


**Figure 6.2:** Measurement spheres inside the sample

### 6.2.1 Stress-strain responses

The stress-strain relationships obtained from the drained triaxial compression tests are plotted in Figure 6.3, which shows deviatoric stress against axial strain, for samples with a coating hydrate pattern (Figure 6.3(a) (c) (e) (g)) and contact-gathering hydrate pattern (Figure 6.3(b) (d) (f) (h)) at  $S_h=10\% \sim 40\%$ , with an increase in the bonding strength of the hydrate particles from 0 MPa to 0.5 MPa.

Firstly, at the bonding strength increased, the strength of the hydrate-bearing soil samples was enhanced at each given hydrate saturation. For each model at a given saturation, it can be observed that from the initial state the stiffness of all the various bonding strength samples was the same, but as a larger axial strain was reached, the strength of the higher bonding strength sample kept increasing while the strength of

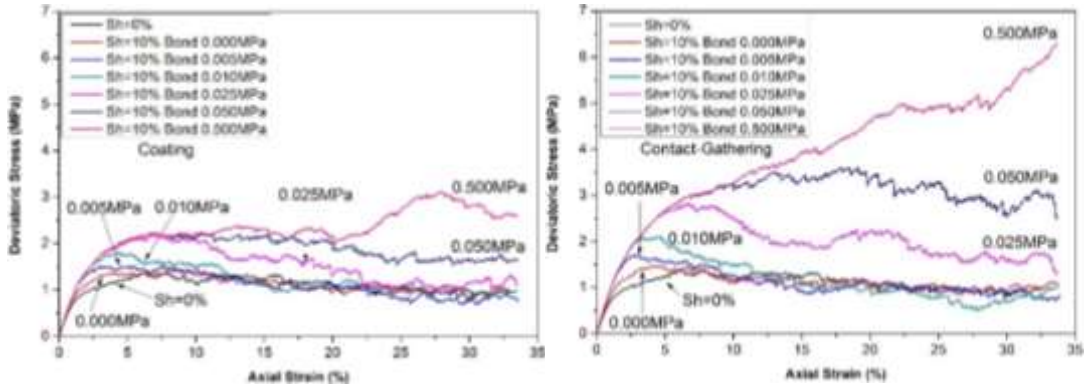
the lower bonding strength sample began to reach a failure. As the bonding strength increased, a larger axial strain was needed to reach the peak strength, and the failure was delayed.

Secondly, however, when the bonding strength was as high as 0.500 MPa, as shown in Figure 6.3(b) (c) (d) (e) (f) (g) (h), a large axial strain of 33% was not enough to lead the sample to a failure. The only exception can be seen in Figure 6.3(a) when the hydrate saturation was 10% in the coating model. Except 0.500 MPa bonding strength samples, all the other samples with a relatively lower bonding strength reached a failure and dropped to the constant critical state strengths at the large axial strain. Hence, it is suggested in the data that the bonding strength of 0.500 MPa was not a reasonable value. And it can be seen that the bonding strength value 0.005 MPa and 0.010 MPa made the samples have the very close and reasonable axial strain for reaching the peak strength state, although the higher bonding strength caused a larger peak strength; and the critical state strength of both models was very close. It seems that the two bonding strength value 0.005 MPa and 0.010 MPa are reasonable for the DEM hydrate-bearing soil model in this research.

Thirdly, at the same hydrate saturation, the critical state strength exhibited a higher value in the higher bonding strength sample, especially when the bonding strength was 0.025 MPa and 0.050 MPa. The similar observations to the first and third points have been discussed in Chapter 2. As shown in Figure 6.4 (a) and Figure 6.4 (b) (Masui et al., 2005) of the experimental data and Figure 6.4 (c) (Jiang et al., 2013) of the 2-Dimension DEM data, as the bonding strength increased from weak bond to strong bond, at the same hydrate saturation, the strength increased accordingly. In addition, in Figure 6.4 (c) the increase in the bonding strength did not further increase the elastic phase stiffness, while it increased the peak strength and critical state strength.

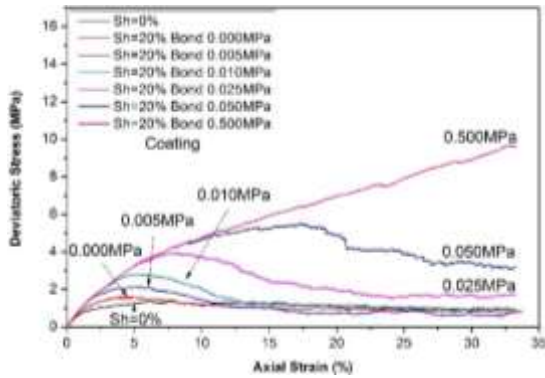
Furthermore, in the same bonding strength and hydrate saturation conditions, the strength of the soil-soil contact gathering model was larger than that of the soil surface coating model, which can be observed when comparing Figure 6.3(a) (c) (e) (g) and Figure 6.3(b) (d) (f) (h). The contact-gathering hydrate particles strengthened the soil skeleton more than the coating hydrate particles by bonding the inter-granular contacts.

6. Effects of hydrate growth patterns and bonding strength in the cementation model



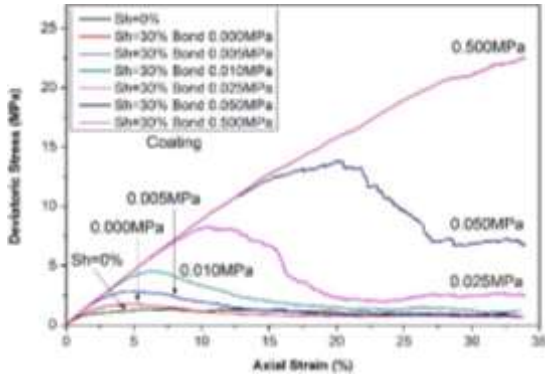
(a) Coating  $S_h=10\%$

(b) Contact-gathering  $S_h=10\%$



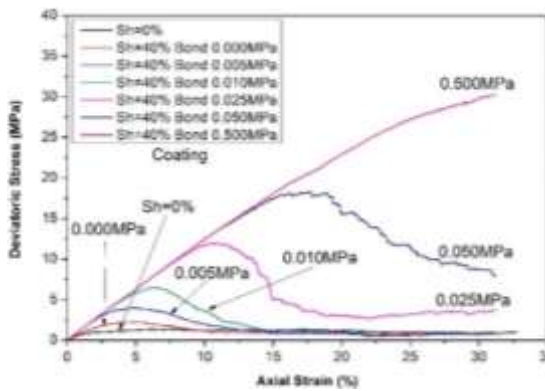
(c) Coating  $S_h=20\%$

(d) Contact-gathering  $S_h=20\%$



(e) Coating  $S_h=30\%$

(f) Contact-gathering  $S_h=30\%$



(g) Coating  $S_h=40\%$

(h) Contact-gathering  $S_h=40\%$

**Figure 6.3:** Deviatoric stress as a function of axial strain of the Coating and Contact-gathering models

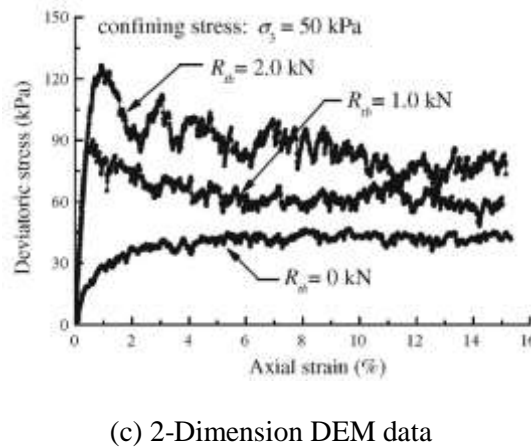
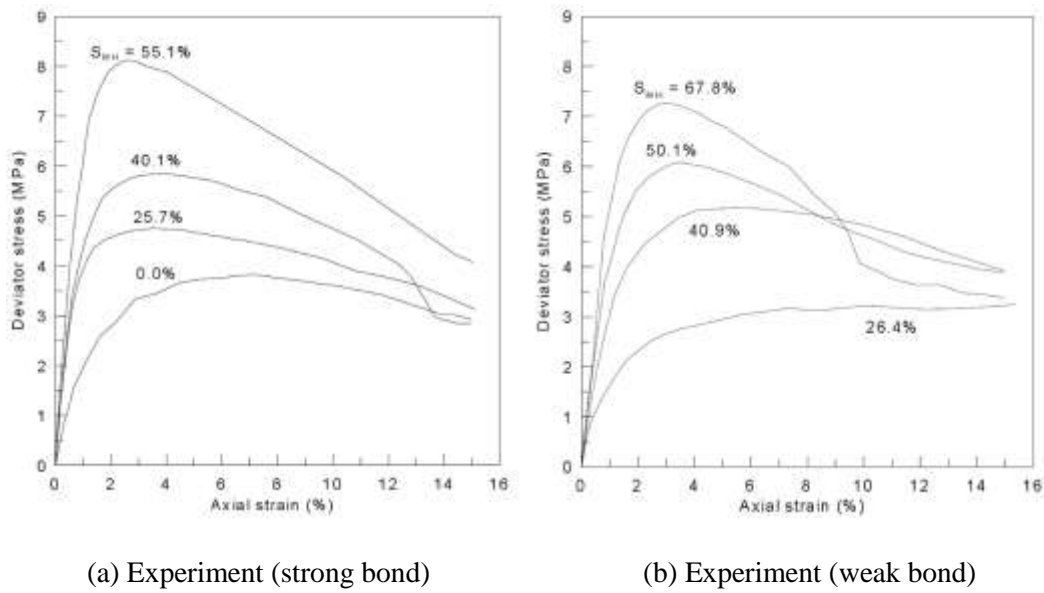


**Figure 6.4:** Deviatoric stress against axial strain at various hydrate saturation: (a) experiment strong bond samples (Masui et al., 2005); (b) experiment weak bond samples (Masui et al., 2005); (c) 2-Dimension DEM data (Jiang et al., 2013), where  $R_b$  refers to the bonding strength applied to the hydrate particles.

In addition, by increasing or decreasing the bonding strength in the DEM model, it is shown that the simulated results could be closer to the experimental data. This could also be an effective method to optimize the Discrete Element Modelling in order to obtain a proper quantitative comparison with the obtained in-situ and laboratory studies rather than the only qualitative comparison. However, this optimization should be implemented with other optimization methods, because it was also observed in Figure 6.3 that although the increase in the strength by the increased bonding strength was obvious, the bonding strength increase did not increase the initial stiffness which is also an essential issue of the limitation of this DEM study.

### **6.2.2 Strength**

As for both coating and contact-gathering models, it can be seen clearly in Figure 6.5 (a) that the peak strength  $q'_{(\max)}$  (maximum deviatoric stress) steadily increased with the higher hydrate saturation at a given bonding strength. The difference in the rate of increase depended on both the hydrate growth pattern and the bonding strength.

Firstly, at the same hydrate saturation, the magnitude of the increase in  $q'_{(\max)}$  of the contact-gathering model was always larger than that of the coating model. It is found in the following three points:

(1) At the low hydrate saturation (from  $S_h=0\%$  to 10%), the rate of the increase in  $q'_{(\max)}$  of the contact-gathering model was higher than that of the coating model.

(2) But at the low bonding strength of 0.005 MPa ~ 0.025 MPa, the rates of both models were relatively similar when the saturation increased from 10% to 40%.

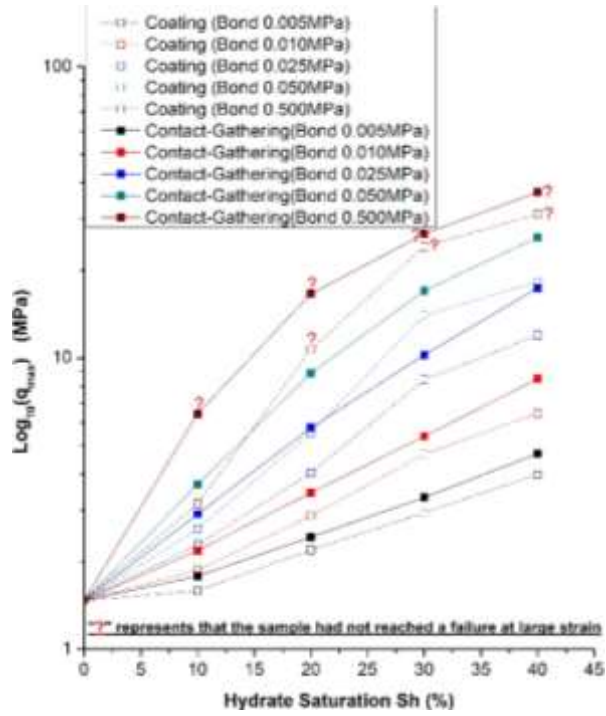
(3) Moreover, at the higher bonding strength of 0.050 ~ 0.500 MPa, the rate of the coating model was obviously larger than that of the contact-gathering model when the saturation increased from 10% to 30%, and then became smaller instead when the saturation increased from 30% to 40%.

In the contact-gathering model, hydrates formed at the soil-soil particles' contacts with a set bonding strength, and contributed to the increase in strength. However, the hydrate particles along the soil surface of coating model did not make as much contribution as the contact-gathering model, because the bonded hydrate particles at the soil-soil contact strengthened the skeleton of the sample. This is why at the same hydrate saturation, the strength of the contact-gathering model was higher than that of the coating model.

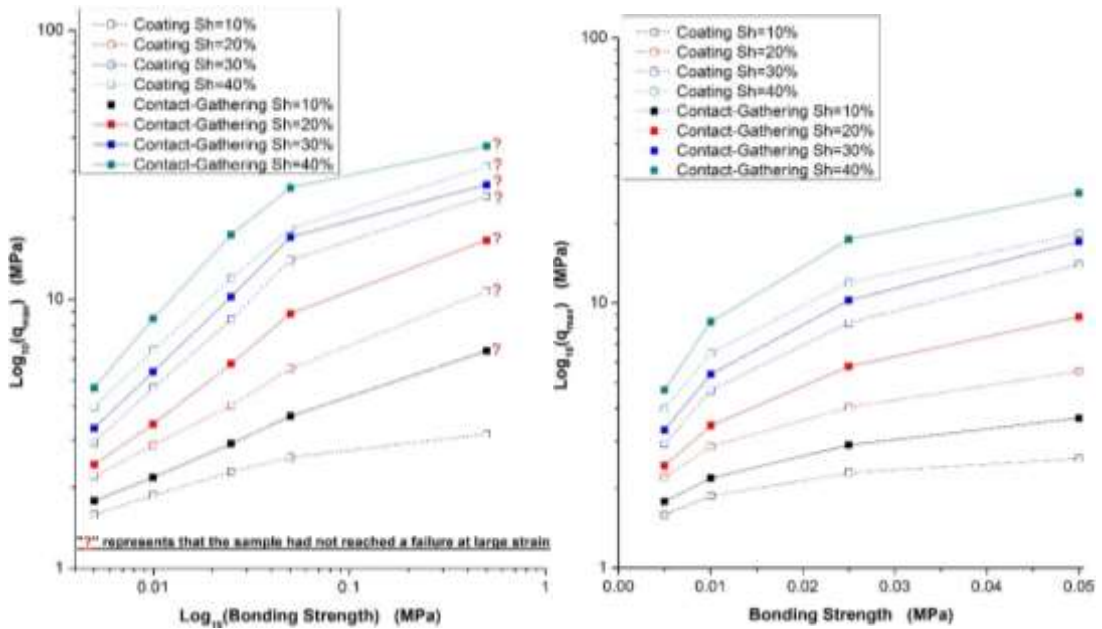
It is also necessary to note that, when the bonding strength was set 0.500 MPa, the samples had not reached a failure at the large axial strain, as shown in Figure 6.3. Hence, in Figure 6.5, at the bonding strength of 0.500 MPa, the peak strength was

6. Effects of hydrate growth patterns and bonding strength in the cementation model

marked “?” because the value was chosen at the axial strain of 30%, which was not the failure strength.



(a) Peak strength against hydrate saturation



(b) Peak strength against bonding strength ① (c) Peak strength against bonding strength ②

Figure 6.5: Peak deviatoric strength of the Coating and Contact-gathering models at various bonding strength at  $S_h = 10\% \sim 40\%$

In addition, it is also shown in Figure 6.5 (b) that, at the same hydrate saturation, the increased bonding strength enhanced the maximum deviatoric stress in both models. At the same saturation, the increase rate of the peak strength became much more obvious when the bonding strength was larger. For example, at  $S_h=40\%$ , the increase of the peak strength in both models reached around 10 times that of the original value when the bonding strength increased from 0.005 MPa to 0.500 MPa. Contributing to this was both the bonding strength and the large number of bonding contacts at a high hydrate saturation.

Despite the results at the bonding strength of 0.500 MPa, which were not the real failure strength, the increased curves of all the models in Figure 6.5 (b) showed a linear relationship on the  $\log(q_{max}) - \log(\text{bonding strength})$  space. The relationship may be defined as  $\log_{10}(q_{max}) = K \log_{10}(B_n)$ , where  $K$  is the linear coefficient, and  $B_n$  refers to the bonding strength. Hence, the Figure 6.5 (c) is plotted accordingly.

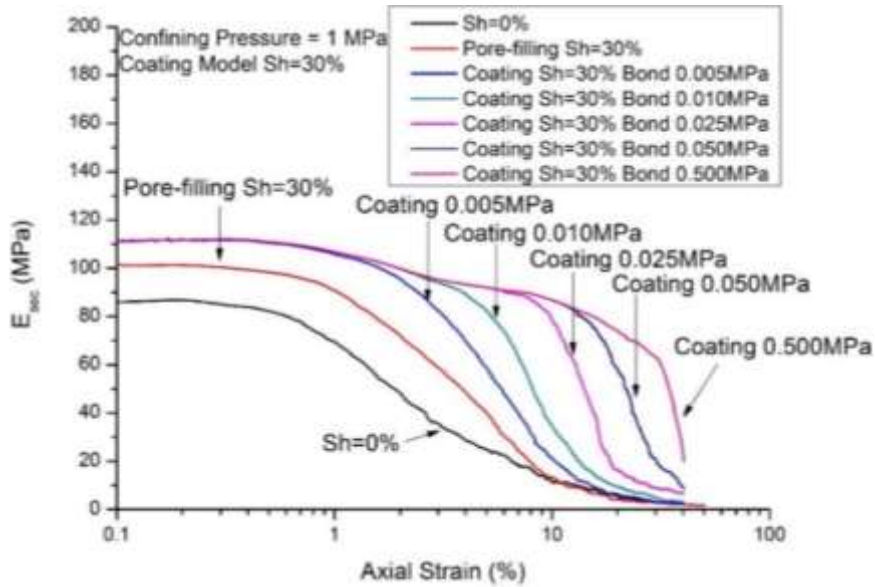
### 6.2.3 Stiffness

Figure 6.6 shows the stiffness  $E_{sec}$  degradation curves against axial strain of the coating and contact-gathering models at  $S_h=30\%$  with various bonding strengths. Firstly, as discussed in Chapter 4, the stiffness increased with hydrate saturation. In Figure 6.6, it can be seen that the stiffness of the hydrate-bearing soil sample ( $S_h=30\%$ ) was larger than that of the pure soil sample ( $S_h=0\%$ ). Secondly, the bonded hydrates exhibited greater effect on stiffness than the pore-filling case, as shown in Figure 6.6(a) and Figure 6.6(b). At the same hydrate saturation of 30%, the initial stiffness of both the coating and contact-gathering models was larger than that of the pore-filling model.

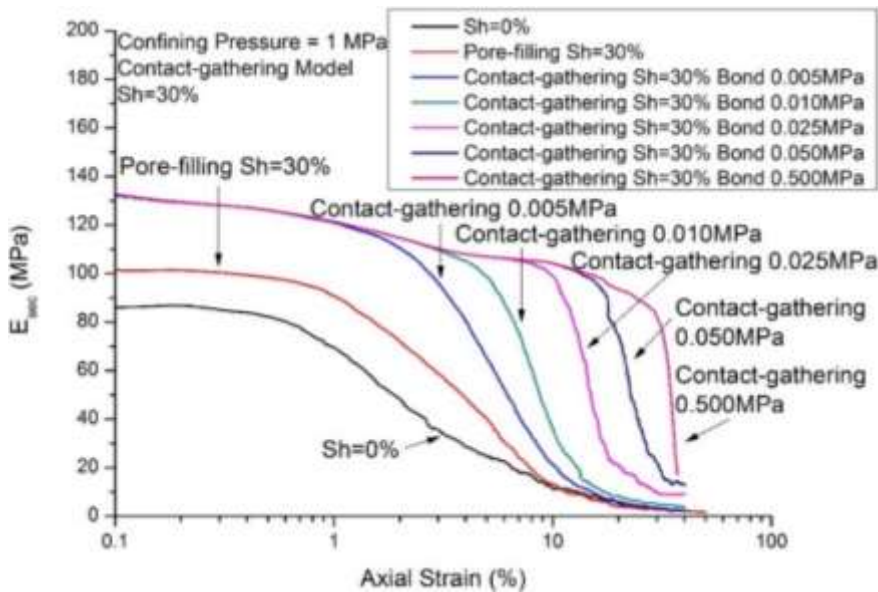
Thirdly, the initial stiffness of the contact-gathering model was larger than that of the coating model. This is due to the large number of bonded hydrate particles gathering at the soil-soil contacts strengthening the skeleton more effectively than the coating hydrate particles on the soil surface.

However, the increase in bonding strength from 0.005 MPa to 0.500 MPa did not increase the initial stiffness of the sample. This was because the initial skeleton played

the essential role at the beginning of the triaxial tests. The assemblies with different bonding strength are exactly the same in terms of hydrate distribution and the locations of the bonding. And so they are exactly the same before bond breakage regardless of bonding strength.



(a) Coating  $S_h=30\%$



(b) Contact-gathering  $S_h=30\%$

**Figure 6.6:** Stiffness  $E_{sec}$  degradation curves against axial strain (Coating and Contact-gathering models at  $S_h=30\%$ )

But as the shearing continued, the increased bonding strength started to work on the strength of the sample. The values of the stiffness with different bonding strength

started to deviate; and the higher the bonding strength is, the later the evident stiffness degradation began.

### **6.2.4 Volumetric responses**

Regarding the volumetric responses of the coating and contact-gathering patterns, the volumetric strain against axial strain was plotted in Figure 6.7. In Figure 6.7(a) and Figure 6.7(b), at the hydrate saturation of 10%, a high bonding strength caused a larger dilation at large axial strains. The dilation of the coating pattern was smaller than that of the contact-gathering pattern.

The above observations in this 3-Dimension DEM study were similar to and at the same time different from the 2-Dimension DEM study by Jiang et al. (2013), as shown in Figure 6.8. From the planar void ratio responses, it can be seen that, in this case, the dilation only happened when there was a bonding strength of the hydrate particles, while in this PhD research, the dilation also happened when there was no bonding strength. However, the similarity between these two DEM studies was that the dilation was enhanced by the increased in the bonding strength.

As shown in Figure 6.7(c) (d) (e) (f) (g) (h), as hydrate saturation increased, the dilation was enhanced in both hydrate growth patterns. And at a low bonding strength, the increased bonding strength enhanced the dilation. However, at a high bonding strength, 0.500 MPa, 0.050 MPa and even 0.025 MPa, the samples exhibited a lower dilation than the samples with a low bonding strength, and the rate of the dilatancy was also lower.

But in the contact-gathering samples at  $S_h=30\%$  and  $40\%$  in Figure 6.7(f) and (h), the rate of the dilatancy at a higher bonding strength exhibited larger although the dilation started later than a lower bonding strength sample. This also means the increased bonding strength had a clear delayed effect on the dilation, in which the delay was caused by the delay of bond breakage which is discussed in Section 6.3 in this Chapter.

6. Effects of hydrate growth patterns and bonding strength in the cementation model

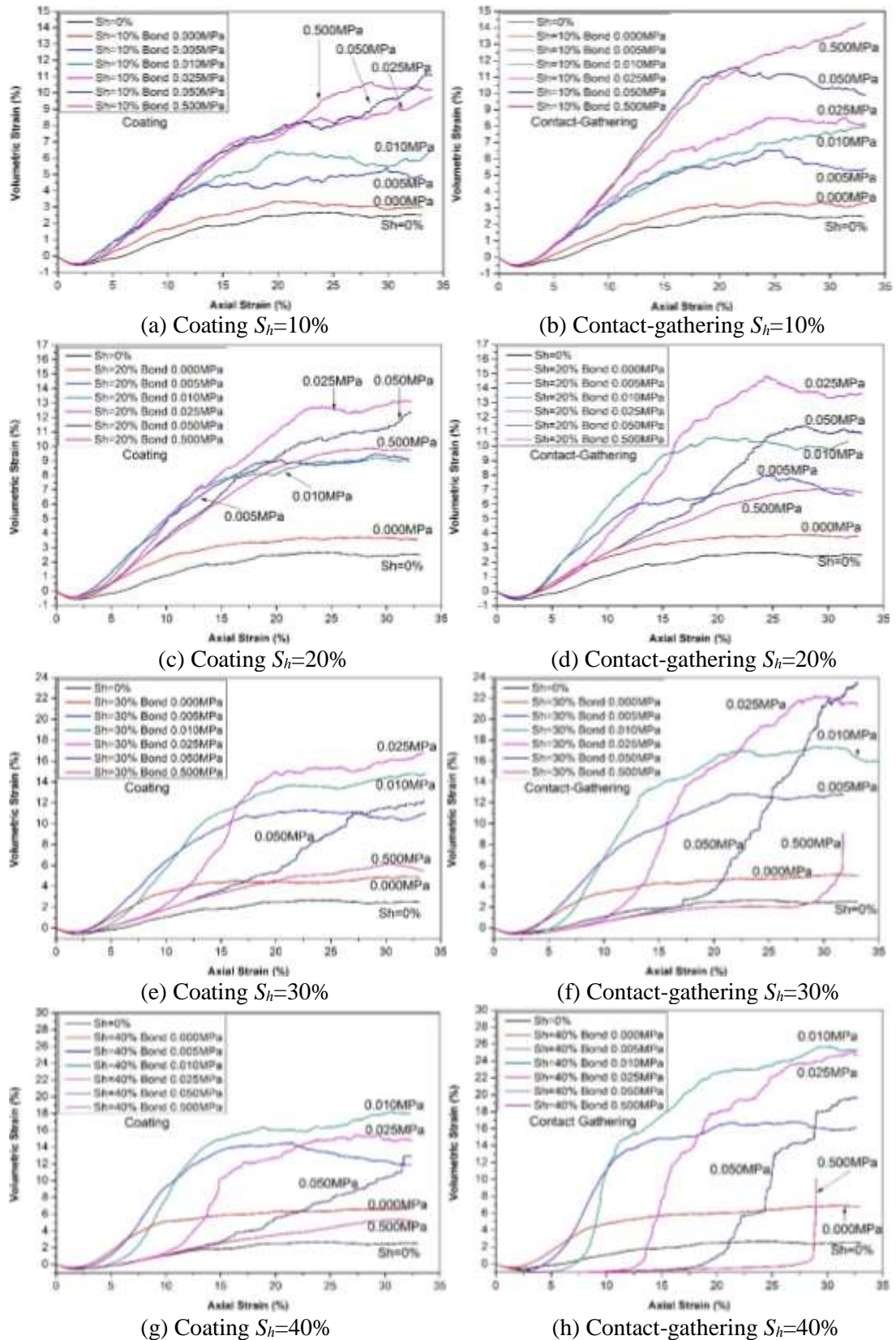
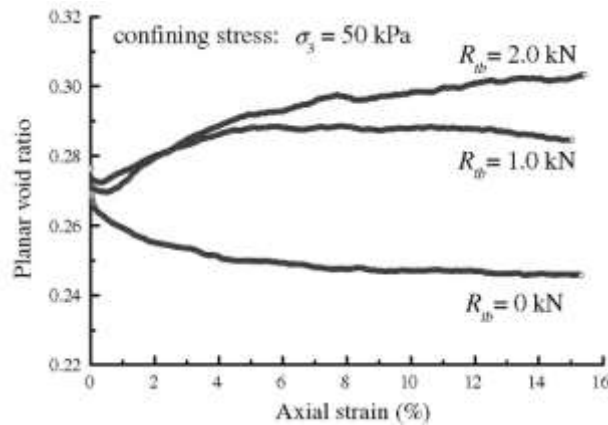


Figure 6.7: Volumetric strain as a function of axial strain of the Coating and Contact-gathering models ( $S_h=10\% \sim 40\%$ )



**Figure 6.8:** Volumetric responses from the biaxial test under various bonding strength (Jiang et al., 2013), where  $R_{ib}$  refers to the bonding strength applied to the hydrate particles.

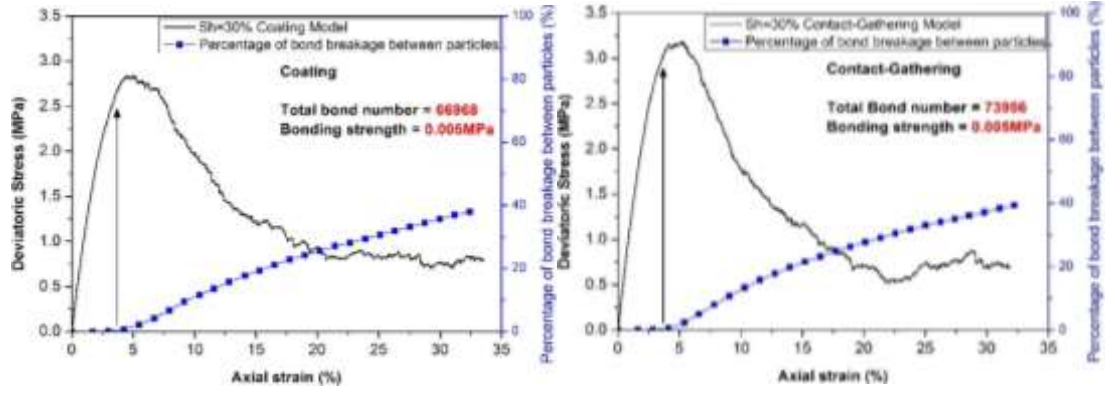
When the bonding strength is very large, grains could not move and the deformation was controlled by the elastic deformation of the particles themselves. However, when the grains do start to move relative to each other, and as the bonds were broken, dilation started to occur and big clusters of bonded particles caused larger dilation, especially using the contact-gathering pattern. It appears that hydrate particles gathered at the grain contacts tend to form big hydrate clusters, which in turn gives more dilation.

## 6.3 Bond breakage between particles during the tests

### 6.3.1 Bond breakage

Figure 6.9 plotted the percentage of bond breakage of all bonded particles against the axial strain during the triaxial tests of  $S_h=30\%$  for both the coating (Figure 6.9(a)(c)(e)) and the contact-gathering (Figure 6.9(b)(d)(f)) models at various bonding strength. With the same number of hydrate particles, the number of the bonding contacts in the contact-gathering model was slightly larger than that of the coating model at  $S_h=30\%$ : 73956 bonding contacts in the contact-gathering model and 66968 bonding contacts in the coating model. This also contributed to the higher strength of the contact-gathering model.

6. Effects of hydrate growth patterns and bonding strength in the cementation model

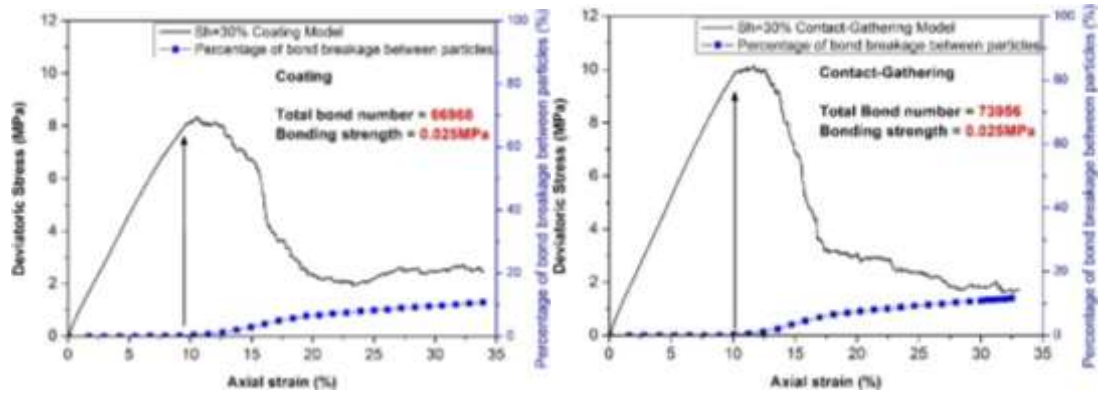


(a) Coating

Bonding strength 0.005MPa

(b) Contact-gathering

Bonding strength 0.005MPa

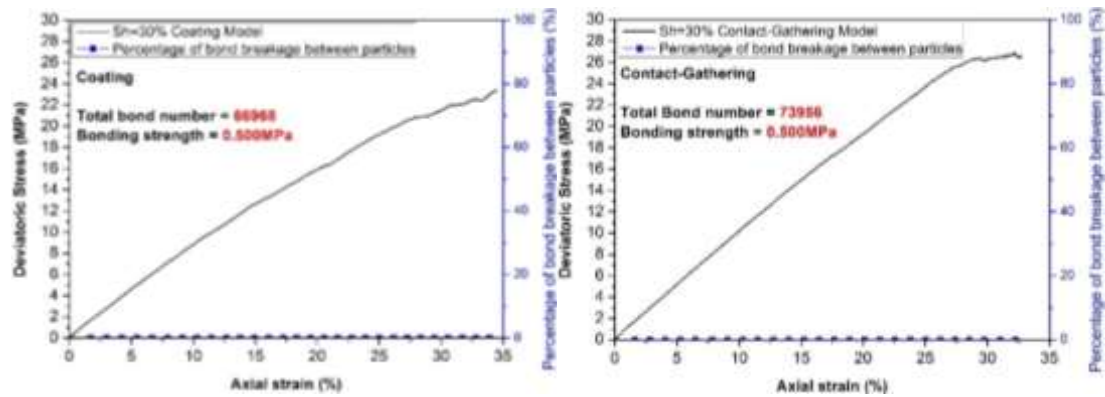


(c) Coating

Bonding strength 0.025MPa

(d) Contact-gathering

Bonding strength 0.025MPa



(e) Coating

Bonding strength 0.500MPa

(f) Contact-gathering

Bonding strength 0.500MPa

Figure 6.9: Bond breakage between particles during the triaxial tests of  $S_h=30\%$  Coating and Contact-gathering models at various bonding strength

When the bonding strength was set to 0.005 MPa, as shown in Figure 6.9(a) and Figure 6.9(b), the evident bond breakage began to happen just after the elastic phase and before the peak strength at around 4% axial strain, and the percentage of bond breakage in total bonds increased faster at the beginning and slowed down at the critical state. The higher rate corresponded to the significant decrease in the secant stiffness  $E_{sec}$  (Figure 6.6), whereas the slower rate was seen when the critical state was reached. As discussed in the Section 4.4 of Chapter 4, this means there began to be a number of unbound hydrate particles in the pores, at the soil-soil contacts or in the soil skeleton due to the movement of these hydrate particles after the bond breakage. At the large strain of 33%, the percentage of bond breakage in total bonds of both models reached about 40%.

However, in Figure 6.9(c) and Figure 6.9(d), when the bonding strength increased to 0.025 MPa, the evident bond breakage was delayed to 10% axial strain, so as the peak failure. At the large strain of 33%, the percentage of bond breakage in total bonds of both models only reached about 10% which was significantly lower than 40% for 0.005 MPa bonding strength. In addition, when the bonding strength was set to 0.500 MPa, as shown in Figure 6.9(e) and Figure 6.9(f), a large axial strain of 33% was not enough to break any bond, so there was no observed failure. This implied that the beginning of evident bond breakage is closely related to the beginning of the failure of these hydrates bonded samples. Peak strength failure only occurred if bond strength was weak enough to start breaking. If breakage was delayed, failure also delayed to higher axial strain.

In order to investigate this further, Figure 6.10 plotted the axial strain at the beginning of the evident bond breakage (0.5% of the total bonding contacts) against bonding strength. It is that as the bonding strength increased, a larger axial strain was needed to make an evident bond breakage happen inside the sample. In addition, at the same hydrate saturation and bonding strength, the axial strain at the beginning of the evident bond breakage of the contact-gathering model was slightly larger than that of the coating model.

In Figure 6.9, it can already be seen that there was no obvious bond breakage happening even at the large axial strain at the bonding strength of 0.500 MPa.

Therefore, at the bonding strength of 0.500 MPa in Figure 6.10, the axial strain at the beginning of obvious bond breakage was only marked “?”. Hence, it can be suggested that, in the numerical simulations of hydrate-bearing sediments or other materials with bonding contacts, the choice of bonding strength should be considered very carefully, as it is related closely to the macroscopic behaviours, such as strength and stiffness.

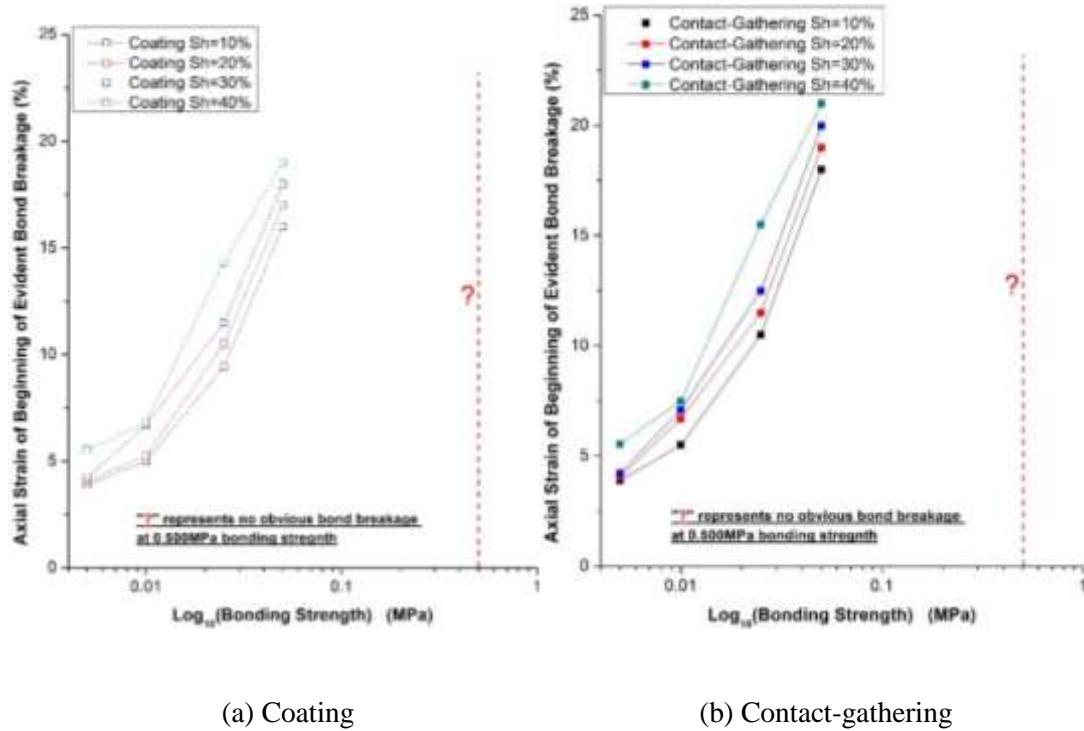


**Figure 6.10:** Axial strain at the beginning of obvious bond breakage (0.5% of total bonding contacts) at various bonding strength

### 6.3.2 Particle-scale mechanism analysis

A brief particle-scale mechanism analysis was made to interpret the obtained data on the strength, stiffness, volumetric responses, as well as the bond breakage discussed in this chapter, as shown in Figure 6.11.

In the pore-filling model, when shearing started, the main skeleton of the sample was still the soil-soil matrix, and the hydrate particles were inside the pore space, as shown in Figure 6.11(a), which has already been discussed in Chapter 4.

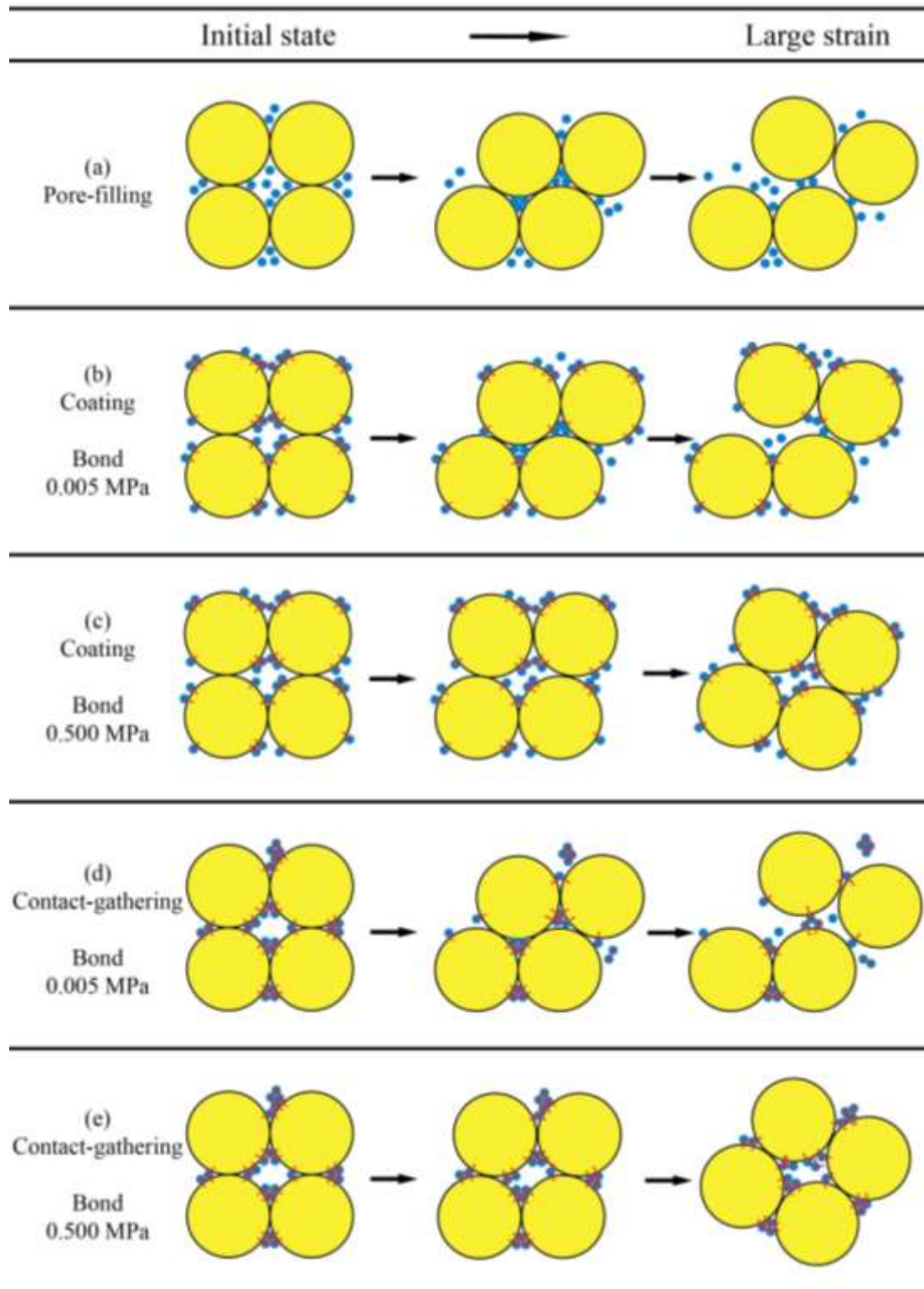


**Figure 6.11:** Sketch diagram of the particle-scale mechanisms of particle movements in the deformation process of the coating, contact-gathering and pore-filling models

However, in the coating model, hydrate particles grew along the soil surface to form a hydrate-coating model based on the consolidated soil skeleton. As illustrated in Figure 6.11(b), when the shearing began, the hydrate particles with the bonding strength of 0.005 MPa, which were close to the soil-soil contacts, started to support the skeleton. And at the large strain, more hydrate particles on the soil surface would be involved in the matrix of the skeleton and move to the pore space during the deformation process. However, in Figure 6.11(c), when the bonding strength increased to 0.500 MPa, no evident bond breakage occurred in the deformation process, whereas the strong bonding strength restrained the particles' movement. And in the large axial strain of the deformation process, the big clusters bonded by soil and hydrate particles with the strong bonding strength began to rotate, hence causing the dilation.

In the contact-gathering model, because of the accumulated force chains by the hydrate-hydrate contacts at the soil-soil contacts during the deformation process illustrated in Figure 6.11 (d) and (e), the large number of hydrate particles at the soil-soil contacts in the contact-gathering model made it stiffer than the coating model. In Figure 6.11 (d), at the bonding strength of 0.005 MPa, the hydrate particles gathered at the soil-soil contacts. The deformation process induced the bond breakage, in which some clusters of bonded hydrate particles moved to the pore space or even started to support the sample's skeleton. But in Figure 6.11 (e), when the bonding strength increased to 0.500 MPa, no evident bond breakage occurred, and the strong bonding strength restrained the particles' movement. And in the large, the big clusters began to rotate, hence causing the dilation.

### **6.4 Particle-particle contact force contribution and effect of hydrate/soil contact stiffness ratio**

#### **6.4.1 Particle-particle contact force contribution to the total deviatoric stress**

Figure 6.12 shows the different components of the deviatoric stress in the triaxial tests of both the coating and contact-gathering models at  $S_h=30\%$ , at various bonding strengths. Figure 6.12 (a) (c) (e) show the coating model at the bonding strength 0.005

6. Effects of hydrate growth patterns and bonding strength in the cementation model

MPa, 0.025 MPa and 0.500 MPa respectively, and Figure 6.12 (b) (d) (f) show the contact-gathering model at the bonding strength 0.005 MPa, 0.025 MPa and 0.500 MPa respectively.

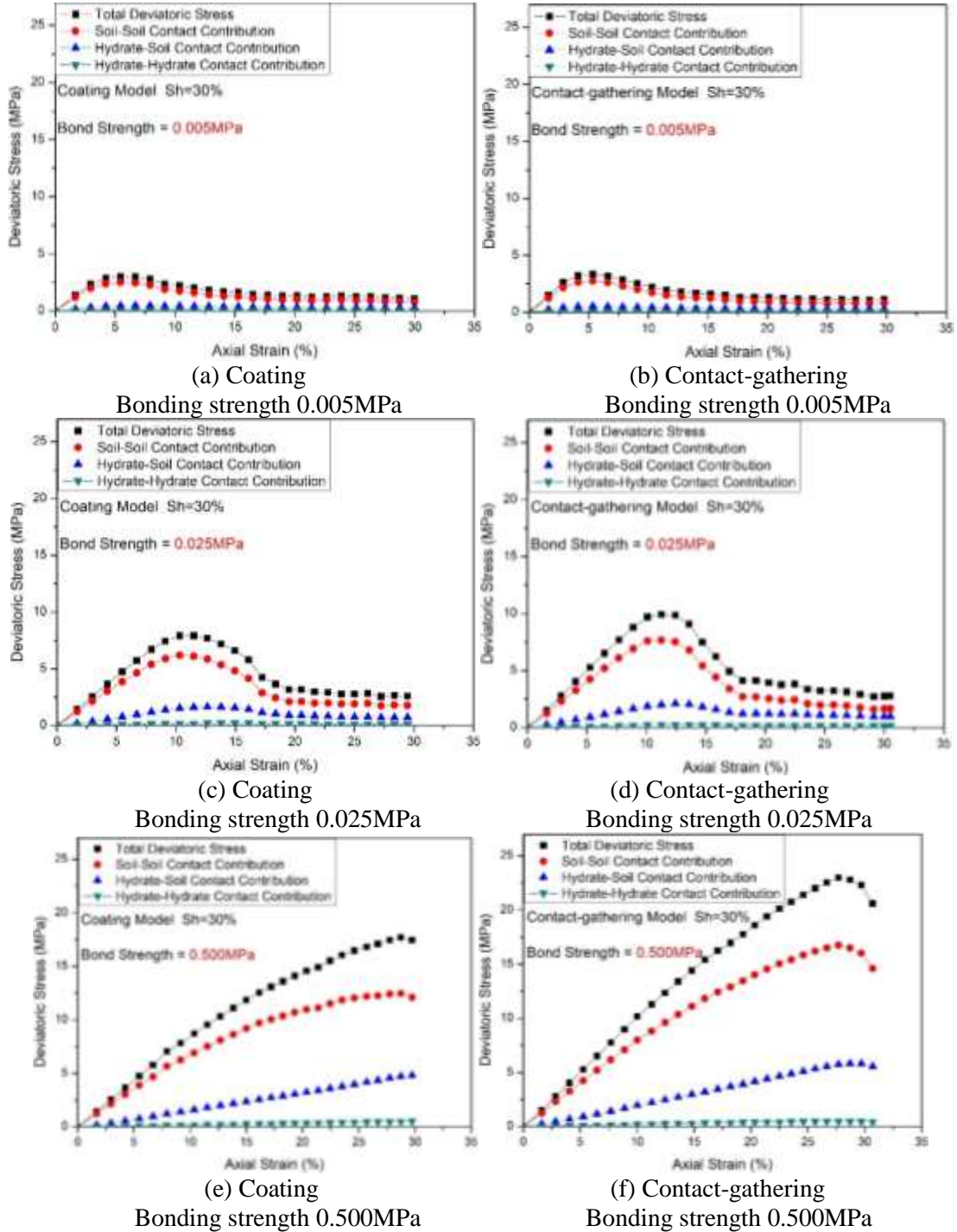


**Figure 6.12:** Particles' contacts contribution to the deviatoric stress in the triaxial tests with various bonding strength (Coating and Contact-gathering model at  $S_h=30\%$ )

Firstly, it can be seen that as the bonding strength increased, the increase in the deviatoric stress was mainly affected by the soil particles' contact forces. The particles' contact force contribution increased with the bonding strength for all the particles' contact types: soil-soil, soil-hydrate and hydrate-hydrate. As discussed in Chapter 4, the main skeleton of the hydrate-bearing sample was built by the soil-soil contacts. And as all the particles' contacts were bonded, a larger stress was needed to break the bonded contacts and to deform the sample during the triaxial tests. When the bonding strength increased, all the contacts between particles were strengthened. Due to this, all the particles' contact forces increased and contributed a larger value to the total deviatoric stress.

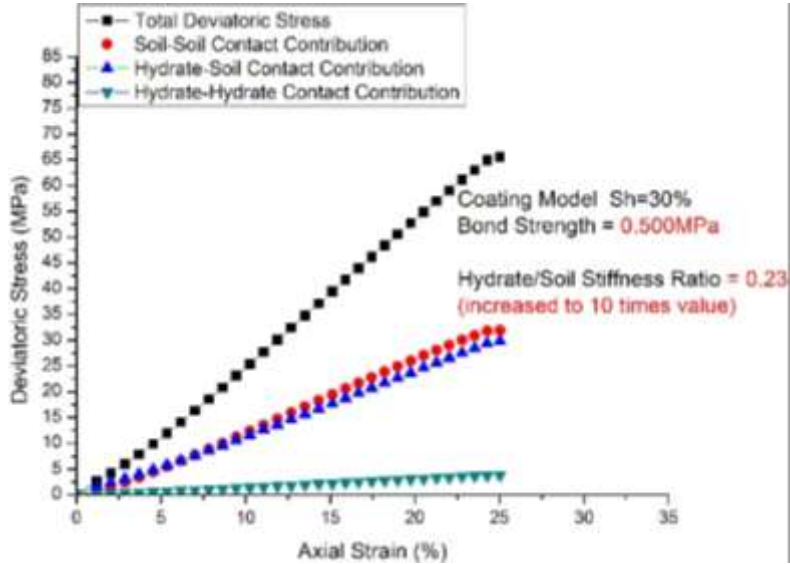
### 6.4.2 Effect of hydrate/soil contact stiffness ratio

It can also be noted that the main contact force contribution was from the soil-soil contacts, and the second was from the soil-hydrate contacts, while the hydrate-hydrate contacts contributed the least to the total strength. The essential reason for this is that the stiffness of the hydrate particles was much lower than that of the soil particles. As mentioned in Chapter 3, the hydrate/soil stiffness ratio  $k_n^{hyd} / k_n^{soil} (D_{50})$  was only 0.023 due to the hydrate/soil particle size ratio and the hydrate/soil elastic modulus ratio  $E_c^{hyd} / E_c^{soil}$ , according to  $k_n = 2DE_c$  (Equation 3.1 in Chapter 3).

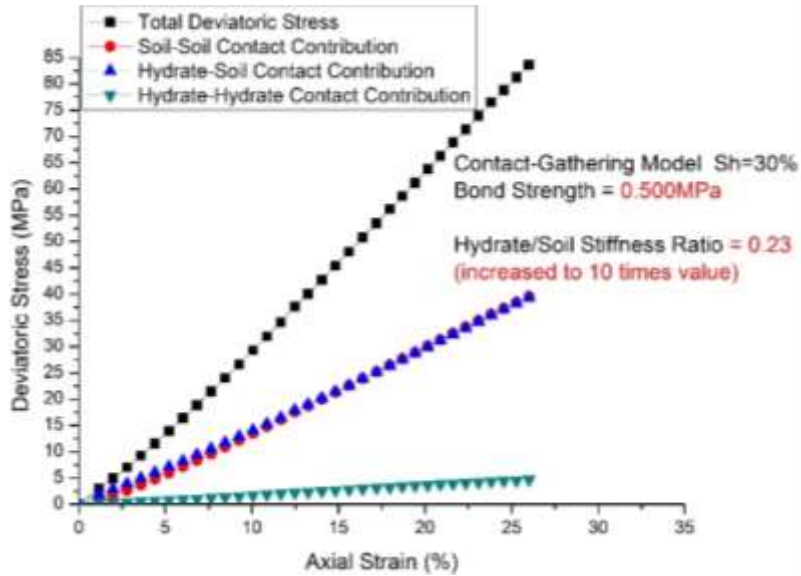
If the stiffness of hydrate particles increased, there might be an increase of the contact force contribution of hydrate particles' contacts. Hence, there was a series of trial simulations conducted on the effect of hydrate/soil stiffness ratio.

Figure 6.13 shows the particles' contact contribution to the deviatoric stress in the triaxial tests of both the coating and contact-gathering models at  $S_h=30\%$  and with the high hydrate/soil stiffness ratio of 0.23 at the bonding strength of 0.500 MPa. The hydrate/soil stiffness ratio  $k_n^{hyd} / k_n^{soil} (D_{50})$  value 0.23 was 10 times of the chosen ratio normally presented throughout this PhD research, which is when the hydrate/soil elastic modulus ratio  $E_c^{hyd} / E_c^{soil}$  was set to 1.0. Compared to Figure 6.12 (e) and (f), it is clearly shown in Figure 6.13 that the increase in the stiffness of hydrate increased

both the total strength and the deviatoric stress contribution of hydrate-soil contacts and hydrate-hydrate contacts. Also, the hydrate-soil contact stress contribution to the total deviatoric stress was very close to the soil-soil contact contribution.



(a) Coating



(b) Contact-gathering

**Figure 6.13:** Particles' contacts contribution to the deviatoric stress in the triaxial tests with the hydrate/soil stiffness ratio of 0.23 at the bonding strength of 0.500 MPa (Coating and Contact-gathering model at  $S_h=30\%$ )

From the simulation results in Figure 6.13, it can be explained why in our previous simulations the hydrate-soil and hydrate-hydrate contacts could not become

the main contact contribution to the total force, even though the number of hydrate-soil and hydrate-hydrate contacts was much larger than that of the soil-soil contacts.

As mentioned Section 2.3 of Chapter 2, Brugada et al. (2010) also explored the hydrate-soil contact stiffness  $E_c^{hyd} / E_c^{soil}$  ratio from 0.001 to 0.1 at  $S_h=20\%$  of the pore-filling model. As shown in Figure 6.14, it can be seen that hydrates only contributed to the strength when the ratio was at the value of 0.1. Regarding other ratios, the behaviours were quite similar to the pure soil sample's responses.

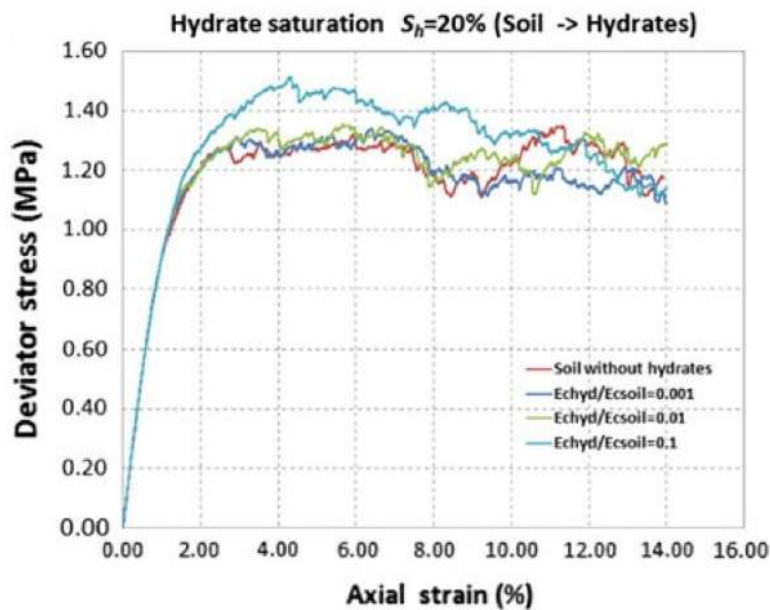


**Figure 6.14:** Triaxial compressional test result of the stress-strain responses under various hydrate-soil contact stiffness ratios (Brugada et al., 2010)

However, Soga et al. (2006) stated that the hydrate stiffness is only slightly larger than the ice stiffness, which is itself much smaller than the soil stiffness. Hence, the simulation results in this PhD research with the hydrate/soil stiffness ratio  $k_n^{hyd} / k_n^{soil} (D_{50})$  value 0.023 was reasonable.

Further research on the stiffness of the hydrates is necessary for both the experimental and the numerical studies. And the stiffness issue may greatly influence the quantitative DEM study compared with the in-situ and laboratory studies.

## 6.5 Local and global measurement

As mentioned in Section 6.2, in this chapter the measurement method of measurement spheres was used to measure the stresses and strains, which is called local measurement. However, there were another two measurement methods used in this PhD research: (1) the average contact force of particle-particle and particle-wall, which is called global measurement; (2) the wall-based logic that measured the forces on walls, which is called boundary measurement.

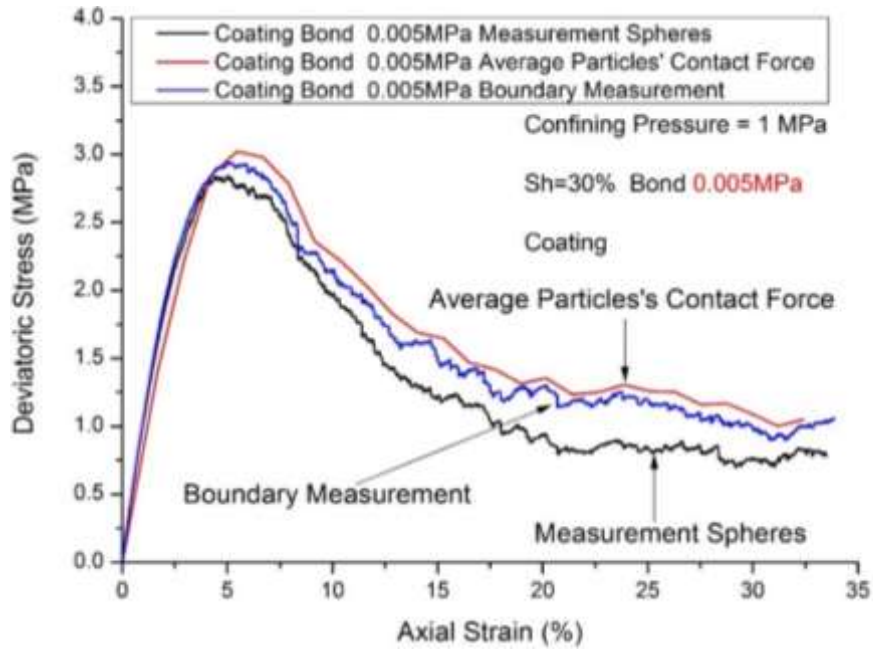
In order to compare the three measurement techniques mentioned above, comparisons were made on the stress-strain responses measured by the measurement spheres (local measurement), the average particles' contact forces (global measurement) and the wall-based logic (boundary measurement) at  $S_h=30\%$  with 0.005 MPa and 0.500 MPa bonding strength, as shown in Figure 6.15 and Figure 6.16.

At the bonding strength of 0.005 MPa in Figure 6.15, the stresses measured by the three measurement methods were quite close. But the measured stresses by the measurement spheres in both coating and contact-gathering models were smaller than those by the average particles' contact forces and the boundary measurement.

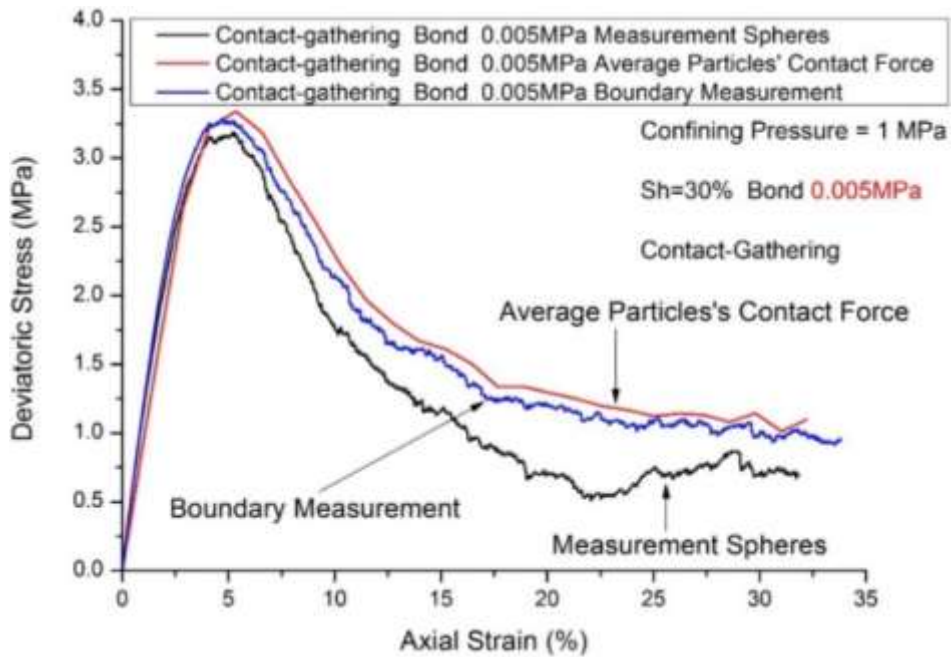
However, when the bonding strength was increased to 0.500 MPa in Figure 6.16, the measured stresses by the measurement spheres in both coating and contact-gathering models were larger at the large axial strain than those by the average particles' contact forces and the boundary measurement.

If the bonding strength between particles was too large, the large strain deformation might cause the lack of the ball-wall contacts, so that the average force on the walls might be smaller, as shown in Figure 6.17. Figure 6.17 can also explain why at the bonding strength of 0.500 MPa, the large axial strain of 30% was not enough to lead to failure.

In addition, it is also proved that the loading rate on the top and bottom walls in the triaxial test was chosen reasonably because the simulation results obtained by the boundary measurement and the average particles' contact force were very close.

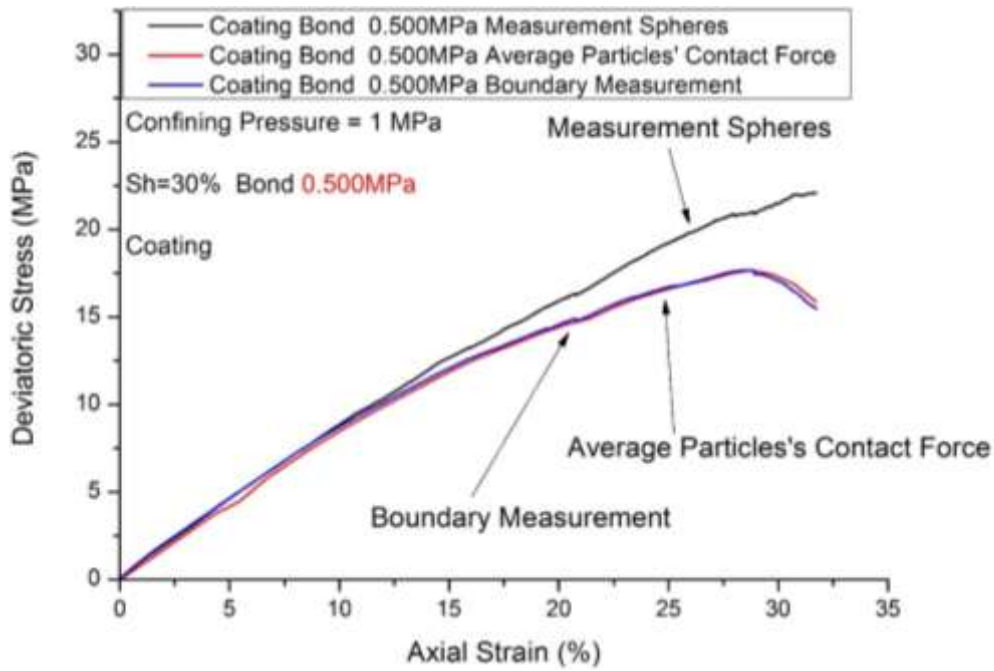


(a) Coating  $S_h=30\%$  with 0.005 MPa bonding strength

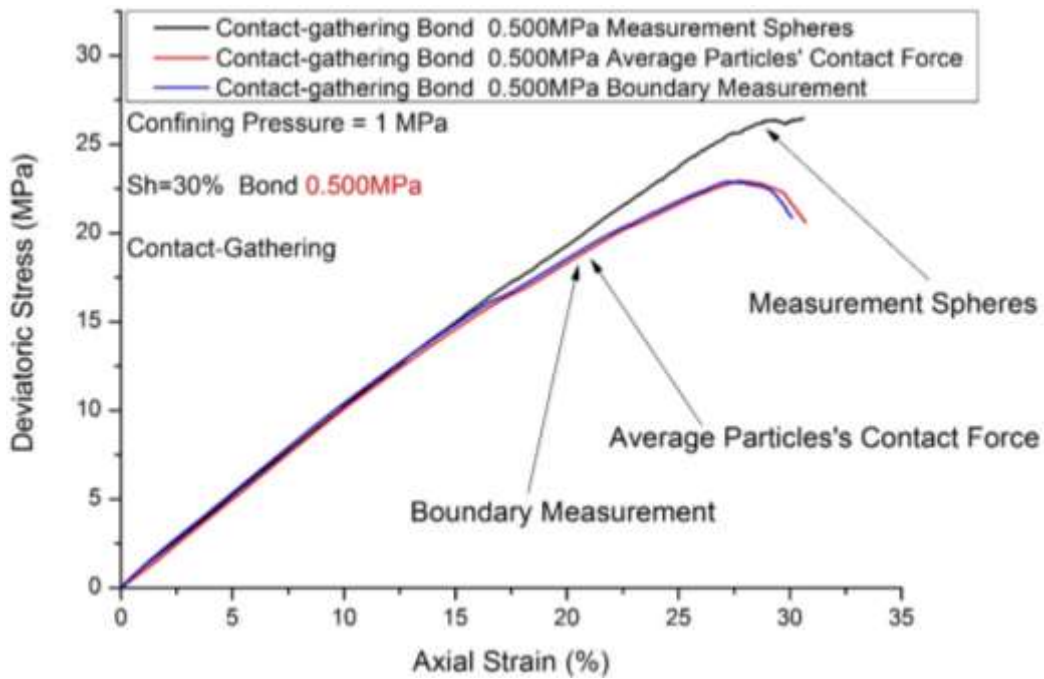


(b) Contact-gathering  $S_h=30\%$  with 0.005 MPa bonding strength

**Figure 6.15:** Stress-strain responses measured by measurement spheres (localization), average particles' contact forces (homogenization) and the wall-based logic (boundary measurement) at  $S_h=30\%$  with 0.005 MPa bonding strength



(a) Coating  $S_h=30\%$  with 0.500 MPa bonding strength



(b) Contact-gathering  $S_h=30\%$  with 0.500 MPa bonding strength

**Figure 6.16:** Stress-strain responses measured by measurement spheres (localization), average particles' contact forces (homogenization) and the wall-based logic (boundary measurement) at  $S_h=30\%$  with 0.500 MPa bonding strength

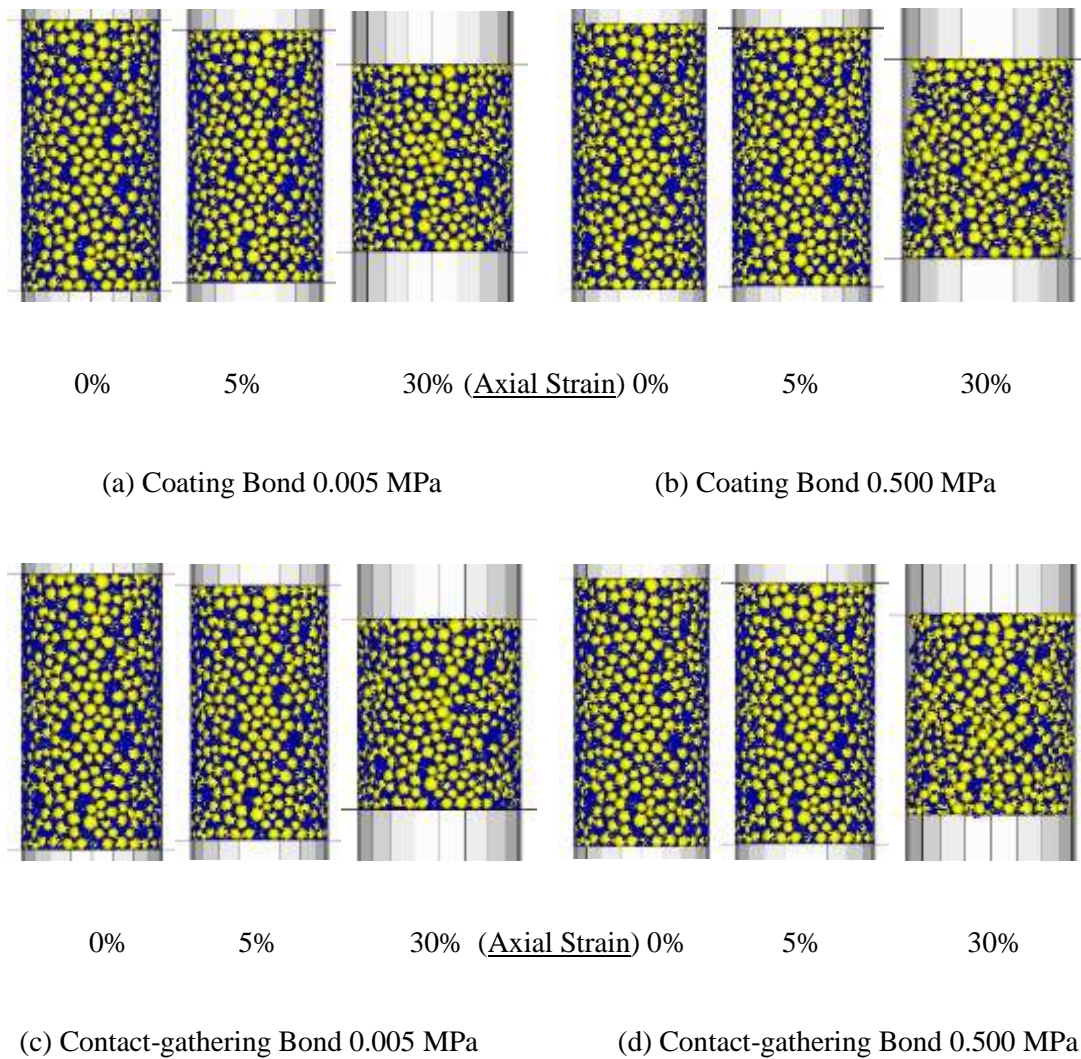


**Figure 6.17:** Coating and contact-gathering samples at the axial strains of 0%, 5% and 30% at  $S_h=30\%$  with 0.005 MPa and 0.500 MPa bonding strength

## 6.5 Summary

In the cementation model, the hydrate growth patterns governed the sediment's mechanical behaviour. The cementation hydrate particles either gathered at the soil-soil contacts or bonded to the soil surface. The location of these two different types of cementation hydrate particles influenced the mechanical behaviour differently. A comparison was conducted in order to study the effect of hydrate growth patterns in the cementation hydrate-bearing soil model.

It is found that the hydrate growth patterns in the cementation model greatly influenced the mechanical behaviour of the hydrate-bearing sediments, especially when the bonding strength and hydrate saturation were increased. For a given bonding strength and hydrate saturation, the stiffness and the strength of a sample with hydrates gathering near grain contacts was greater than that of a sample with hydrates coating around the grain surface. This is because of the larger number of contacts which are bonded in the contact-gathering case. The increased bonding strength did not increase the initial stiffness, but delayed the change of stiffness and the peak failure, which required a larger strain.

When a high bond strength was assigned, the deformation at small strains was controlled by the deformation of the particles themselves, and the dilation was therefore delayed. When grains started to move relative to each other by starting to show evident bond breakage, samples exhibited dilation. There was a greater dilation observed in the grain coating case compared with the contact gathering case. When the bonding strength was increased, the evident bond breakage was delayed as the failure was delayed, and the percentage of bond breakage in total bonds at the large strain decreased obviously. In addition, when the bonding strength was set to a very large value, there was no obvious bond breakage happening throughout the tests, with a larger axial strain perhaps being needed to reach a failure. Hence, the big bonded particle clusters at the inter-granular contacts induced a larger dilation than the surface coating hydrate particles.

The particles' contact force contribution to the total stress increased with the bonding strength for all the particles' contact types: soil-soil, soil-hydrate and hydrate-hydrate. But the main contact force contribution was always from the soil-soil contacts for the essential reason that the stiffness of the soil particles was much larger than that of the hydrate particles. When the hydrate/soil stiffness ratio was increased to 10 times the value, which means the hydrate particles became stiffer, the force contribution of hydrate particles increased dramatically. However, further research on the stiffness of the hydrates is necessary for both the experimental and numerical studies.

Comparisons were made on the stress-strain responses measured by the measurement spheres (local measurement), the average particles' contact forces

(global measurement) and the wall-based logic (boundary measurement) with both low and high bonding strength. It is also proved that the loading rate on the top and bottom walls in the triaxial test was chosen reasonably because the simulation results obtained by the boundary measurement and the average particles' contact force were very close. However, the measured stress-strain responses by the measurement spheres showed a different value at the large strain.

## Chapter 7

### Effects of elongated soil particle shape

#### 7.1 Introduction

As noted in Chapter 2, in most of the previous DEM studies on methane hydrate soil sediments (i.e. Brugada et al. 2010; Jung et al. 2012; Jiang et al. 2013), DEM was only applied with the assumption that all the soil and hydrate particles were spherical. However, the actual shapes of the natural soil particles are much more complex and could govern the sediment's geomechanical behaviour. Thus, this study will investigate the shape effect of elongated soil particles on the stress-strain and volumetric responses. The soil particles were generated separately using three models: spherical particles and elongated clumps with two different aspect ratios, as shown in Figure 7.1.

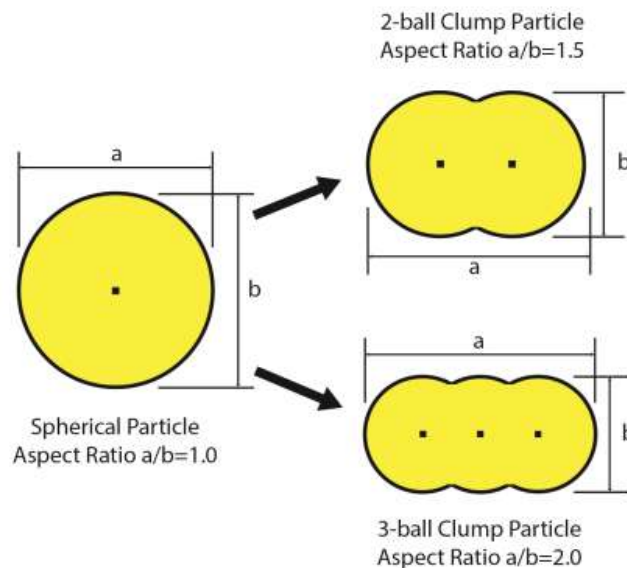


**Figure 7.1:** Replacement of spherical soil particles by elongated clumps.

The sample preparation method has been discussed in Chapter 3. To make the DEM samples using the elongated soil particles, soil samples with spherical particles

were first generated and consolidated under the given confining pressure. Elongated soil particles were prepared by replacing spherical soil particles by elongated clump particles of the same volume as the replaced spherical particles, in the consolidated DEM spherical soil samples under the controlled confining pressure. This will ensure the total solid volume was not changed. The particle replacement process could not be finished simultaneously, because that will totally change the original fabric. Hence, it was performed by replacing one after another with a time interval for each replace in order that the induced particles' overlap was reduced. This is a trial and error process.

As shown in Figure 7.1, two aspect ratios were chosen for the elongated particles: 1.5 (2-ball clump) and 2.0 (3-ball clump). These were used in order to investigate the influence of soil particle shape on the geomechanical behaviour of hydrate-bearing sediments. Three soil models of different aspect ratios were generated by the same grain size distribution and inter-particle friction. A series of DEM drained triaxial compression tests were conducted to make a comparison between how pore-filling and cementation models interacted with both spherical and elongated soil particles.

## **7.2 Simulation results and analysis**

### **7.2.1 Stress-strain responses**

Under a confining pressure of 1 MPa, the stress-strain relationships of the three different soil particle shape samples are illustrated in Figure 7.2, when there was no hydrate. Three different samples are shown at  $S_h = 0\%$ : sphere soil particles (aspect ratio = 1.0), 2-ball clump soil particles (aspect ratio = 1.5) and 3-ball clump soil particles (aspect ratio = 2.0).

It can be seen in Figure 7.2 that the elastic stiffness and the peak stress increased with the aspect ratio, and the magnitude of the increase was influenced by the aspect ratio. Peak strength increased by about 100% from the sphere soil sample to the 3-ball clump soil sample. Critical state strength increased with the increase in aspect ratio as well.

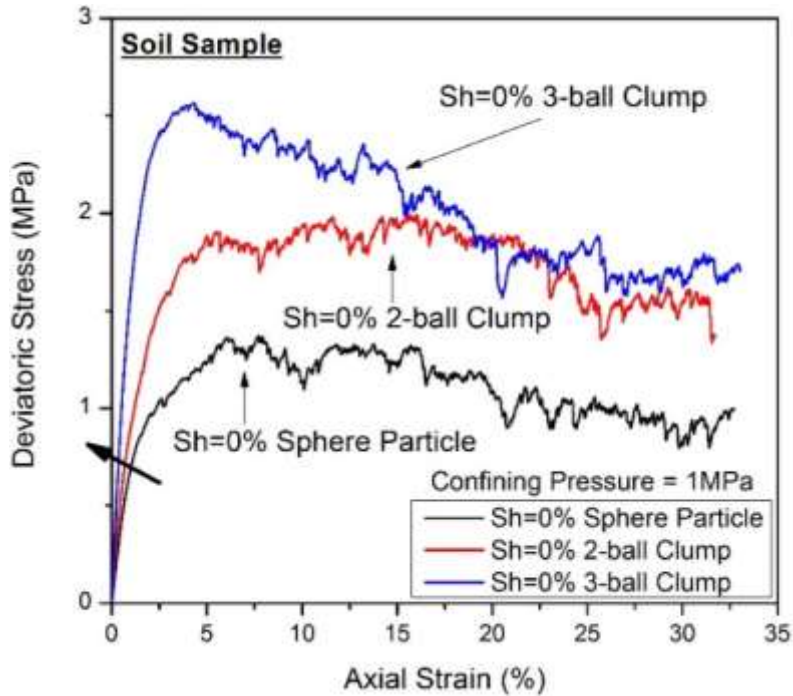


**Figure 7.2:** Comparisons of deviatoric stress as a function of axial strain of three soil models ( $S_h=0\%$ ).

As expected, in the hydrate-bearing samples, the aspect ratio of soil particles also played an important role in the strength. In both the pore-filling models and the cementation models, the elastic stiffness and the peak strength of the hydrate-bearing soil sample at  $S_h = 20\%$  and  $40\%$  increased with the increase in aspect ratio as shown in Figure 7.3. The magnitude of increase was not as evident as the no-hydrate case because hydrate particles in the pores greatly influenced the shear resistance, especially when the saturation was as high as  $40\%$ .

At the high hydrate saturation of  $40\%$ , as shown in Figure 7.3(c), the critical state strengths of the pore-filling models with elongated soil particles were similar to that of spherical soil particles. This suggests that soft hydrate particles were contributing largely to the shear resistance. In the cementation model (Figure 7.3(d)), on the other hand, the critical state strength increased with the increase in aspect ratio of the soil particles. This indicates that soil particles were still contributing to the shear resistance even when there were a large number of hydrate particles in the sample.

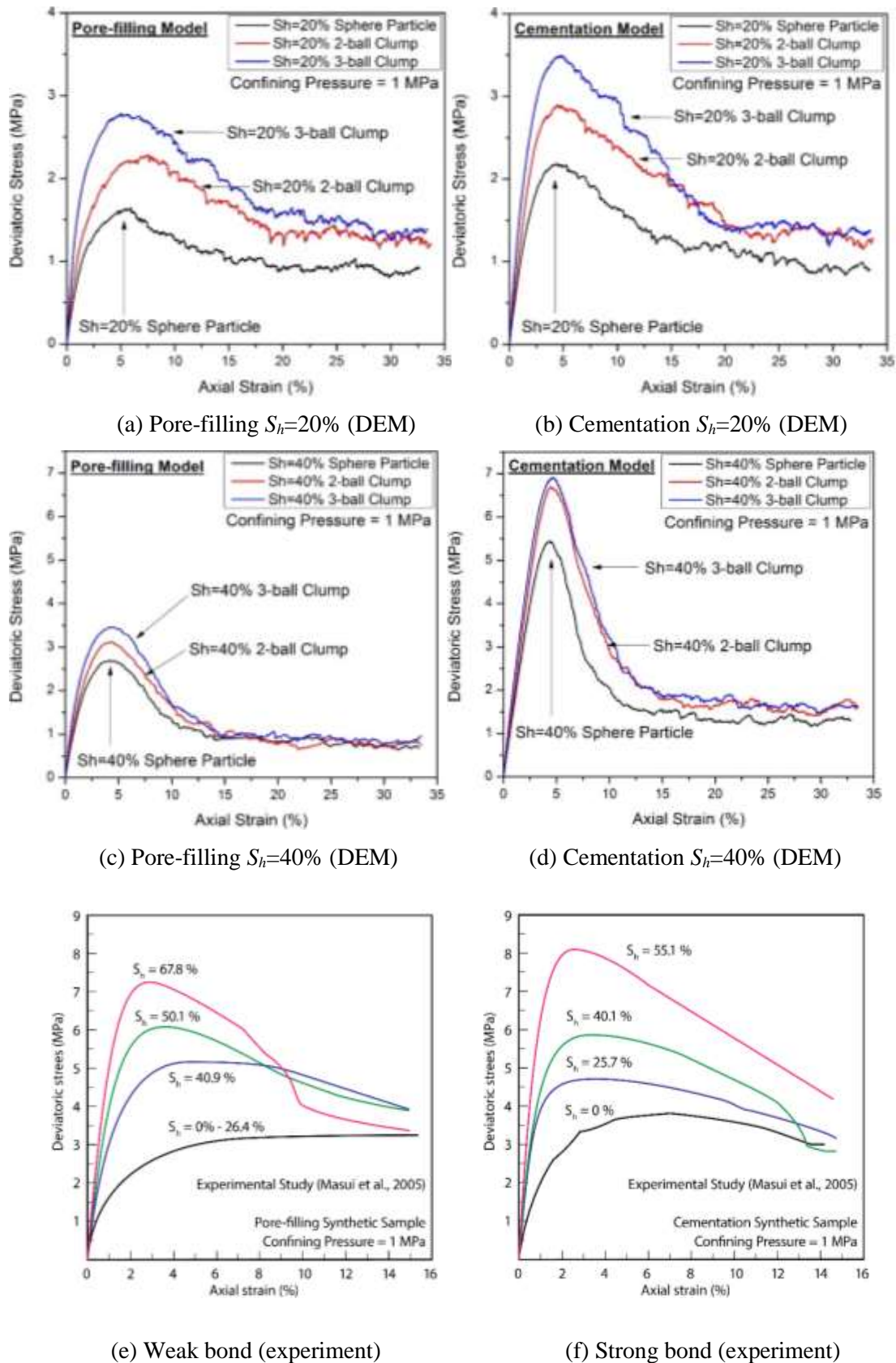


**Figure 7.3:** Comparisons of deviatoric stress as a function of axial strain: (a)-(d) of three different soil particle shapes models at  $S_h= 20\%$  and  $40\%$  with DEM; (e) experiment weak bond samples (Masui et al., 2005); (f) experiment strong bond samples (Masui et al., 2005)

Figure 7.3 (e) and (f) show the experimental data of the weak bond samples and strong bond samples at various hydrate saturation by Masui et al. (2005). Compared to the experimental data, it is suggested that as the aspect ratio of the soil particles increased, the strength value obtained from the DEM study got close to the experimental data with the natural sands, especially when comparing the DEM cementation model with the experiment strong bond model in Figure 7.3 (f). However, the DEM pore-filling samples' data were still not close to the data in Figure 7.3 (e) because the experimental sample was only assumed to be pore-filling sample but actually there was still weak bond of the hydrates. Hence, as discussed in Chapter 6, bonding strength effect should be considered carefully in the research of hydrate-bearing sediments.

### 7.2.2 Stiffness

Figure 7.4 illustrates the degradation of the secant Young's modulus  $E_{sec}$  of the three different soil particle shape samples when there was no hydrate. The stiffness increased with the increase in aspect ratio. The initial stiffness increased dramatically from about 88 MPa in the sphere soil sample to about 200 MPa in the 3-ball clump soil sample, which is getting closer to that of the natural soil sediments under the confinement of 1 MPa.

The degradation curves of secant Young's modulus as a function of axial strain of the three soil models ( $S_h = 20\%$  and  $40\%$ ) are plotted in Figure 7.5 (a) (b) (c) (d). It is clearly suggested that: (1) stiffness increased with hydrate saturation; and (2) bonded hydrates exhibited a greater effect on stiffness.

In comparisons with Figure 7.5 (e), the elongated soil samples exhibited a closer stiffness value to that of the synthetic samples in the experimental study (Masui et al., 2005), although the DEM results were still lower than that of the experimental study for many reasons (i.e. particle stiffness, density, initial void ratio, sample size, etc.). The limitation of conducting the DEM study should be considered carefully, and how to decrease the magnitude of the value difference needs further investigation.

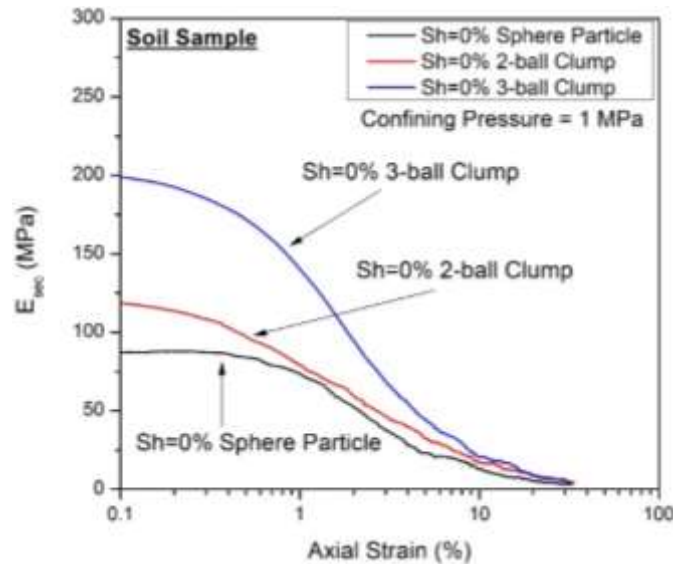


**Figure 7.4:** Degradation of secant Young's modulus as a function of axial strain of three soil models ( $S_h=0\%$ ).

However, after adding hydrate particles in the elongated soil particle samples, the extra increase in the stiffness due to the hydrate particles was not as evident as the increase because of the shape changes of soil particles. Thus, the shape of soil particles had more influence on stiffness than the hydrate saturation. The choice of 0.1% as the starting point of recording the axial strain has been mentioned in Chapter 4.

As can be seen in Figure 7.6, the mid-strain stiffness  $E_{50}$  was plotted at the various hydrate saturations of the three soil particle model. Generally, Figure 7.6 suggests that: (1) the higher aspect ratio of soil particles increased the mid-strain stiffness  $E_{50}$ , especially when it was 2.0; (2)  $E_{50}$  increased with hydrate saturation; (3) the increase in  $E_{50}$  of the pore-filling cases became a bit more obvious when hydrate saturation was higher than 20%, while the increase in the stiffness of the cementation cases started to apparently increase with hydrate saturation, but the high soil particle aspect ratio of 2.0 increased the  $E_{50}$  of the pore-filling model evidently even when the saturation was low; (4) at the same hydrate saturation,  $E_{50}$  of the cementation model was higher than that of the pore-filling model; (5) the rate of stiffness increase was higher when the saturation was higher.

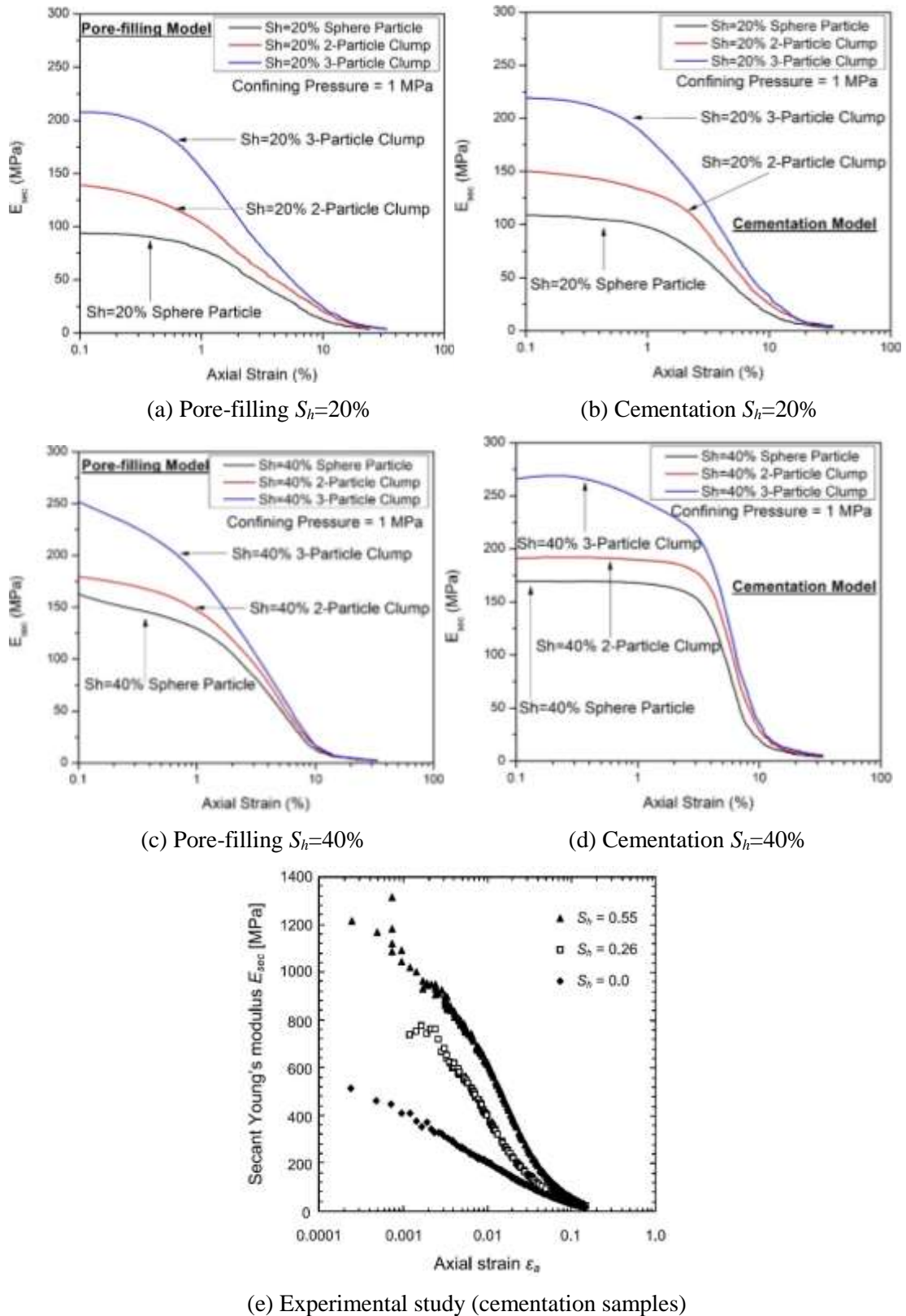


**Figure 7.5:** (a)~(d) degradation of secant Young's modulus as a function of axial strain of the three soil models ( $S_h = 20\%$  and  $40\%$ ); (e) change in the secant stiffness of cementing type synthetic hydrate-bearing soils during drained triaxial compression test by Masui et al. (2005)

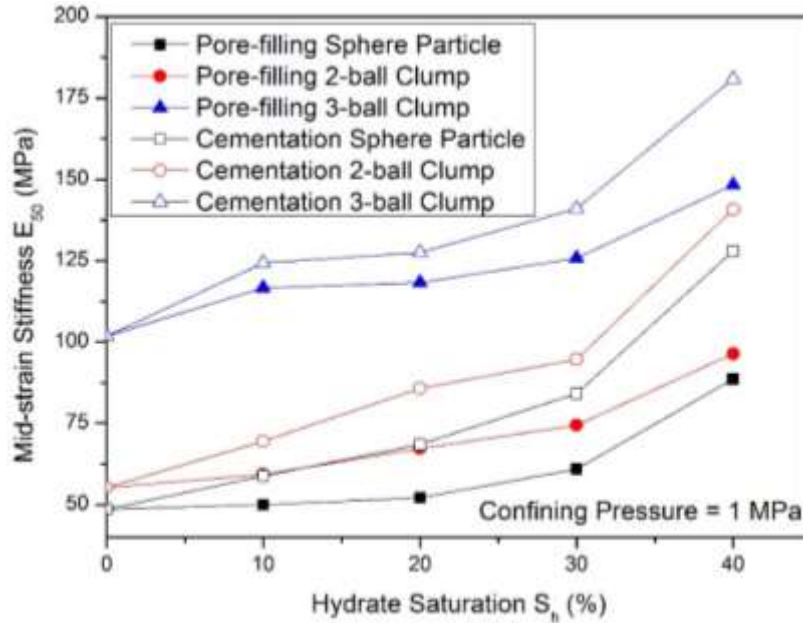


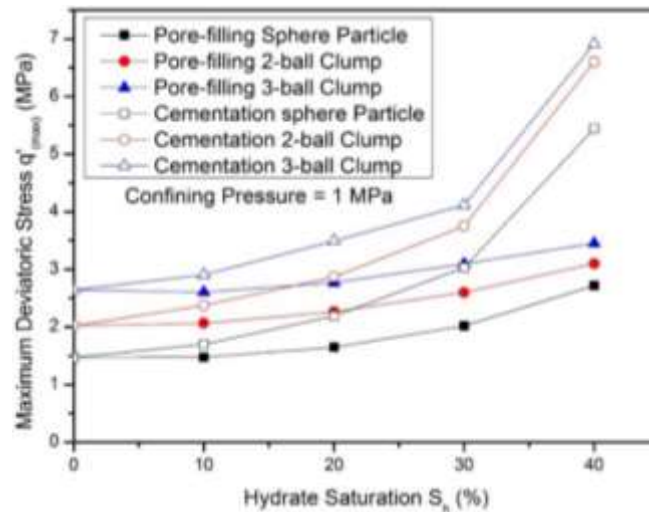
**Figure 7.6:** Mid-strain stiffness  $E_{50}$  at various hydrate saturations of three soil particle model

### 7.2.3 Strength

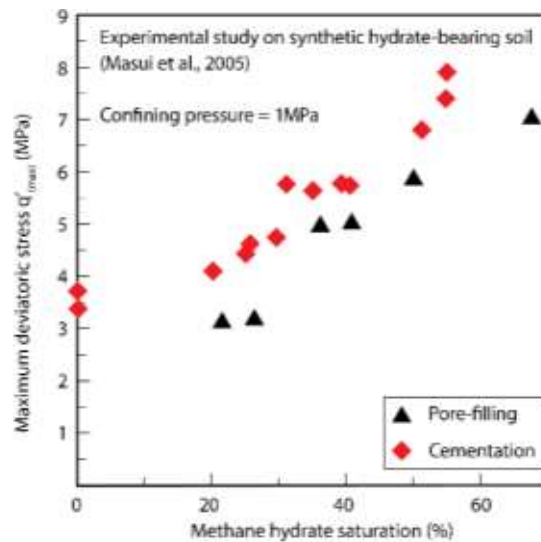
The computed peak strength  $q'_{(max)}$  (maximum deviatoric stress) is plotted in Figure 7.7 (a) at different hydrate saturations. It is clearly shown that the peak strength increased with the aspect ratio in both hydrate-bearing models. At the same hydrate saturation, the peak strength of the cementation case was larger than that of the pore-filling case for each soil particle model. As the saturation increased, hydrate particles in the pores played an essential role in shear resistance. The increased aspect ratio of soil particles did not weaken the influence of the hydrate particles at all, but absolutely strengthened the main skeleton of the hydrate-bearing soil samples. In comparisons with the experimental study (Masui et al., 2005) shown in Figure 7.7 (b), the increased aspect ratio definitely brought the strength of the DEM models closer to that of the experimental samples.

However, as shown in Figure 7.8, the computed critical state strength  $q'_{(cs)}$  showed a different result. In the pore-filling model, the critical state strength decreased with the increasing hydrate saturation. This may be due to the inclusion of the softer hydrate particles in the soil matrix in the critical state. In the cementation model, when the hydrate saturation was at 10%, the critical state strength exhibited a slightly lower

value than that of hydrate-free soil sediments, because some inter-particle bonds were broken and the hydrate moved into the sediment's skeleton. However, the higher saturation and more frequent bonding contacts increased the critical state strength. This increase was more obvious in the spherical soil model with cementation hydrates. In addition, it is also clearly shown that the critical state strength increased with the aspect ratio in both hydrate-bearing models.



(a) DEM study



(b) Experimental study

**Figure 7.7:** Peak strength (1) of three soil models in DEM study and (2) in experimental study (Masui et al., 2005)

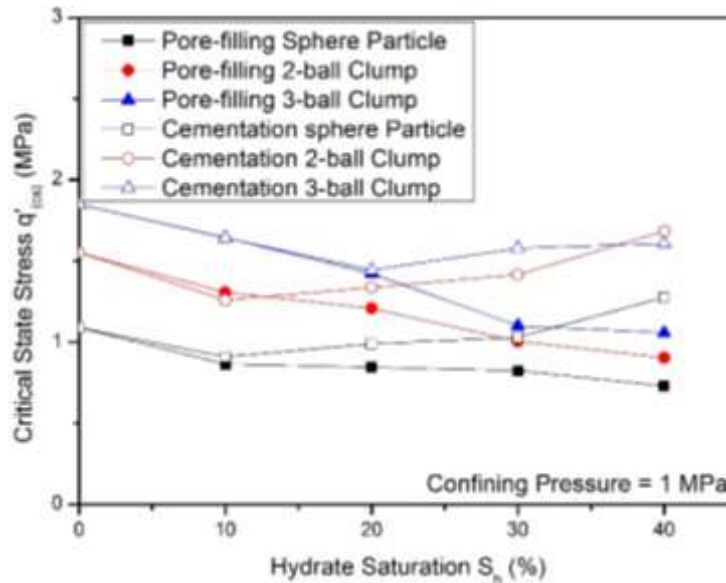


**Figure 7.8:** Critical state strength of three soil models

Figure 7.9 with the failure envelopes on  $p'-q'$  plane indicates the stress states at failure for the pore-filling model and the cementation model at the three different aspect ratios of the soil particles. It can be clearly seen that: (1) the shear strength increased with the aspect ratio; (2) the shear strength also increased with the mean effective stress. In the pore-filling model, the increase in the peak strength became obvious when the saturation was above 20%. While in the cementation model, the rate of increase in the shear strength exhibited higher results even at low hydrate saturation.

As shown in Figure 7.10, the critical state lines (CSL) plotted on the  $p'-q'$  plane show that the shear strength increased with the mean effective stress in the three soil models. The CSL plots of the pore-filling model revealed skeleton softening behaviour with an increase in hydrate saturation. This may be due to the inclusion of hydrate particles in the soil matrix at the critical state. When the saturation increased, the magnitudes of the decrease in the strength became larger at a higher aspect ratio.

However, the cementation model CSL plots showed a different result. At the aspect ratio of 1.0, the critical state strength of the cementation hydrate-bearing sediments at  $S_h=10\%$  and  $20\%$  exhibited lower strength than that of the hydrate-free soil sediments, while the critical state strength for hydrate saturations of  $30\%$  and  $40\%$  were higher than the pure soil sample. When the aspect ratio of soil particles increased,

the critical state strength of hydrate-bearing sediments became lower than that of the pure soil sample.

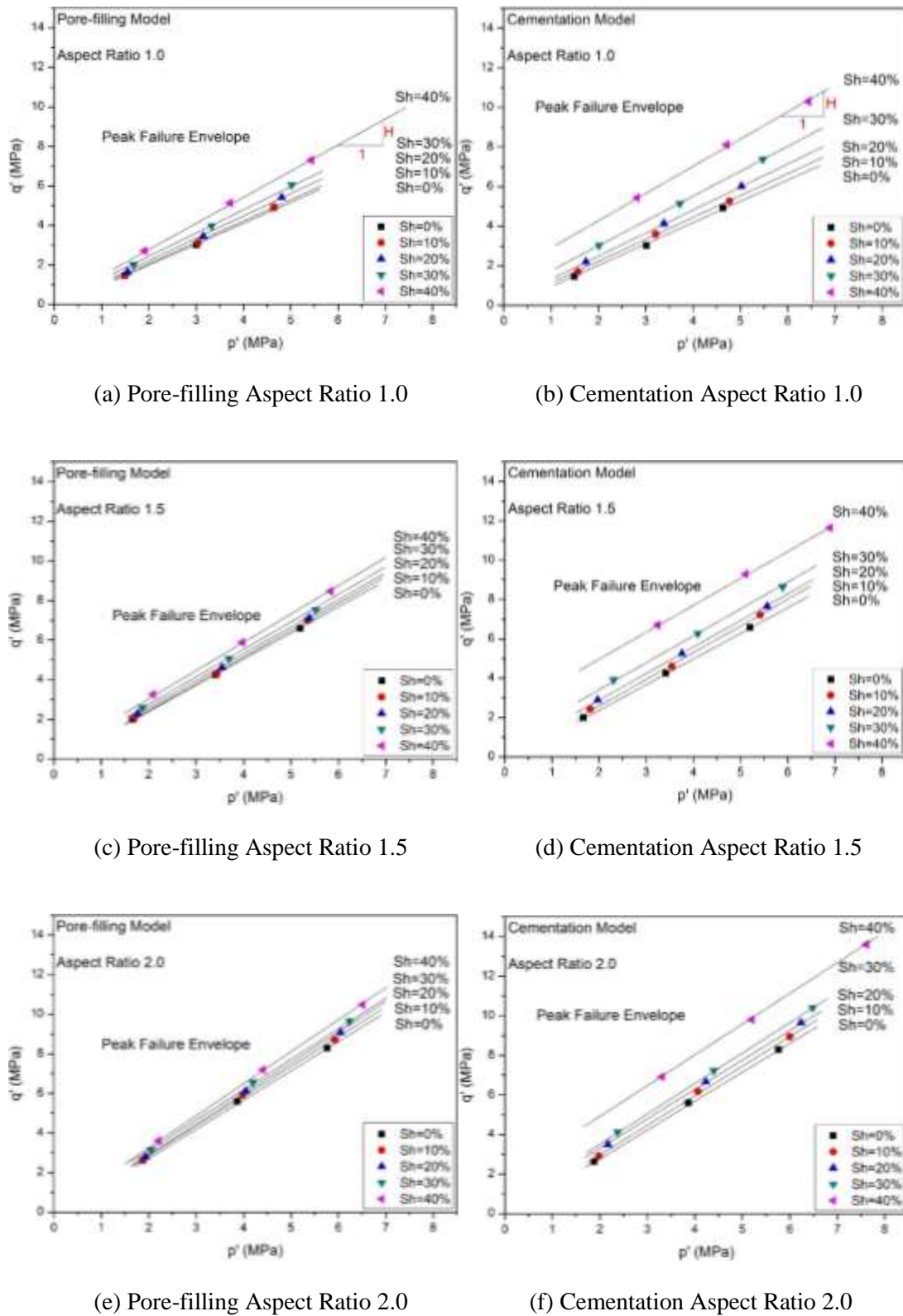
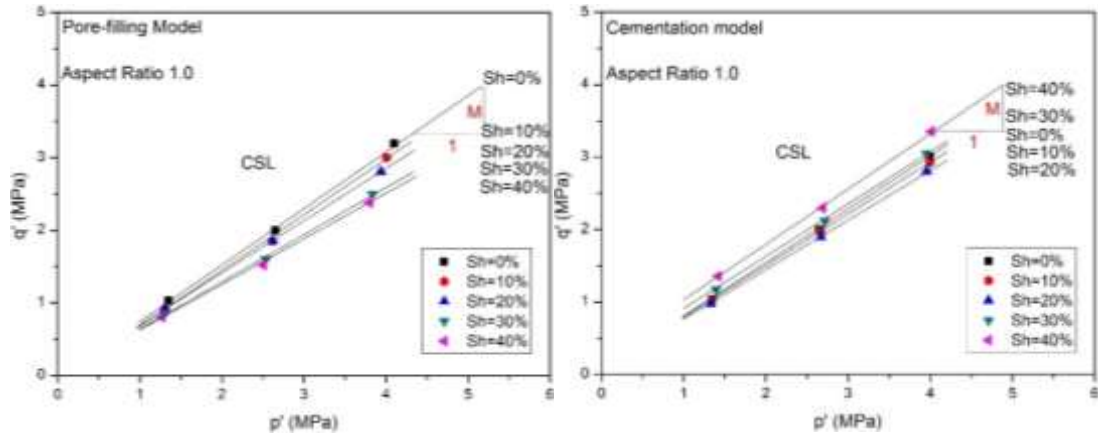
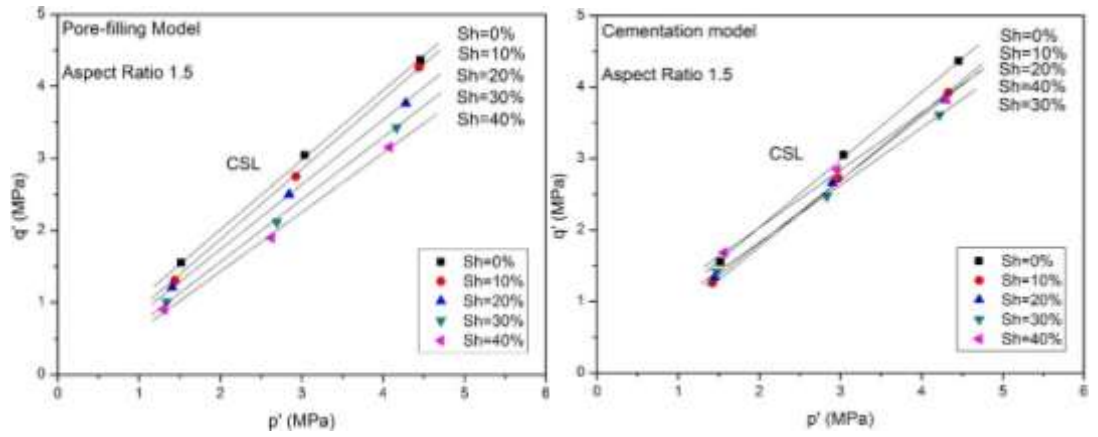


Figure 7.9: Peak Failure Envelopes on  $p' - q'$  plane



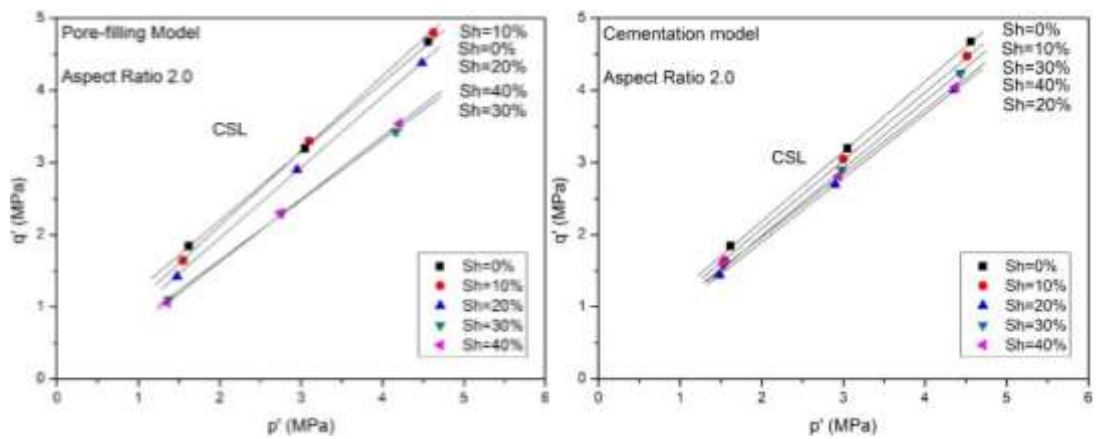
(a) Pore-filling Aspect Ratio 1.0

(b) Cementation Aspect Ratio 1.0



(c) Pore-filling Aspect Ratio 1.5

(d) Cementation Aspect Ratio 1.5



(e) Pore-filling Aspect Ratio 2.0

(f) Cementation Aspect Ratio 2.0

Figure 7.10: Critical State Line projection on  $p'-q'$  plane

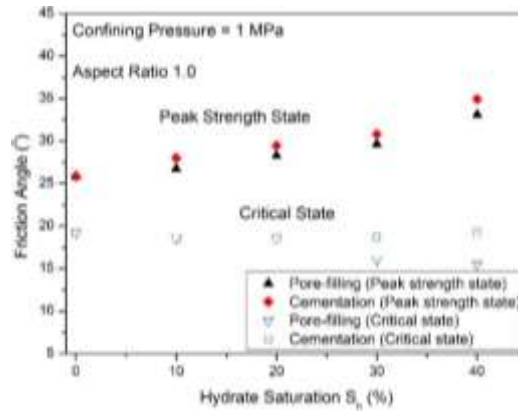
### 7.2.4 Friction and cohesion

The derived friction angle values were plotted against the hydrate saturation as shown in Figure 7.11 at three different aspect ratios of soil particles. The calculation method has been discussed in Chapter 4. It is suggested that the peak friction angle of  $S_h=0\%$  sample evidently increased with the aspect ratio.

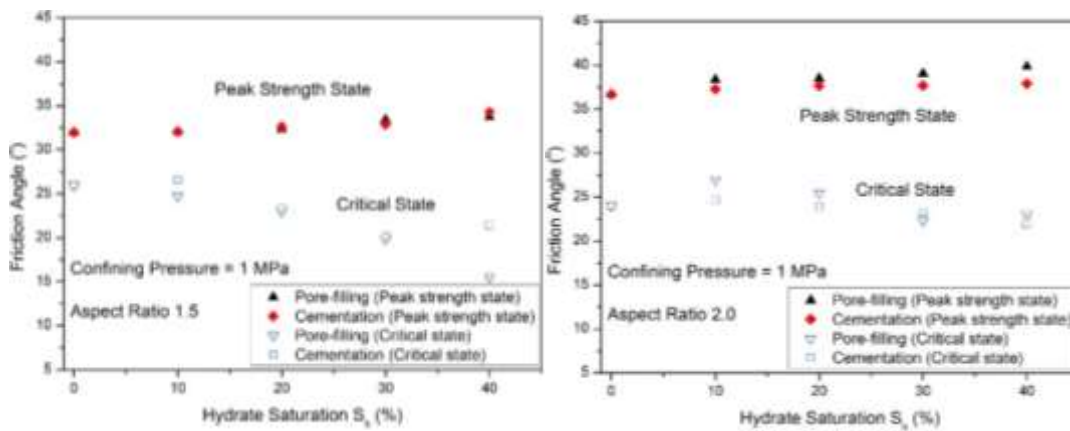
However, as the aspect ratio increased, the increase in the friction angles with hydrate saturation became less obvious. When the aspect ratio was 1.0, the peak strength state friction angle of the cementation model was larger than that of the pore-filling model. However, when the aspect ratio was 1.5, the friction angle of the cementation model was similar to that of the pore-filling model. As mentioned in Chapter 2, friction angle is largely independent of hydrate saturation (Waite et al., 2009), as shown in Figure 7.11 (d). Hence, the samples with elongated soil particles showed a closer behaviour to the natural sediments. In addition, when the aspect ratio was 2.0, the friction angle of the cementation model was smaller than that of the pore-filling model. However, generally the friction angles in the critical state showed a decrease for both the hydrate models as the hydrate saturation got higher at different aspect ratios.

To correspond to the plotted increased cohesion with saturation in the experimental data in Figure 7.11 (d), the cohesion values were plotted against the hydrate saturation of the three soil models in Figure 7.12.

It is firstly found that the comparisons between the pore-filling model and the cementation model indicates that the only contribution to the increase in the cohesion was the bonds between hydrates and other particles (hydrates and soils). Thus, the cohesion values were zero in the pore-filling model. Secondly, out of the bond breakage during the triaxial tests, the cohesion at the peak strength state was higher than that at the critical state in the cementation model, especially at high saturation. Thirdly, at the same saturation, the peak strength state cohesion increased with the aspect ratio, especially at higher saturation. Lastly, it is also suggested that the increased aspect ratio did not change the critical state cohesion.

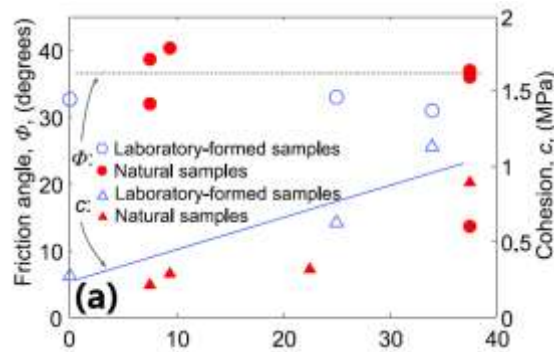


(a) Aspect Ratio 1.0



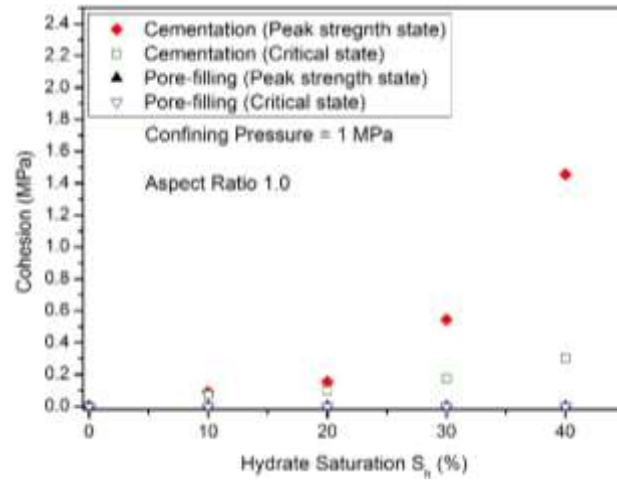
(b) Aspect Ratio 1.5

(c) Aspect Ratio 2.0

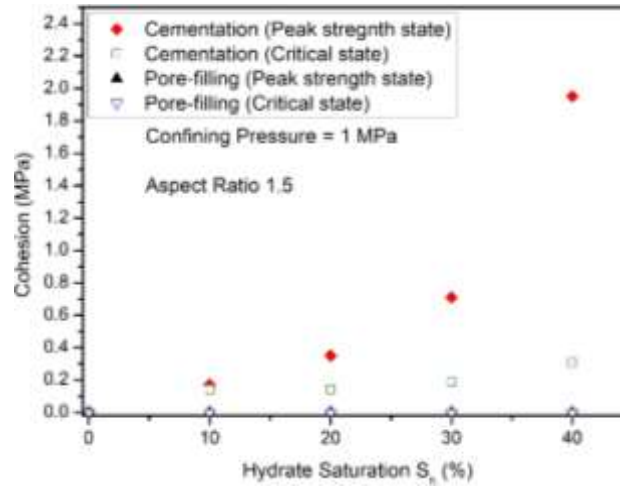


(d) Experiment study on the friction angle and cohesion

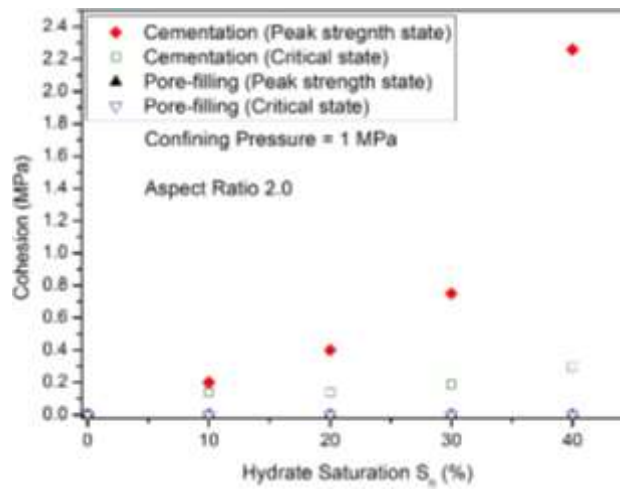
**Figure 7.11:** Angles of friction of three soil models: (a) – (c) DEM study with different aspect ratios of soil particles; (d) Experiment study on the friction angle and cohesion (Masui et al., 2005)



(a) Aspect Ratio 1.0



(b) Aspect Ratio 1.5

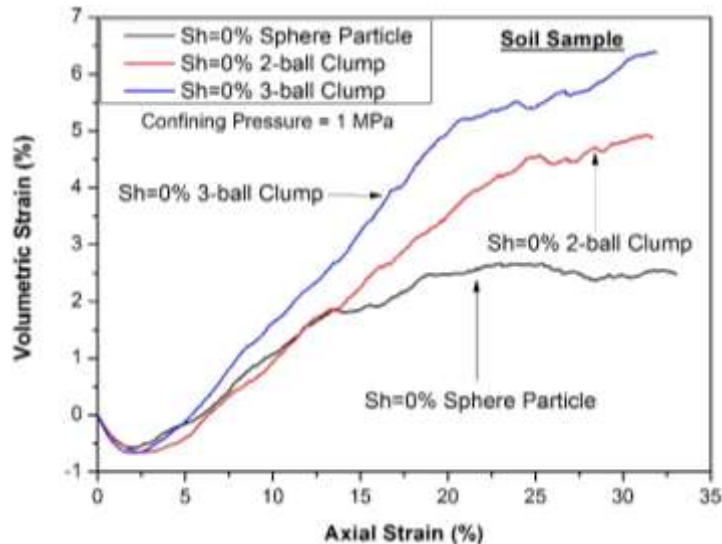


(c) Aspect Ratio 2.0

**Figure 7.12:** Cohesions of three soil models

### 7.2.5 Volumetric responses

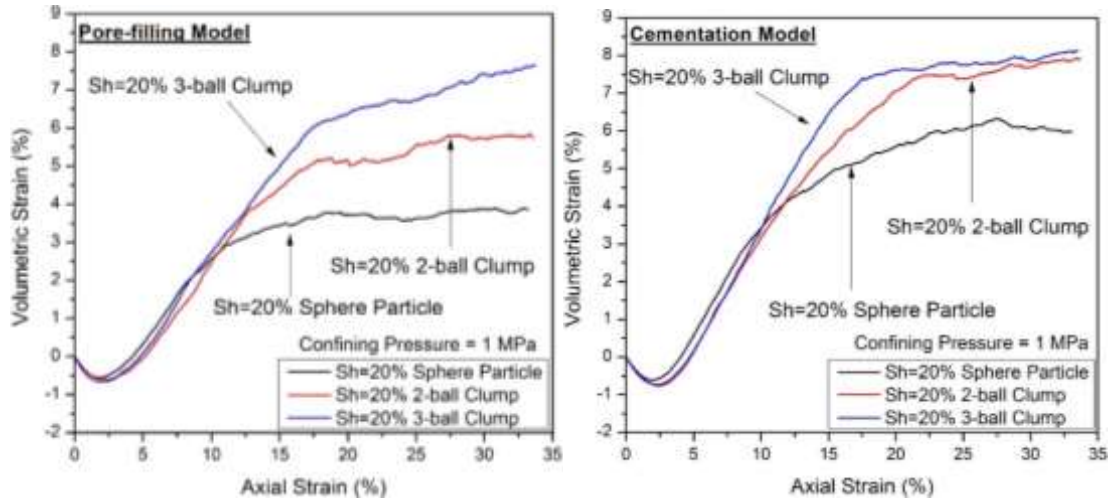
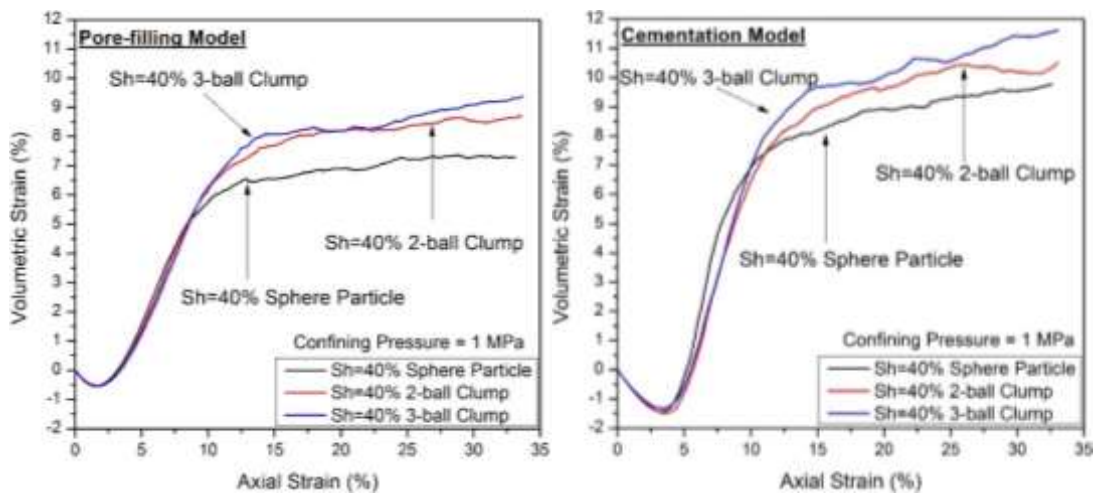
Under the confining pressure of 1 MPa, the volumetric strain – axial strain relationships of hydrate-bearing samples in the three soil models are illustrated in Figure 7.13 and Figure 7.14. Figure 7.13 shows the comparisons of the volumetric responses among the three kinds of soil shapes in the hydrate-free (pure soil) sediments. The elongated soil samples showed a slightly larger contractive behaviour. In addition, the elongated soil sample's rate of dilatancy was more obvious, while the dilatation of the 2-ball clump soil sample was delayed. In the critical state, both soil samples with the elongated soil particles reached a larger critical state volume than that of the spherical soil sample. The critical state volume also increased with aspect ratio.



**Figure 7.13:** Comparisons of volumetric strain as a function of axial strain of three kinds of soil models ( $S_h=0\%$ )

As shown in Figure 7.14, in the hydrate-bearing soil samples, the aspect ratio did not influence the samples' contractive behaviour in both the pore-filling model and the cementation model. However, the elongated soil particles induced a larger critical state volume which increased with aspect ratio. The critical state volume of the cementation model was also larger than that of the pore-filling model at the same saturation and aspect ratio of soil particles. In addition, the critical state volume increased with hydrate saturation. However, as the hydrate saturation increased, the two elongated soil models exhibited the closer critical state volumes, especially for the cementation

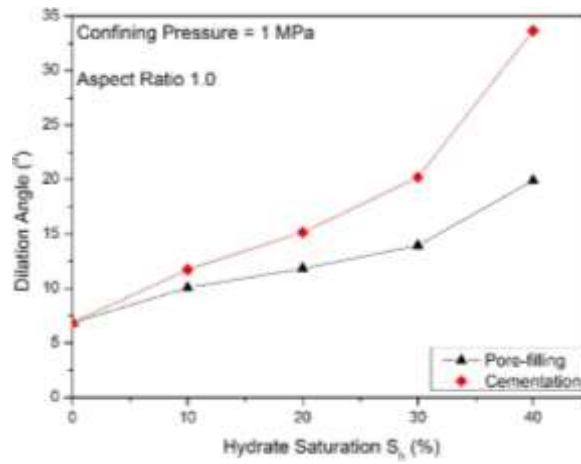
model. It is suggested that the dilation was influenced and dominated by several factors: (1) the soil particle shape, (2) the hydrate saturation, and (3) the bonds between particles.

(a) Pore-filling  $S_h=20\%$ (b) Cementation  $S_h=20\%$ (c) Pore-filling  $S_h=40\%$ (d) Cementation  $S_h=40\%$ 

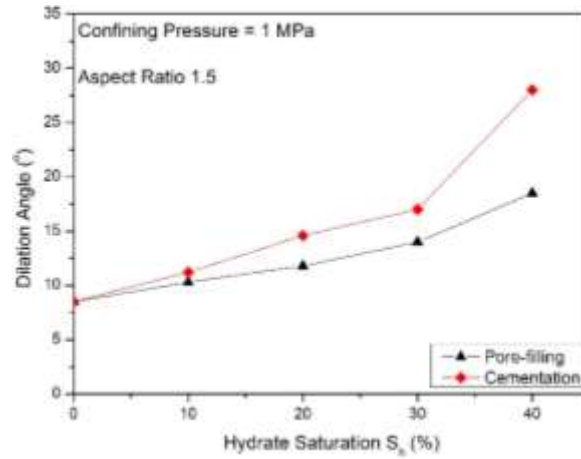
**Figure 7.14:** Comparisons of volumetric strain as a function of axial strain of three kinds of soil models at  $S_h = 20\%$  and  $40\%$

Figure 7.15 shows that the increase in the hydrate saturation enhanced the dilative characteristics of the hydrate-bearing sediments, and the increase was more obvious the higher the saturation was. However, the rate of dilatancy of the hydrate-bearing samples with elongated soil particles was slightly smaller than that of the samples with

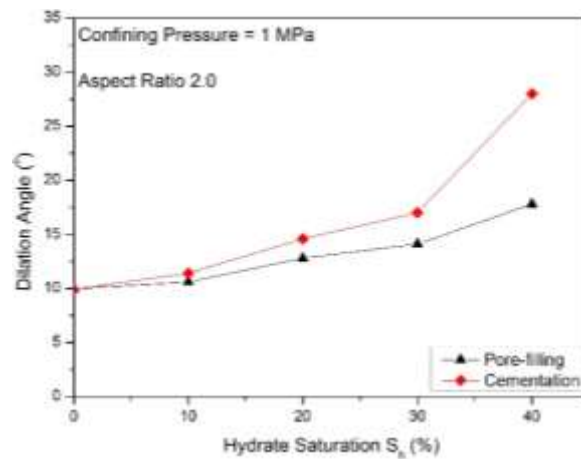
spherical soil particles, especially when the hydrate saturation was higher. In addition, the angles of dilation for both elongated soil models were close.



(a) Aspect Ratio 1.0



(b) Aspect Ratio 1.5



(c) Aspect Ratio 2.0

**Figure 7.15:** Dilation angle as a function of hydrate saturation at different aspect ratios

The critical state granular void ratio  $e - \ln p'$  projections were plotted in Figure 7.16.

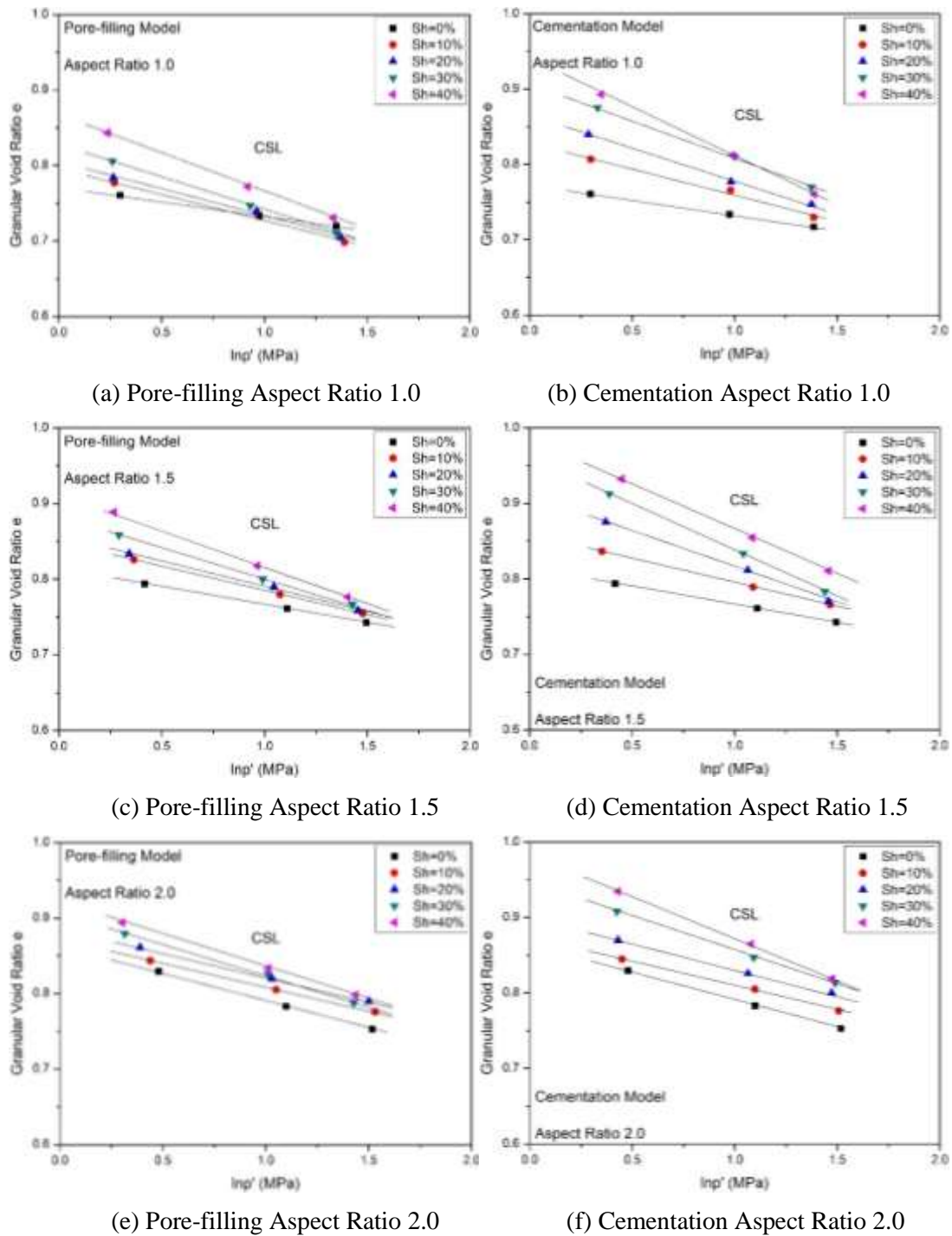


**Figure 7.16:** Critical State Line projection on Granular Void Ratio  $e - \ln p'$  plane

It can be seen clearly that in both pore-filling and cementation models, the critical state void ratios of the elongated soil models were larger than those seen in the

spherical soil model. It is found that in all the three soil models, the hydrate effects on dilation produced higher critical state void ratios as the saturation increased. It is also suggested that the hydrate-induced dilatancy was less evident at a high confining pressure. As the confining pressure increased, the dilation characteristic tended to diminish in the pore-filling model. The dilation behaviour was also weakened by the confining pressure in the cementation model, although due to the remaining bonds it could not be similar to the pore-filling case.

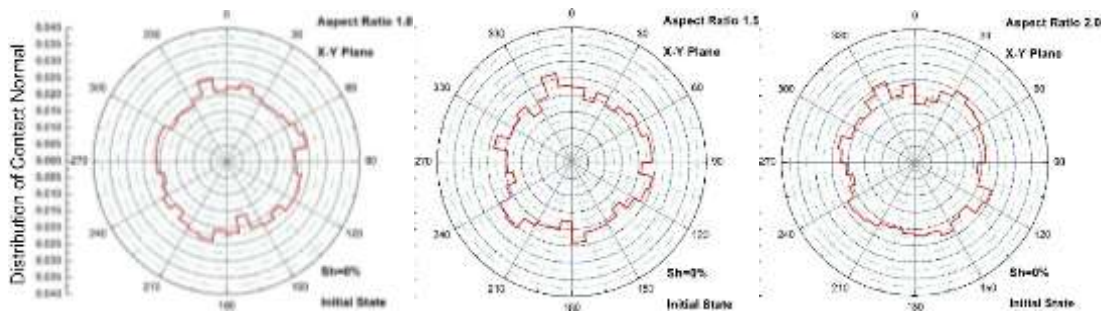
### **7.3 Rose diagram**

As discussed in Chapter 4, using the DEM simulation results, the particle-scale interactions during the triaxial compression tests can be analysed. The evolution of the fabric (contact normal) can be obtained and analysed for the three different soil models. A quantitative assessment of the distribution of the contact normal was made using rose diagrams as shown in Figure 7.17 to Figure 7.22. All normal contact forces which were non-zero were considered in the development of these plots. Because the samples were axisymmetric, only the horizontal plane (X-Y plane) and one vertical plane (X-Z plane or Y-Z plane) needed to be considered. Each 10° bin in the diagram were considered as one group of contact normal distribution. The magnitude of each bin represented the percentage of the contact normal number in this orientation group of the total number of all the contact normal.

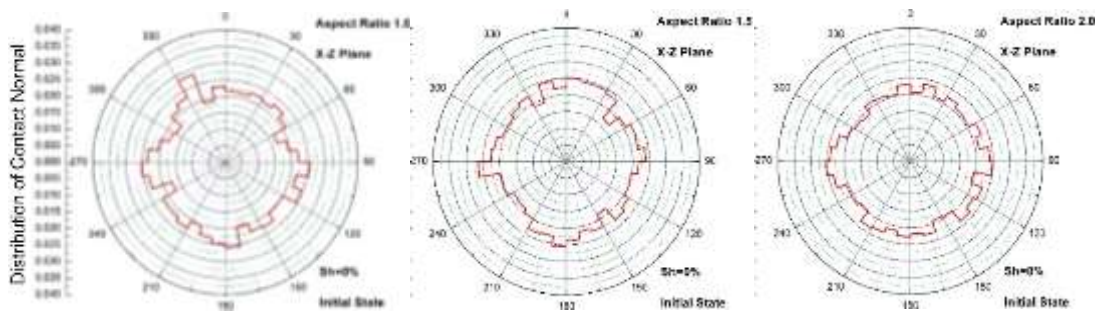
Figure 7.17 to Figure 7.22 show the rose diagrams which represent the distribution of contact normal at the initial state, peak strength state and critical state on the X-Y plane (horizontally) and X-Z plane (vertically). These figures also include the three soil models with the aspect ratios of 1.0, 1.5 and 2.0, respectively, for both the pure soil samples ( $S_h=0\%$ ) and the pore-filling and cementation hydrate-bearing samples at  $S_h=40\%$ .

Due to the axisymmetric system of the sample, the distribution of the contact normal in the horizontal plane (X-Y plane) was approximately uniform at the initial, peak strength and critical state, as shown from Figure 7.17 to Figure 7.22. In addition,

as the samples were isotropically consolidated before the triaxial tests, the distribution on all the planes was also approximately uniform at the initial state.



(a) X-Y planes (aspect ratio = 1.0, 1.5 and 2.0 respectively)

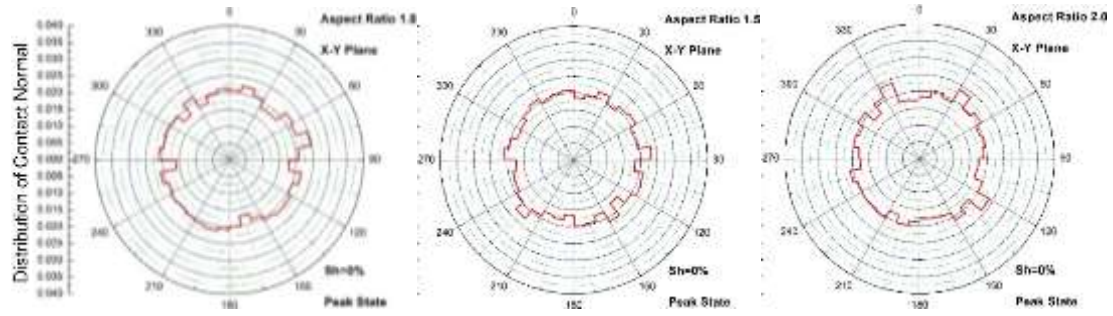


(b) X-Z planes (aspect ratio = 1.0, 1.5 and 2.0 respectively)

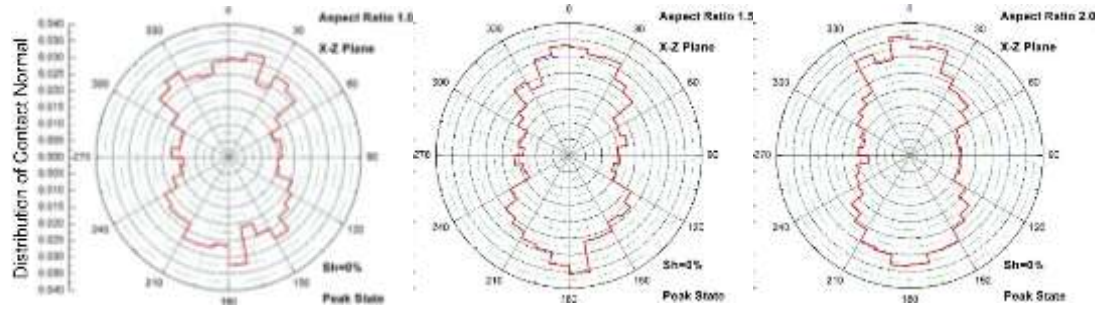
**Figure 7.17:** Rose diagram of contact normal distribution at initial state ( $S_h=0\%$ )

However, at the peak strength state and the critical state, the anisotropy in contact normal was observed in the simulations on the vertical planes. As shown in Figure 7.18 and Figure 7.19, as the loading of the triaxial tests was set vertically, there were more contact normal orientated vertically than horizontally. This anisotropy in the contact normal was more pronounced in the samples with elongated soil particles.

The evolution of the overall anisotropy for the duration of the simulations in the hydrate-bearing samples ( $S_h=40\%$ ) with the three different soil models is illustrated in Figure 7.20 to Figure 7.22 at the initial state, the peak strength state and the critical state, respectively.

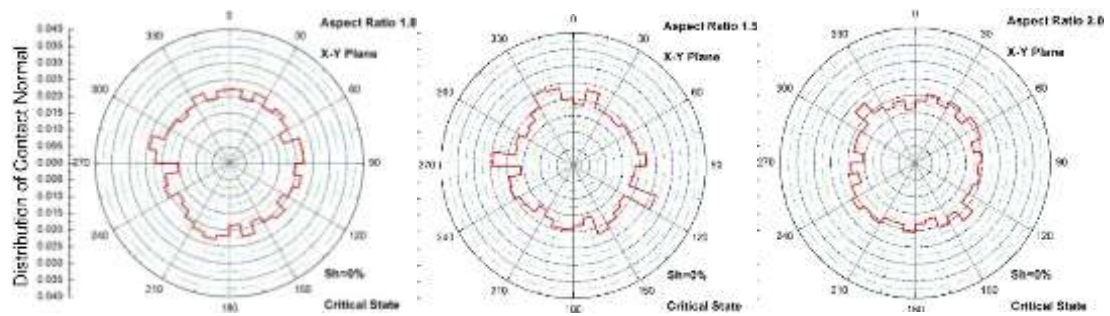


(a) X-Y planes (aspect ratio = 1.0, 1.5 and 2.0 respectively)

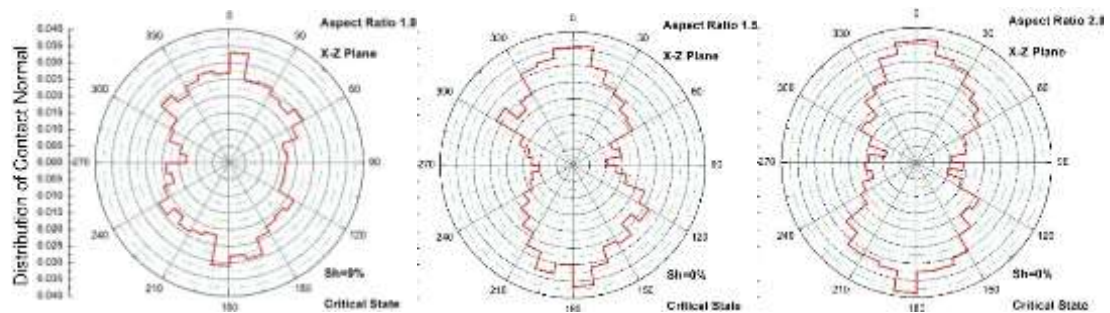


(b) X-Z planes (aspect ratio = 1.0, 1.5 and 2.0 respectively)

**Figure 7.18:** Rose diagram of contact normal distribution at peak state ( $S_h=0\%$ )

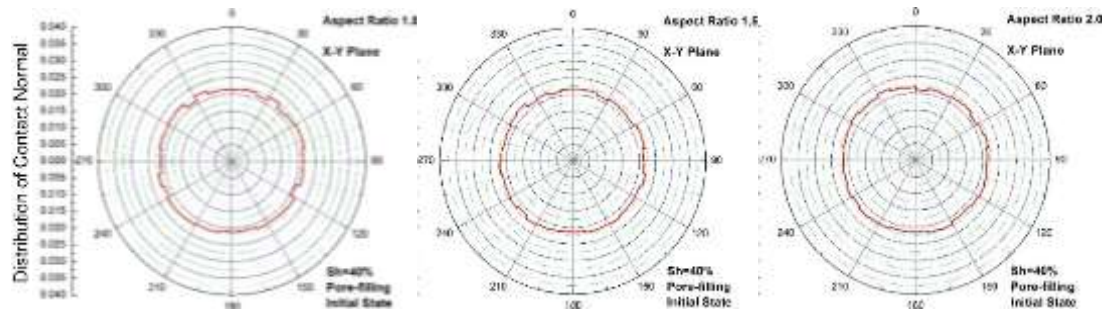


(a) X-Y planes (aspect ratio = 1.0, 1.5 and 2.0 respectively)

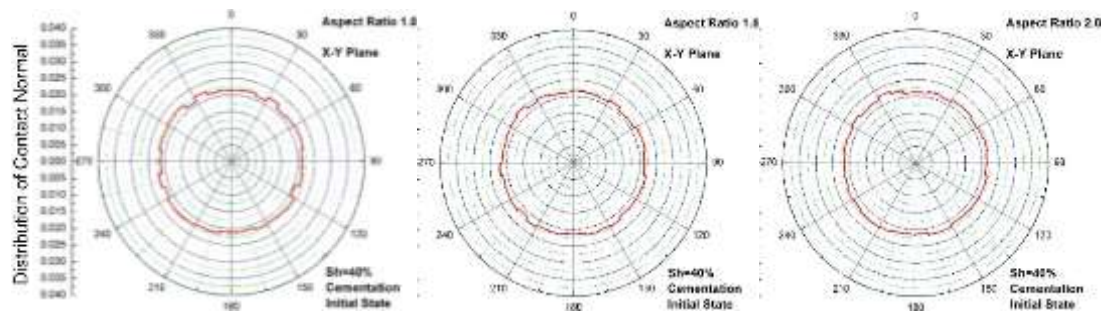


(b) X-Z planes (aspect ratio = 1.0, 1.5 and 2.0 respectively)

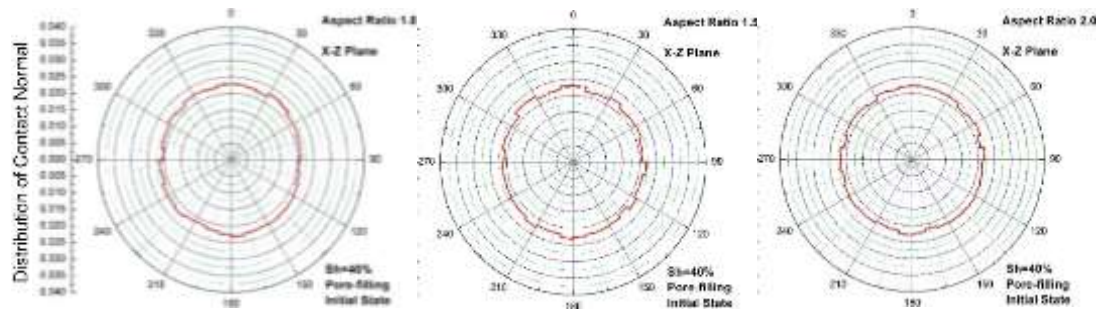
**Figure 7.19:** Rose diagram of contact normal distribution at critical state ( $S_h=0\%$ )



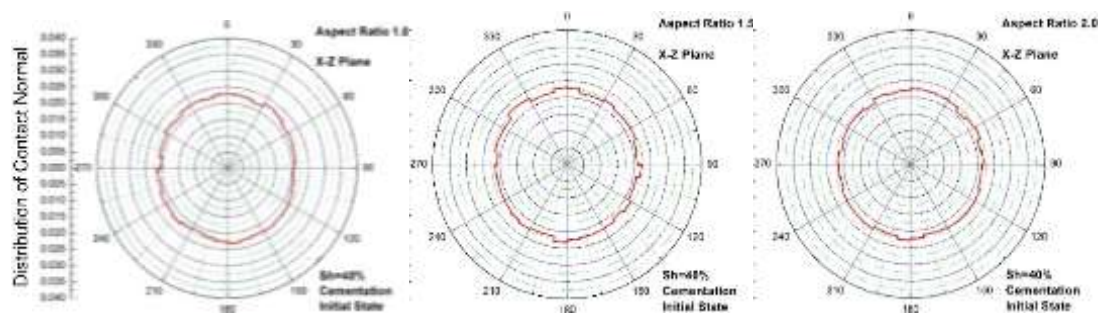
(a) X-Y planes (Pore-filling: aspect ratio = 1.0, 1.5 and 2.0 respectively)



(b) X-Y planes (Cementation: aspect ratio = 1.0, 1.5 and 2.0 respectively)

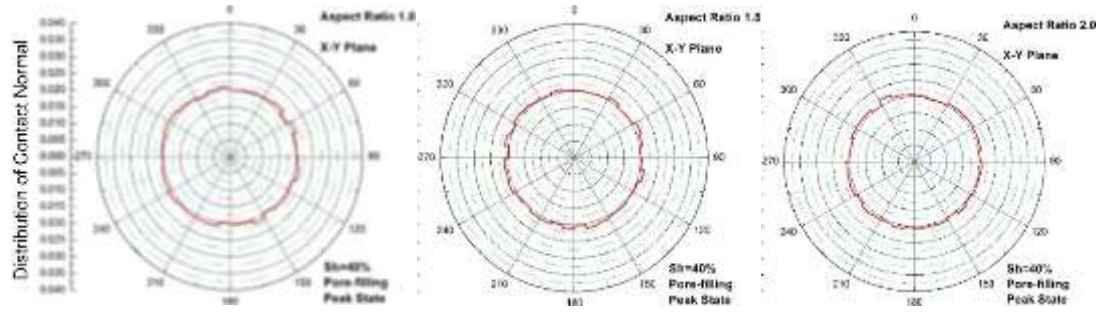


(c) X-Z planes (Pore-filling: aspect ratio = 1.0, 1.5 and 2.0 respectively)

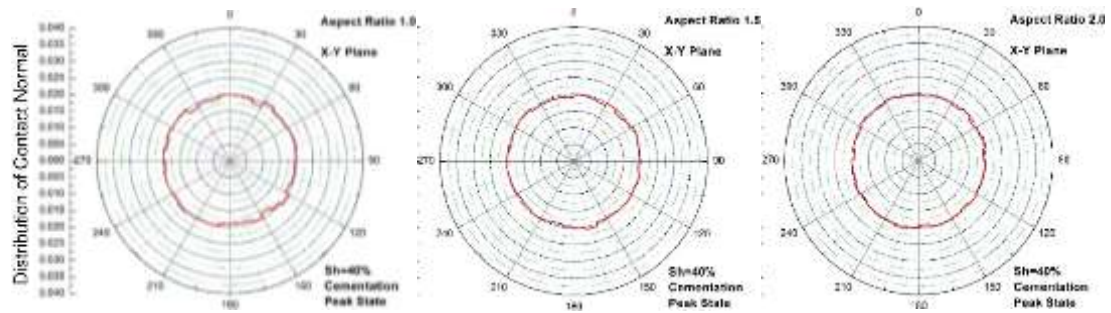


(d) X-Z planes (Cementation: aspect ratio = 1.0, 1.5 and 2.0 respectively)

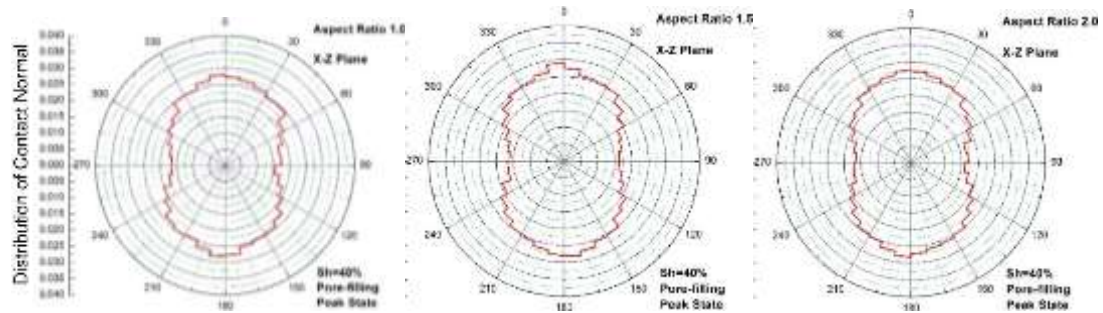
**Figure 7.20:** Rose diagram of contact normal distribution at initial state ( $S_h=40\%$ )



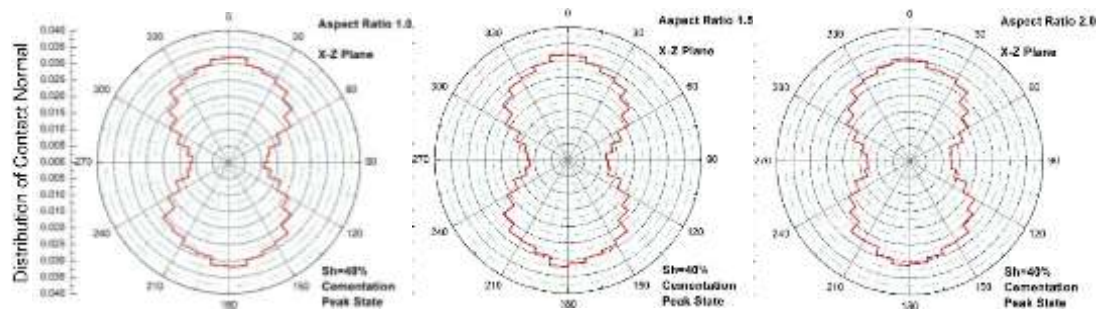
(a) X-Y planes (Pore-filling: aspect ratio = 1.0, 1.5 and 2.0 respectively)



(b) X-Y planes (Cementation: aspect ratio = 1.0, 1.5 and 2.0 respectively)

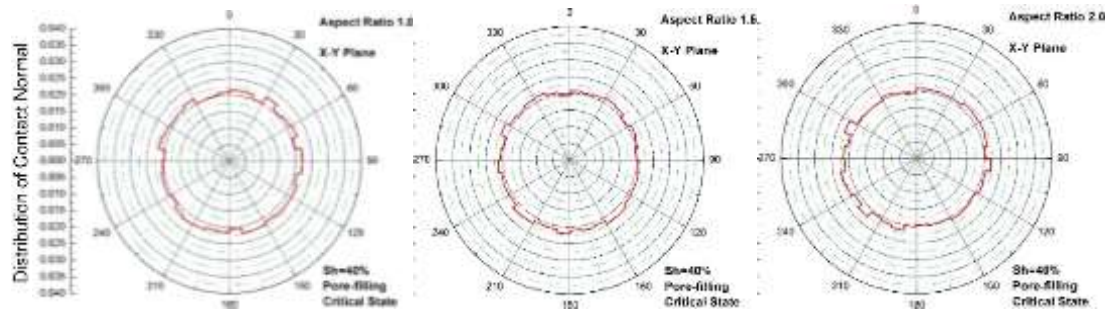


(c) X-Z planes (Pore-filling: aspect ratio = 1.0, 1.5 and 2.0 respectively)

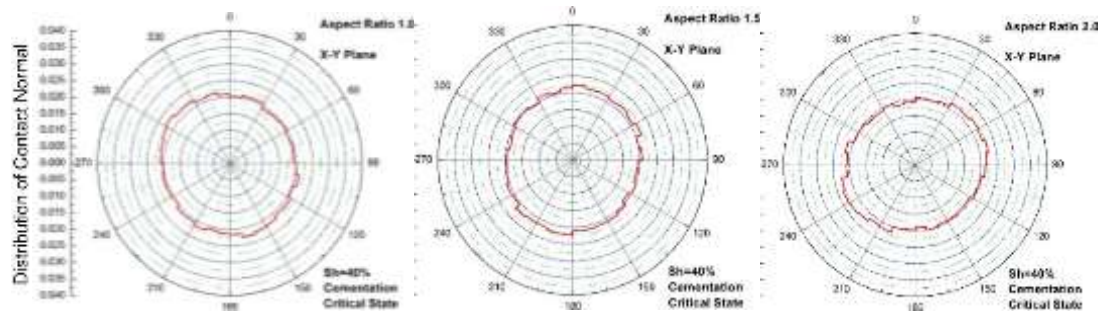


(d) X-Z planes (Cementation: aspect ratio = 1.0, 1.5 and 2.0 respectively)

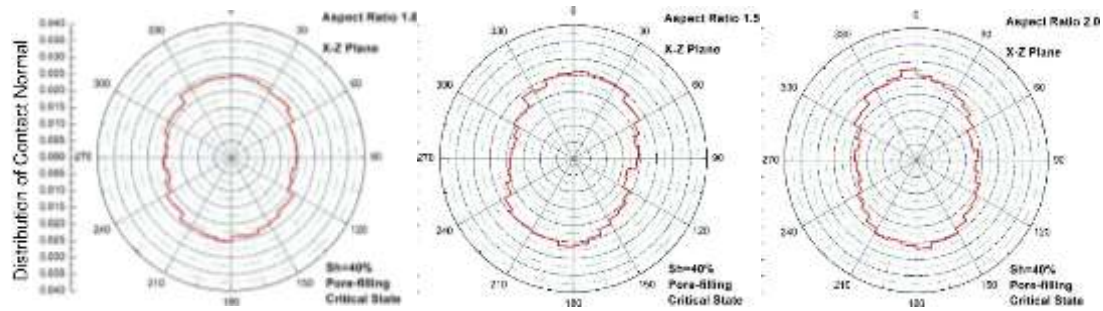
**Figure 7.21:** Rose diagram of contact normal distribution at peak state ( $S_h=40\%$ )



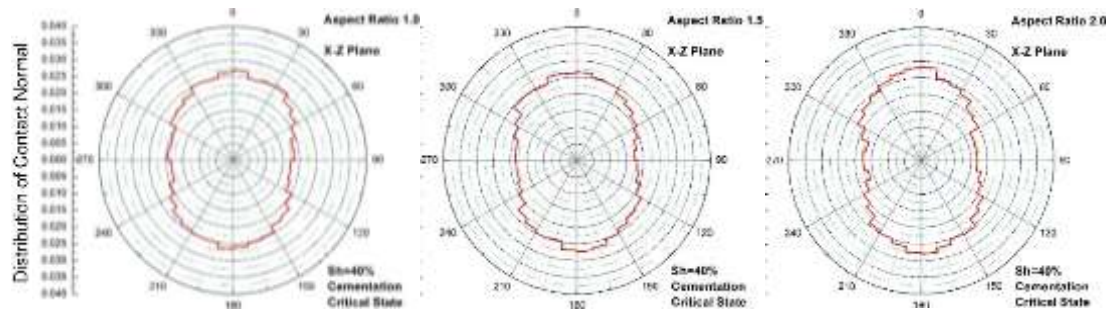
(a) X-Y planes (Pore-filling: aspect ratio = 1.0, 1.5 and 2.0 respectively)



(b) X-Y planes (Cementation: aspect ratio = 1.0, 1.5 and 2.0 respectively)



(c) X-Z planes (Pore-filling: aspect ratio = 1.0, 1.5 and 2.0 respectively)



(d) X-Z planes (Cementation: aspect ratio = 1.0, 1.5 and 2.0 respectively)

**Figure 7.22:** Rose diagram of contact normal distribution at critical state ( $S_h=40\%$ )

Firstly, after the adding of hydrate particles, the distribution of the contact normal in the horizontal plane (X-Y plane) was more uniform at the initial, peak strength and critical state than that of the pure soil samples, as shown from Figure 7.20 to Figure 7.22. Secondly, the effect of the increase in aspect ratio of soil particles on the anisotropy diminished because of the existing large number of hydrate particles on the vertical planes at both the peak and critical state.

As noted above, as the samples were isotropically consolidated before the tests, the distribution on all the planes was also more uniform at the initial state, as shown in Figure 7.20. At the peak strength state shown in Figure 7.21, the anisotropy was more obvious in the cementation model than in the pore-filling model. However, in the critical state (Figure 7.22) the anisotropy was similar in both hydrate-bearing models.

## **7.4 Summary**

In this chapter, the soil particles were modelled separately using spherical particles or elongated clumps with two different aspect ratios for investigate the influence of the shape effect of soil particles on the geomechanical behaviours of hydrate-bearing sediments. The results of the DEM samples shearing at the same initial void ratio were compared. It was found that the behaviour of methane hydrate soil sediments with elongated shape soil particles seemed to be similar to that of the natural methane hydrate sandy samples retrieved from the Nankai Trough.

The stiffness and strength were both evidently enhanced with an increase in aspect ratio of soil particles. The values of stiffness and strength obtained from the DEM modelling became closer to the experimental results (Masui et al. 2005) as the aspect ratio of soil particles increased. In addition, the hydrate saturation also played an essential role in the mechanical behaviour of the sediments. The hydrates not only strengthened the sediments' skeleton in the initial and peak states, but also induced the softening behaviour in the critical state as the softer hydrates moved into the soil matrix. Furthermore, it was found that the hydrate growth patterns greatly influenced the

hydrate-bearing soil sediments. For the given particle shape, the cementation case gave larger stiffness and strength than the pore-filling case.

However, as the aspect ratio increased, the increase in the friction angles with hydrate saturation became less obvious. But the cohesion at the peak strength state was enhanced with the increase in aspect ratio of soil particles. In addition, the increased aspect ratio of soil particles also induced a larger dilation. It is suggested that the dilation was influenced and dominated by several factors: (1) the soil particle shape, (2) the hydrate saturation, and (3) the bonds between particles.

It is also found that the anisotropy in contact normal was more pronounced in the pure soil samples with elongated soil particles. In the hydrate-bearing sediments, due to the adding of hydrate particles, the distribution of the contact normal in the horizontal plane was more uniform at the initial, peak strength and critical state than that of the pure soil samples. However, the effect of the increase in aspect ratio of soil particles on the anisotropy tended to diminish because of the existing large number of hydrate particles on the vertical planes at both the peak and critical state. In addition, the anisotropy was more obvious in the cementation model than in the pore-filling model at the peak strength state, while in the critical state the anisotropy was similar in both hydrate-bearing models.

It is suggested that in the future work, one sample should contain the soil particles with various aspect ratios, because the real soils consist of different aspect ratios. Further considerations should also be made on the DEM sample preparation method of the elongated soil particles with a better particle size distribution definition and better solutions of keeping the same volume and void ratio of the sample.

## Chapter 8

# Conclusions and recommendations for future work

### 8.1 Conclusions

In this PhD research, a numerical method Discrete Element Method (DEM) was employed to provide the unique particle-scale insight into the granular geomechanical behaviours of hydrate-bearing sediments. A comprehensive DEM research was performed using two typical hydrate-related geomechanical investigation methods: the triaxial compression test and seismic wave propagation. Accordingly, this DEM research mainly contributes six major advances which are summarized below.

#### 8.1.1 Sample preparation of DEM hydrate-bearing sediment

**Contribution 1:** two typical types of microscopic hydrate distribution patterns within soil pores were investigated via a consistent basic soil model: the pore-filling model and the cementation model.

It should be noted that the initial state before the testing plays an essential role, and the initial state totally depends on the sample preparation. In order to make a comprehensive study of hydrate-bearing sediment and a proper comparison between various hydrate distribution patterns, a consistent DEM soil model should be considered carefully. The input parameters for the particles and boundary conditions are also essential to the accuracy of the DEM modelling.

#### 8.1.2 Large deformation behaviour of pore-filling and cementation models

**Contribution 2:** the large-strain deformation and the critical state behaviours were explored.

**Contribution 3:** comprehensive particle-scale microscopic discussions and analysis were conducted to assist the interpretation of the macro responses in the in-situ, laboratory and numerical studies.

Firstly, compared to the published experimental and numerical data, this DEM triaxial compression tests also proved that the hydrate contribution to the mechanical behaviour of the sediments was of a frictional nature for the pore-filling hydrate distribution pattern, whilst of both a frictional and cohesive nature for the cementation case. It is revealed that the mechanical behaviours of hydrate-bearing soil sediments were governed by both the hydrate saturation and hydrate distribution patterns. The hardening effect of the increase in hydrate saturation were shown obviously in both hydrate growth pattern cases. The presence of hydrates caused the increase in stiffness, strength and dilative tendency, especially when  $S_h \geq 20\%$  for the pore-filling hydrate distribution pattern, and  $S_h > 0\%$  for the cementation model, which was also enhanced by the bonding strength effect and hydrate growth locations at the soil-soil contacts or along the soil surface. In addition, at the same hydrate saturation, the cementation model showed higher values than the pore-filling model in terms of initial stiffness, mid-strain stiffness, peak shear strength, friction angle, cohesion, dilation and granular void ratio. It was also found that the stiffness and strength of the samples was enhanced with the greater effective confining pressure, while the dilation appeared to diminish. Yet, the bonding effect at very high saturation in the cementation model caused the sediments' stiffness to become relatively independent of the confining pressure, and produced the dilation, though less evident than that seen at the lower confining pressure.

This research extended to the samples' large strain and critical state behaviours. For the pore-filling model, hydrate effects on strength produced lower critical state strength as the saturation increased, while in the cementation model the critical state behaviours were shown to be different. In both of the hydrate growth patterns, due to the movements of soil and hydrate particles, the softer hydrates became involved in the soil matrix and transmitted the main contact forces in the skeleton. The hydrates in the skeleton weakened the strength of the critical state. However, the remaining bonding contacts in the cementation samples appeared to produce a resistance to the critical state, weakening behaviour of the soil-hydrate matrix.

In addition, from the particle-scale investigations of the bond breakage between particles throughout the cementation model tests, it is found that the hydrate-soil bonding contacts were the main bonding contacts, and also played the main role in the bond breakage process, although hydrate-hydrate bond breakage also happened during the deformation process. The obvious bond breakage started just after the elastic phase, and this number increased steadily. This means there began to be a number of unbound hydrate particles in the pores, at the soil-soil contacts or in the soil skeleton after the bond breakage, because at  $S_h=10\%$  and  $S_h=20\%$  the critical state strength of the cementation models was smaller than that of the pure soil sample. There was however still more than half of the bonding contacts remaining in the sample at the large strain. This may explain why, at high saturations of 30% and 40% in the cementation model, the critical strength was greater than that of the pure soil sample.

The particles' contact information was also monitored. The contact number domination of soil-soil contacts changed into hydrate-contact domination with the changing saturation. However, from the research of particle-particle contact force contribution, although the soil-soil contact contribution decreased and the hydrate-contact contribution increased as the hydrate saturation increased, all the samples still showed the soil-particle-dominated behaviour. Hence, it is also important to note that the stiffness of hydrate particles was much smaller than that of the soil particles. This is the reason that hydrate particles could not play the dominant role in the particle matrix. However, the bonding effect of hydrates at the soil-soil contacts and along the soil surface still played an important role in strengthening the skeleton in the cementation model.

The large deformation was studied till as high as 33% axial strain. From some macroscopic data, such as deviatoric stress, the curves of the DEM results stabilized for the axial strain range from 15% to 33%. But the larger deformation from 15% to 33% allowed the volumetric changes stabilized at different axial strains because of the various hydrate saturations; it also allowed the stiffness degradation to continue. Moreover, as the deformation got larger, the number of bond breakage still steadily increased, and the microstructure evolution still continued. DEM proved to be a useful tool to conduct a macro- and micro- study on a larger deformation behaviour of the

hydrate-bearing sediments. This is why our interest in the sediments' behaviours extended to the large strain behaviours in the triaxial tests.

### 8.1.3 Small-strain stiffness

**Contribution 4:** wave propagation was simulated within the DEM hydrate-bearing sediment samples.

The wave velocity measurement and the particle-scale analysis show that the small-strain mechanical properties of hydrate-bearing sandy sediments are governed by not only the pore space hydrate saturation, but also the hydrate formation and distribution patterns. The influence of the cementation hydrate pattern on small-strain behaviour becomes obvious from low hydrate saturation, because hydrates grow first at the grain contacts and the existing soil skeleton structure was cemented. This restriction cuts down the energy loss and shortens the wave propagation time. However, pore-filling hydrate does not have impact on the small-strain behaviour of the sediment's grain skeleton at low hydrate saturation. As the volume of hydrate increases to higher saturation however, the small strain stiffness increases for both the cementation and pore-filling cases. It was also found that the wave velocity and the small-strain stiffness generally increased with confining pressure.

It may be concluded that the initial state behaviours have an influence on the large strain behaviour of hydrate-bearing sediments. As the hydrate saturation increased, the small-strain stiffness increased. Accordingly, the corresponding mid-strain stiffness and the peak strength increased with the saturation and the small-strain stiffness. This could be a regular pattern for predicting the large-strain behaviours through the wave propagation. However, the critical state strength did not follow the trend of the observations mentioned above. According to this DEM data, it is suggested that the small-strain stiffness or initial state wave velocity should be not related to the critical state of the hydrate-bearing sediment.

#### 8.1.4 Bonding strength effect and hydrate growth patterns in the cementation model

Contribution 5: the bonding strength effect in the cementation model was systematically discussed.

It is found that the hydrate growth patterns in the cementation model greatly influenced the mechanical behaviour of the hydrate-bearing sediments, especially when the bonding strength and hydrate saturation were increased. For a given bonding strength and hydrate saturation, the stiffness and the strength of a sample with hydrates gathering near grain contacts was greater than that of a sample with hydrates coating around the grain surface. This is because of the larger number of contacts which are bonded in the contact-gathering case. The increased bonding strength did not increase the initial stiffness, but delayed the change of stiffness and the peak failure, which required a larger strain.

When a high bond strength was assigned, the deformation at small strains was controlled by the deformation of the particles themselves, and dilation was therefore delayed. When grains started to move relative to each other by starting to show evident bond breakage, samples exhibited dilation. There was greater dilation observed in the grain coating case compared with the contact gathering case.

When the bonding strength was increased, the evident bond breakage was delayed as the failure was delayed, and the percentage of bond breakage in total bonds at the large strain obviously decreased. In addition, when the bonding strength was set to a very large value, there was no obvious bond breakage happening throughout the tests, with a larger axial strain perhaps being needed to reach failure. Hence, the big bonded particle clusters at the inter-granular contacts induced a larger dilation than the surface coating hydrate particles.

The particles' contact force contribution to the total deviatoric stress increased with the bonding strength for all the particles' contact types: soil-soil, soil-hydrate and hydrate-hydrate. However, the main contact force contribution was always from the soil-soil contacts for the essential reason that the stiffness of the hydrate particles was

much lower than that of the soil particles. When the hydrate particles were set stiffer in the simulation, the force contribution of hydrate particles increased dramatically. However, further research on the stiffness of the hydrates is necessary for both the experimental and numerical studies.

Comparisons were made on the stress-strain responses measured by the measurement spheres (local measurement), the average particles' contact forces (global measurement) and the wall-based logic (boundary measurement) with both low and high bonding strength. It is also proved that the loading rate on the top and bottom walls in the triaxial test was chosen reasonably because the simulation results obtained by the boundary measurement and the average particles' contact force were very close. However, the measured stress-strain responses by the measurement spheres showed a different value at the large strain.

### 8.1.5 Effects of elongated soil particle shape

**Contribution 6:** the effect of elongated soil particles on the geomechanical behaviours of sediments was studied.

It was found that the behaviour of methane hydrate soil sediments with elongated shape soil particles seemed to be similar to that of the natural hydrate-bearing sandy sediments retrieved from the Nankai Trough.

The stiffness and strength were both evidently enhanced with an increase in aspect ratio of soil particles. The values of stiffness and strength obtained from the DEM modelling became closer to the experimental results (Masui et al. 2005) as the aspect ratio of soil particles increased. In addition, the hydrate saturation also played an essential role in the mechanical behaviour of the sediments. The hydrates not only strengthened the sediments' skeleton in the initial and peak states, but also induced the softening behaviour in the critical state as the softer hydrates moved into the soil matrix. Furthermore, it was found that the hydrate growth patterns greatly influenced the hydrate-bearing soil sediments. For the given particle shape, the cementation case gave larger stiffness and strength than the pore-filling case.

However, as the aspect ratio increased, the increase in the friction angles with hydrate saturation became less obvious. However, the cohesion at the peak strength state was enhanced with the increase in aspect ratio of soil particles. In addition, the increased aspect ratio of soil particles also induced a larger dilation. It is suggested that the dilation was influenced and dominated by several factors: (1) the soil particle shape, (2) the hydrate saturation, and (3) the bonds between particles.

It was also found that the anisotropy in the contact orientation was more pronounced in the pure soil samples with elongated soil particles. In the hydrate-bearing sediments, due to the adding of hydrate particles, the contact normal in the horizontal plane was more uniform at the initial, peak strength and critical state than that of the pure soil samples. However, the effect of the increase in aspect ratio of soil particles on the anisotropy tended to diminish because of the existing large number of hydrate particles on the vertical planes at both the peak and critical state. In addition, the anisotropy was more obvious in the cementation model than in the pore-filling model at the peak strength state, while in the critical state the anisotropy was similar in both hydrate-bearing models.

It is suggested that in the future work, one sample should contain the soil particles with various aspect ratios, because the real soils consist of different aspect ratios. Further considerations should also be made on the DEM sample preparation method of the elongated soil particles with a better particle size distribution definition and better solutions of keeping the same volume and void ratio of the sample.

### 8.2 Recommendations for future DEM work

Although the DEM simulation results in this study are compared well to the published experimental data, the values in the experimental data were different than the simulated data in this study. This presents the limitations of this DEM work. Firstly, regarding the sample preparation, there is no fluid or gas included in this DEM model, so that the comparison cannot be made properly. Secondly, the DEM hydrates are sphere particles rather than the hydrate mass. Due to the limitations of the DEM modelling of spherical particles, this study is qualitative rather than quantitative. The

study on the effect of elongated soil particle shape in Chapter 7 discusses more about this issue although there are still difference between the DEM results and the laboratory results. In addition, the input parameters of the soil and hydrate particles was also the reason. For example, in this DEM research, the elastic modulus of the particles were chosen at relatively small values, which caused the DEM results smaller than the laboratory ones. And the chosen simple contact model may be another reason of the limitations. As discussed in Chapter 3, it is now generally recognized by the research community that the main objective of DEM-based investigation is not to provide quantitatively reproduction of material behaviour, but to understand qualitatively the particle-scale mechanism affecting the continuum-scale responses.

Looking forwards, DEM will certainly not replace the continuum modelling as a means to predict hydrate-bearing sediment deformations, nor will it replace the in-situ and laboratory studies as a means to advance the fundamental understanding of the sediment responses. However, it is definitely a useful tool to provide a unique insight into the geomechanical investigations of hydrate-bearing sediments. Based on this PhD research, some recommendations for the future DEM work are proposed as follows.

### 8.2.1 Further parametric studies

From the DEM simulation results and analysis, it can be found that care should be taken in the choice of the input parameters used to accurately model the hydrate-bearing sediment, such as the particle size, friction, initial void ratio, bonding strength, stiffness, etc., because they play an essential role in the accuracy of the simulated results. By the comparisons with data of the in-situ and laboratory studies, how to decrease the magnitude of the value difference between the DEM study and the experimental study is crucial and needs further and careful investigations.

For example, regarding the bonding strength, after the discussions in Chapter 6, it is found that the setting of the bonding strength governs the behaviour of the DEM samples. Although Chapter 6 compared a series of bonding strength values, a more detailed research should be considered carefully to relate the observed experimental

data to the DEM simulation for a more accurate bonding strength value with the numerical changes in a specific modelling.

In addition, further work on the hydrate/soil contact stiffness ratio is needed to evaluate the mechanical properties of hydrates. It can also be found in this research that the change in the stiffness of hydrate in the DEM simulation has an impact on the domination of the particles' contact behaviour.

### **8.2.2 Hydrate distribution patterns**

Although pore-filling and cementation hydrate distribution patterns are the most typical among all the patterns, a comprehensive study on other patterns needs to be carried out, such as load-bearing, supporting-matrix, patchy, and fracture-filling patterns.

However, the control of a consistent soil model with various hydrate patterns should be considered very carefully, as some of the patterns develop and break the original compacted soil skeleton. Hence, it is challenging for comparisons and analysis, but the study is still necessary and beneficial because they do exist in nature.

### **8.2.3 Particle shape**

In nature, the particle shapes of soil are complex. It cannot be simply assumed to be spherical or elongated. It has been found in Chapter 7 that the shapes of soil particles govern the mechanical behaviour of hydrate-bearing sediment. In addition, hydrates in the pore space cannot be supposed to be spherical if further work considers the shape effect of modelled particles. Hence, the simulated particle shapes and its distribution should be considered carefully in further studies.

### **8.2.4 Sizes of soils**

It has been discussed in Chapter 2 that the current exploration of hydrate mainly focuses on the sandy sediments, hence in this research only sand was considered.

However, as the numerical simulations can assist in overcoming the difficulties and limitations of in-situ and laboratory studies, different sizes of soils should be studied in order to provide scientific support and to meet future scientific and industrial needs.

### 8.2.5 Fluid and gas

In the static drained triaxial compression tests of this research with PFC<sup>3D</sup>, the effective stress could be obtained without considering the pore pressure and the influence of fluid and gas. However, an in-depth DEM numerical multi-phase simulation should take fluid and gas into account. Further DEM work coupled with fluid and gas needs to be carried out.

### 8.2.6 Temperature

In this research, the temperature issue was not considered, with the assumption that the temperature was low enough for any deformation of the sediment. However, considering the gas in the pore space, during the deformation process and the volumetric change, the temperature should change accordingly, and there should be an energy loss. In addition to this, the change of temperature may also cause the dissociation of hydrate in the sediment. Hence, temperature should also be considered in future work, as it is one of the two most important conditions for the existence and development of methane hydrate.

### 8.2.7 Dissociation of hydrate

This research only considered the effects of the hydrate formation in the sediment, as well as the geomechanical behaviours during the deformation process. However, a very important research topic should definitely be carried out: the structure degradation of the hydrate-bearing sediment due to hydrate dissociation, which plays a significant role in the exploitation of methane hydrate and the safety production of the drilling well.

### **8.2.8 Contact models**

In this research, only the linear contact model, slip model and contact bond model were used. However, considering the influence of the contact models on the particles' contacts, more realistic contact models should be built.

### **8.2.9 Up-scale research**

Due to current computational power, the time and computation cost of the DEM simulation in a research project needs to be taken into account. Therefore, in this research, the size of the sample was set relatively small, hence the limited number of particles. In fact, this constraint imposes a limitation not only on DEM particle-scale research but also field- and industrial-scale simulations.

Obviously, there exist two issues for future DEM research work: one is to increase the sample size and particle number for obtaining a more accurate simulation result; the other is to relate particle-scale micro-investigations with macro-scale and even industrial-scale investigation. These issues should be considered further in future work.

## Appendix A

### Calculation of hydrate saturation in DEM study

As previously noted in Chapter 3, the hydrate saturation computed in this DEM research may not be the same as the hydrate saturation measured in the laboratory. Because of the spherical shape of the soil and hydrate particles in the DEM model, after adding  $S_h = 40\%$  of hydrate particles within the pores of the soil sample, there would be no single void space for placing a single hydrate particle inside, although the total remaining void space volume would still be large. If adding more hydrate particles inside the sample, the sample would expand because the overlapping of hydrate particles would cause higher mean contact force than the confining pressure. Following this, the volume and void ratio would also be changed.

Thus, the simulated hydrate saturation ( $S_h$ ) in DEM should correspond to a higher hydrate saturation than the natural hydrate-bearing soil sediments. However, as already mentioned in Chapter 3, the actual 40% saturation could not simply be assumed as 100% saturation, as there were still void spaces in the sample. Hence, the behaviour observed in this study was examined qualitatively rather than quantitatively.

In order to obtain a more accurate hydrate saturation in future DEM studies, in this Appendix, three methods are proposed for the calculation of hydrate saturation when all the particles are spherical: accurate calculation, close packing and wasted void space volume at particle contacts.

#### 1. Accurate calculation

The accurate calculation has been mentioned in Chapter 3 and used in this DEM study, as shown in Equation A-1:

$$\text{Hydrate saturation: } S_h = \frac{\text{Volume}_{(\text{hydrates})}}{\text{Volume}_{(\text{pores})}} \quad (\text{A-1})$$

However, as discussed above, the results from the accurate calculation may be underestimated. An assumption should be made regarding the appropriate saturation value. Thus, the next two calculation methods may provide some new thoughts over the spherical hydrate saturation assumption.

## **2. Close packing**

Close packing refers to an empirical method for obtaining the maximum volume occupied by the solid objects which are packed closely in a regular space. The maximum occupied volume depends on not only the object shape, but also the packing method. In the current DEM research of hydrate-bearing sediments, spheres are particle shape mainly discussed. Regarding the packing methods, there are a few for packing sphere particles listed by Dullien (1992) with different maximum occupied volumes: thinnest regular packing, loose random packing, poured random packing, close random packing, thickest regular packing, etc..

To obtain the assumption value of the largest hydrate saturation in the DEM study, the maximum occupied volume may be related to it. Compared to the hydrate generation procedure in this study, random close packing seems similar. In the process of random close packing, when the particles are filled in the box, to shake the box can reduce the volume occupied by the particles, and can also spare space for adding more particles.

Song et al. (2008) concluded analytically that the maximum occupied volume of spherical particles takes up to 63.4% of the total volume of the space. There is also a theoretical packing method with the maximum theoretical occupied volume of 74.05% (Dullien, 1992) – hexagonal close packing, as shown in Figure A-1. The hexagonal close packing is a dense, regular and infinite arrangement of sphere particles.

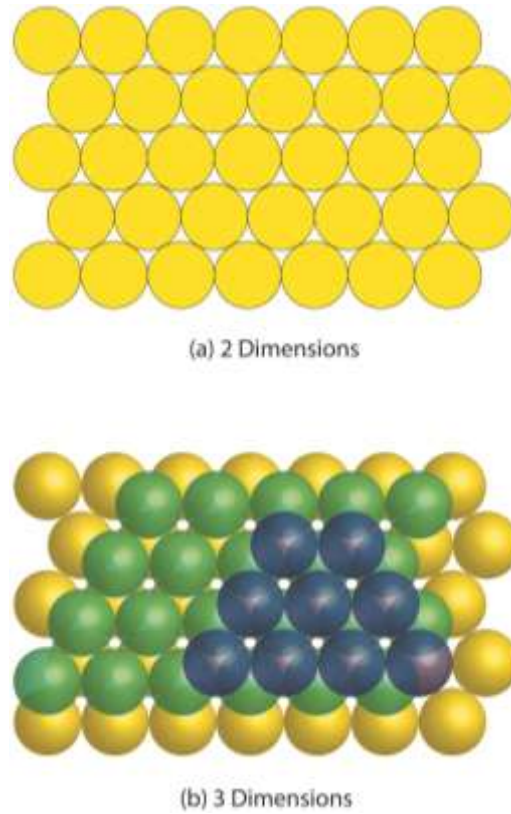


**Figure A-1:** Hexagonal close packing of spherical particles

Hence, an assumption value of hydrate saturation may be made in the DEM study with spherical hydrate particles according to the maximum occupied volume of the close packing methods, as calculated by Equation A-2. Table A-1 lists the assumption values of the hydrate saturation in the DEM study according to the close packing theory.

$$\frac{S_{h(\text{accurate-DEM})}}{S_{h(\text{max-DEM})}} = \frac{S_{h(\text{assumption})}}{S_{h(\text{max-packing})}} \quad (\text{A-2})$$

However, the void spaces within the sample are not in a regular shape. The boundaries of those void spaces are the surfaces of the soil particles, which means the boundary conditions for the close packing are more complex. Furthermore, the volume of the void space is limited, and the number of the hydrate particles which can be filled inside the space is also limited. So it is impossible to reach the theoretical maximum value of the close packing. Thus, the close packing method seems too idealistic for this

research, but it also leads to a new step for the assumption of hydrate saturation in the DEM study.

**Table A-1:** Assumption value of hydrate saturation in DEM study according to close packing theory

<b>Accurate Calculation  (DEM)</b>	<b>Assumption Value</b>	
	According to <b>Random close packing</b>	According to <b>Hexagonal close packing</b>
$S_h = 10\%$	15.85%	18.51%
$S_h = 20\%$	31.70%	37.02%
$S_h = 30\%$	47.55%	55.53%
$S_h = 40\%$ (maximum value)	63.40% (maximum value)	74.05% (maximum value)

### 3. Wasted void space volume at particle contacts

Regarding the wasted space volume in particle contacts, it refers to the volume of space at the particle contacts which cannot fill a hydrate sphere particle, as illustrated in Figure A-2. In the theory of this saturation calculation method, the wasted void space actually has been occupied by the existing contact, hence the volume of this space should also be taken into account in the saturation calculation by Equation A-1.

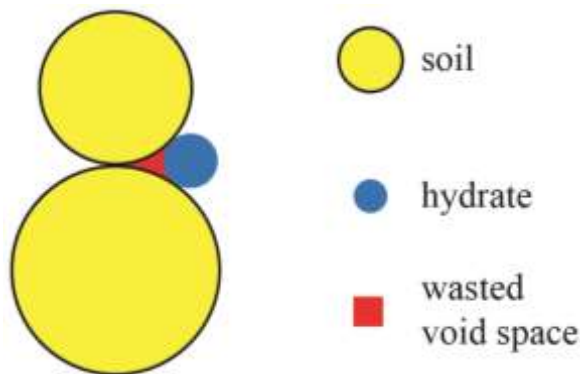


**Figure A-2:** 2-Dimension sketch of wasted space at particle contacts



In a 3-Dimension volume calculation of the wasted void space, the volume of the rotation shape of the wasted void space in 2 Dimensions should be calculated. The rotation axis for each contact type can be found in Figure A-3. Evidently, the volume of the wasted void space depends on the contact type and the particle size.

This method seems to be a good means of obtaining an improved hydrate saturation value in the DEM hydrate-bearing sediments. However, there are still several essential disadvantages:

(1) If 1000 hydrate particles are generated in the soil sample and form as a pore-filling or cementation model, the contact number of the cementation model must be larger than that of the pore-filling model, because the cementation hydrate particles form at the soil-soil contact and along the soil surface while the pore-filling hydrate particles are floating in the pore space. Through the wasted void space volume calculation, these two hydrate-bearing sediments should have different hydrate saturations, but there are the same number of hydrate particles inside the sample. If this is the case, the calculation appears to be incorrect.

(2) Secondly, when adding more hydrate particles to the sample, there is an uncertainty in the pore-filling sample that the added hydrate particles contact with the existing hydrate particles and then cause a movement of both, hence the existing conditions of contact types will be changed accordingly. However, in the cementation model, the newly added hydrate particles are only coated to the existing soil & hydrate skeleton with a given bonding strength. Once again, this calculation does not seem to be correct.

(3) Thirdly, from the calculation of the soil-soil contact type, it can be seen that there is already wasted void space in the existing soil skeleton even though there are no hydrate particles added. This means when there is no hydrate particle inside the soil sample, through this calculation method, there is already an assumed hydrate saturation. This does not seem reasonable.

## 4. Discussions

The three proposed calculation methods provide an insight into the assumption of the hydrate saturation in the DEM models. To some extent, the assumptions can be necessarily used in the DEM research. However, this assumption method seems to be too idealistic.

When the saturation was at a low value, it may not simply be assumed to be a higher value through the calculations and assumptions. The existing hydrate particles may not be able to perform the characteristics for the corresponding assumed higher value saturation. The geomechanical behaviours of the DEM hydrate-bearing sediments at a low hydrate saturation were similar to the behaviours of the experimental results at almost the same saturation value. For example, in the DEM pore-filling model in Chapter 4 and Chapter 7, the strength increased evidently only when the hydrate saturation was above 20%, which was similar to the experimental results that the strength increased obviously when the pore-filling hydrate saturation was over 20% ~ 25% (Waite et al., 2009).

However, when the accurate saturation of the DEM samples increased to 30% ~ 40%, the behaviours seemed to correspond to the experimental results with a higher saturation. The first example is that the magnitude of the increase in strength was much more evident, as discussed in Chapter 4 ~ 7. Secondly, from the small-strain stiffness study in Chapter 5, it can be seen that the trend of the increase in the small-strain shear modulus  $G_{max}$  at  $S_h=30\% \sim 40\%$  was similar to the trend in the experimental study at a very high saturation about 70% ~ 100% (Soga et al., 2006; Waite et al., 2009).

Hence, from the discussions above, it may be suggested that the hydrate saturation calculation in the DEM study should be considered more carefully, and one calculation method may not be able to apply to all situations. Further studies are needed for more accurate hydrate saturation values for interpreting the behaviours of the DEM hydrate-bearing samples.

## Appendix B

### Yield surface

As discussed above, the geomechanical behaviour of granular hydrate-bearing soil is similar to that of structured soils. Hence, it is natural to suggest that a constitutive model of methane hydrate sediment should also cover all the geomechanical behaviours (i.e. increased stiffness and strength, dilatancy, and structure degradation) as previously mentioned. Hydrate-bearing soil is unique in its mechanical behaviour. A better understanding and modelling of the geomechanical behaviour of hydrate-bearing soil is very important. Thus, there is a demand for developing soil constitutive models that incorporate the effects of hydrate in order to predict the behaviour of hydrate soil. To this day, because of the material limitations of mechanical experimental data, the precise constitutive characteristics of the hydrate-bearing soil structure is yet unknown. As mentioned above in Section 2.2.2, the experimental data currently obtained has not shown very large strain and critical state behaviours of the sediment.

On the basis of critical state soil mechanics and the most recent constitutive models for hydrate-bearing sediments (Roscoe et al., 1968; Freiji-Ayoub et al., 2007; Rutquist et al., 2007; Kimoto et al., 2010; Klar et al., 2010;), Uchida et al. (2012) developed a new constitutive model ‘Methane Hydrate Critical State model’ (MHCS) which captured the behaviour of hydrate-bearing soil. This new proposed constitutive model, MHCS, incorporated most of the essential elements including stiffness, strength, dilation, softening, volumetric yielding and bond degradation. In the MHCS model, the yield function  $f$  is:

$$f = q^2 + M^2(p' - p'_{cc})[p' - (p'_{cs} + p'_{cd} + p'_{cc})] \quad (\text{B-1})$$

where  $q$  is the deviatoric stress,  $p'$  is the effective mean stress,  $p'_{cs}$  is the yield locus of soil and  $M$  is the property of the material which is related to the frictional behaviour

of the sediment.  $p'_{cc}$  is the hardening parameter for cohesion, and  $p'_{cd}$  is the hardening parameter for dilation, where both hardening parameters are connected with hydrate saturation:

$$p'_{cd} = a(S_h)^b \quad (\text{B-2})$$

$$p'_{cc} = c(S_h)^d \quad (\text{B-3})$$

where a, b, c and d are the material constants.

Figure B-1 and Figure B-2 illustrate the mechanisms of dilation enhancement and cohesion enhancement to the yield surface expansion. The added  $p'_{cd}$  causes the yield surface to expand to the right side in the  $p' : q$  space. While the added  $p'_{cc}$  enlarges the yield surface concordantly with both the left and right sides, which offers an increase in cohesion but does not affect the dilation upon yielding. This enhanced yield surface is illustrated in Figure B-3.

The fact is that there is no clear separation between the elastic and plastic state in real soils. Hence, for the purpose of smooth transition from the elastic behaviour to the plastic phase, Hashiguchi's (1989) sub-loading surface ratio  $R'$  is employed:

$$f = q^2 + M^2(p' - p'_{cc})[p' - R'(p'_{cs} + p'_{cd} + p'_{cc})] \quad (\text{B-4})$$

$$dR' = -u \left( 1 + \frac{p'_{cd} + p'_{cc}}{p'_{cs}} \right) \ln R' | d\varepsilon^p | \quad (\text{B-5})$$

where  $u$  is the material constant that dominates the plastic deformation within the yield surface.  $dR' > 0$  refers to the plastic phase while  $dR' < 0$  represents elastic phase of the soil.

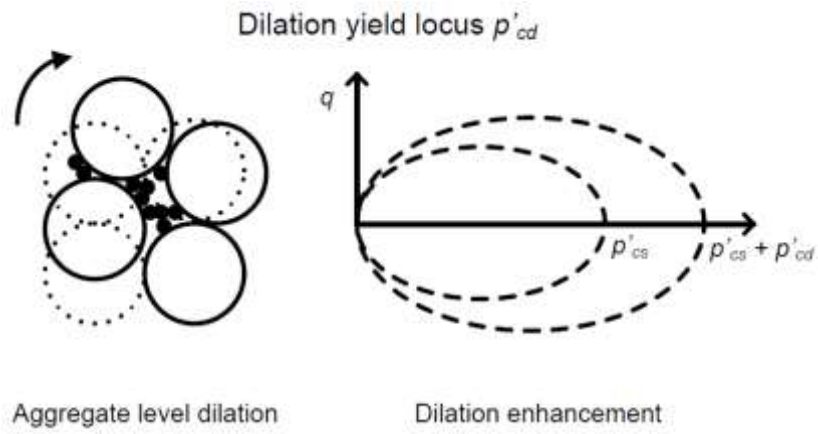


**Figure B-1:** Dilation enhanced by hydrates (Uchida et al., 2012)

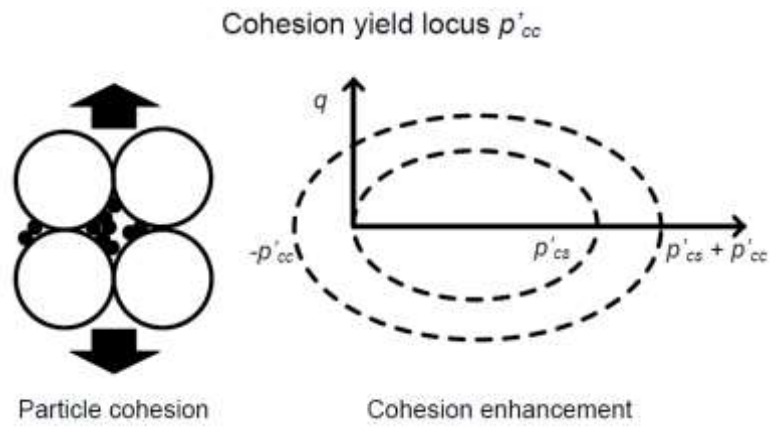


**Figure B-2:** Cohesion enhanced by hydrates (Uchida et al., 2012)

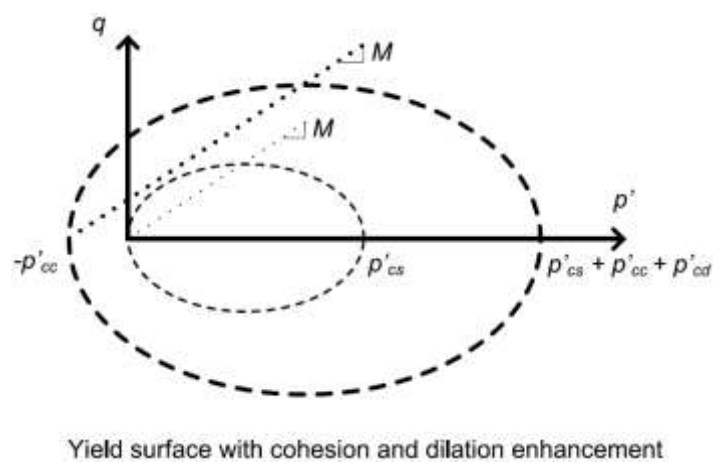


**Figure B-3:** Yield surface of MHCS model (Uchida et al., 2012)

On the whole, the MHCS model performed by Uchida et al. (2012) was devised so as to produce more realistic hydrate-bearing soil behaviour. It provides the reference model for the geomechanical investigations of sediments in order to verify the acquired results. Nevertheless, to perform further and more precise studies, not only the well-controlled on-site and laboratory tests, but also appropriately designed numerical simulations are required.

According to the MHCS model (Uchida et al, 2012), compared to the pure soil sediment, the shear strength of methane hydrate-bearing soil sediment exhibits the geomechanical behaviour which are enhanced by both dilation effect and cohesion effect. This is because of the existence of hydrates which occupy the pore space (pore-filling and cementation) contributing to the dilation effect, as well as the bonded contacts (cementation) contributing to the cohesion effect. From the simulation results presented in Chapter 4 ~ 7, it was also shown that the presence of pore-filling hydrates increased the strength, whereas the presence of cementation hydrates with bonding strength increased the strength of the sediments even more. Hence, the DEM simulations reflected the same behaviours as what the MHCS model does.

In this appendix, the hydrate-bearing sediment samples under 1 MPa confining pressure as described in Chapter 4 were programmed for a general stress-path test, as shown in Figure B-4 and Figure B-5 by yellow lines. The yield surfaces in the  $p'$ - $q'$  space were formed by connecting the yield points of different stress path for various hydrate saturations. The yield points are defined by the peak failure of a particular shear test. The numerical results from simulations of these stress paths were then compared with those of the traditional triaxial tests conducted under the confining pressure of 1 MPa, 2 MPa and 3MPa, of which the yield points generally corresponded to the same location of derived yield surfaces.

Figure B-4 illustrates the yield surface expansion in the  $p'$ - $q'$  space, due to the presence of the pore-filling hydrate particles in the pore-filling model. There is an expansion of the yield surface with an increase in hydrate saturation. The yield surfaces were also extended to a higher stress range by adding the data of traditional triaxial tests under 3 MPa confining pressure.

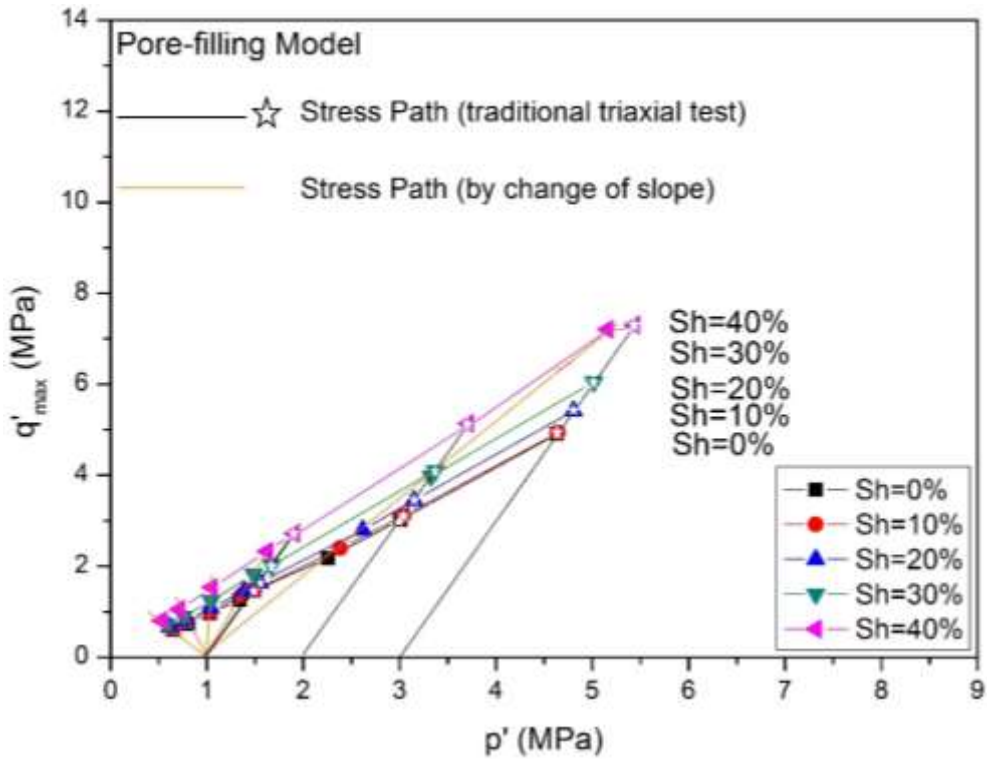


**Figure B-4:** Stress paths of DEM simulations and yield surfaces obtained from the yield points at various hydrate saturations: pore-filling model

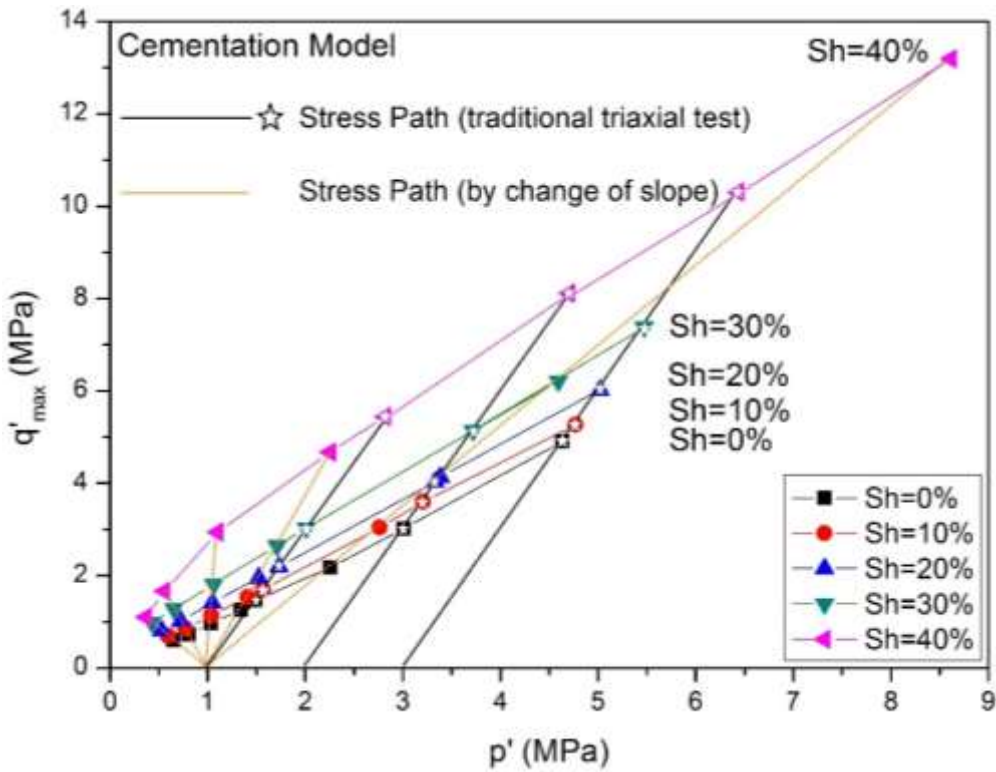


**Figure B-5:** Stress paths of DEM simulations and yield surfaces obtained from the yield points at various hydrate saturations: cementation model

Figure B-5 evidently shows a more significant expansion of the yield surfaces in the  $p' - q'$  space, compared to the pore-filling model in Figure B-4, regardless of only a small increase in dilation angle. This is because of the mechanism of cohesion enhancement which contributed to enlarging the yield surfaces.

The expansion of the yield surfaces of the DEM hydrate-bearing samples in the  $p' - q'$  space exhibits the contribution of the presence of hydrates to the pore-filling and cementation sediments' strength. It can also be found that the cohesion enhancement contributed to a further increase in strength, as shown in Figure B-6.

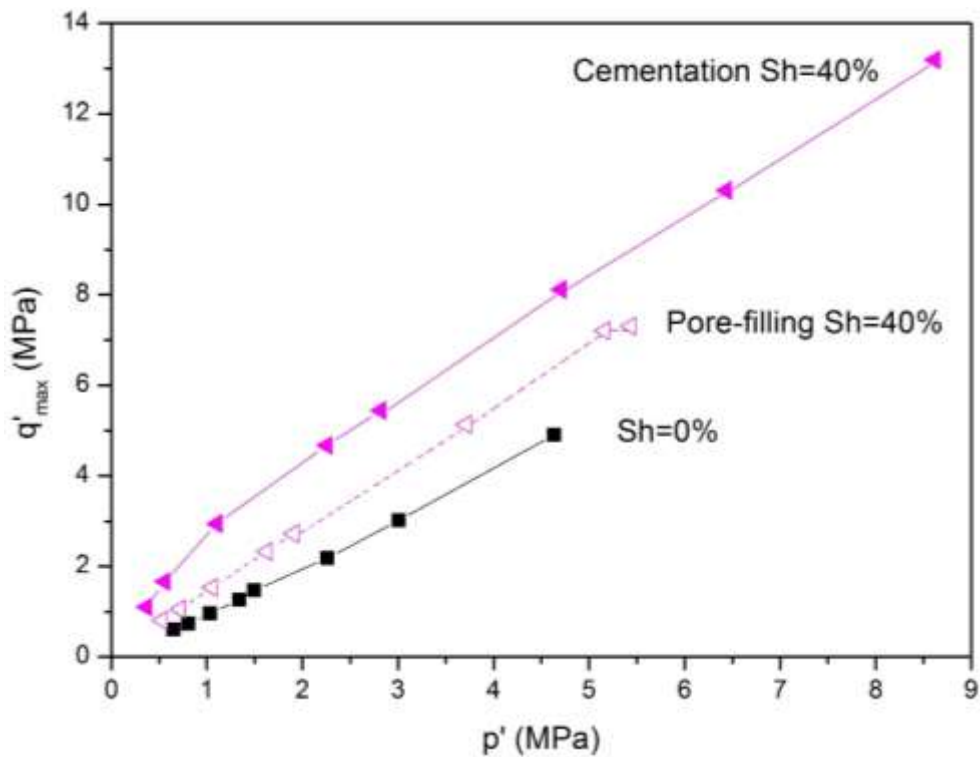


**Figure B-6:** Comparisons of yield surfaces of the pure soil samples ( $S_h=0\%$ ), pore-filling samples ( $S_h=40\%$ ) and cementation samples ( $S_h=40\%$ )

## Appendix C

### Microstructure evolution

During the shearing process of the triaxial test, there was a complex and continuous evolution of the particle-particle contacts. In this microstructure evolution, the shearing caused the anisotropy of the distribution of the contact normal and contact force, so that the loading force was mainly transmitted through the principle stress directions. In this process, the existing particle-particle contacts disappeared and the new contacts appeared. This rearrangement of the contacts made the fabric anisotropy evolve, especially for the hydrate-bearing soil samples of a mixture of hydrate and soil particles with different stiffness and sizes. Hence, in this appendix, the microstructure anisotropy evolution during the shearing process is depicted in three aspects: contact normal ( $a_d^r$ ), normal contact force ( $a_d^n$ ) and tangential contact force ( $a_d^t$ ) accordingly.

There are a few internal parameters which interpret the state of the particle-scale sample – the contact number, the density of contact (or coordination number), contact vectors and contact normal, normal contact forces and tangential contact forces, contact force directional distributions. Sitharam et al. (2009) summarized that a second-order fabric tensor can describe the contact normal distribution. The symmetric fabric tensor is interpreted by the distribution function  $E(\Omega)$  (Rothenburg and Bathurst, 1989; Sitharam et al., 2002):

$$E(\Omega) = \frac{1}{4\pi} (1 + a_{ij}^r n_i^c n_j^c) \quad (\text{C-1})$$

Where  $n^c$  is contact normal orientation, the coefficient term  $a_{ij}^r$  is related to the fabric tensor obtained from the measured discrete information.

Sitharam et al. (2009) described that, for an isotropic assembly, the coefficients in Equation (C-1) are zero and the  $E(\Omega)$  is  $\frac{1}{4\pi}$ . If  $a_{ij}^r > 0$ , the implication is that the

contact density is greater than that of the isotropic assembly; and if  $a_{ij}^r < 0$ , the implication is that the contact density is smaller than that of the isotropic assembly. Additionally, the deviatoric anisotropy coefficients can be expressed as:

$$a_d^r = \sqrt{\frac{3}{2} a_{ij}^r a_{ij}^r} \quad (\text{C-2})$$

$$a_d^n = \sqrt{\frac{3}{2} a_{ij}^n a_{ij}^n} \quad (\text{C-3})$$

$$a_d^t = \sqrt{\frac{3}{2} a_{ij}^t a_{ij}^t} \quad (\text{C-4})$$

where  $a_{ij}^r$ ,  $a_{ij}^n$ , and  $a_{ij}^t$  are the symmetric second-order deviatoric tensor describing the coefficient of contact normal (fabric anisotropy), normal contact force anisotropy and tangential contact force anisotropy.

In this appendix, the pure soil samples (with spherical soil particles or elongated soil particles) and the according hydrate-bearing sediment samples under 1 MPa confining pressure as described in Chapter 4 and Chapter 7 were programmed for a microstructure evolution study. The initial data are presented in Figure C-1 ~ C-4.

Figure C-1 shows the fabric anisotropy evolution during the triaxial tests of the hydrate-free soil sample ( $S_h = 0\%$ ), pore-filling sample ( $S_h = 20\%$ ) and cementation sample ( $S_h = 20\%$ ) when the soil particles were spherical. Throughout the whole shearing process, the three samples's anisotropy evolutions were obviously different.

Figure C-1 (a) shows the contact normal anisotropy  $a_d^r$  evolution against the axial strain. As the axial strain increased, the contact normal anisotropy increased first and then decreased. The peak and large strain  $a_d^r$  was different for the three samples: the  $S_h = 0\%$  sample's  $a_d^r$  was the largest, while the hydrate-bearing samples'  $a_d^r$  was smaller than the soil sample, and the cementation model's  $a_d^r$  was the smallest. Figure C-1 (b) shows the normal contact force anisotropy  $a_d^n$ . It is shown that the hydrate-

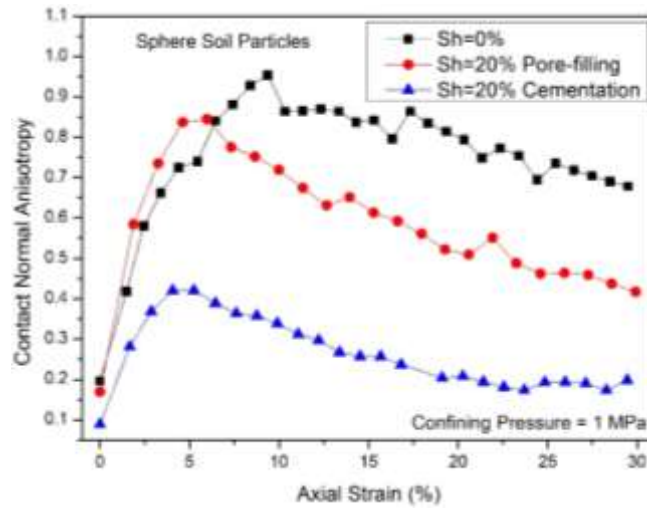
bearing samples'  $a_d^n$  was larger than that of the hydrate-bearing soil sample. And the cementation model shows a larger  $a_d^n$  than the pore-filling model. In addition, Figure C-1 (c) presents the tangential contact force anisotropy  $a_d^t$ . It increased to the different peak values and then decreased to a similar value range. Regarding the different peak values, the hydrate-bearing samples'  $a_d^t$  was larger than that of the hydrate-bearing soil sample. And the cementation model shows a larger  $a_d^t$  than the pore-filling model.

It can be summarized that, during the shearing process of the assembly, the contact normal anisotropy, normal contact force anisotropy and tangential contact force anisotropy experienced a dramatic evolution process. Due to the involvement of the hydrate particles, the contact normal is closely related to the particle material deformation. While the normal contact force anisotropy and tangential contact force anisotropy are more related to the sample's strength. In addition, the hydrate growth pattern influences the anisotropy evolution.

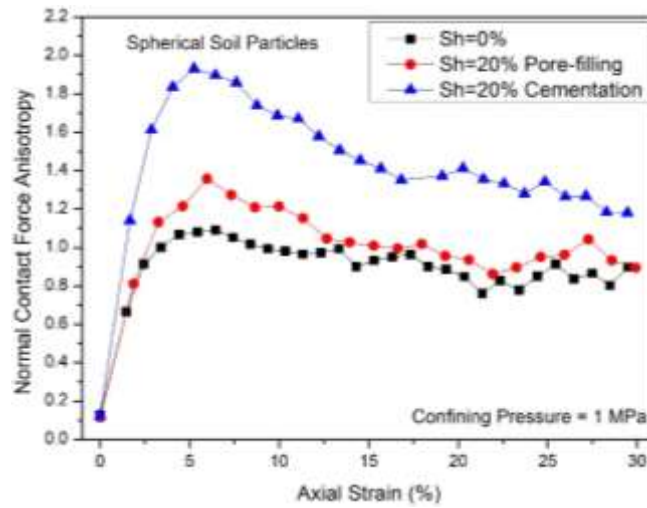
In order to study the shape effect of the soil particles on the microstructure evolution, a series of comparisons were made among the spherical soil particles (aspect ratio = 1.0), 2-particle clump soil particles (aspect ratio = 1.5) and 3-particle clump soil particles (aspect ratio = 2.0).

Figure C-2 shows the comparisons of the hydrate-free soil samples; Figure C-3 shows the comparisons of the pore-filling hydrate-bearing samples; and Figure C-4 shows the comparisons of the cementation samples. In each figure, the comparisons were made separately in contact normal anisotropy, normal contact force anisotropy and tangential contact force anisotropy accordingly.

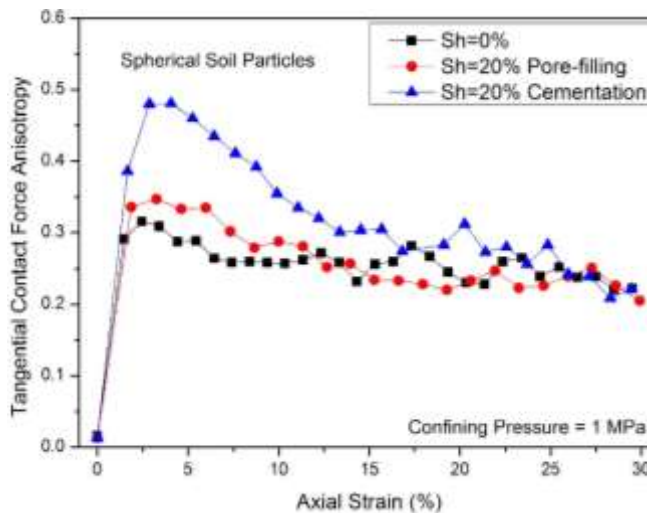
Generally, it can be seen that as the aspect ratio increased, the contact normal anisotropy, normal contact force anisotropy and tangential contact force anisotropy all increased obviously. And in these cases, the hydrate particles' influence was not very evident.



(a) Contact normal anisotropy

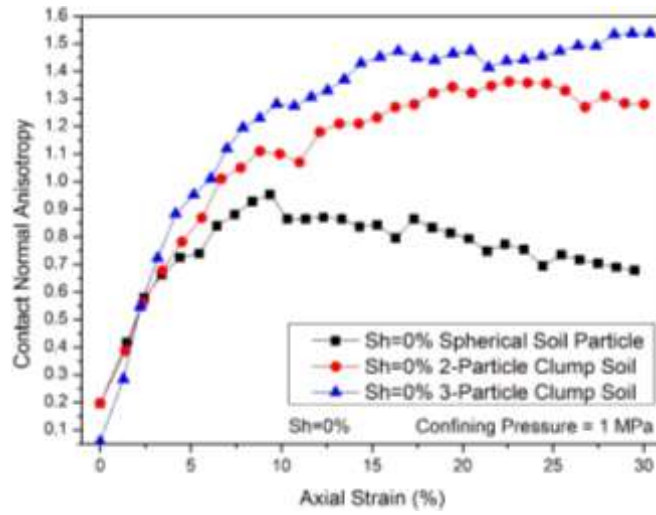


(b) Normal contact force anisotropy

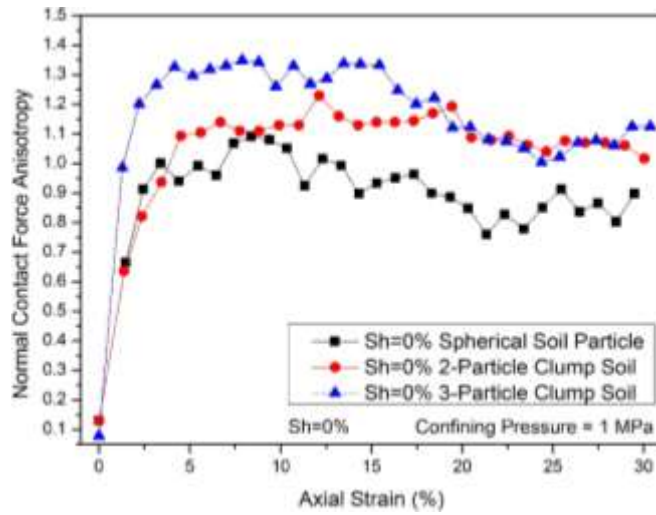


(c) Tangential contact force anisotropy

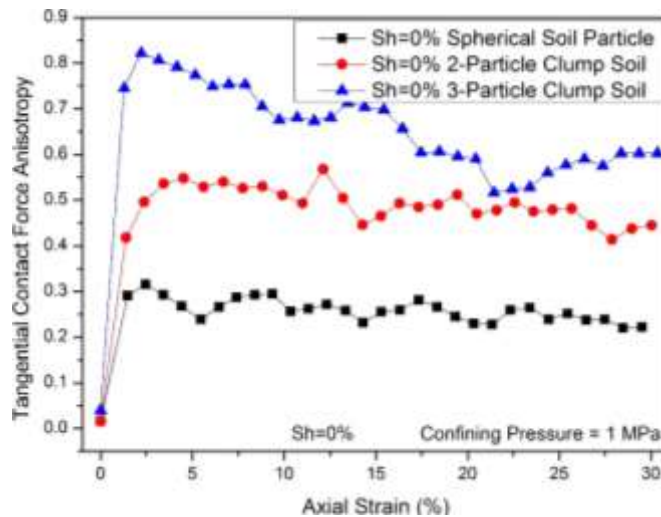
Figure C-1: Anisotropy evolution during the triaxial tests (spherical soil particles)



(a) Contact normal anisotropy

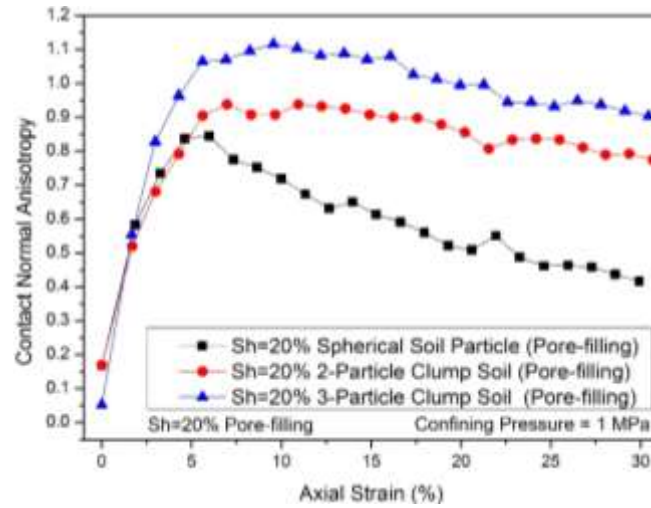


(b) Normal contact force anisotropy

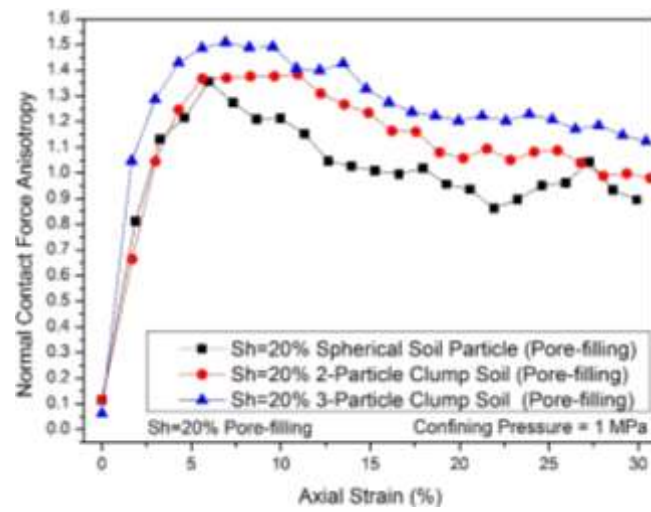


(c) Tangential contact force anisotropy

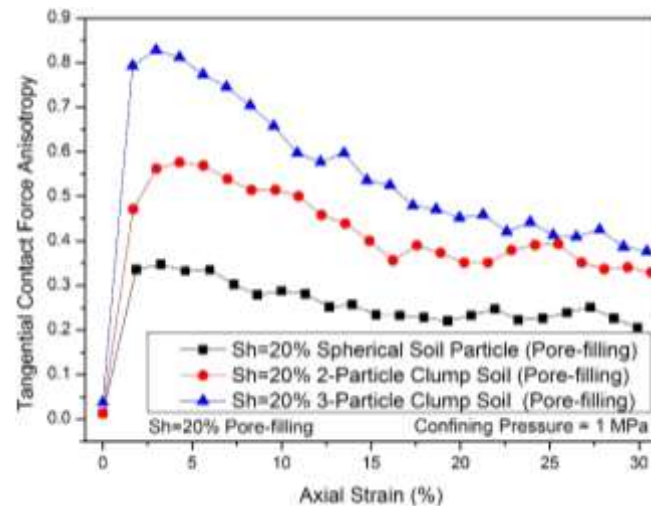
Figure C-2: Anisotropy evolution during the triaxial tests ( $S_i=0\%$  with various soil shapes)



(a) Contact normal anisotropy

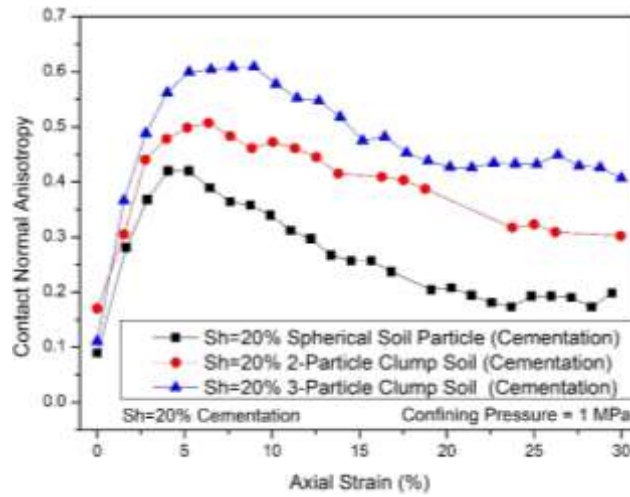


(b) Normal contact force anisotropy

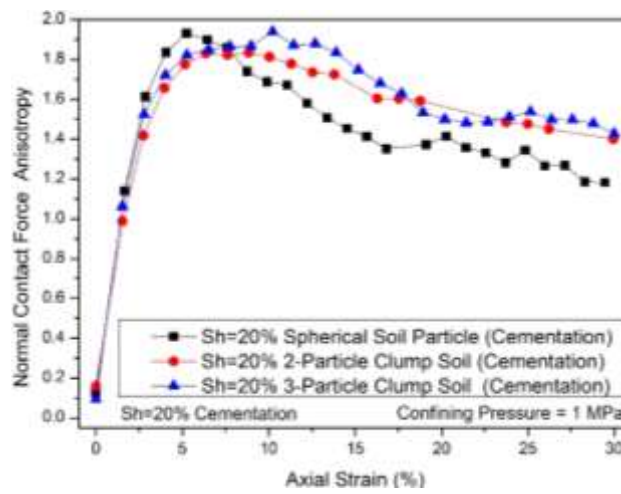


(c) Tangential contact force anisotropy

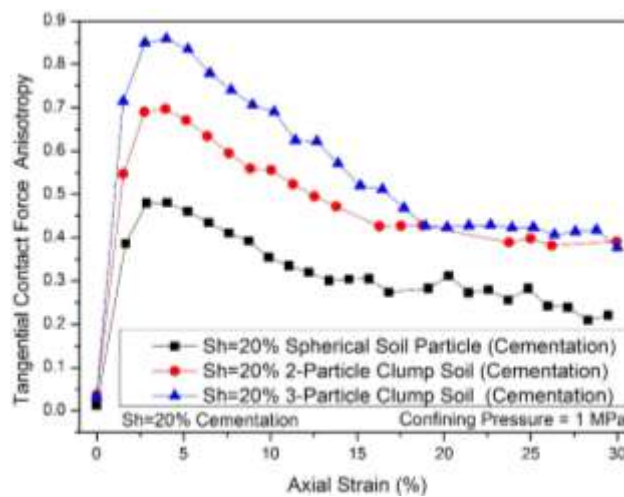
**Figure C-3:** Anisotropy evolution during the triaxial tests ( $S_r=20\%$  pore-filling samples with various soil shapes)



(a) Contact normal anisotropy



(b) Normal contact force anisotropy



(c) Tangential contact force anisotropy

**Figure C-4:** Anisotropy evolution during the triaxial tests ( $S_i=20\%$  cementation models with various soil shapes)

## Appendix D

# Commercial potential and exploitation of methane hydrate

**Acknowledgement:** This Appendix D is finished under the requirement of UCL Advances Enterprise Scholarship.

As introduced in Chapter 1, methane hydrate, which is also called “Burning Ice” or “Fiery Ice”, attracts worldwide interest because of the huge amounts of methane gas that can be extracted from hydrate-bearing sediment through large-scale commercial exploitation. Methane gas is the predominant element of natural gas. It is well known that there is huge commercial potential in the immense global deposits of methane hydrate under deep seabeds and permafrost regions.

Increasing global attention was attracted after Japan announced on 12<sup>th</sup> March 2013, that Japan Oil, Gas and Metals National Corporation (JOGMEC) had launched an industrial-scale experimental exploration and successfully extracted methane from deep-sea methane hydrate sediment layers near the Aichi Prefecture of Japan through the means of depressurization technology. This made Japan the first country to master the technique of excavating natural gas hydrate from the seabed. This was the first time in the world that someone had successfully extracted methane gas from deep seabeds. It is big news for Japan, a country where natural resources are scarce. It was also a big breakthrough in new energy development for the world.

In this appendix, the commercial potential of methane hydrate is presented, and the commercial exploitation methods and current technology difficulties of the methane hydrate industry are discussed.

## 1. The increasing global needs of natural gas

The BP Outlook 2035 (BP plc., 2014) presented figures for past global energy consumption, reaching back as far as 1990 and stretching into the future until 2035, as illustrated in Figure D-1. Regarding energy resources in the BP Outlook 2035 (BP plc., 2014), they are classified into two categories: conventional energy resources and unconventional energy resources. The conventional energy includes the fossil fuels – coal, oil and natural gas. And the unconventional energy includes nuclear, hydroelectricity and renewables (i.e. wind power, solar electricity).

It is clearly suggested in Figure D-1 that the total energy consumption increased steadily in the past, and the increase will keep relatively constant in the future until 2035. Conventional energy played the most important role in the past, and it also keeps this significant role in the future with a steady consumption increase, although unconventional energy consumption will also increase.

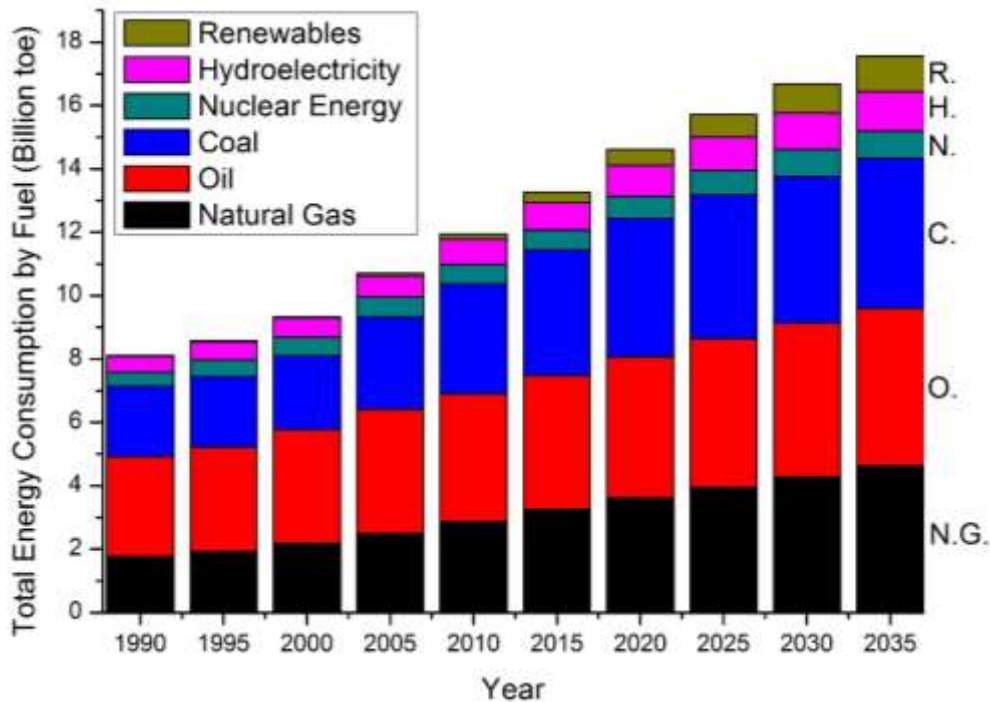


**Figure D-1:** Global total energy consumption by fuel (BP plc., 2014)

From Figure D-1, it can be seen that coal, oil and natural gas have equal importance. However, from the perspective of resource deposits, coal and oil resources

are much rarer than natural gas under the earth. Secondly, from the view of environmental protection, natural gas is a relatively clean burning energy compared to coal and oil. Although natural gas cannot replace the important role of coal and oil in their industrial and commercial use, the exploitation of natural gas seems to be more profitable as an energy resource from a long-term perspective. In addition to this, methane is the predominant natural gas, so that its exploitation is essential to the natural gas industry.

## **2. Commercial potential of methane hydrate**

Just like the already massively developed shale gas, methane hydrate is also expected to be one of the main energies of the future. The International Energy Agency (IEA) optimistically estimates that the development and utilization of methane hydrate will bring about an “energy revolution”. As the main resource of methane gas, methane hydrate attracts worldwide interest, because methane hydrate is not only widespread, but also possesses a huge deposit under the earth. An estimate from the data released by the United States Geological Survey (2013) says that the total organic carbon contained in methane hydrate amounted to twice as much as the carbon content of the world’s known fossil fuels.

Every 1 m<sup>3</sup> methane hydrate can release 164 m<sup>3</sup> methane gas. It is estimated that methane hydrate is typically distributed within a 1000 meters range beneath seabeds and permafrost regions. The seabed deposit is much larger than the permafrost region deposit. It is estimated that the distribution areas of seabed methane hydrate covers about 10% of the total area of the oceans’, with this distribution area reaching up to 40 million m<sup>2</sup>. It is generally believed that the world’s conventional gas reserves are 300 trillion m<sup>3</sup> and shale gas reserves nearly 200 trillion m<sup>3</sup>. According to these estimations, methane reserves under the seabed are over 1000 trillion m<sup>3</sup>, which is double the sum of the world’s shale gas and conventional gas reserves, and sufficient for human being to use for a very long time.

Methane hydrate has been labelled “one of the best alternative energy in the future” due to its inherent advantages such as wide distribution, huge deposit and high density

of energy. There is also, within the industry, a well-known feeling that “whoever masters the technology to exploit natural gas hydrate shall dominate the world energy development of the 21st century”.

At present, most energy importing countries, which are open to the sea, possess rich natural gas reserves of methane hydrate. Four countries, U.S., Japan, India and China, import per year about a quarter of the international total trade volume of natural gas. If any of the energy departments of these countries could make a breakthrough in the commercialized exploitation of methane hydrate natural gas, it would immediately influence today’s world energy structure.

Today, revolutionary changes in the balance of energy sources has already occurred in the world’s natural gas market, and it is believed that the development of methane hydrate natural gas may be the next factor that can shake the world’s energy system. Even if methane hydrate’s development has not seen any benefit and not been proved effective so far, this kind of fuel may lead a revolution in the world’s energy market along with the birth of new technologies. Thus, the technology of methane hydrate exploitation has a cheerful prospect, and the cost of methane hydrate natural gas exploitation could be as competitive as that of shale gas and other unconventional gas exploitation.

### **3. Conditions of methane hydrate formation**

Generally, methane hydrate develops and exists in the pores of highly compacted soil sediments in various distribution patterns. The formation of methane hydrate requires three basic conditions: temperature, pressure and the methane gas source.

Firstly, the temperature cannot be too high. It is capable for methane hydrate to form above zero, in which 0°C~10°C is desirable, and 20°C is the upper limit. Methane hydrate will be dissociated at higher temperatures. Secondly, the pressure needs to be sufficient, although not be too high, to be capable of forming at 100 kPa and –80 °C, or at 2.5 MPa and 0 °C (Brugada et al., 2010). These are the reasons that methane hydrate is usually found in deep seabed sediment or terrestrial permafrost regions,

because only under both high pressure and low temperature conditions, can it maintain stability.

Thirdly, there should be methane gas source. Generally, there are two views regarding the cause of formation of methane hydrates. One considers that methane originates in the bacteria beneath the sea. The remains of a great many organisms in the sea, when corruptingdecaying?, produce bacteria which releases methane; the methane gas produced by the bacteria is locked into hydrate provided a high-pressure and low-temperature condition. Another theory considers that methane results from oceanic plate movement. When oceanic plate is subsiding, the older oceanic crust goes under the earth's interior, and the oil and gas in the seabed upwells to surface along the plate boundary. Once exposed to cold seawater, under the deep-sea pressure, methane gas and sea water form into hydrate via chemical action.

#### **4. Exploitation methods of methane hydrate**

In fact, the promising energy resource methane hydrate is a prickly rose that can both cheer the world up and bring the world down. Up until now, the way of safely, environmentally-friendly and economically exploiting methane hydrate remains a problem for the whole world. Although nations are eager for methane hydrate, there is a mutual bottom line for everyone: before an ideal exploitation method is proposed, methane hydrate must not be massively exploited as conventional mineral resources are. It is believed that whether methane hydrate will become one of the main energy resources in the 21st century depends on whether a breakthrough will be made regarding the exploitation technology. The seabed deposit is much larger than the permafrost region deposit, yet the technology issues prove more difficult for deep see exploitation.

Due to the complex conditions of the development and existence of methane hydrate in the hydrate-bearing sediment under the deep seabeds and permafrost regions, currently there are three main methods proposed for the commercial exploitation of methane hydrate:

The first method is “thermal injection”, in which hot water is injected into the well so as to cause an increase in temperature. Methane hydrate dissociates when being heated. The first problem of this method is the difficulty of collecting methane gas. The porous medium under the sea does not behave as a “mass”, nor is it a block of rock, but is dispersed evenly. The problem to be solved lies in the way of laying pipelines and collecting efficiently. The second problem is the very high cost in both capital and energy in pouring the hot water. It could be considered as exchanging energies.

The second method is “chemical replacement by carbon dioxide (CO<sub>2</sub>)”. If CO<sub>2</sub> is injected into the seabed methane hydrate reservoir, as CO<sub>2</sub> forms hydrate more easily than methane does, it can “squeeze out” methane molecules in the hydrate, and replace methane to form carbon dioxide hydrate. This method is also a good way of depositing greenhouse gas CO<sub>2</sub> and protecting the environment. However, one of the problems of this method is the carbon dioxide hydrate near the well may block the flow of methane into the well.

The third one is “depressurization”. The well pressure is decreased in order to allow flow into the well and cause the methane hydrate dissociation by the pressure reduction in the surrounding soil sediment. On March 2013, Japan launched the industrial-scale experimental exploration and successfully extracted methane from a deep-sea methane hydrate sediment layer near Aichi Prefecture of Japan by means of this depressurization technology. By pumping the water out of the methane hydrate so as to depressurize it, the methane is separated from the water and finally extracted. This is the world’s first success of dissociating methane hydrate under the sea.

## **5. Difficulties of large-scale commercial exploitation of methane hydrate**

Currently, including all of the exploitation technology development issues, the large-scale exploitation of methane hydrate from hydrate-bearing sediments still confronts several main problems:

(1) Global warming:

It is believed that methane contributes to global warming 20 times as much as carbon dioxide does. If methane hydrate is induced to automatically dissociate or overflow during the exploitation, there will be a much more serious greenhouse effects which will challenge the atmosphere and eco-environment. In consideration of the environmental hazards that may be induced by improper exploitation, all countries in the world are cautious before taking actions.

(2) Geological disasters:

Since methane hydrate typically exists as a cement of the sediment, its formation and dissociation effects on the sediment's strength, which may induce submarine landslide and other geological disasters. The changes in temperature and pressure caused by natural or human factors can dissociate hydrates, leading to submarine landslide, species extinction, climate warming and other environmental hazards. Studies released by the United States Geological Survey indicate that methane hydrate may induce continental slope landslides which are an enormous threat to the various undersea facilities. Therefore, methane hydrate as the energy of the future is also a dangerous energy.

(3) Expensive cost:

Due to the current technology limitations, the high cost of exploitation is inevitable. The United States previously estimated the exploitation cost of seabed methane hydrate. They managed to collect methane hydrate by submarine, and to dissociate it on land. It was found that the cost was 200 dollars per cubic meter. If 1 m<sup>3</sup> methane hydrate amounted to 164 m<sup>3</sup> gas, the gas production cost would be 1.2 dollars / m<sup>3</sup>, while the U.S. gas importing price in 2012 was only 0.087 dollar / m<sup>3</sup>.

(4) No feasible and systematic exploitation technology:

It is of great urgency to conduct researches regarding methane hydrate's indoor and outdoor dissociation, synthesis and drilling-production methods. As mentioned above, the currently proposed exploitation methods are still immature technologies, in respect of cost, long-term exploitation, etc..

(5) Difficulties in transportation and reservoir management:

Because methane hydrate cannot stably exist under normal pressure and dissociates when the temperature is above 20°C, the solution of transportation and reservoir management is one of the key issues to the large-scale exploitation of methane hydrate. Currently, samples collected from exploration are typically stored in sealing containers which are full of helium gas under low temperature. As for large-scale means of storage and transportation, researches on relevant technologies and facilities are being conducted intensely all over the world.

The above challenges have become enormous obstacles in the way of the large-scale exploitation of methane hydrate. Nevertheless, these problems will undoubtedly be solved, as technology improves and science develops.

## **6. Industry of methane hydrate**

Since the 1960s, the research of exploration of methane hydrate has drawn more and more attention globally. In the early 1960s, the former Soviet Union discovers the first methane hydrate reservoir in Siberia. The U.S. government commenced the investigation of methane hydrate in 1969, and listed methane hydrate as strategic energy for national development in the national long-term plan in 1998.

So far, many countries, including the US, Canada, Russia, China, India, South Korea and others, have established long-term research projects regarding methane hydrate. However, the high cost of exploitation has become the biggest obstacle in methane hydrate exploitation. Due to the crisis of energy shortage, many countries are still enthusiastic for this new type of clean energy, and for this reason, have all contributed to the large-scale exploration as well as exploitation technology research.

China also announced a plan in the research of methane hydrate within the next twenty years. A national research and development project in Japan is aiming for commercial large-scale exploitation by 2018. Another reserve with rich economic potential is in the Gulf of Mexico where the huge deposit of methane resource may be deposited. Regarding the exploitation plan, for example, China launched its special study on methane hydrate in 2011. The established development schedule indicates that the exploration survey and technical preparation will be fulfilled between 2008

and 2020, the commercialized pilot production will be carried out between 2021 and 2035, and the offshore large-scale commercial exploitation will be conducted between 2036 and 2050.

Another successful example is the National Methane Hydrate Development Program of Japan which is carried out in 3 stages. In the first stage, two successful experiments were performed in 2002 and 2008 respectively, when methane gas was extracted from land deposits. In the second stage, which is from 2009 to 2015, two production trials should be performed in the Japanese surrounding seas. In this stage, economic efficiency and environmental impact of extracting methane gas from seabed geosphere should also be verified. The third stage of this Methane Hydrate Development Program will be from 2016 to 2018, in which the commercial production value, exploitation effectiveness and environmental impact of methane hydrate will be ultimately overall assessed on the basis of the research and test results of the two former stages.

On the 12<sup>th</sup> March, 2013, the success of the experiment to disassociate and extract methane gas from methane hydrate in the seabed strata near Aichi Prefecture was announced by the Agency for Natural Resources and Energy of Japan's Ministry of Economy, Trade and Industry. This is the world's first time to successfully extract methane gas from the seabed. It is good news for Japan, a country where natural resources are scarce. It is also reported that methane hydrate reserves around Japan is equivalent to 100 years of Japanese gas consumption. Methane hydrate might contribute to Japan's energy demand in the future. Japan expects to decrease or even cast off its dependency on foreign countries and to realize energy self-sufficiency through the commercialized production of methane hydrate.

## **7. Summary**

Methane hydrate draws global attention as a promising natural gas resource with a huge worldwide deposit due to the increasing needs of natural gas. Its wide distribution, huge deposit and high density of natural gas will definitely influence the world energy structure of the future. Its commercial potential may be underestimated due to the

limitations of the current exploration technologies, and there will be more reserve sites being found in the near future.

Due to the complex formation process of methane hydrate, the instability of its chemical property and the complexity of its soil deposit's geological properties, severe problems may occur in the large-scale commercial exploitation. Hence, technological progress is crucial to the solution of the challenges. The technology issues are the main obstacles facing commercial exploitation, although many countries have been contributing to this significant technology development for many years. However, the success of the large-scale experimental exploitation of methane hydrate in Japan means this promising energy resource could be a reality. This may also lead the world to take further steps forward for the future of the large-scale commercial exploitation of methane hydrate.

---

## Reference

Al-Bulushi, S. (2012). Quantification of gas hydrates in fractured marine sediments, Krishna Godavari Basin, India. Master of science thesis, May 2012, Oklahoma State University.

Berge, L. I., Jacobsen K. A., and Solstad A. (1999). Measured acoustic wave velocities of R11(CCl<sub>3</sub>F) hydrate samples with and without sand as a function of hydrate concentration, *J. Geophys. Res.*, 104, 15,415–15,424, doi:10.1029/1999JB900098.

Bolton, M. D. (1986). The strength and dilatancy of sands, *Geotechnique* 36, No. 1, 65-78.

Boswell, R., and Collett T. (2006). The gas hydrates resource pyramid, *Fire in the Ice: Methane Hydrate Newsletter*, fall, pp. 5–7, Off. of Fossil Energy, Natl. Energy Technol. Lab., U.S. Dep. of Energy, Washington, D. C.

BP plc. (2014). BP Outlook 2035, assessed by BP official website, [bp.com/energyoutlook](http://bp.com/energyoutlook).

Briaud, J. L., and Chaouch, A. (1997), Hydrate melting in soil around hot conductor, *J. Geotech. Geoenviron. Eng.*, 123, 645–653, doi:10.1061/(ASCE)1090-0241(1997)123:7(645).

Brugada, J., Cheng, Y. P., Soga, K., and Santamarina, J. C. (2010). Discrete element modelling of geomechanical behaviour of methane hydrate soils with pore-filling hydrate distribution, *Granular Matter*, 2010, vol. 12, no. 5, pp. 517-525.

Burland, J. B., (1989). Small is beautiful: the stiffness of soil at small strains. *Canadian Geotechnical Journal*, Vol. 16, No. 4, pp. 499-516.

Chand, S., Minshull, T. A., Gei, D. and Carcione, J. M. (2004), Elastic velocity models for gas-hydrate-bearing sediments—A comparison, *Geophys. J. Int.*, 159, 573–590, doi:10.1111/j.1365-246X.2004.02387.x.

Chand, S., Minshull, T. A., Priest, J. A., Best, A. I., Clayton, C. R. I., and Waite, W. F. (2006). An effective medium inversion algorithm for gas hydrate quantification and its application to laboratory and borehole measurements of gas hydrate-bearing sediments, *Geophys. J. Int.*, 166, 543–552, doi:10.1111/j.1365-246X.2006.03038.x.

Chand, S., Minshull, T.A., Gei, D., and Garcione, J.M. (2004), Elastic velocity models for gas-hydrate-bearing sediments – a comparison, *Geophys. J. Int.* (2004) 159, 573-590. DOI: 10.1111/j.1365-246X.2004.02387.x

Cheng, Y. P., (2004). Micromechanical investigation of soil plasticity. Cambridge University, PhD thesis.

Cheng, Y. P., Nakata, Y., Bolton, M. D., (2003). Discrete element simulation of crushable soil. *Geotechnique*, 53, No. 7, 633-641.

Cheng, Y.P., Bolton, M.D. and Nakata, Y. (2004) Crushing and plastic deformation of soils simulated using DEM. *Geotechnique*, 54, (2), 131-141.

Clayton, C. R. I., Priest, J. A. & Best, A. I. (2005). The effects of disseminated methane hydrate on the dynamic stiffness and damping of a sand. *Geotechnique* 55(6), 423–434.

Clayton, C. R. I., Priest, J. A. and Rees, E. V. L. (2010). The effects of hydrate cement on the stiffness of some sands. *Geotechnique* 60(6), 435–445.

Collett, T. S., Johnson, A. H., Knapp, C. C., and Boswell, R., (2009). Natural Gas Hydrates: A Review, in T. Collett, A. Johnson, C. Knapp, and R. Boswell, eds., *Natural gas hydrates—Energy resource potential and associated geologic hazards: AAPG Memoir 89*, p. 146– 219.

Collett, T.S. and Ladd, J., (2000). Detection of gas hydrate with downhole logs and assessment of gas hydrate concentrations (saturations) and gas volumes on the Blake Ridge with electrical resistivity log data, in Proceedings of the Ocean Drilling Program, Scientific Results 164, pp. 179-191, eds Paull, C.K., Matsumoto, R., Wallace, P.J. and Dillon, W.P., Texas A&M University, College Station, Texas, Ocean Drilling Program

Collett, T.S., Lewis, R.E., Dallimore, S.R., Lee, M.W., Mroz, T.H. and Uchida, T., (1999). Detailed evaluation of gas hydrate reservoir properties using JAPEX/JNOC/GSC Mallik 2L-38 gas hydrate research well downhole well-log displays, in Scientific Results From JAPEX/JNOC/GSC Mallik 2L-38 gas hydrate research well, Mackenzie Delta, Northwest Territories, Canada, Geological Survey of Canada Bulletin 544, pp. 295-312, eds Dallimore, S.R., Uchida, T. and Collett, T.S., Geological Survey of Canada, Ottawa, Canada.

Cundall, P. A., and Strack, O. D. L., (1979). A discrete numerical model for granular assemblies. *Geotechnique*, 29, No. 1, 47-65.

Dai, S., Santamarina J.C., Waite W.F. and Kneafsey T.J., (2012). Hydrate morphology: Physical properties of sands with patchy hydrate saturation, *Journal of Geophysical Research*, Vol. 117, B11205, doi: 10.1029/2012JB009667

Dai, J., Snyder F., Gillespie D., Koesoemadinata A., and Dutta N. (2008). Exploration for gas hydrates in the deepwater, northern Gulf of Mexico: Part I. A seismic approach based on geologic model, inversion, and rock physics principles, *Mar. Pet. Geol.*, 25, 830–844, doi:10.1016/j.marpetgeo.2008.02.006.

Dai, J., Snyder, F., Gillespie, D., Koesoemadinata, A., and Dutta, N. (2008), Exploration for gas hydrates in the deepwater, northern Gulf of Mexico: Part I. A seismic approach based on geologic model, inversion, and rock physics principles, *Mar. Pet. Geol.*, 25, 830–844, doi:10.1016/j.marpetgeo.2008.02.006.

Drnevich, V. P. (1978), Resonant column testing - problems and solutions, in *Dynamic Geotechnical Testing*, ASTM Spec. Tech. Publ., 654, 394–398.

Dullien, F.A.L. (1992). *Porous Media. Fluid Transport and Pore Structure*, 2nd edition, Academic Press Inc., 1992.

Duran, J. (1999). *Sands, Powders, and Grains: An Introduction to the Physics of Granular Materials* (translated by A. Reisinger). November 1999, Springer-Verlag New York, Inc., New York, ISBN 0-387-98656-1.

Dvorkin, J., M. B. Helgerud, W. F. Waite, S. H. Kirby, and A. Nur (2000). Introduction to physical properties and elasticity models, in *Natural Gas Hydrate: In Oceanic and Permafrost Environments*, edited by M. D. Max, pp. 245–260, Kluwer Acad., Dordrecht, Netherlands.

Dvorkin, J., Prasad M., Sakai A., and Lavoie D. (1999). Elasticity of marine sediments: Rock physics modeling, *Geophys. Res. Lett.*, 26, 1781–1784, doi:10.1029/1999GL900332.

Ebinuma, T., Kamata, Y., Minagawa, H., Ohmura, R., Nagao, J. and Narita, H. (2005), Mechanical properties of sandy sediment containing methane hydrate, in *Fifth International Conference on Gas Hydrates*, pp. 958–961, Tapir Acad., Trondheim, Norway.

Ebinuma, T., Katama, Y., Minagawa, H., Uchida, T., Nagao, J., Takeya, T., Oomura, M., Narita, H. and Chuvilin, E.M. (2003). "Preparation of synthetic methane hydrate specimens and their mechanical properties," *Proceedings of H15 Annual Meeting, Minings and Materials Institute of Japan*, pp. 237-240, in Japanese

Elhakim, A. F., (2005). Evaluation of shallow foundation displacements using soil small-strain stiffness. PhD thesis, Georgia Institute of Technology, August 2005.

Francisca, F., Yun, T.-S., Ruppel, C. and Santamarina, J. (2005). Geophysical and geotechnical properties of near-seafloor sediments in the northern Gulf of Mexico gas hydrate province. *Earth and Planetary Science Letters* 237(3-4), 924–939.

- Freiji-Ayoub, R., Tan, C., Clennell, B., Tohidi, B., and Yang, J., (2007). A wellbore stability model for hydrate bearing sediments. *Journal of Petroleum Science and Engineering*, 57 (1-2), 209–220.
- Guerin, G. and Goldberg, D. (2002). Sonic waveform attenuation in gas hydrate-bearing sediments from the Mallik 2L-38 research well, Mackenzie Delta, Canada. *Journal of Geophysical Research* 107(B5), 1–11.
- Guerin, G., Goldberg, D. & Meltser, A. (1999). Characterization of insitu elastic properties of gas hydrate-bearing sediments on the Blake Ridge. *Journal of Geophysical Research* 104(B8), 17781–17795.
- Guerin, G., Goldberg, D. and Meltser, A., (1999). Characterization of in situ elastic properties of gas hydrate-bearing sediments on the Blake Ridge, *J. Geophys. Res.*, 104, 17781-17795
- Hadley, C., Peters, D., Vaughan, A., and Bean, D. (2008), Gumusut-Kakap project: Geohazard characterisation and impact on field development plans, paper IPTC 12554 presented at the International Petroleum Technology Conference, Soc. of Pet. Eng., Kuala Lumpur, Malaysia, 3–5 Dec. Anderson, B. J., et al. (2008), Analysis of modular dynamic formation test results from the Mount Elbert-01 stratigraphic test well, Milne Point unit, North Slope Alaska, paper presented at the 6th International Conference on Gas Hydrates, Chevron, Vancouver, B. C., Canada, 6–10 July.
- Hardin, B. O., and Drnevich, V. P., (1972). Shear modulus and damping in soils: design equations and curves. *Journal of the Soil Mechanics and Foundations Division*, ASCE, Vol. 98, No. SM 7, pp. 667-692.
- Hashiguchi, K. (1989). Subloading surface model in unconventional plasticity. *International Journal of Solids and Structures* 25(8), 917–945.
- Helgerud, M. B., Dvorkin J., Nur A., Sakai A., and Collett T. (1999). Elastic-wave velocity in marine sediments with gas hydrates: Effective medium modeling, *Geophys. Res. Lett.*, 26, 2021–2024, doi:10.1029/1999GL900421.

Hutchinson, D. R., et al. (2008). Site selection for DOE/JIP gas hydrate drilling in the northern Gulf of Mexico, paper presented at the 6th International Conference on Gas Hydrates, Chevron, Vancouver, B. C., Canada, 6–10 July.

Hyodo, M., Yoneda, J., Nakata, Y., Yoshimoto, N., (2011). Strength and dissociation property of methane hydrate bearing sand. Proceedings of the 7th International Conference on Gas Hydrates (ICGH2011), Edinburgh, Scotland, United Kingdom, July 17-21, 2011.

Itasca (2008), PFC3D: Particle flow code. User's guide version 4.0, Minneapolis, USA, 2008.

Jiang, M. J., Sun, Y. G., Yang, Q. J. (2013), A simple distinct element modelling of the mechanical behaviour of methane hydrate-bearing sediments in deep seabed, *Granular Matter*, 15: 209-220, doi: 10.1007/s10035-013-0399-7.

JIP Leg II Science Team (2009). Gulf of Mexico gas hydrate drilling and logging expedition underway, *Fire in the Ice: Methane Hydrate Newsletter*, spring, pp. 1–6, Off. of Fossil Energy, Natl. Energy Technol. Lab., U.S. Dep. of Energy, Washington, D. C.

Jones, E., et al. (2008). Scientific objectives of the Gulf of Mexico gas hydrate JIP leg II drilling, paper OTC 19501 presented at the Offshore Technology Conference, Am. Assoc. of Pet. Geol., Houston, Tex., 5–8 May.

Jung, J.W, Santamarina, J.C. and Soga, K. (2012) : Stress-Strain Response of Hydrate-Bearing Sands: Numerical Study Using DEM Simulations, *Journal of Geophysical Research - Solid Earth*, Vol. 117, B04202, 12 pp., doi:10.1029/2011JB009040

Kezdi, A. (1974). *Handbook of Soil Mechanics*. Elsevier, Amsterdam.

Kimoto, S., Oka, F., Fushita, T., (2010). A chemothermomechanically coupled analysis of ground deformation induced by gas hydrate dissociation. *International Journal of Mechanical Sciences*, 52 (2), 365–376.

Klar, A., Soga, K., and Ng, M. Y. A. (2010). Coupled deformation-flow analysis for methane hydrate extraction. *Geotechnique*, 60 (10), 765–776.

Kleinberg, R. L. and Dai, J. (2005). Estimation of mechanical properties of natural gas hydrate deposits from petrophysical measurements. OTC 17205, Offshore Technology Conference, Houston, TX, 2–6 May 2005.

Kvenvolden, K. A., (1998). A primer on the geological occurrence of gas hydrate. In: Henriot J. P. & Mienert J. (eds). *Gas hydrates: Relevance to world margin stability and climate change*. Geological Society London Special Publication, 137. pp 9-30.

Kwok, C. Y., (2008). *Micromechanical Modelling of Soil Creep*. Cambridge University, PhD thesis.

Kwon, T.-H., Cho, G.-C., and Santamarina, J. C., (2008), Gas hydrate dissociation in sediments: Pressure-temperature evolution, *Geochem. Geophys. Geosyst.*, 9, Q03019, doi:10.1029/2869 2007GC001920.

Lee, M. W., and Collett, T. S. (2005). Assessments of gas hydrate concentrations estimated from sonic logs in the JAPEX/JNOC/GSC et al. Mallik 5L-38 gas hydrate research production well, in *Scientific Results From the Mallik 2002 Gas Hydrate Production Research Well Program, Mackenzie Delta, Northwest Territories, Canada [CD-ROM]*, edited by S. R. Dallimore and T. S. Collett, *Bull. Geol. Surv. Can.*, 585.

Lee, M. W., and Waite, W. F. (2008), Estimating pore-space gas hydrate saturations from well log acoustic data, *Geochem. Geophys. Geosyst.*, 9, Q07008, doi:10.1029/2008GC002081.

Lee, M. W., Hutchinson, D. R., Collett, T. S. & Dillon, W. P. (1996). Seismic velocities for hydrate-bearing sediments using weighted equation. *Journal of Geophysical Research* 101(B9), 20347–20358.

Lee, M.W., (2000). Gas hydrates amount estimated from acoustic logs at the Blake Ridge, Sites 994, 995 and 997, in *Proceedings of the Ocean Drilling Program*,

---

Scientific Results 164, pp. 193-198, eds Paull, C.K., Matsumoto, R., Wallace, P.J. and Dillon, W.P., Texas A&M University, College Station, Texas, Ocean Drilling Program

Lo Presti, D. C. F., Jamiolkowski, M., Oronzo, P., and Cavallaro, (1996). Rate and creep effect on the stiffness of soils. *Measuring and Modeling Time Dependent Soil Behavior*. GSP No. 61, ASCE, New York, pp. 1263-1280.

Masui, A., Haneda, H., Ogata, Y. and Aoki, K. (2005). The effect of saturation degree of methane hydrate on the shear strength of synthetic methane hydrate sediments. *Proceedings of the 5th Int. Conf. on Gas Hydrates*. June 13-16, Trondheim, Norway. Paper No. 2037.

Masui, A., Haneda, H., Ogata, Y. and Aoki, K. (2005). Mechanical properties of Toyoura sand containing synthetically produced gas hydrate in a triaxial pressure vessel. *The 2nd Int. Workshop on Gas Hydrate Studies and Other Related Topics for the Future Energy and Environment Considerations*. October 22-23, Kitami, Japan.

Masui, A., Haneda, H., Ogata, Y., and Aoki, K. (2006). Triaxial compression test on submarine sediment containing methane hydrate in deep sea off the coast of Japan (in Japanese), paper presented at the 41st Annual Conference, Jpn. Geotech. Soc., Kagoshima, Japan, 12–14 July.

Mavkov, G., Mukerji, T. and Dvorkin, J. (1998). *The Rock Physics Handbook: Tools for Seismic Analysis in Porous Media*, Cambridge University Press, New York

Minh, N. H., and Cheng, Y. P. (2013). A DEM investigation of the effect of particle-size distribution on one-dimensional compression. *Geotechnique*, 63 (1) 44 - 53. 10.1680/geot.10.P.058.

Minh, N.H., Cheng, Y.P., and Thornton, C. (2014). Strong force networks in granular mixtures, *Granular Matter*, February 2014, Volume 16, Issue 1, pp 69-78

O’Sullivan, C. (2002). *The Application of Discrete Element Modelling to Finite Deformation Problems in Geomechanics*. University of California, Berkeley, PhD thesis.

- O'Sullivan, C. (2011). *Particulate Discrete Element Modelling: A Geomechanics Perspective*, Spoon Press, Applied Geotechnics Volume 4, pp. 175-208
- Prat, M., Bisch, E., Millard, A., Mestat, P., and Cabot, G. (1995). *La modelisation des ouvrages*. Hermes, Paris.
- Priest, J. A. (2005). A laboratory investigation into the seismic velocities of methane gas hydrate-bearing sand. *Journal of Geophysical Research* 110(B4), 1–13.
- Priest, J. A., Best, A. I., and Clayton, C. R. I. (2005). A laboratory investigation into the seismic velocities of methane gas hydrate-bearing sand, *Journal of Geophysical Research*, 2005, vol. 110, DOI: 10.1029/2004JB003259
- Priest, J. A., Rees, E. V. L., and Clayton, C. R. I. (2009), Influence of gas hydrate morphology on the seismic velocities of sands, *J. Geophys. Res.*, 114, B11205, doi:10.1029/2009JB006284.
- Priest, J.A., Best, A.I., and Clayton, C.R.I. (2005). A laboratory investigation into the seismic velocities of methane gas hydrate-bearing sand. *Journal of Geophysical Research*, Vol. 110, B04102, doi:10.1029/2004JB033259
- Radjai, F. and Dubois, F. (2011). *Discrete-element of Modeling of Granular Materials*. Preface xv.
- Richart, F. E., Hall, J. R., and Woods, R. D. (1970). *Vibration of Soils and Foundations*, Prentice-Hall, Upper Saddle River, N. J.
- Roscoe, K. H., and Burland, J. B., (1968). *On the generalised stress-strain behaviour of 'wet' clay*. Cambridge University Press, Cambridge.
- Rothenburg, L. and Bathurst, R. J. (1989). Analytical study of induced anisotropy in idealised granular materials. *Geotechnique* 39, No. 8, 1099-1119.

---

Rutqvist, J., and Moridis G. J., (2007), Numerical studies of geomechanical stability of hydrate-bearing sediments, paper presented at the Offshore Technology Conference, Am. Assoc. of Pet. Geol., Houston, Tex., 30 April to 3 May.

Rutqvist, J., Moridis, G. J. , Grover, T., and Collett T., (2008). Geomechanical response of known permafrost hydrate deposits to depressurization-induced production, paper 5726 presented at the 6th International Conference on Gas Hydrates, Chevron, Vancouver, B. C., Canada, 6–10 July.

Santamarina, J. C. and Ruppel, C. (2008). The impact of hydrate saturation on the mechanical, electrical, and thermal properties of hydrate-bearing sand, silts, and clay. In: The 6th International Conference on Gas Hydrates. Vancouver, Canada.

Sitharam, T. G., Dinesh, S. V. and Shimizu, N. (2002). Micromechanical modelling of monotonic shear behaviour of granular media using three dimensional DEM. *Int. J. Numer. Analyt. Methods Geomech.* 26, No. 12, 1167-1189.

Sitharam, T. G., Vinod, J. S. and Ravishankar, B. V. (2009). *Geotechnique* 59, No. 9, 739-749.

Soga, K., Lee, S.L., Ng, M.Y.A. and Klar, A. (2006). Characterisation and engineering properties of methane hydrate soils. *Characterisation and Engineering Properties of Natural Soils*, Taylor and Francis, Vol. 4, pp.2591-2642.

Song, C.; Wang, P. & Makse, H.A. (2008). A phase diagram for jammed matter. *Nature* 453 (7195): 629–632. arXiv:0808.2196. Bibcode:2008Natur.453..629S. doi:10.1038/nature06981. PMID 18509438

Stokoe, K. H., Darendeli, M. B., Andrus, R. D., and Brown, L. T. (1999). Dynamic soil properties: Laboratory, field and correlation studies, paper presented at 2nd International Conference on Earthquake Geotechnical Engineering, Portuguese Geotech. Soc., Lisbon, Portugal

- U. S. Department of Energy (2011). Energy Resource Potential of Methane Hydrate: An introduction to the science and energy potential of a unique resource. National Energy Technology Laboratory, February 2011.
- Uchida, S., Soga, K., and Yamamoto, K. (2012). Critical state soil constitutive model for methane hydrate soil. *Journal of Geophysical Research: Solid Earth* (1978-2012), 117 (B3)
- US Geological Survey (2013), Gas hydrate: What is it?, accessed 21 March 2013
- Waite, W. F., Santamarina, J. C., Cortes, D. D., Dugan, B., et al., (2009). Physical properties of hydrate-bearing soils. *Rev. Geophys*, 47(RG4), 3–41.
- Waite W., Bratton, P. M., Mason, D. H. (2011). Laboratory formation of non-cementing, methane hydrate-bearing sands. Proceedings of the 7<sup>th</sup> International Conference on Gas Hydrates (ICGH 2011), Edinburgh, Scotland, United Kingdom.
- Walia, R., Mi, Y., Hyndman, R.D. and Sakai, A., (1999). Vertical seismic profile (VSP) in the JAPEX/JNOC/GSC Mallik 2L-38 gas hydrate research well downhole well-log displays, in *Scientific Results From JAPEX/JNOC/GSC Mallik 2L-38 gas hydrate research well, Mackenzie Delta, Northwest Territories, Canada*, Geological Survey of Canada Bulletin 544, pp. 341-355, eds Dallimore, S.R., Uchida, T. and Collett, T.S., Geological Survey of Canada, Ottawa, Canada.
- Walsh, M. R., Hancock, S. H., Wilson, S. J., Patil, S. L., Moridis, G. J., Boswell, R., Collett, T. S., Koh, C. A., and Sloan, E. D. (2009), Preliminary report on the commercial viability of gas production from natural gas hydrates, *Energy Econ.*, 31, 815–823, doi:10.1016/j.eneco.2009.03.006.
- Westbrook, G. K., et al. (2005), Measurement of P- and S-wave velocities, and the estimation of hydrate concentration at sites in the continental margin of Svalbard and the Storegga region of Norway, paper 3004 presented at the Fifth International Conference on Gas Hydrates, pp. 726–735, Tapir Acad., Trondheim, Norway.

Wilder, J. W., et al. (2008). An international effort to compare gas hydrate reservoir simulators, paper presented at the 6th International Conference on Gas Hydrates, Chevron, Vancouver, B. C., Canada, 6–10 July.

Winters, W. J. (2000), Stress history and geotechnical properties of sediment from the Cape Fear Diapir, Blake Ridge Diapir, and Blake Ridge, Proc. Ocean Drill. Program Sci. Results, 164, 3439 421–429.

Winters, W. J., Pecher, I. A., Waite, W. F. & Mason, D. H. (2004). Physical properties and rock physics models of sediment containing natural and laboratory-formed methane gas hydrate. *American Mineralogist* 89(8-9), 1221–1227.

Winters, W. J., Waite, W. F., Mason, D. H., Dillon, W. P., and Pecher, I. A. (2002), Sediment properties associated with gas hydrate formation, paper presented at the Fourth International Conference on Gas Hydrates, Jpn. Natl. Oil Corp., Yokohama, Japan, 19–23 May.

Wood, W.T. and Ruppel, C., (2000). Seismic and thermal investigations of the Blake Ridge gas hydrate area: A synthesis, in Proceedings of the Ocean Drilling Program, Scientific Results 164, pp. 253-264, eds Paull, C.K., Matsumoto, R., Wallace, P.J. and Dillon, W.P., Texas A&M University, College Station, Texas, Ocean Drilling Program

Xu, X., Ling, D., Cheng, Y. P., and Chen, Y. (2012). The proceedings of the International Symposium on Discrete Element Modelling of Particulate Media, Birmingham, RSC Publishing, March 2012, pp. 255-263.

Yun T.S., (2005). Mechanical and thermal study of hydrate bearing sediments, Georgia Institute of Technology, PhD thesis

Yun, T. S., Francisca F. M., Santamarina J. C., and Ruppel C. (2005). Compressional and shear wave velocities in uncemented sediment containing gas hydrate, *Geophys. Res. Lett.*, 32, L10609, doi:10.1029/2005GL022607.

Yun, T. S., Lee, C., Lee, J.-S., Bahk, J. J. and Santamarina, J. C. (2011). A pressure core based characterization of hydrate-bearing sediments in the Ulleung Basin, Sea of Japan (East Sea). *Journal of Geophysical Research* 116(B2), 1–12.

Yun, T. S., Santamarina, J. C., and Ruppel, C. (2007). Mechanical properties of sand, silt, and clay containing tetrahydrofuran hydrate, *J. Geophys. Res.*, 112, B04106, doi:10.1029/2006JB004484.

Yun, T.S., Santamarina, J.C., and Ruppel, C. (2007), Mechanical properties of sand, silt, and clay containing tetrahydrofuran hydrate, *Journal of Geophysical Research*, VOL. 112, B04106, doi:10.1029/2006JB004484